LABORATÓRIO NACIONAL
DE ENGENHARIA CIVIL

DEPARTAMENTO DE ESTRUTURAS
Núcleo de Engenharia Sísmica e Dinâmica de Estruturas

Proc. 0305/1/15027

CYCLIC TESTS OF JOINTS FROM A REINFORCED CONCRETE PRECAST BUILDING SYSTEM

Trabalho realizado para o projecto:
PRECAST STRUCTURES EC8 – Seismic Behaviour of Precast Concrete Structures with Respect to Eurocode 8

Lisboa • Fevereiro de 2007

I&D ESTRUTURAS

RELATÓRIO 30/**2007 – NESDE**

TABLE OF CONTENTS

FIGURE INDEX

TABLE INDEX

1 INTRODUCTION

This report describes the second phase activity of the Portuguese group in the *Precast Structures EC8* research project. The Portuguese group is composed by *Laboratório Nacional de Engenharia Civil* (LNEC) and the *Civibral, S.A.* precast company. This phase follows the shaking table tests of a 2 stories structure of the same precast system, which is commercialized by *Civibral*. More information about these tests can be found in the report [Mendes et al. 2006].

The goal of the work presented in this document is to assess the seismic behaviour of column-foundation and beam-column connections from the same precast system. To help achieve this goal, 4 column-foundation and 10 beam-column connections were tested using quasi-static, monotonic and cyclic tests, which were made imposing displacements to the specimens. The column-foundation connections (CFC) can be categorized as socket connections and the beam-column connections (BCC) as dry connections using only mechanical devices to transmit forces between elements. All the specimens were supplied and mounted by *Civibral* personal.

It was decided to test also scaled connections as used in the 2 stories structure tested in the shaking table (1:3 geometric scale). This strategy allows a direct comparison to the results from the previous tests, with improved accuracy, because, this way scaling problems are avoided.

This report presents the results and the seismic behaviour analysis of the tested connections. The text is organized in 7 sections. After this introduction, is discussed the prototype-model idealization, and afterwards the results and analysis of the precast connections. At last, the test conclusions, acknowledgments and bibliography are presented. To make the text more readable, the majority of the test data is presented in 8 annexes and only summaries of results are presented in the main text.

2 PROTOTYPE – MODEL IDEALIZATION

As mentioned before, 1:3 scaled joints were used in the tests in order to improve the comparison with the results from the shaking table tests (see Figure 2.1 and [Mendes et al. 2006]).

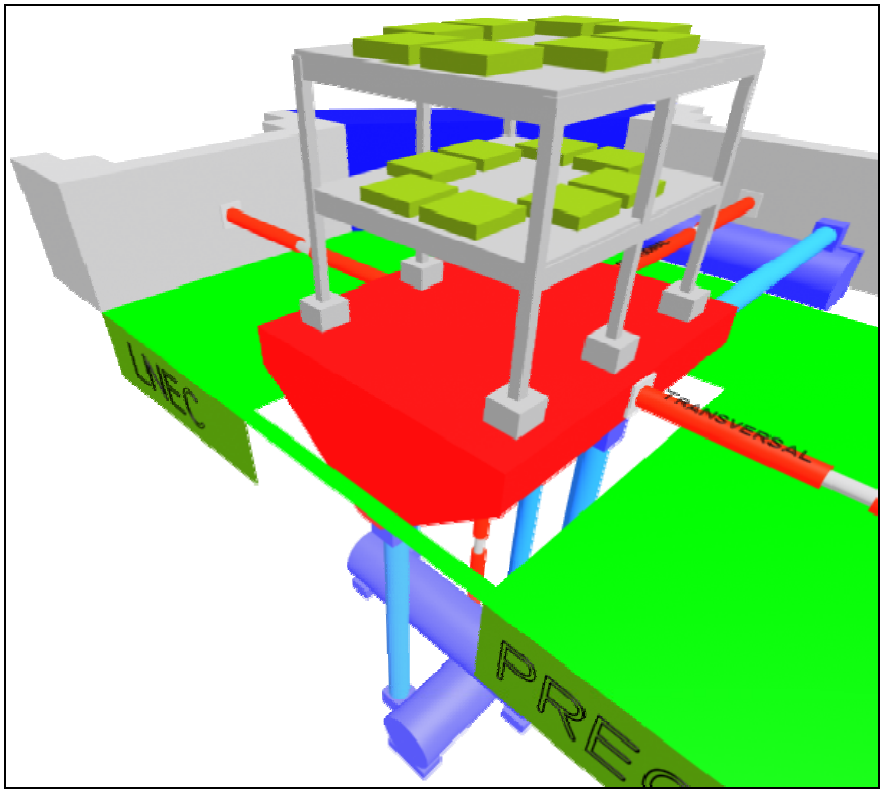

Figure 2.1: 3D Visualization of the two stories structure tested on LNEC's shaking table.

The similitude conditions are based in the following relationships: i) the same materials of the prototype – RC (2.1); and ii) a 1:3 geometric scale (2.2):

$$E_P / E_M = 1, \tag{2.1}$$

$$L_P / L_M = \lambda = 3. \tag{2.2}$$

These relations defines all the relevant scale factors for a quasi-static test (see Table 2.1).

The data presented in Table 2.1, reveals that for obtaining the equivalent prototype displacements it is necessary to multiply by 3 (λ) the values obtained in the model, and, for the forces and moments by 9 (λ^2) and 27 (λ^3), respectively. Because the rotations and strains are dimensionless, the equivalent values in the prototype are equal to the measured in the model, so no scaling is required.

Parameter	Unit	Symbol	Scale Factor $(\ )_P/(\ )_M$
Length	L	L	$L_P/L_M=\lambda=3$
Modulus of elasticity	$F.L^{-2}$	E	$E_P/E_M=1$
Area	L^2	A	$\lambda^2=9$
Volume	L^3	V	$\lambda^3=27$
Displacement	L	d	$\lambda=3$
Rotation	–	θ	1
Weight	F	w	$\lambda^2=9$
Force	F	F	$\lambda^2=9$
Moment	F.L	M	$\lambda^3=27$
Stress	$F.L^{-2}$	σ	1
Strain	–	ε	1
Energy	F.L	W	$\lambda^3=27$

Table 2.1: Similitude scale factors.

3 COLUMN–FOUNDATION CONNECTIONS

3.1 Introduction

Four column-foundations connections (CFC) were tested (specimens P1 to P4). These connections can be categorized as socket connections and were concreted by *Civibral*, in their facilities, into two distinct elements: i) the footings and ii) the columns. A cavity was left on the footings top, where, afterwards, part of the column was inserted during mounting. The gaps between the two elements were filled with mortar resulting in the final layout of the specimens tested (see Figure 3.1). All the elements, including the mortar filling the gaps, were tested after completing more than 28 days after concreting.

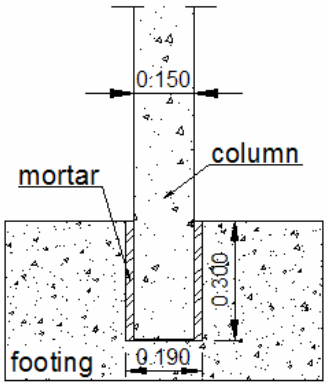

Figure 3.1: Socket connection scheme.

Although, this type of connection was not used in the specimen tested in the shaking table, as the column and footings were cast in one monolithic element (see [Mendes et al. 2006]), it was considered relevant to test these type of elements, which are part of the precast system commercialized by *Civibral* and very common in other precast solutions.

3.2 Test setup

The tests were made using the LNEC's uniaxial shaking table to impose displacements to the specimens (see Figure 3.2). To ensure that the displacement imposed were not affected by the flexibility and/or gaps of the layout, resulting in different values measured on the displacement transducers LVDT D1 and LVDT D2 (see Figure 3.2), a digital PID algorithm [NI 2001] was implemented to control the real displacements imposed to the specimen. A guiding system was also used to avoid truss deviations in the push movements.

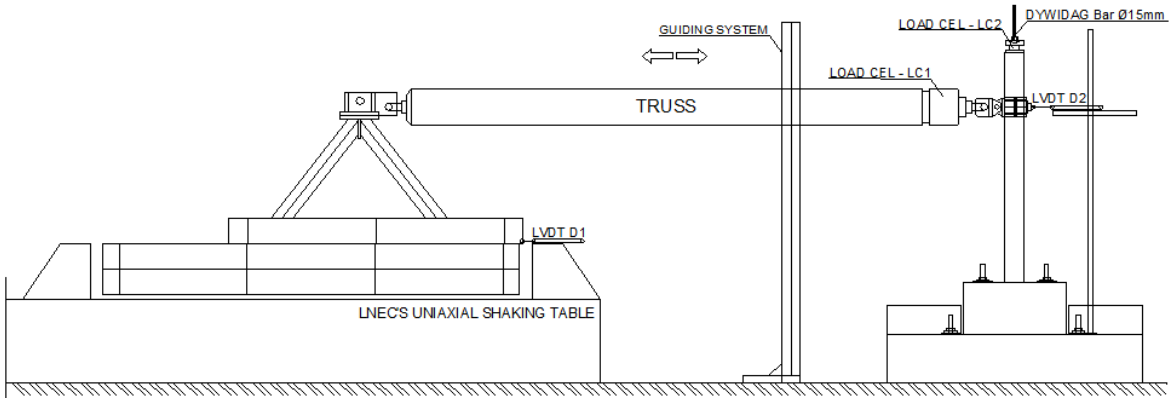

Figure 3.2: Schematic view of the test setup.

More detailed information of the test setup is presented in the Annex A drawings and a selection of photographs in Annex C (Figures C.1 to C.4).

The column axial load was simulated using a *Dywidag* bar inside the column that allows choosing different levels of compression (see Figure 3.2).

The specimen was instrumented with the following type of sensors:

1. 3D optical displacement measuring system – Model K600 manufactured by *Krypton/Metris*, was used to measure the displacements of several point in the specimens (see Drawing nº12 and nº13 in Annex A);
2. Inductive displacement transducers – Models manufactured by *RDP Electronics* were used to measure the shaking table and specimen top displacements. The last one was also used to implement the PID algorithm;
3. Piezoelectric accelerometers – *PCB Piezotronic*s, model 393A03, were used for the dynamic characterization tests;
4. Load cells – *Instron*, model 2518-121 was used to measure the load installed in the truss. A ring load cell, manufactured by LNEC, was used to measure the axial load applied to the columns.

More information about these sensors technical specifications is available in Annex B.

Photographic and video recording were also made during the tests. The photographs were taken using a digital camera and the video records were made using a tripod mounted camera.

3.3 Test programme

The first specimen (P1) was tested monotonically up to 6.2% of drift and the specimens P2 to P4 were tested cyclically up to 5.1%. The value of the column's axial load, applied by the Dywidag bar, was chosen independently of the prior dynamic shaking table test, because this type of connection was not implemented on that specimen. The initial idea was to adopt usual service levels of axial load and then try to establish a basic parametric study, to assess the effect of this parameter in the connection response. Due to reasons presented afterwards, it was decided to stop the CFC tests with only 4 specimens tested, and consequently, the parametric study was not completed has initially programmed. The mean axial load installed on the column varied from about 100 kN (ν=0.13) to 140 kN (ν=0.19), see Table 3.1.

Specimen	**Test Type**	**Disp. Range** [cm]	**Max. Drift** [%] (h[mm])	**Mean Axial Load** [kN]	$\nu = N/(A_c f_{cm})$
P1	Monotonic	[0.00; 10.20]	6.2 (1500)	-101.7	-0.14
P2	Cyclic	[-7.00; 7.00]	5.1 (1375)	-97.0	-0.13
P3	Cyclic	[-7.00; 7.00]	5.1 (1375)	-113.3	-0.15
P4	Cyclic	[-7.00; 7.00]	5.1 (1375)	-139.7	-0.19
Note: f_{cm} (C25/30) = 33 MPa [CEN 2001]					

Table 3.1: Test programme.

The monotonic test (specimen P1) was used to provide some basic characteristics of the RC element, like the yielding displacement (δ_y) which was 3.70 cm (see Figure E.4). However, the position where the displacements were imposed to the specimen, changed from P1 (h=1.500 mm) to P2 and subsequent (h=1.375mm), to improve the maximum available drift. To take in account this layout change, the equivalent δ_y for the new situation, was computed with the displacement curve of a cantilever column:

$$d(x) = \frac{d_{\max}}{L^3}\left(\frac{3}{2}L x^2 - \frac{x^3}{2}\right) \Leftrightarrow \begin{cases} d_{\max} = 0.037\,m \\ d(1.375) = 0.875\ 0.037 = 0.0323\,m \end{cases}. \quad (3.1)$$

This value (δ_y=3.23 cm) was used to define the cycles adopted in the following tests as presented in Table 3.2. The last series of cycles (cycle #9 in Table 3.2) were made with increased velocity and with the maximum amplitude. This last series ended only when the full collapse of the section occurred (in all cases with the rupture of steel reinforcements), so the number of cycles varied from specimen to specimen.

Cycle	Nº cycles	Amplitude		Drift	Velocity
#1	3	16.7% δ_y	±0.54 cm	0.39%	0.1 cm/s
#2	3	33.3% δ_y	±1.07 cm	0.78%	0.1 cm/s
#3	3	66.7% δ_y	±2.16 cm	1.57%	0.1 cm/s
#4	3	100.0% δ_y	±3.23 cm	2.35%	0.1 cm/s
#5	3	133.3% δ_y	±4.30 cm	3.13%	0.1 cm/s
#6	3	166.7% δ_y	±5.38 cm	3.91%	0.1 cm/s
#7	3	200.0% δ_y	±6.46 cm	4.70%	0.1 cm/s
#8	3	Max. range	±7.00 cm	5.09%	0.1 cm/s
#9	n	Max. range	±7.00 cm	5.09%	0.5-1 cm/s

Table 3.2: Definition of the cycles.

3.4 Observed behaviour

During the tests was possible to observe the following behaviour:

- Initially, well defined bending cracks appeared through the column length (see Figure C.5, C.9 and C.11);
- Gradually, damage concentrated at about 0.35 m from the footing (see Figure C.5, C.9, C.11 and Drawing nº4 in Annex A);
- Some inclined cracks appear near the most damaged zone (see Figure C.4, C.5, C.9 and C.11), probably due to shear caused by moment variations;
- The element collapsed after sustaining severe damage and reinforcement failure;
- The base of the column and the column-foundation connection revealed a good response, with very small relative displacements and very low visible damage (see Figure C.5 to C.12);
- After inspecting the reinforcements, additional bars were found inside the column (see Figure C.6, C.12 and Drawing nº4 in Annex A).

In all CFC specimens, the collapse occurred in the column (≈0.35 m from the footing), so the column-footing connection was not involved in the collapse mechanism. For this reason, the CFC tests were interrupted after testing 4 specimens.

3.5 Experimental frequencies

Just before the CFC tests, the specimens were subject to dynamic characterization tests in order to obtain some basic dynamic properties. It was identified the specimen's natural frequency in the direction of the cyclic tests, in order to compare them with the results from analytical models and to access the relative stiffness of the specimens, enabling the detection of any abnormal behaviour (e.g a major construction defect), that could produce erroneous results. The experimental frequencies were identified using impact or ambient vibrations and are presented in Table 3.3 and in Annex D.

Specimen	**Excitation**	**Frequency [Hz]**
P1	Ambient	23.8
P2	Impact	20.3
P3	Impact	20.2
P4	Impact	19.1
Mean	**–**	**20.9**

Table 3.3: Experimental frequencies (before the tests).

The results for each specimen reveal very similar numeric values, with only a slightly difference in the higher frequency obtained for specimen P1 (23.8 Hz). This specimen's natural frequency was identified with ambient vibration, which in this case, produced results with less quality (see Figure D-1), and proven to be less reliable than the impact tests used in the following specimens (see Figure D-2 to D4). In conclusion, no abnormal behaviour was identified in the specimens.

These values can be compared to the analytical results of a cantilever system with distributed mass. The expression for calculation the natural frequencies can be found in the literature [Clough et al. 1993]. Computing for an uncracked specimen:

$$\begin{cases} f_1 = \dfrac{(\alpha_1)^2}{2\pi}\sqrt{\dfrac{EI}{m}} = \dfrac{1.04167^2}{2\pi}\sqrt{\dfrac{31\times10^6 \;\; 0.15^4/12}{5.733\times10^{-2}}} = 26.1\,Hz \\ \alpha_1 = \dfrac{1.875}{L} \end{cases} . \qquad (3.2)$$

As expected, the value obtained in (3.2) is higher than the ones from the experimental campaign, mainly due to rotational flexibility of the footing-column base and due to additional flexibility in the element (e.g cracking). The values obtained experimentally are considered as coherent with the analytical model.

3.6 Global forces and displacements

The time histories of the global forces, bending moments, displacements and rotations are presented in Annex E. To compute some of those values it was necessary to take in consideration the effect of the axial load system to the effective force applied to the column. Analysing the Figure 3.3, it is possible to conclude that in a cross section where the Dywidag bar is inclined from the vertical, the column receives less lateral force that the one measured in the load cell, because part is contra balanced by the horizontal component of the force installed in the Dywidag bar. Using the two measured displacements (L2 and L3 in Drawing 13 of Annex A) it was possible to compute the rotation of the column and then remove this effect, resulting in the effective forces and moments, identified with the subscript "eff".

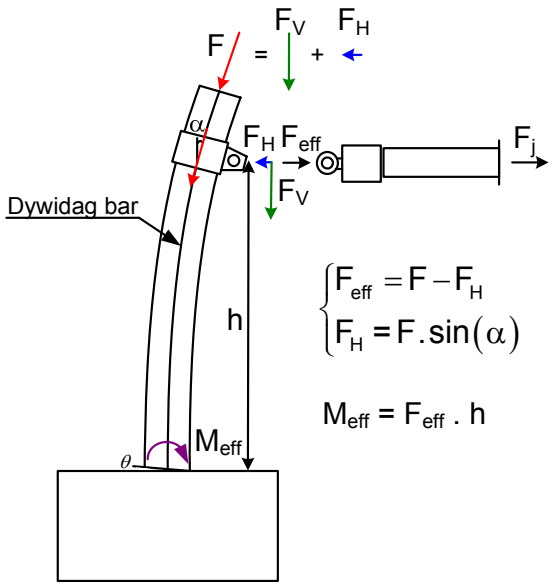

Figure 3.3: Effect of the axial load system in the effective force applied to the column.

A summary of the maximum global forces and displacements is presented in Table 3.4. These results are very coherent, especially between the cyclic tests where the numeric values are very close. The results from the monotonic test indicate smaller maximum forces/moments and displacements, even after reaching higher drifts (6.2% vs. 5.1%). This can result of very low residual stiffness in the monotonic specimen, so for the additional drift (displacement) increment does not result in a real increment of force. On the other hand, the cyclic tests can reach higher forces/moments due to incomplete crack closure between cycles, which results in new contact points that allow reaching higher forces for the same maximum drift.

Specimen	Applied Load (F_j) [kN]	Effective Load (F_{eff}) [kN]	Connection Moment (M_{eff}) [kN.m]	Connection Rotation (θ) [º]
P1	17.6	12.7	19.1	0.23
P2	19.1	15.9	21.8	0.34
P3	19.3	15.4	21.2	0.36
P4	19.9	14.3	19.7	0.27
Mean*	**19.4**	**15.2**	**20.9**	**0.32**
Note: * Mean values refer only to cyclic tests.				

Table 3.4: Maximum forces and displacements.

With the simplified model presented in Figure 3.4, it was possible to compute an estimation of the maximum resistance of the section. The maximum resisting bending moment is presented in Table 3.5, for the case of an axial load of 111.4 kN (ν=0.15).

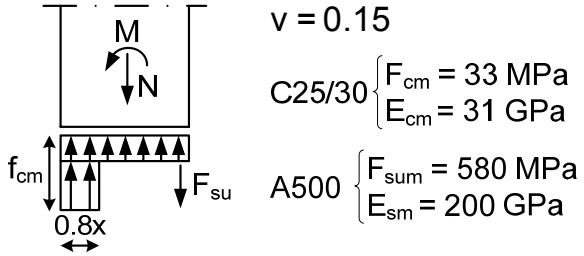

Figure 3.4: Simplified model for estimating the ultimate resisting moment.

Reinforcements	M_{RU} [kN.m]
$4\phi12$	25.2
$2\phi12$	15.1

Table 3.5: Ultimate resisting moment.

The bending moment distributes linearly in the column, so this value where the number of reinforcements changes from 4 to 2 (h≈0.35m, see Drawing nº4 in Annex A), can be calculated from the maximum moment at the connection (20.9 kN.m):

$$M(h=0.35) = 20.9 \times (1.50 - 0.35) / 1.50 = 16.0\,\text{kN.m}\,. \tag{3.3}$$

When compared with the results obtained with the simplified model presented in Figure 3.4, where for $2\phi12$ the ultimate resisting moment is 15.1 kN.m, it is possible to conclude that the collapse where the number of reinforcements changes is coherent with these calculations.

The graph presented in Figure 3.5 represents a typical plot of the force vs. displacement at the top of the column. In this case all the cycles until the full collapse of the element are

represented. The behaviour of the element was of good quality and typical of a monolithic RC structure. It is visible stable hysteretic cycles resulting in high energy dissipation. During the cycles pinching is not much present due to the presence of axial forces that improves crack closing. The full collapse of the element occurred after cover spalling of the compressed concrete, buckling of reinforcements, and finally, with the rupture of the reinforcements, weakened by the concentration of rotations, buckling and fatigue (see Figure C-8 and C-12).

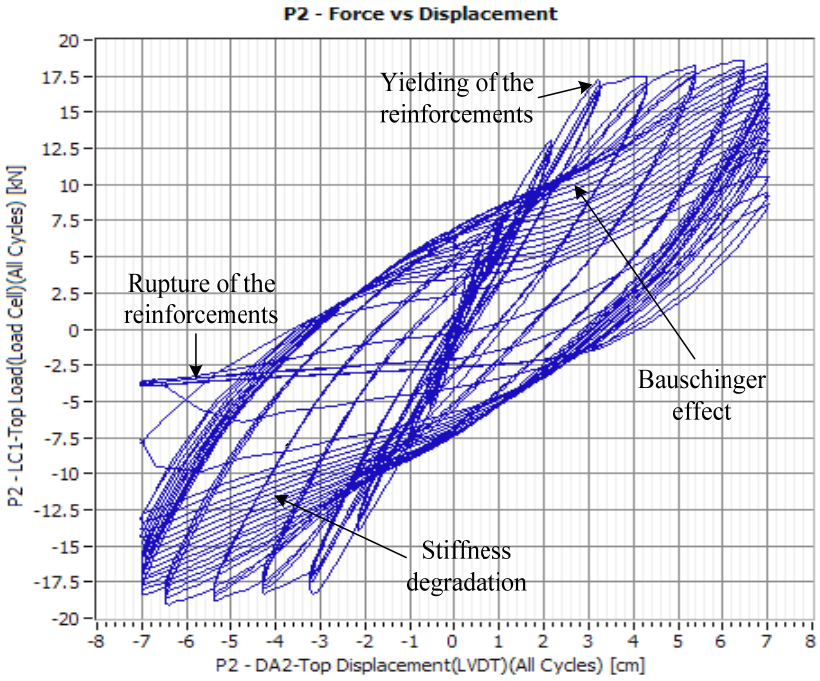

Figure 3.5: Typical hysteretic cycles.

3.7 Local displacements

The relative displacements between column and footing were measured during the tests on specimen P4. It was used two groups of two nearby measuring points, one connected to the column and one connected to the footing (the position of the measured points is indicated in Drawing nº13 on Annex A, see Figure C-11). The maximum values are presented in Table 3.6.

These numeric values reveal that the relative displacements were very small (all ≤0.53 mm), even after very large drifts (>5%). This response indicate that the column and footing move together as one element and the mortar in the joint is effective, confirming the observed behaviour.

Specimen	Position	Direction	**Relative Displacement** [mm]
P4	L24-25	x (horiz.)	0.22
P4	L24-25	z (vert.)	0.48
P4	L24-25	$\sqrt{dx^2 + dz^2}$	0.53
P4	L26-27	x (horiz.)	0.22
P4	L26-27	z (vert.)	0.43
P4	L26-27	$\sqrt{dx^2 + dz^2}$	0.48

Table 3.6: Maximum relative displacement between footing and column base.

3.8 Energy balance

In the system composed by the external forces, applied by the shaking table, and internal forces, developed in the specimen, the total work W_t must be null (even for non-conservative systems):

$$W_t = W_e + W_i = 0\,. \tag{3.4}$$

The internal work W_i includes the recoverable elastic strain energy E_s and the irrecoverable hysteretic energy E_h:

$$W_i = E_s + E_h\,. \tag{3.5}$$

Starting and ending the calculation of the accumulated internal work, with the specimen not subjected to external forces, the accumulated internal work is due to the dissipated hysteretic energy, which is equal to the input energy.

The total work done by the external forces, or input energy, is presented in Annex G and a summary in Table 3.7. These values were obtained using the expression:

$$E_i = \sum_{i=1}^{NS-1} \frac{F_i + F_{i+1}}{2}\left(d_{i+1} - d_i\right), \tag{3.6}$$

where:

- F (F_{eff}) – is the force measured in the load cell LC1 (effective force applied to the column, see Figure 3.3);
- d – is the imposed displacement measured at LVDT D2.

The input energy calculated using the effective force (F_{eff}) can be considered as the symmetric of the work done by the specimen's internal forces. In contrast, using the measured force in the load cell (F) to compute (3.6), will result in the symmetric of the internal forces of both specimen and Dywidag bar.

Specimen	Type	Force	Total Input Energy [kN.m]	Difference
P1	Monotonic	Measured	1.47	1.3%
P1	Monotonic	Effective	1.49	
P2	Cyclic	Measured	13.64	42.5%
P2	Cyclic	Effective	9.57	
P3	Cyclic	Measured	11.89	–
P3	Cyclic	Effective	*	
P4	Cyclic	Measured	11.50	15.3%
P4	Cyclic	Effective	9.97	

Notes:
* value not presented due to synchronization problems between equipment;
In the cyclic tests the time histories were cropped at the end of the third 7 cm cycle.

Table 3.7: Total input energy.

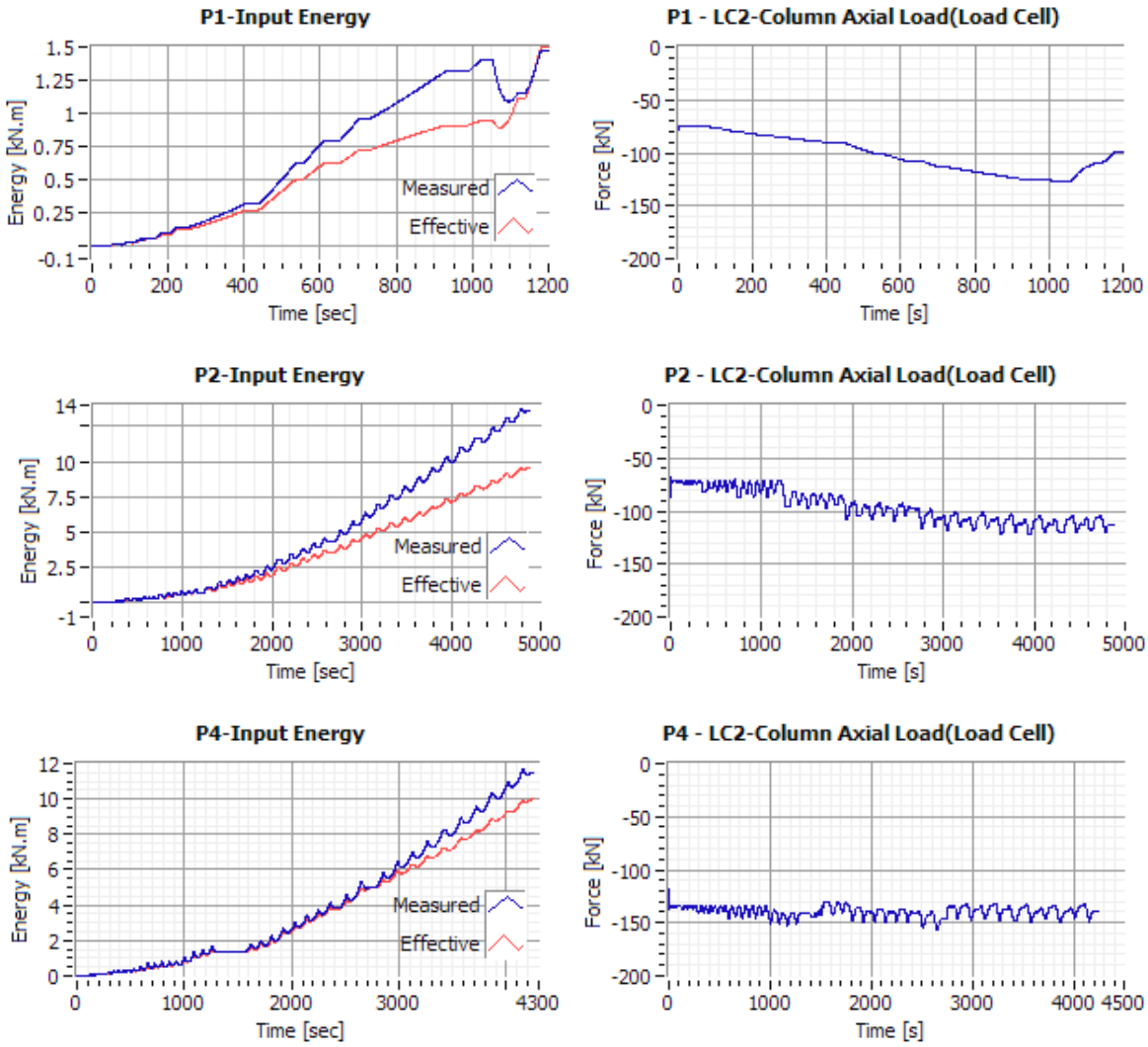

Figure 3.6: Comparison between input energy calculated with the measured and effective force.

If all internal work done by the Dywidag bar is elastic, the resulting total work should not be changed, because this recoverable energy reduces the amount of external energy

necessary during the return to origin displacements. This is the case of the P1 monotonic test (see Figure 3.6), where this effect is perceptible at the end of the time history.

Analysing the numeric results presented in Table 3.7 is possible to observe that for each specimen the values obtain with the measured vs. effective force, differs up to 42.5% (specimen P2). An explanation for this behaviour is related with the variations in the axial load, which increases and decreases in each cycle due to element elongation, caused by geometric configurations, and globally increases throughout the test due to concrete dilatancy in the damage areas (see Figure 3.6). The changes in the axial load are already taken in consideration in the effective force, but are not in the forces measured at the load cell, so these values are influenced by this phenomenon. In conclusion, the value of the total energy obtained by the measured force is higher then the obtained from the effective force and this effect is more significant in the specimens where the variation of axial load is higher, like specimen P2 (see Figure 3.6). These differences can also be related to non-linear phenomena in the Dywidag bar or with synchronization errors.

In the tests for the specimens P3 and P4 the variation of axial load were reduced by releasing some axial load during the test.

Analysing the data presented is possible to observe and conclude the following:

- Around ten times more energy was dissipated in the cyclic tests than in the monotonic test;
- The total input energy required for the cyclic tests of each specimen was similar;
- The cycles are stable and the specimens were able to dissipate energy steadily. This is visible through the gradual increments of input energy required to deform the specimens in successive cycles.

It is interesting to notice that the variations on the energy input within each cycle are higher for the input energy computed using the measured force, because it includes also the energy absolved elastically by the Dywidag bar, which requires more energy but gives it back to the system, causing higher variations in the accumulated energy time histories (see Figure 3.6).

3.9 Conclusions

With the data of the CFC tests presented in this report was possible to extract the following conclusions:

- The tested socket connections revealed a very good response in the monotonic and cyclic tests;
- The connections had enough resistance and presented no relevant stiffness degradation during the tests;
- The relative displacements between the two precast elements (column and foundation) were very small;
- The connection was not part in the collapse mechanism, which in all cases occurred in the span of the element;
- The collapse mechanism was typical of a monolithic reinforced concrete structure;
- The additional reinforcements found inside the column are the cause of the collapse mechanism at approximately 35 cm from the footing (see Drawing nº4 in the Annex A);
- The total area of reinforcements in the base of the column exceeds the maximum value prescribed by some design codes $A_s / A_c > 4\%$ (e.g. [CEN 2001];
- The amount and distribution of the reinforcements found inside the column could be optimized and improved to produce a more efficient response to seismic loads.

4 BEAM–COLUMN CONNECTIONS

4.1 Introduction

Two types of beam-column connections (BCC) were tested in a total of 10 specimens (5 VL and 5 V type specimens). In the VL specimens the columns are connected to L shaped beams (see Figure 4.1–b). During the erection of the structure, the beams are supported by hollow box sections that are firmly connected inside the columns. On top of the beams there is a steel plate where a pre-stressed bolt connects the plate to the hollow box. The steel plate is also connected to the column using welded bolts. The voids in the connections are filled with a mortar through an inclined hole. In the V specimens the connection is similar to the VL type (see Figure 4.1–a). The major difference consists in using another steel plate instead of the hollow box referred before.

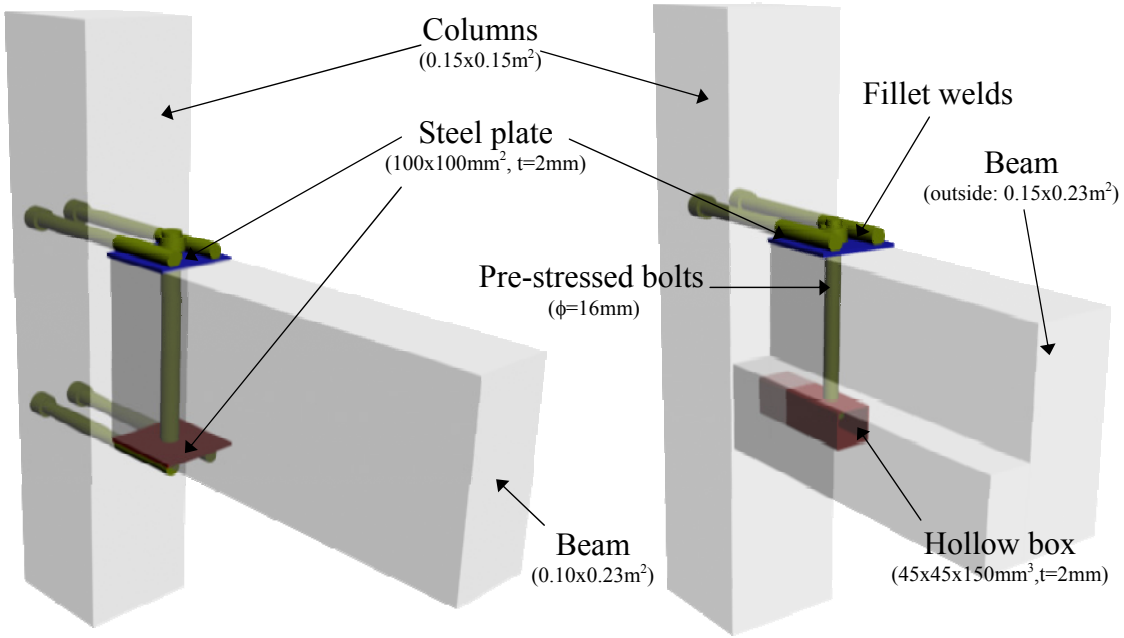

Figure 4.1: Schematic view of the tested connections types.

This two types of BCC are similar to the ones used in the specimen tested in the shaking table (see [Mendes et al. 2006]), with the only difference in the V specimens, which has a second steel plate instead of an angle steel section. All these connections are part of the precast building system commercialized by *Civibral*, who supplied and mounted all specimens. All the elements, including the mortar filling the voids, were tested after completing more than 28 days after concreting.

4.2 Test setup

The test setup used in the BCC tests is similar to the one from the CFC tests (see §3.2). The LNEC's uniaxial shaking table was used to impose displacements to the specimens and the PID control algorithm was also used to control deviations from the prescribed displacements, due to flexibility and/or gaps of the layout. The guiding system and the truss, connecting the shaking table and the specimen, were also used (see Figure 4.2).

More detailed information about the test setup is presented in Annex A drawings and a selection of photographs in the Annex C (Figures C.1 to C.4).

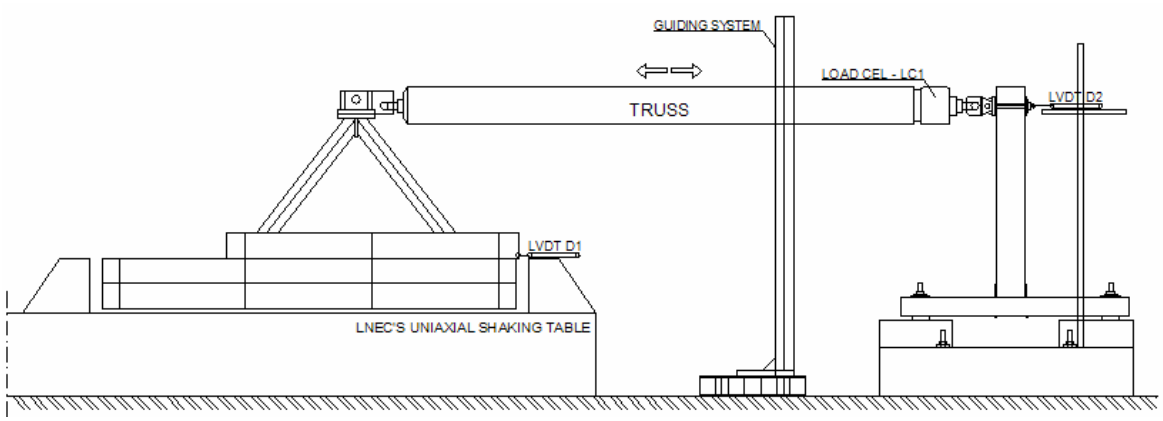

Figure 4.2: Schematic view of the test setup.

One important characteristic of the BCC test layout is related with the inversion of the position of the columns and beams, meaning that the columns are in the horizontal position and the beams in the vertical (see Figure 4.2). This position swap is caused by using the shaking table to impose displacements and produces a slight compression at the joint, caused by the self weight of the beam (123-144 kgf) and ½ the weight of the truss (≈150 kgf). In the author's opinion, although not an ideal solution, this fact did not influence significantly the overall results of the BCC tests.

The sensors used in the measurements are identical to the ones used in the CFC tests (see §3.2). The only difference consists in not using the ring load cell because no axial load is required. Photographic and video recording were also made during the tests.

More information about the sensors technical specifications is available in Annex B.

4.3 Test programme

As mentioned before, 5 V type and 5 VL type specimens were tested. The first specimen of each group was tested monotonically to about 8-9% of drift. The rest of the specimens were tested cyclically up to 4.3% of drift (see Table 4.1).

Specimen	**Test Type**	**Disp. Range** [cm]	**Max. Drift** [%] (h[mm])	**Cycles** (see Table 4.2)
V1	Monotonic	[0.00; 13.51]	9.0 (1500)	–
V2	Cyclic	[-6.50; 6.50]	4.3 (1500)	#3, #4, #5, #6
V3	Cyclic	[-6.50; 6.50]	4.3 (1500)	#1, #2, #3, #4, #5, #6
V4	Cyclic	[-6.50; 6.50]	4.3 (1500)	#1, #2, #3, #4, #5, #6
V5	Cyclic	[-6.50; 6.50]	4.3 (1500)	#1, #2, #3, #4, #5, #6
VL1	Monotonic	[0.00; 13.00]	8.7 (1500)	–
VL2	Cyclic	[-6.50; 6.50]	4.3 (1500)	#2, #3, #4, #5, #6
VL3	Cyclic	[-6.50; 6.50]	4.3 (1500)	#2, #3, #4, #5, #6
VL4	Cyclic	[-6.50; 6.50]	4.3 (1500)	#1, #2, #3, #4, #5, #6
VL5	Cyclic	[-6.50; 6.50]	4.3 (1500)	#1, #2, #3, #4, #5, #6

Table 4.1: Test programme.

The sequence and the amplitude of the cycles are presented in Table 4.2. Not all specimens were subjected to the complete group of cycles as indicated in Table 4.1.

Cycle	**Nº cycles**	**Amplitude**		**Drift**	**Velocity**
#1	3	12.5%	±0.81 cm	0.54%	0.05 cm/s
#2	3	25.0%	±1.63 cm	1.09%	0.05 cm/s
#3	3	50.0%	±3.25 cm	2.17%	0.05 cm/s
#4	3	75.0%	±4.88 cm	3.25%	0.05 cm/s
#5	3	100.0%	±6.50 cm	4.33%	0.05 cm/s
#6	n	100.0%	±6.50 cm	4.33%	0.5-1 cm/s

Table 4.2: Definition of the cycles.

4.4 Observed behaviour

During the tests was possible to observe the following behaviour:

- Most of the damage was concentrated in the connection. Away from this zone, the columns and beams sustained very low visible damage;
- The columns did not show signs of movement;
- In all V specimens, the reinforcements connected by welds to the top steel plate lost all connection to the RC beam, after spalling the concrete in a sudden, brittle local failure (Figures C.17, C.19, C.21, C.23 and C.26). An inspection to the

reinforcements revealed that the reinforcements connected to the top steel plate were not inside the stirrups (see Drawing nº5 in Annex A);

- Most of the steel plates showed signs of gaps or high flexibility in the connection to the beams (see Figures C.20, and C.31). The connection between the steel hollow box and beam showed the same signs of inefficiency (see Figure C.30), but the connection of the hollow box to the column, made by transversal welded reinforcements had a much better behaviour and sustained lower visible damage;
- The bolt's washers were also a source of flexibility (see Figure C.22);
- In all cases, the collapse of the connection happen after severe damage in the concrete between the edge of the beam and the bolt connecting the plates (see Figure 4.3, C.18, C.21, C.23, C.28, C.38 and C.40);
- After the tests, an inspection to the cross section of the beams found additional reinforcements from those in the detailing drawings (see Drawings nº2, nº3 and nº5 in Annex A).

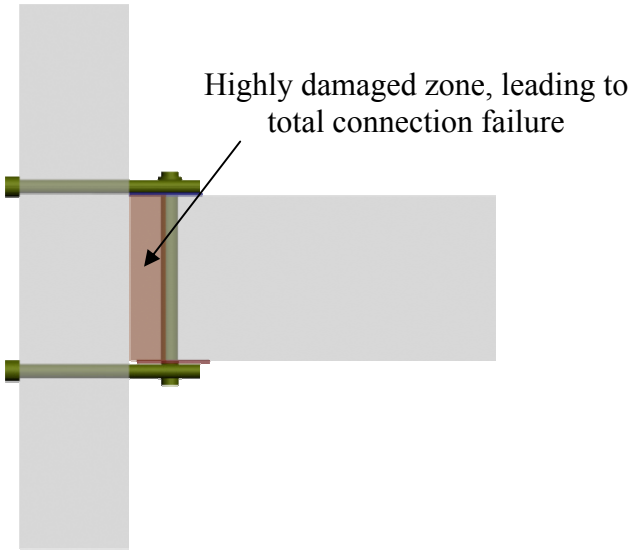

Figure 4.3: BCC tests – Damage location.

4.5 Experimental frequencies

Just before the BCC tests, the specimens were subject to dynamic characterization tests, in order to obtain some basic dynamic properties. Like in the BCC tests, it was identified the specimen's natural frequency in the direction of the cyclic tests, using impact or ambient vibrations. The results obtained are presented in Table 4.3 and in Annex D. Very similar values were obtainned, especially in the VL specimens. The V specimens have greater

dispersion probably due to variations in the plate vs. element stiffness, but still give coherent data. In conclusion, no abnormal behaviour was identified in the specimens, through the experimental frequencies.

Specimen	Excitation	Frequency [Hz]
V1	Ambient	26.7
V2	Impact	22.0
V3	Impact	27.5
V4	Impact	22.8
V5	Impact	23.7
Mean	–	24.5
Std. dev.	–	2.4

Specimen	Excitation	Frequency [Hz]
VL1	Ambient	25.5
VL2	Impact	24.7
VL3	Impact	24.8
VL4	Impact	24.6
VL5	Impact	23.8
Mean	–	24.7
Std. dev.	–	0.6

Table 4.3: Experimental frequencies (before the tests).

Like in the CFC tests, these values can be compared to the analytical results from a cantilever system with distributed mass (see §3.5). Computing for an uncracked specimen:

For the V specimens:

$$\begin{cases} f_1 = \dfrac{(\alpha_1)^2}{2\pi}\sqrt{\dfrac{E\,I}{m}} = \dfrac{1.1364^2}{2\pi}\sqrt{\dfrac{31\times10^6\ 1.318\times10^{-4}}{7.620\times10^{-2}}} = 47.6\,Hz \\ \alpha_1 = \dfrac{1.875}{L} \end{cases} . \qquad (4.1)$$

For the VL specimens:

$$\begin{cases} f_1 = \dfrac{(\alpha_1)^2}{2\pi}\sqrt{\dfrac{E\,I}{m}} = \dfrac{1.1364^2}{2\pi}\sqrt{\dfrac{31\times10^6\ 1.541\times10^{-4}}{8.894\times10^{-2}}} = 47.6\,Hz \\ \alpha_1 = \dfrac{1.875}{L} \end{cases} . \qquad (4.2)$$

The specimens have a very similar relation of stiffness and mass, confirmed by the experimental and analytical results. As expected, the value obtained in (4.1) and (4.2) is much higher than the ones from the experimental campaign, mainly due to high rotational flexibility of the beam-column connection, which is not simulated in the analytical model.

Using a linear dynamic numeric model in a commercial finite element software [CSI 1997] was possible to determinate a discrete number of frequency values, changing the rotational stiffness of the beam-column connection. These values are presented numerically in Table 4.4 and graphically in Figure 4.4. Only the characteristics of the VL specimens were used

because, as mentioned before, both specimen types have a very similar dynamic response, resulting in similar frequencies.

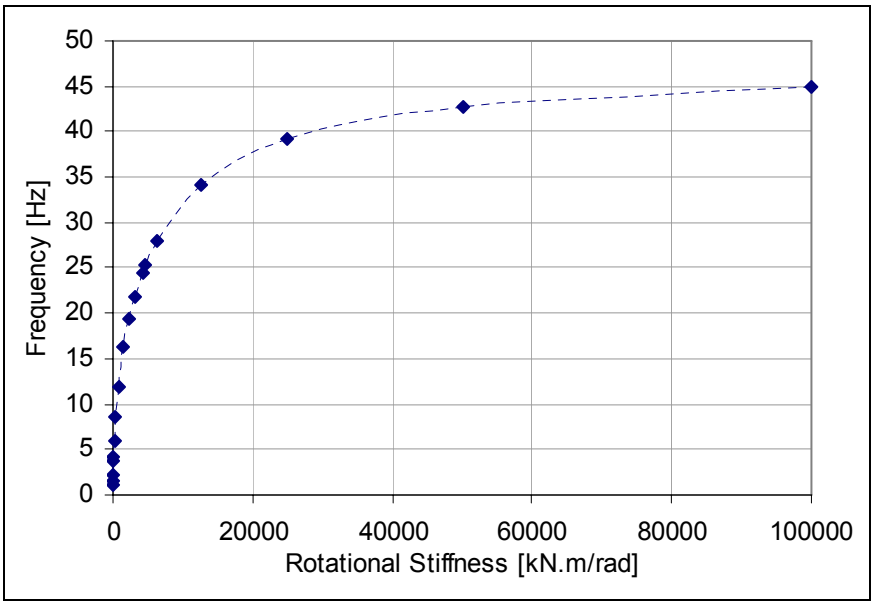

Figure 4.4: Numerical model – Frequency vs. rotational stiffness.

K_θ [kN.m/rad]	Frequency [Hz]	K_θ [kN.m/rad]	Frequency [Hz]
Inf.	47.56	2344	19.33
100000	45.02	1563	16.23
50000	42.84	781	11.82
25000	39.27	391	8.48
12500	34.17	195	6.05
6250	28.00	98	4.29
4688	25.36	49	3.65
4250	24.47	24	2.15
3125	21.74	12	1.52

Table 4.4: Numerical model – Frequency vs. rotational stiffness.

Analysing the data expressed in Table 4.4, it is possible to conclude that, before the tests, the experimental frequencies (around 24-25 Hz) are compatible with a connection rotational stiffness around 4250-4500 kN.m/rad.

Through the analysis of the time histories from the connection bending moments and rotations, was also possible to compute an estimation of the connection rotational stiffness. These values are presented in Annex H and in Figure 4.5 to Figure 4.8. The data computed represent the initial secant stiffness measured in the first increment of load in each direction ($\Delta M \approx 1$ kN.m) and at the end of the first cycle of every amplitude increment.

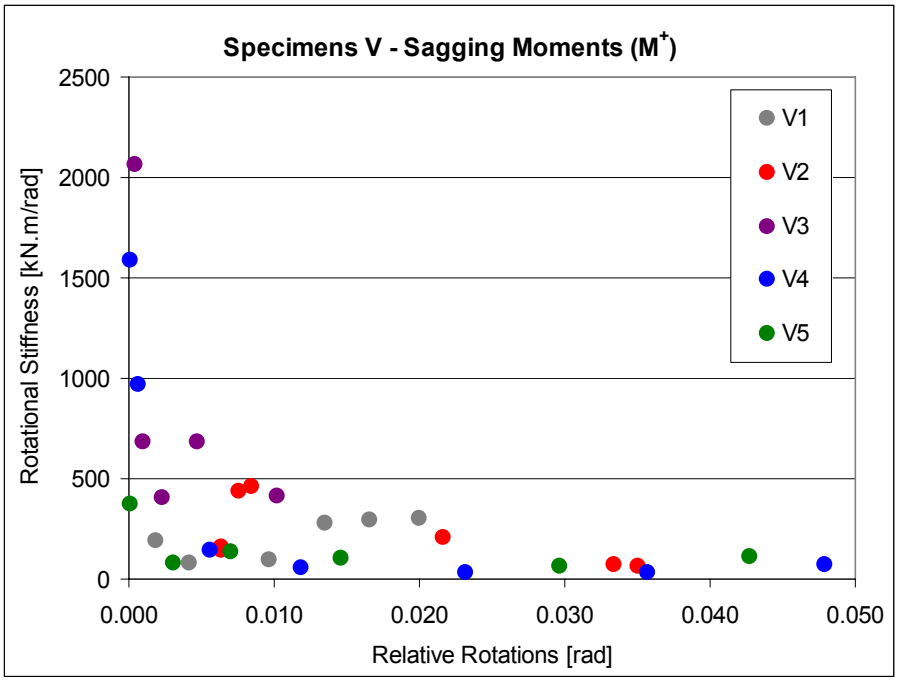

Figure 4.5: Connection rotational stiffness – Specimens VL – Sagging Moments.

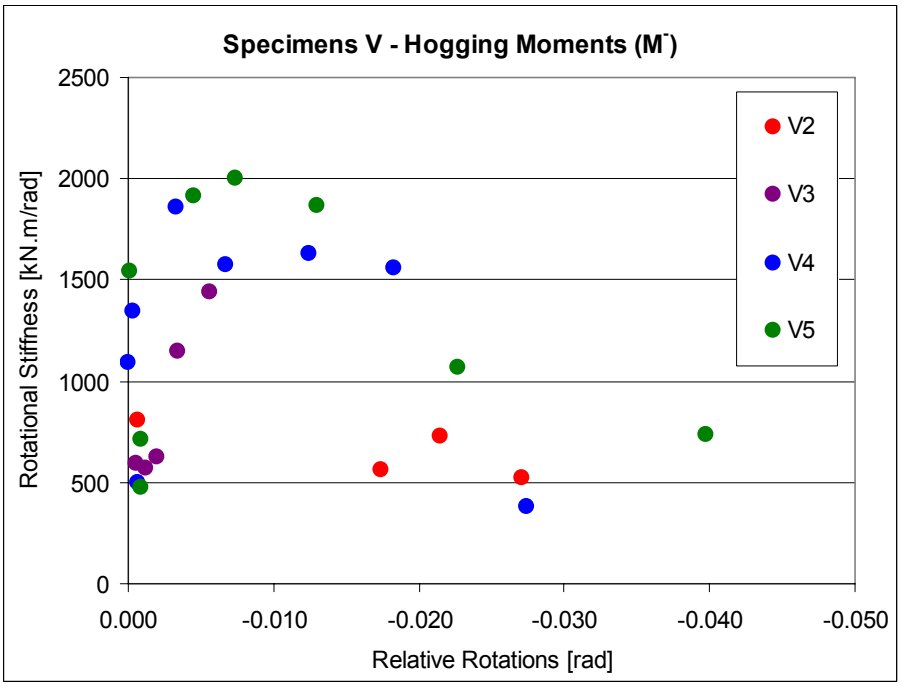

Figure 4.6: Connection rotational stiffness – Specimens VL – Hogging Moments.

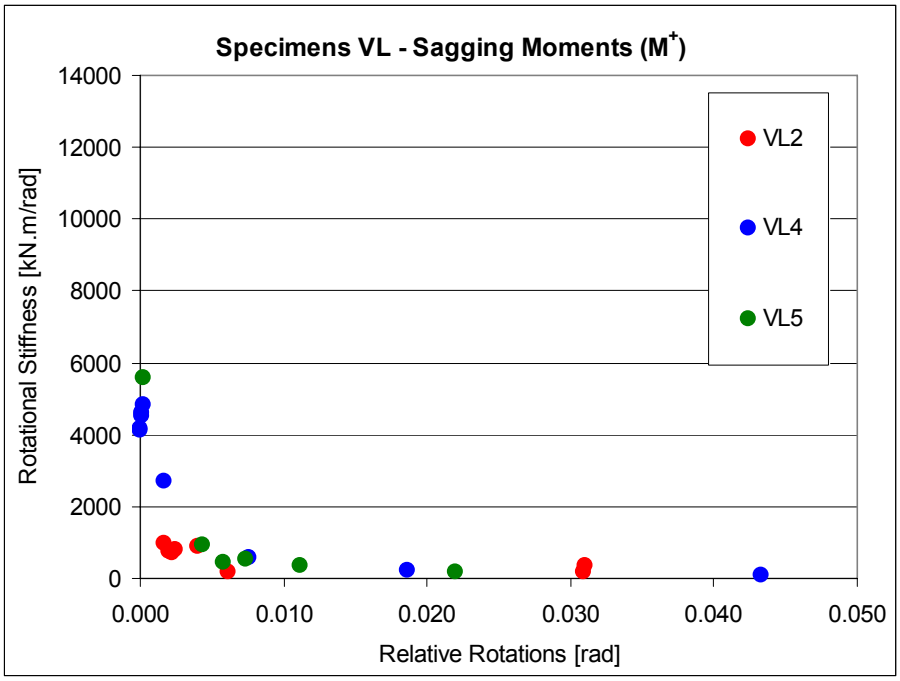

Figure 4.7: Connection rotational stiffness – Specimens V – Sagging Moments.

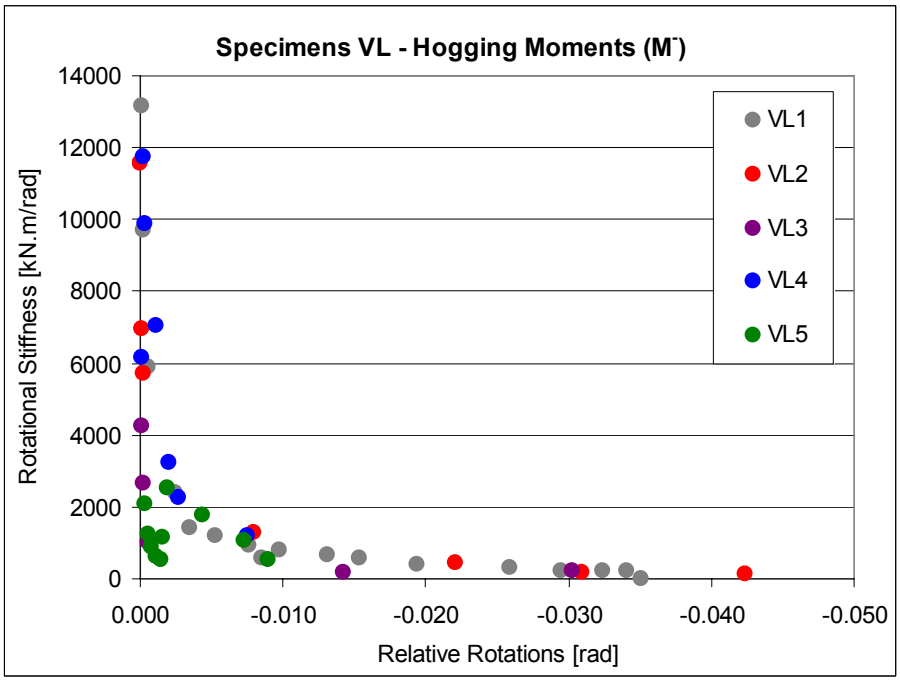

Figure 4.8: Connection rotational stiffness – Specimens V – Hogging Moments.

This data can be summarized in the values presented in Table 4.5. These results reveal asymmetry in the response for each direction, and also, that the initial direction of the imposed displacements is also relevant to the global results. In the case of the V specimens, the maximum stiffness is obtain after some deformation (see Figure 4.6). This is probably a consequence of gaps and flexibility in the steel plates connection to the elements (see §4.4).

Rotation [rad]	V Specimens K_θ (M^+) [kN.m/rad]	V Specimens K_θ (M^-) [kN.m/rad]	VL Specimens K_θ (M^+) [kN.m/rad]	VL Specimens K_θ (M^-) [kN.m/rad]
Initial	400-2100	500-1600	4000-5600	2600-13000
0.01	100-450	1500-2000	200-600	500-800
0.02	50-300	650-1500	100-300	300-500
0.03	30-100	400-600	100-300	200-300
0.04	30-100	400-600	100-200	100-200

Table 4.5: Range of values for the secant connection rotational stiffness.

The overall conclusion is that, before the tests, the connection rotational stiffness was between 2000 and 5000 kN.m/rad, and after some cycles, the reduction is very significant to values around 100 to 600 kN.m/rad. These values are considered as coherent with the data from the numerical model (see Table 4.4).

A linear dynamic model using a commercial finite element software [CSI 1997] was also used to compute the modal frequencies for several cases of beam-column connection stiffness. The parameters of those models were the following:

- Model #1 – Fully restraint, $K_\theta = \infty$ kN.m/rad;
- Model #2 – Mean value of the stiffness before the cycles, K_θ=4300 kN.m/rad;
- Model #3 – Longitudinal connections: mean value of the stiffness after the cycles for the, K_θ=300 kN.m/rad. Transversal connections: minimum value of the stiffness after the cycles, K_θ=100 kN.m/rad (see Figure 5.1);
- Model #4 – Pinned connections, $K_\theta = 0$ kN.m/rad.

In Model #3, the BCC stiffness was chosen taken in consideration the high damage in the longitudinal connections and the severe damage in the transversal connections, which are indicated in the shaking table test report [Mendes et al. 2006].

The numerical values obtained are presented in Table 4.6, and also, the updated experimental results from the shaking table tests, which now include also the first torsion mode frequencies and some minor corrections.

Comparing these results is possible to conclude that the data from Model #2 is very similar to the frequencies from *Cat 00* (before the test) and frequencies from Model #3 suits very well the data obtained in *Cat 04* (after the test). In conclusion, the results extracted from the BCC cyclic tests are very coherent with the results from the shaking table test.

Mode Frequency [Hz]	Linear Dynamic Models				Experimental				
	Model #1	Model #2	Model #3	Model #4	Cat 00	Cat 01	Cat 02	Cat 03	Cat 04
1st Trans.	3.04	2.49	1.41	1.32	2.9	2.3	2.0	1.4	1.2
1st Long.	4.01	3.18	1.78	1.32	3.2	2.9	2.7	2.4	1.9
1st Torsion	5.65	4.68	3.16	2.88	4.5	4.2	3.8	3.3	*
2nd Trans.	10.39	9.79	8.69	8.61	9.0	7.7	6.6	5.5	4.9
2nd Long.	11.59	10.66	9.03	8.61	14.3	12.6	11.5	9.6	8.7
2nd Torsion	16.67	15.55	13.67	13.34	-	-	-	-	-
Note: * Value not presented due to insufficient accuracy.									

Table 4.6: Numeric and experimental modal frequencies.

4.6 Global forces and displacements

The time histories of the global forces, bending moments, displacements and rotations are presented in Annex E. A summary of those is presented in Table 4.7.

Specimen	**Applied Load**		**Connection Moment**		**Connection Rotation**	
	F^+ [kN]	F^- [kN]	M^+ [kN.m]	M^- [kN.m]	Θ^+ [º]	Θ^- [º]
V1	3.2	-6.8	4.7	-10.2	6.0	-0.01
V2	3.0	-17.2	4.4	-25.8	1.7	-2.7
V3	3.0	-12.7	4.6	-19.0	0.9	-0.6
V4	3.1	-17.4	4.6	-26.2	3.0	-2.7
V5*	4.6	-15.3	6.9	-23.0	3.5	-2.5
Mean**	**3.4**	**-15.7**	**5.1**	**-23.5**	**2.3**	**-2.1**
VL1	3.1	-6.0	4.7	-9.0	2.4	-0.5
VL2	2.4	-7.1	3.6	-10.6	0.0	-2.5
VL3	3.4	-8.4	5.1	-12.5	1.7	-3.0
VL4	3.2	-8.3	4.8	-12.5	1.0	-3.8
VL5*	2.7	-9.6	4.1	-14.4	1.3	-0.5
Mean**	**3.0**	**-7.9**	**4.5**	**-11.8**	**0.9**	**-0.5**
Notes: * Inversed displacement time history was imposed at the top of specimen (see Figure E.72, E107); ** Mean values refers only to cyclic tests.						

Table 4.7: Maximum forces and displacements.

For the V specimens the maximum force (moment) achieved in the cyclic was higher (around 4.6 times) in the direction of hogging moments. This can result in a beneficial effect, since in real situations the beams are subjected to hogging bending moments due to permanent and live loads. Higher flexibility was also measured in the sagging moment's direction, as indicated in the values from the connection rotation (see Table 4.7). For the VL specimens this behaviour was also visible but less significant (around 2.6 times

higher). The maximum rotation was also achieved in the direction of the sagging moments, which can be related to a worse response of the hollow box vs. beam connection. This asymmetric response was found in all specimens.

Like occurred in the CFC tests, the results from the monotonic tests indicates lower maximum forces/moments and displacements, even after reaching higher drifts (8.7-9.0% vs. 4.3%). This can result of reaching a very low residual stiffness in the monotonic specimen, and also, due to a better use of the available resistance caused by incomplete crack closure between cycles, which results in new contact points that allows reaching higher forces for the same maximum drift.

In the Figure 4.9 to Figure 4.12 is presented the force vs. displacement graph of all the specimens tested. In the cyclic tests is possible to observe a very similar response between the specimens. The only exception was in the VL3 specimen, where a sudden lost of resistance in the hogging moment's direction, changed the response of the specimen away from the typical pattern, which was followed in the first displacement increment. This behaviour could be related to an internal collapse (e.g. concrete crushing leading to a macro-crack caused by a fragile zone or a pre-existing tension state) that reduced prematurely the resistance in that direction.

In Figure 4.13 is represented typical force vs. displacement curves for both specimens' types. Those graphs reveal a poor behaviour of the connection, which is very asymmetric and with very low stiffness in the inversion of the displacements. This response can be associated with the large gaps that develop in the connections due to premature damage. Pinching is also present and is also a direct result of those gaps. The hysteretic cycles have a very narrow shape and presents high degradation in successive cycles, which results in low energy dissipation.

The collapse of the connection occurred after severe damage in the concrete between the bolt, connecting the top and bottom steel plate (or hollow box), and the element's edge. At that stage, the connection resulted only of dowel type resistance and the steel plates/hollow box lost completely their structural contribution (see Figure 4.3).

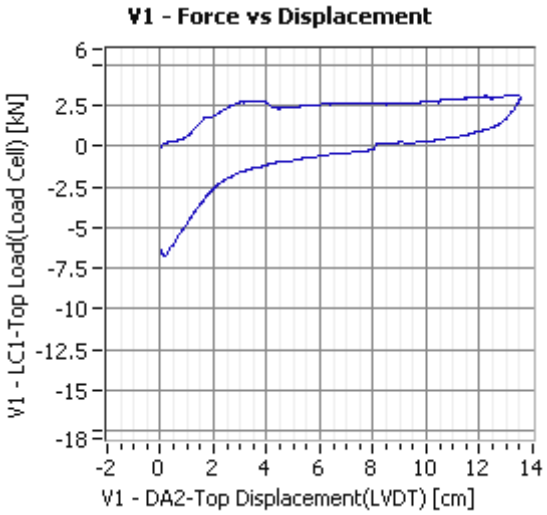

Figure 4.9: V Specimens – Monotonic test – Force-displacement graph.

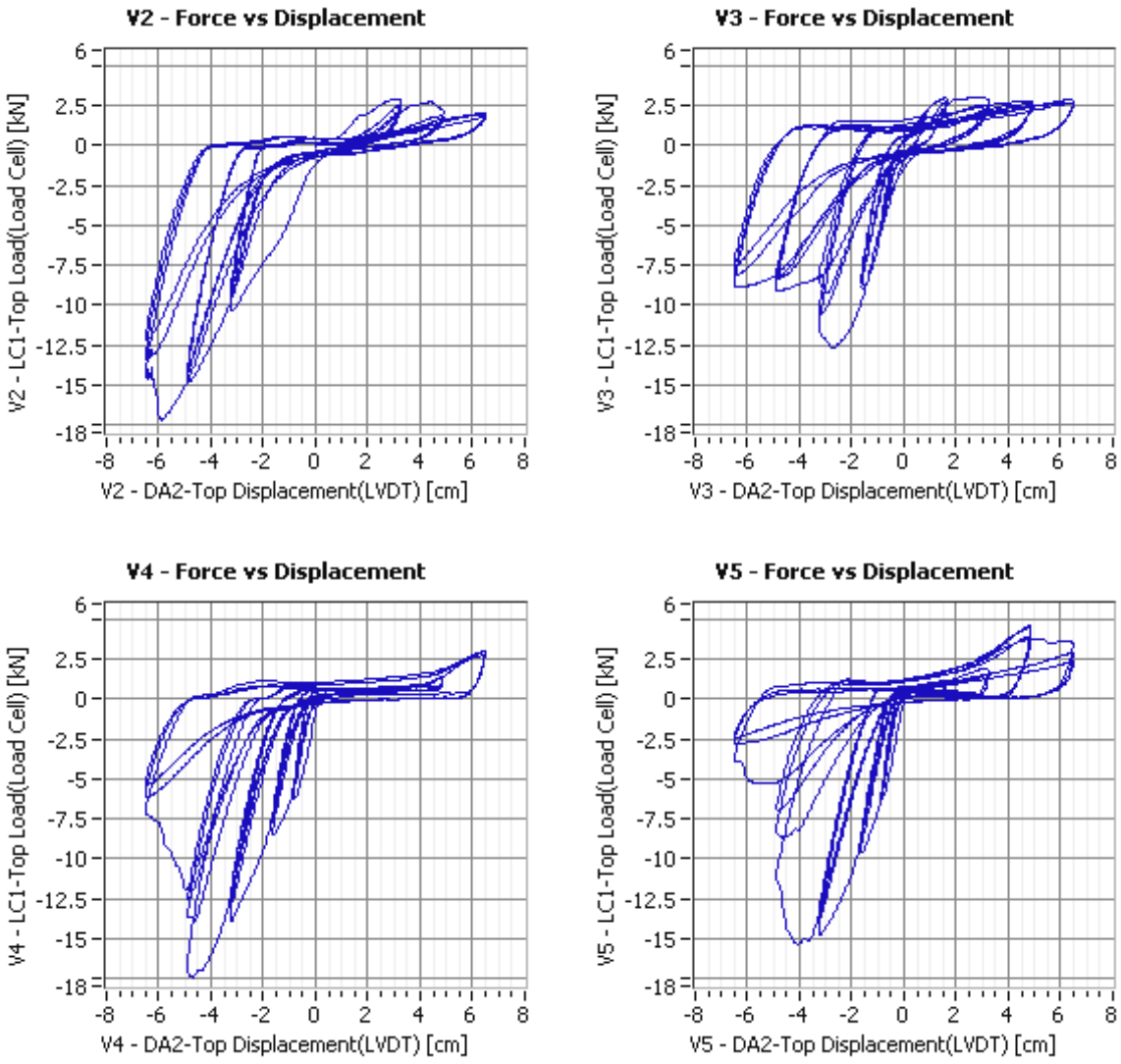

Figure 4.10: V Specimens – Cyclic tests – Force-displacement cycles.

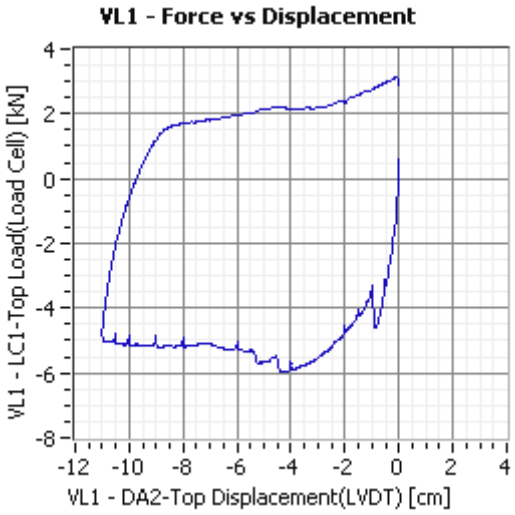

Figure 4.11: V Specimens – Monotonic test – Force-displacement graph.

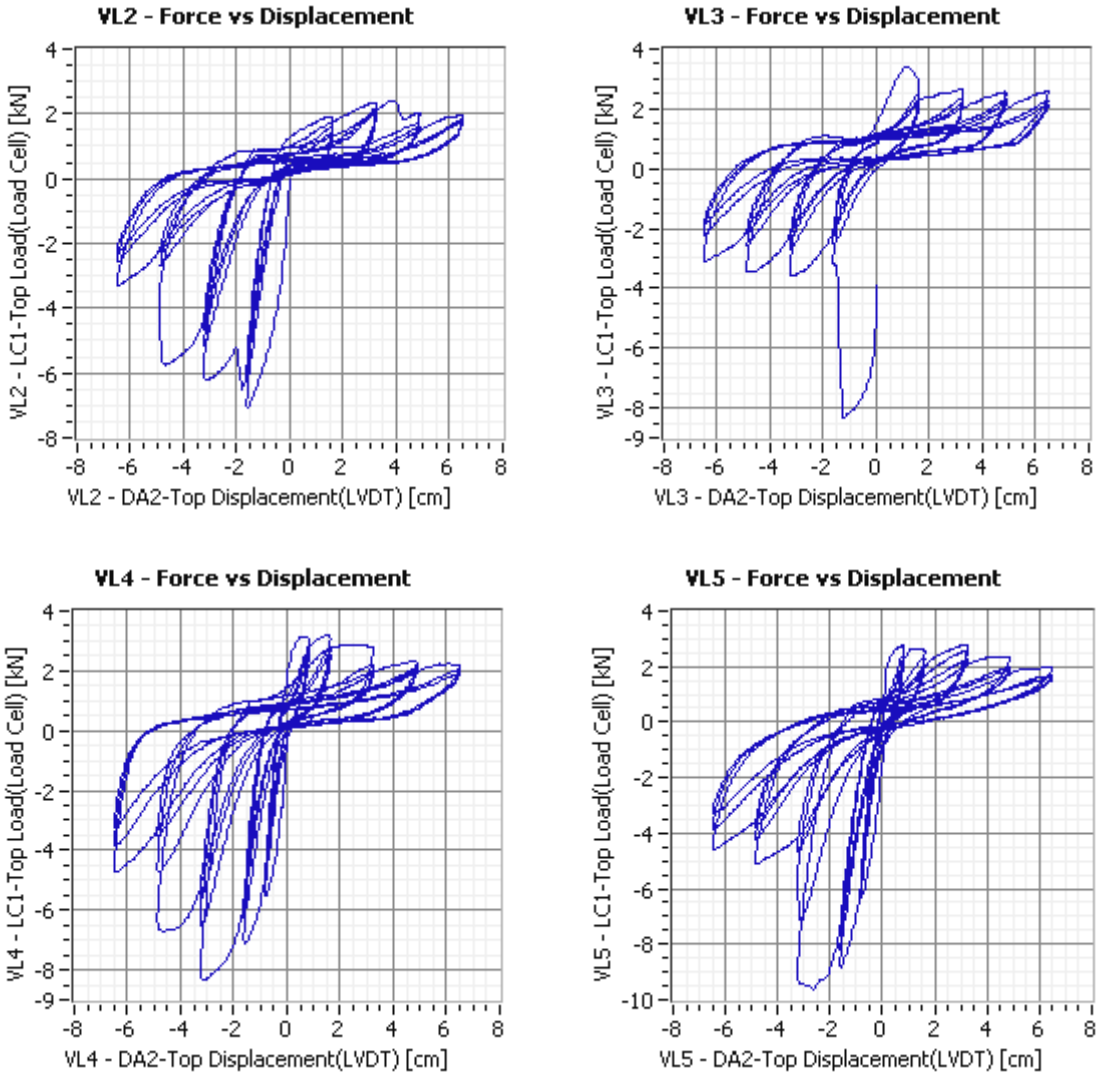

Figure 4.12: V Specimens – Cyclic tests – Force-displacement cycles.

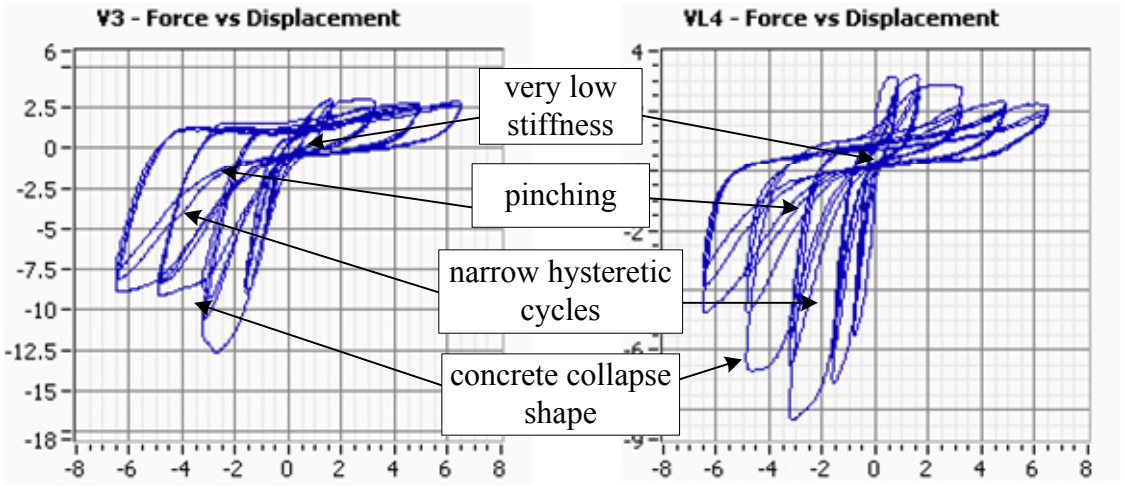

Figure 4.13: Typical force-displacement cycles.

Three of the bolts used in the connections were subjected to tension tests. The results are presented in Figure 4.14:

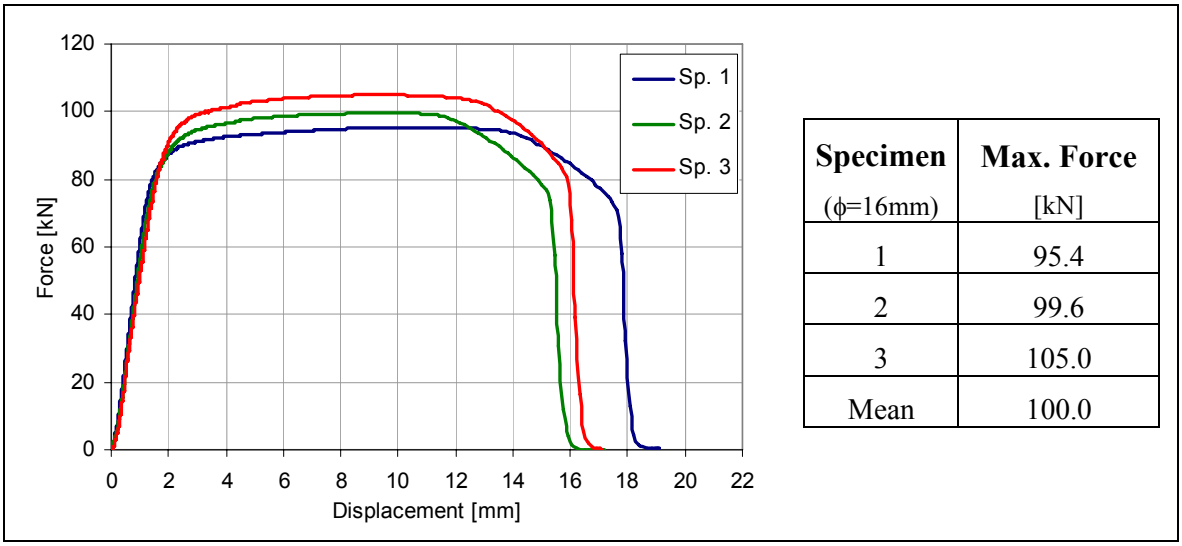

Specimen (ϕ=16mm)	**Max. Force** [kN]
1	95.4
2	99.6
3	105.0
Mean	100.0

Figure 4.14: Results from the bolt's tension tests.

The maximum resistance was around 100 kN and the force-displacement graphs showed that the response is almost linear up to 80 kN of tension. Taking in consideration that the maximum bending moment measured in the connection was of 26.2 kN.m (see Table 4.7), the maximum force for the two bolts in each steel plate was:

$$\frac{1}{2}\frac{26.2}{0.26} = 50.3\,\text{kN}\,. \tag{4.3}$$

Consequently, during the tests the bolts response was probably elastic, not being able contribute adequately to the energy dissipation. This response can be related to a design

strategy that is not optimized for seismic loads or another possible source for this problem is related to scaling. Although correctly designed for the prototype, for any reason, the specimens supplied by *Civibral* did not reproduce the mechanical characteristics of the bolts in the scaled models.

4.7 Local displacements

Almost all of the deformability in the BCC specimens was concentrated in the connection, meaning that neither the columns nor the beams had significant deformations. This behaviour is visible in the very small displacements of the column presented in Table 4.8. The Figures E.48, E.55, E.62, E.69, E.76, E.83, E.90, E.97, E.104 and E.111, which represent the drift of several points in the beams (h=300, 600, 900, 1200 and 1500 mm), shows very similar values, indicating that the beams are moving as a rigid body, with no significant bending or shear deformation, confirming the observed behaviour (see 4.4).

Specimen	**Position** (see Figure 4.15)	**Direction x** (horiz.)	**Direction z** (vert.)	**Rel. Disp.** $\sqrt{dx^2 + dz^2}$
V1	L1	0.003	0.005	0.006
V2	L1	0.036	0.127	0.132
V3	L1	0.014	0.024	0.027
V4	L1	0.060	0.049	0.078
V5	L1	0.008	0.009	0.012
VL1	L1	0.012	0.013	0.018
VL2	L1	0.007	0.007	0.010
VL3	L1	0.006	0.007	0.009
VL4	L1	0.002	0.007	0.007
VL5	L1	0.006	0.008	0.010
Maximum	L1	0.060	0.127	0.132

Table 4.8: Maximum relative displacement of the column.

To analyse the relative displacements between the different connection elements, several measurements were made during the tests. In Figure 4.15 is presented the position of the points (leds) were the displacements were measured, resulting in the data presented in Annex F and in the maximum relative displacements presented in Table 4.9.

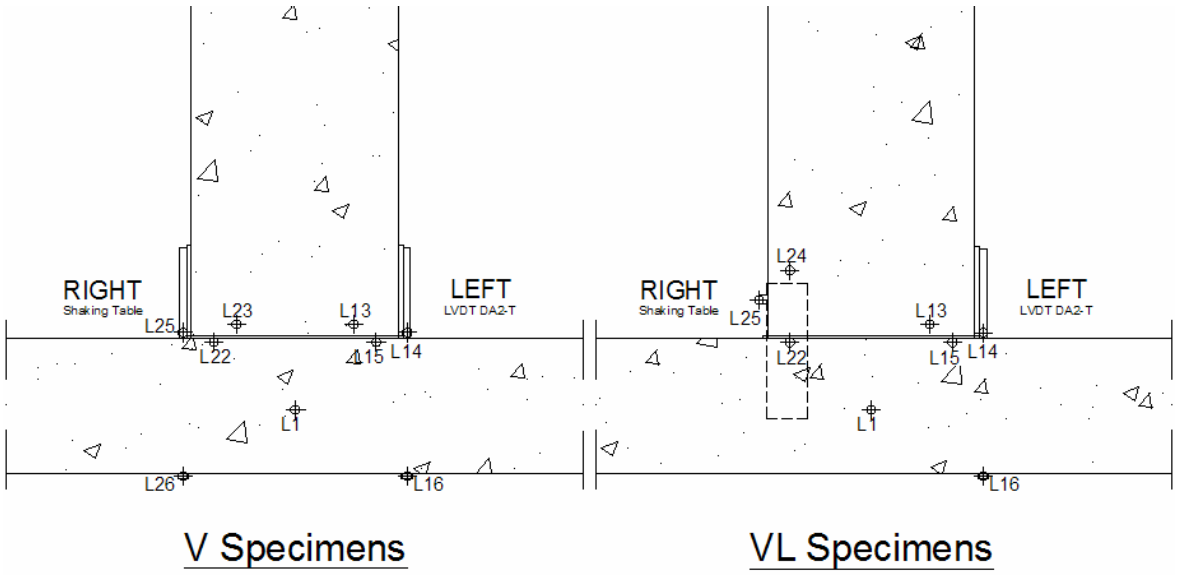

Figure 4.15: Schematic representation of the measurements position.

Specimen	Beam Plate vs. Beam [mm]		Beam Plate vs. Column [mm]		Bolt Head vs. Column [mm]		Bolt Head vs. Beam plate [mm]	
Position (Figure 4.15)	L25-L23* Right	L14-L13 Left	L25-L22 Right	L14-L15 Left	L26-L22 Right	L16-L15 Left	L26-L25 Right	L16-L14 Left
V2	3.48	7.64	3.93	0.52	3.87	0.39	2.38	0.67
V3	2.13	9.63	0.53	0.71	0.15	0.47	0.46	0.31
V4	8.87	9.24	2.13	1.22	3.32	0.31	2.49	1.32
V5	10.66	14.60	0.27	0.43	0.33	0.24	0.31	0.43
Mean	**6.29**	**10.28**	**1.72**	**0.72**	**1.92**	**0.35**	**1.41**	**0.68**
Max	**10.66**	**14.60**	**3.93**	**1.22**	**3.87**	**0.47**	**2.49**	**1.32**
VL2	–	7.01	–	0.63	–	0.72	–	0.35
VL3	9.74	9.10	2.01	0.53	–	1.09	–	0.47
VL4	9.07	31.80	0.49	0.22	–	0.08	–	0.25
VL5	12.24	10.00	1.15	0.41	–	0.56	–	0.53
Mean	**10.35**	**14.48**	**1.22**	**0.45**	–	**0.61**	–	**0.40**
Max	**12.24**	**31.80**	**2.01**	**0.63**	–	**1.09**	–	**0.53**

Notes: * Leds L25-24 were used to measure the relative displacements in the VL specimens.

Table 4.9: Maximum relative displacements between connection elements.

The data presented in Table 4.9 reveals small maximum relative displacements between the bolt head and the beam plate (less than 1.32 mm), which can be related to the bolt's deformation. Higher values were measured, both in the displacements between the bolt head and the column, and, between the beam plate and column. Both of these displacements can be related with the deformability of the washers (see §4.4 and Figure C.22) and due to damage in the concrete. On the other hand, the maximum relative displacements between beam-plates and beams were quite large, reaching values higher than 10 mm and up to 31.80 mm, which is quite large for this scaled specimen. The

connection between steel plates and beams is the major source of deformability found in the connection.

4.8 Energy balance

Using the same procedure used in §3.8, the total work done by the external forces (input energy), which is related with the dissipated energy, is presented in Annex G and a summary in Table 4.10.

Specimen	**Type**	**Cycles** (see Table 4.2)	**Total Input Energy** [kN.m]
V1	Monotonic	–	0.44
V2	Cyclic	#3, #4, #5, #6	1.86
V3	Cyclic	#1, #2, #3, #4, #5, #6	2.65
V4	Cyclic	#1, #2, #3, #4, #5, #6	1.65
V5	Cyclic	#1, #2, #3, #4, #5, #6	2.07
Mean*	–	–	**2.12**
VL1	Monotonic	–	0.73
VL2	Cyclic	#2, #3, #4, #5, #6	0.90
VL3	Cyclic	#2, #3, #4, #5, #6	1.02
VL4	Cyclic	#1, #2, #3, #4, #5, #6	1.38
VL5	Cyclic	#1, #2, #3, #4, #5, #6	1.22
Mean*	–	–	**1.30**

Notes:
* Mean values refers only to cyclic tests that completed the six amplitude levels;
In the cyclic tests the time histories were cropped at the end of the third 6.5 cm cycle.

Table 4.10: Total input energy.

Analysing these results reveals that, although the input energy required to perform the monotonic tests was higher in the VL specimens, for the cyclic tests was required more input in the V specimens. This indicates that stiffness and resistance degradation is more significant in the VL specimens.

Comparing these values of the input energy with the values from the CFC tests (around 10 kN.m, see §3.8) reveals that, although not comparable directly, for a similar amount of reinforcements and geometry (length and cross-section), the monolithic RC section has much larger dissipation capacity then this type of connection (around 5 to 8 times higher).

4.9 Conclusions

The results from the beam-column connection tests made possible to establish the following conclusions:

- Most of the specimen's deformability and damage was concentrated in the beam-column connection and neither the columns nor the beams had significant deformations. The connection between steel plates and beams was the major source of deformability found in the connection;
- The collapse of the connections occurred after severe damage in the concrete between the bolt connecting the top and bottom steel plate (or hollow box) and the beam's edge. At that stage, the connection was only due to dowel type resistance and the steel plates (hollow box) lost completely their structural contribution;
- Analysing the data from the experimental frequency tests, it was possible to conclude that the rotational stiffness of the connections was much smaller that the equivalent for a monolithic element. Comparing with the results form a linear dynamic numerical model, the initial connection rotational stiffness, compatible with the experimental frequencies, is between 4250-4500 kN.m/rad;
- Using the data of the connection's bending moment and rotation, it was possible to compute an estimation of the rotational stiffness evolution. The overall conclusion is that, before the tests, the connection rotational stiffness was between 2000 and 5000 kN.m/rad, and after some cycles, the reduction is very significant, to values around 100 to 600 kN.m/rad;
- In both connections the maximum force (moment) achieved in the cyclic tests was much higher in the direction of hogging moments. This can be beneficial to resist the additional hogging moments due to permanent and live loads. This behaviour was more significant in the V specimens;
- The force vs. displacement graphs of both specimens' types were similar and revealed a poor behaviour with low energy dissipation. The response was characterized by asymmetry, high degradation, low stiffness, pinching and narrow hysteretic cycles;

- Analysing the results of the input energy, it was possible to conclude that, although more effective in the monotonic tests, the VL specimens presented higher degradation resulting in a overall worse response that the one from the V specimens;
- After testing the bolts used in the connections, it was possible to conclude that the bolts behaviour was mainly elastic during the tests, consequently, this element's ductility was not explored for energy dissipation. This can be a consequence of a design criteria, which is not optimized to resist earthquake loads, or caused by a scaling problem;
- The inspection of the beam's cross sections revealed additional reinforcements from those in the detailing drawings. These additional reinforcements did not influence the overall performance of the connection, because they do not contribute, significantly, to the confinement of the concrete near the connection.
- In some cases, the detailing of the beam's reinforcements was not the best solution to resist cyclic or earthquake loads, like the case of the reinforcements found outside the stirrups, which leads premature cover spalling and degradation of the connection.
- These type of beam-column connections have the advantage of being extremely easy to mount, and therefore, reducing the time necessary for the erection of the structure. However, a design revision is advised, especially for structures in medium to high seismic areas. Some possible improvements are redesigning the bolts, in order to make use of the non-linear behaviour, enabling more efficient energy dissipation. Another simple improvement is to increase the resistance and confinement of the concrete near the edge of the beam, using for example stirrups or longitudinal reinforcements. A better seismic response could also be achieved by reducing the flexibility and gaps found in the connections, which contributes to the premature degradation of the connection.

5 FINAL CONCLUSIONS

In this section, is presented an overall analysis of the tested precast building system. This analysis comprehends not only the information collected in the cyclic tests presented in this report, but also, the data from the shaking table test of the 2 stories specimen (see [Mendes et al. 2006]).

The tested prototype is a typical precast system from *Civibral* and it is used mainly for buildings. The structure has 2 stories with 4.5 m of height each and 10.5x12.0 m^2 in plan (see Figure 5.1). This structure was designed by *Civibral* for PGA=0.375g with the elastic stresses reduced by a behaviour factor of q=2.0. The specimen was subjected to earthquake motions, with increasing intensity, in the LNEC's triaxial shaking table.

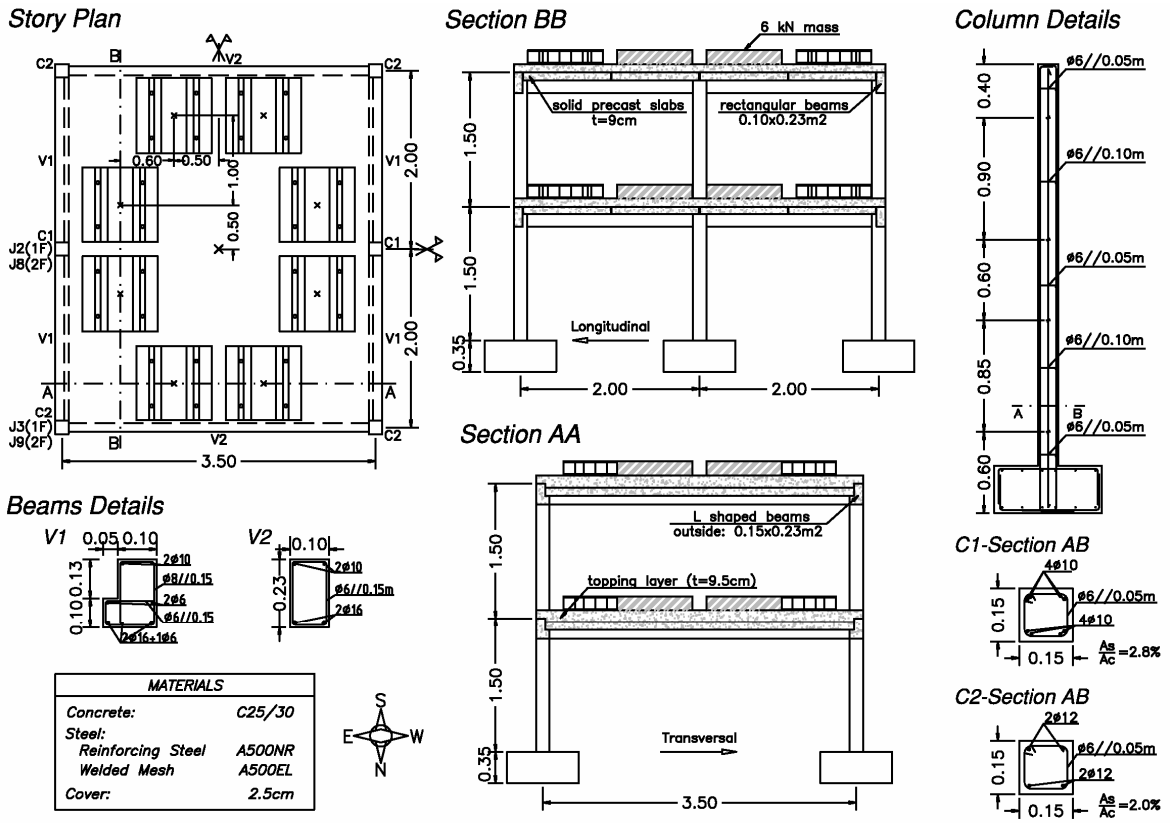

Figure 5.1: Characteristics of the specimen tested in the shaking table.

In the shaking table test the following observations and conclusion were made [Mendes et al. 2006]:

- The majority of the visible damage was concentrated on the beam-column connections;

- The analysis of the modal frequencies revealed a very intense stiffness degradation (around 80% reduction in the transversal direction);
- The interstory drifts reached very high values (around 3% in the last stage) and estimated base shear was also very high (more than 50% the weight of the specimen);
- In the less intense test stages the beam-column connections revealed non-negletable rotational stiffness and the overall behaviour was typical of a frame structure. At the final stages the overall behaviour has governed by cantilever columns (inverted pendulum response);
- The beam-column connections revealed enough ductility to sustain the earthquake input without collapsing, although with severe damage and only residual rotational stiffness;
- To design this structure for collapse prevention a conservative and real model is to consider the beam-column connections as pinned;
- The most probable collapse mechanisms identified were the local failure of the beam-column connections and the global failure of the second floor columns (because of higher interstory drifts and the good response of the column's bases).

Combining this information with the data collected in the CFC and BCC tests, it is possible to conclude.

- Although the column-foundation connections were not implemented in the shaking table specimen, the results from the cyclic tests showed a very good response, and, that the connection is not involved in the collapse mechanism, which occurs in the span of the column. It is possible to conclude that not using the column-foundation connections did not influence significantly the response of the specimen tested in the shaking table;
- The good response of the specimen tested in the shaking table was mainly due to the excellent behaviour of the columns. If also present in that specimen, the additional reinforcements found in the CFC tests, could be responsible for that enhanced column response. In that case, the amount of reinforcements would exceed the maximum value prescribed by some design codes (e.g. [CEN 2001], and could not

be coherent with the design criteria, namely, the behaviour factor used (q=2), and represent a significant over-resistance.

- The data collected in the BCC cyclic tests, confirms the high degradation and premature damage that occurred in the shaking table test. The response was also characterized by narrow shaped hysteretic cycles, low stiffness and pinching, and consequently, by low energy dissipation. These types of beam-column connections have the advantage of being extremely easy to mount, however, the analysis to the seismic behaviour presented in this report advises a design revision, especially for structures to be constructed in medium to high seismic areas. Some possible improvements for this system are mentioned in §4.9.

6 ACKNOWLEDGMENTS

The authors acknowledge the important contributions of other LNEC colleagues, namely Mr. Artur Santos, Mrs. Dulcina Marecos, Mr. Paulo Semedo and Miss Ana Marques and the good cooperation with the technicians form *Civibral*.

7 BIBLIOGRAPHY

CEN (2001) - "Eurocode 2: Design of concrete structures. Part 1: General rules and rules for buildings. Bruxelas.

Clough, R. W. and J. Penzien (1993) - "Dynamics of Structures", McGraw-Hill, Inc, Singapura.

CSI (1997) - "SAP2000 - Structural Analysis Program - Non Linear, Computers & Structures Inc. 1997.

Mendes, L., E. Coelho and A. C. Costa (2006) - "Shaking Table Tests of a Reinforced Concrete Precast Building System". Relatório nº97/2006 - NESDE. Lisboa, Laboratório Nacional de Engenharia Civil.

NI (2001) - "LabVIEW - PID Control Toolset - User Manual" National Instruments Corporation.

Lisbon, Laboratório Nacional de Engenharia Civil, February of 2007,

APPROVED BY

Head of Earthquake Engineering and
Structural Dynamic Division (NESDE)

Eng.ª Ema Coelho

Director of the Structures Department

Eng.º João Almeida Fernandes

AUTHORS

Luís Mendes

Civil Engineer, PhD Grant Holder

Ema Coelho

Civil Engineer, Senior Research Officer

Alfredo Campos Costa

Civil Engineer, Senior Research Officer

ANNEXES

Annex A - DRAWINGS

Annex B - INSTRUMENTATION

Annex C – PHOTOGRAPHIC REPORT

Annex D – NATURAL FREQUENCIES

Annex E – GLOBAL FORCES AND DISPLACEMENTS

Annex F – CONNECTIONS MOMENTS AND ROTATIONS

Annex G – LOCAL DISPLACEMENTS

Annex H – INPUT ENERGY

ANNEX A DRAWINGS

List of Drawings:

Drawing nº1 – Column-Foundation Specimens

Drawing nº2 – Beam-Column Connection Specimens – Type #1

Drawing nº3 – Beam-Column Connection Specimens – Type #2

Drawing nº4 – Column-Foundation Specimens – Real Reinforcements

Drawing nº5 – Beam-Column Specimens – Real Reinforcements

Drawing nº6 – Test Foundation – Plan and Views

Drawing nº7 – Test Foundation – Sections

Drawing nº8 – Test Foundation – Reinforcements – Plans

Drawing nº9 – Test Foundation – Reinforcements – Sections

Drawing nº10 – Test Setup – Plan

Drawing nº11 – Test Setup – Views

Drawing nº12 – Test Setup – Column Foundation – Global View

Drawing nº13 – Test Setup – Column Foundation – Close Up

Drawing nº14 – Test Setup – Beam–Column V – Global View

Drawing nº15 – Test Setup – Beam–Column V – Close Up

Drawing nº16 – Test Setup – Beam–Column VL – Global View

Drawing nº17 – Test Setup – Beam–Column VL – Close Up

Drawing nº18 – Test Setup – Signal Convention

ANNEX B INSTRUMENTATION

Table of Contents:

B.1 Sensors Technical Data

	Manufacture: RDP ELECTRONICS (www.rdpe.com); Model: ACT2000, ACT4000 and ACT6000; Stroke: ±50mm (ACT2000);±100mm (ACT4000);±150mm (ACT6000) Sensitivity: 15 mV/V/mm (ACT6000) to 30 mV/V/mm (ACT2000); Energising supply: 5 Vrms, 5 kHz; Linearity deviation: 0.08% (ACT2000) to 0.3% (ACT60000).

Table B-1: Inductive displacement transducers.

 	Manufacture: METRIS (www.metris.com); Model: K600 Optical CMM; Description: 3D measurement system, using three linear CCD cameras and triangulation of infrared LEDs; Measurement Capabilities: 3 degrees of freedom for each LED or 6 degrees of freedom for each group of 3 LEDs: Sampling Rate: 3000 / # of LEDs (e.g. 20 LEDs - 150 $S.s^{-1}$); Measurement Volume: 17 m^3 (e.g. Zone 2 (H,W,D): 2.4x3.3x5.0m^3); Single Point Accuracy: Up to 60 µm; Volumetric Accuracy: Up to 90 µm; Temperature Range: 15-40 ºC.

Table B-2: Optical displacement transducers.

	Manufacture: PCB PIEZOTRONICS (www.pcb.com); Model: 337A26; Sensitivity: 100 mV/g; Measurement range: ±50 g pk; Broadband Resolution: 0.0001 g rms; Frequency range: 0.5 to 5000 Hz.

Table B-3: Piezoelectric accelerometers.

ANNEX C PHOTOGRAPHIC REPORT

Contents:

List of Figures:

C.1 General View

Figure C.1: Test setup – General view.

Figure C.2: Data acquisition and shaking table control.

C.2 Column-Foundation Connections Tests

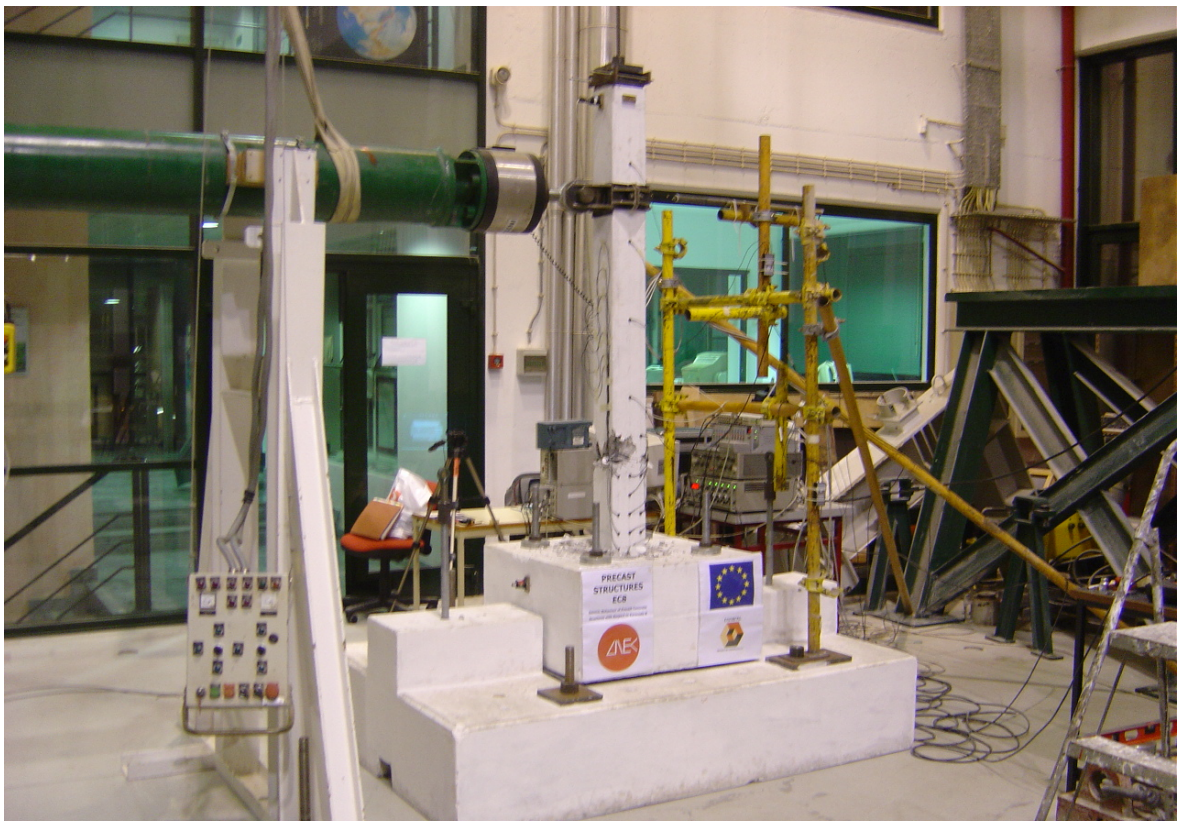

Figure C.3: Column-Foundation Tests – General View.

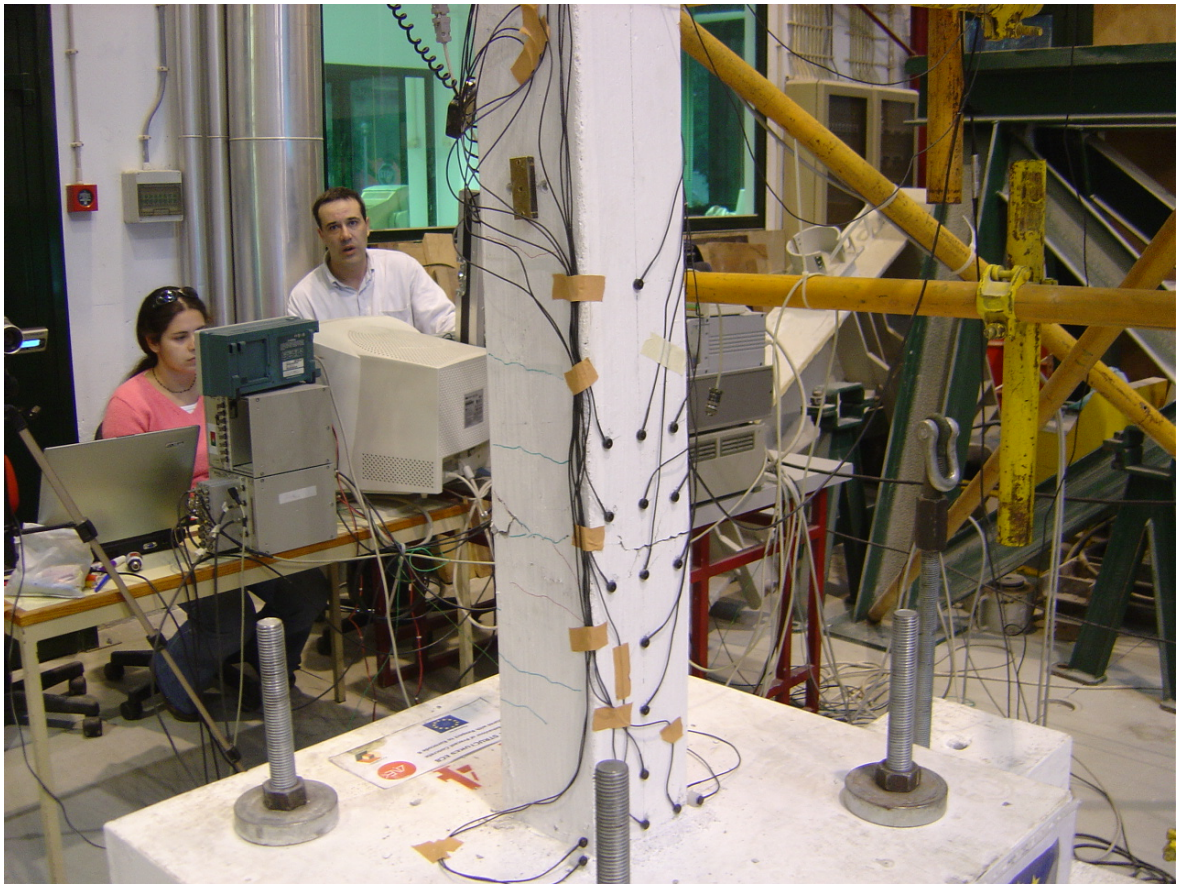

Figure C.4: Column-Foundation Tests – Typical led layout.

C.3 Specimen P1

Figure C.5: Specimen P1 – Cracking evolution.

Figure C.6: Specimen P1 – Reinforcing steel inspection and detail of the column-foundation connection.

C.4 Specimen P2

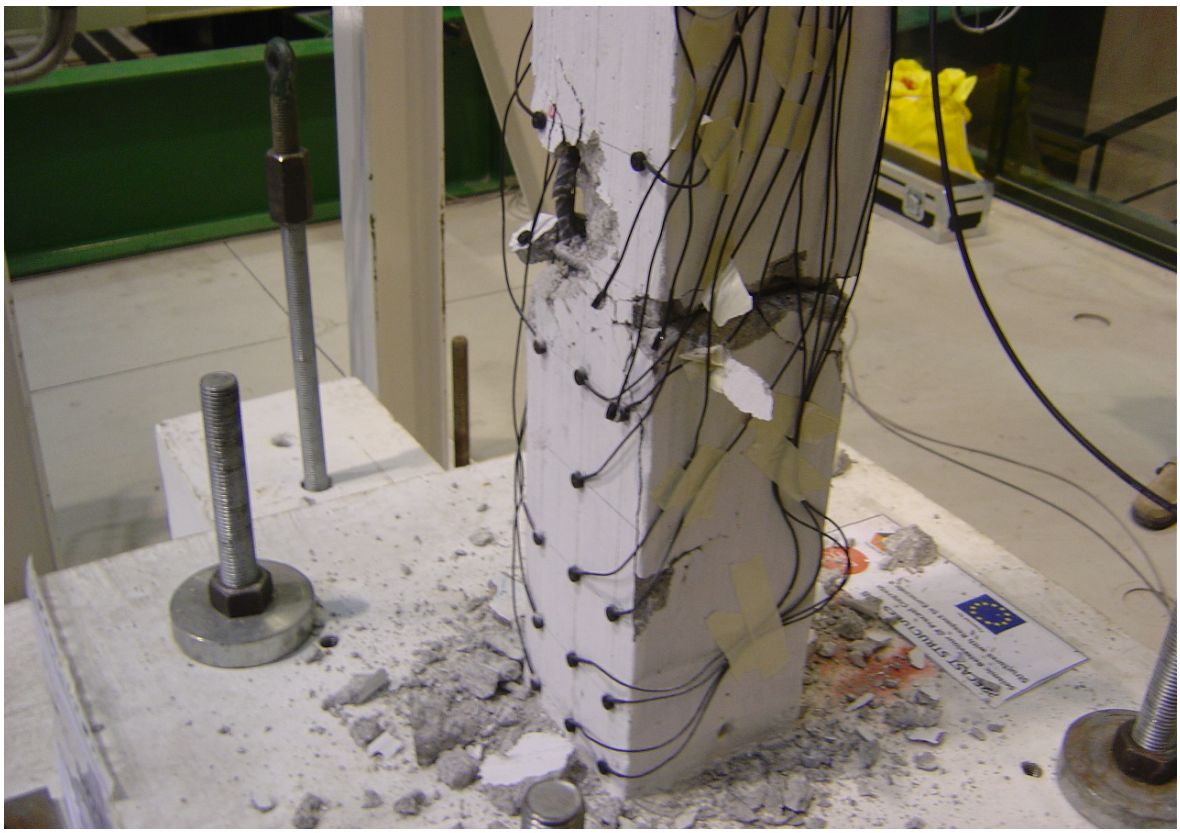

Figure C.7: Specimen P2 – Global view (after the test).

Figure C.8: Sp.P2 – Detail of the collapse zone and of the column-foundation connection.

C.5 Specimen P3

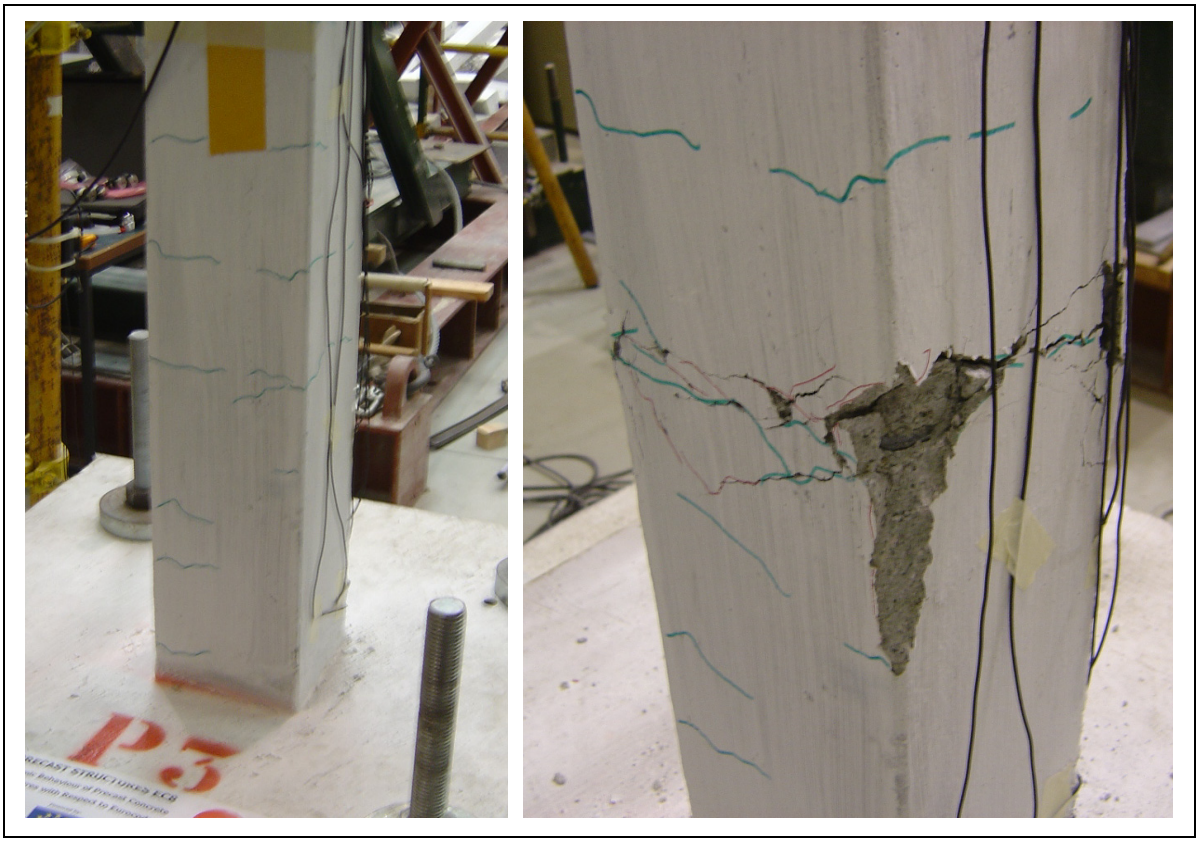

Figure C.9: Specimen P3 – Crack pattern evolution and cover spalling.

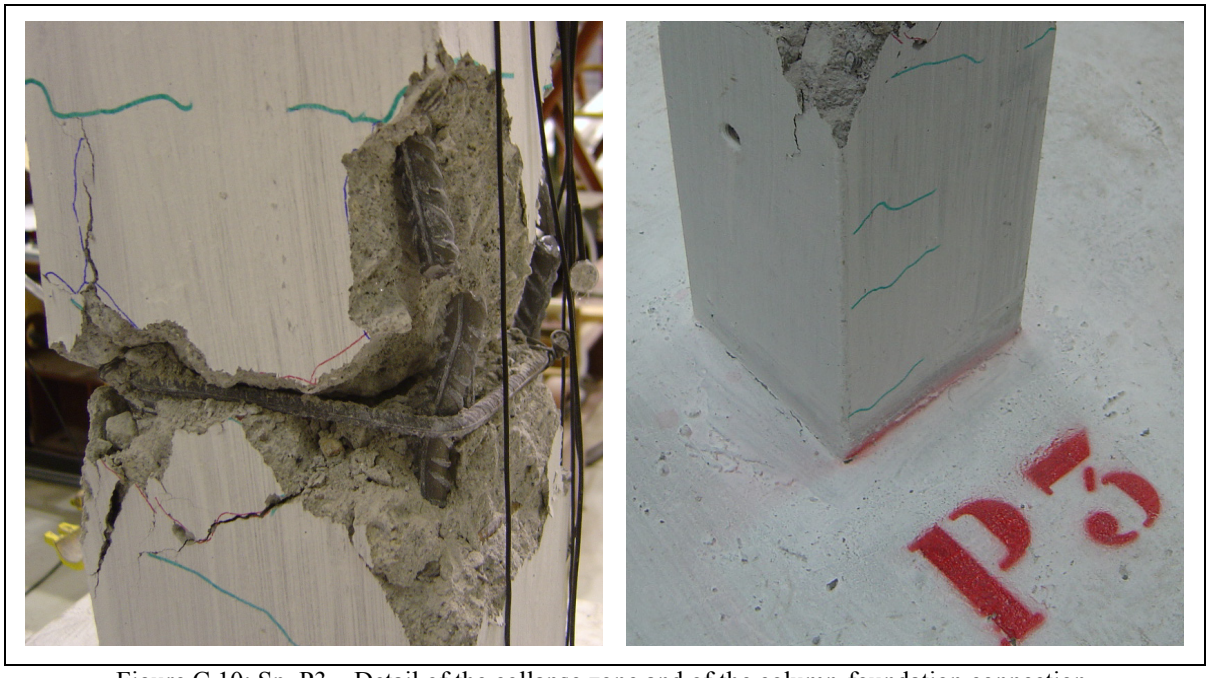

Figure C.10: Sp. P3 – Detail of the collapse zone and of the column-foundation connection.

C.6 Specimen P4

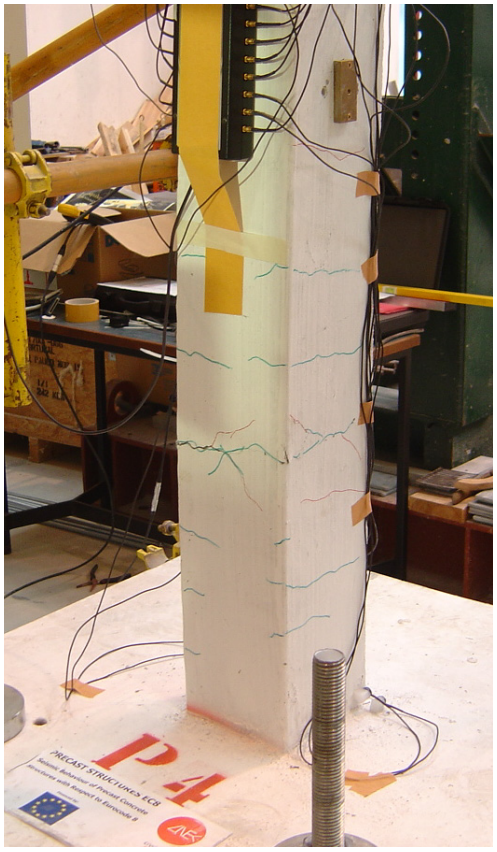

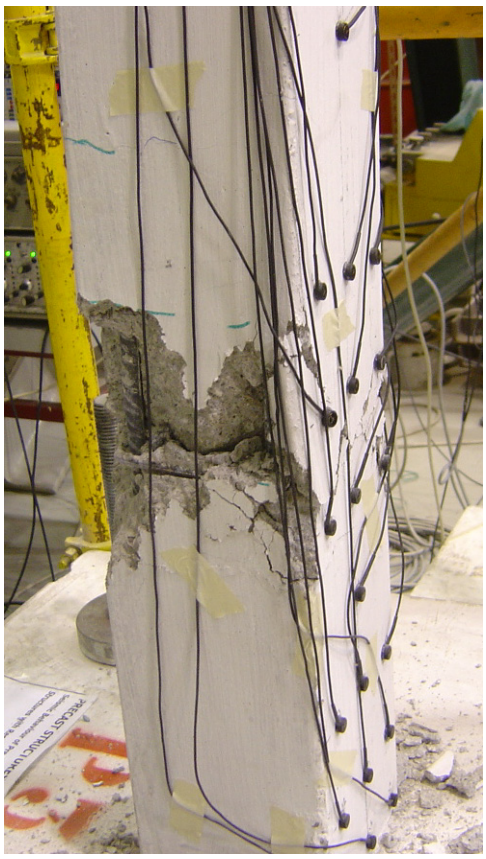

Figure C.11: Specimen P4 – Global view (during the test)..

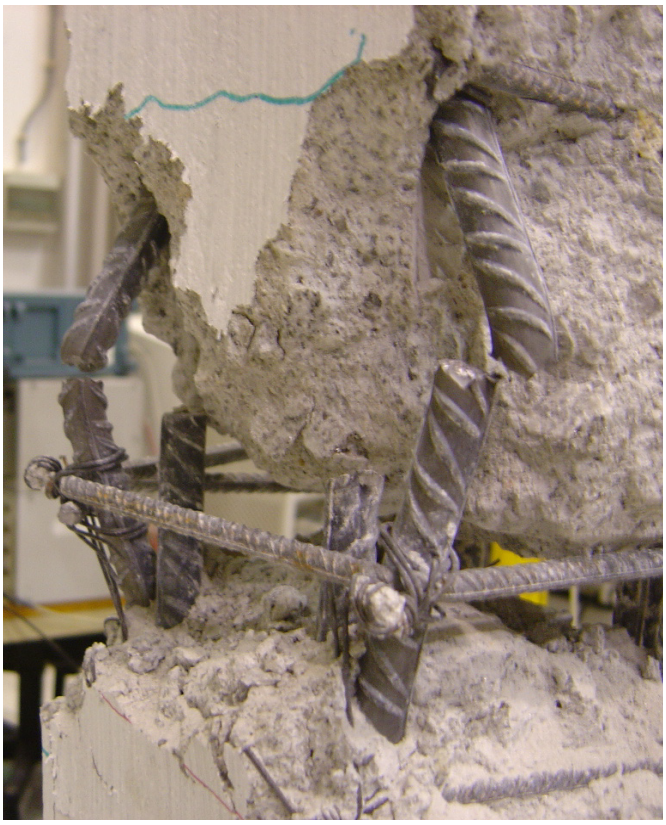

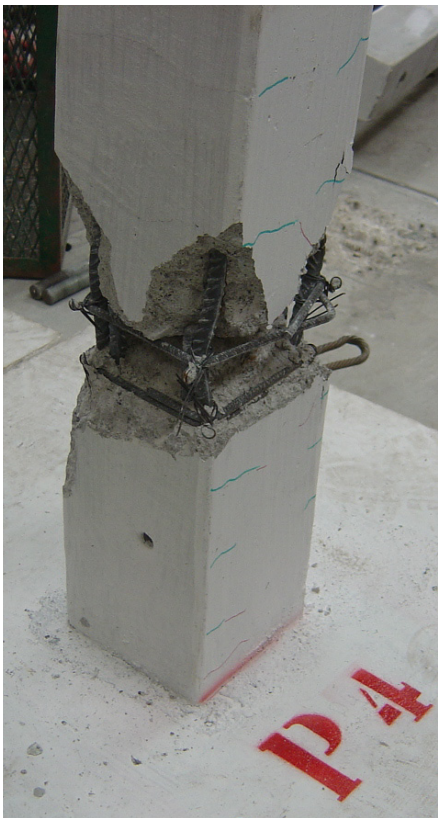

Figure C.12: Sp. P4 – Details of the most damaged zone (all the concrete was loose) and of the column-foundation connection.

C.7 Beam-Column Connections Tests

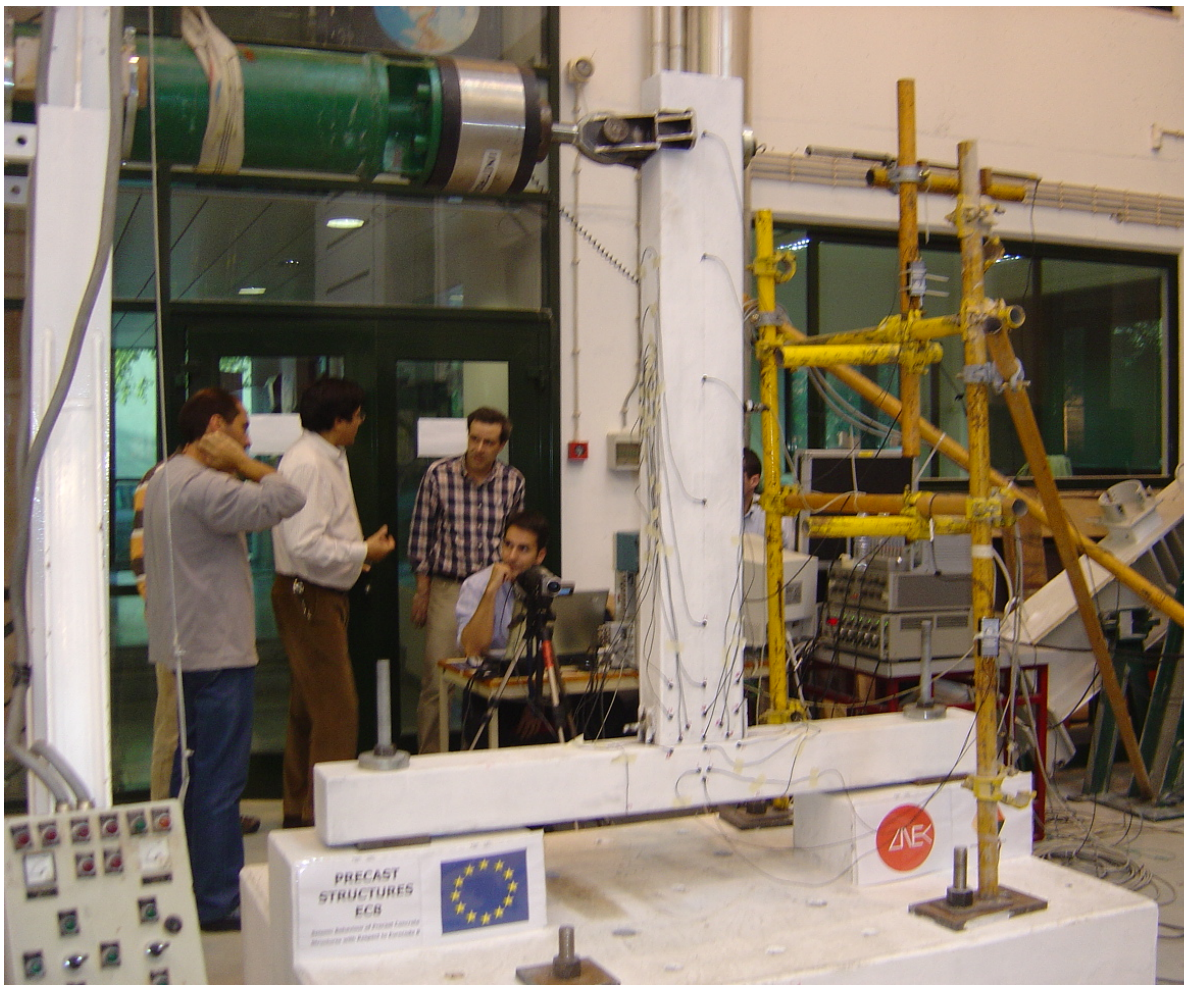

Figure C.13: Beam-Column Tests – General View.

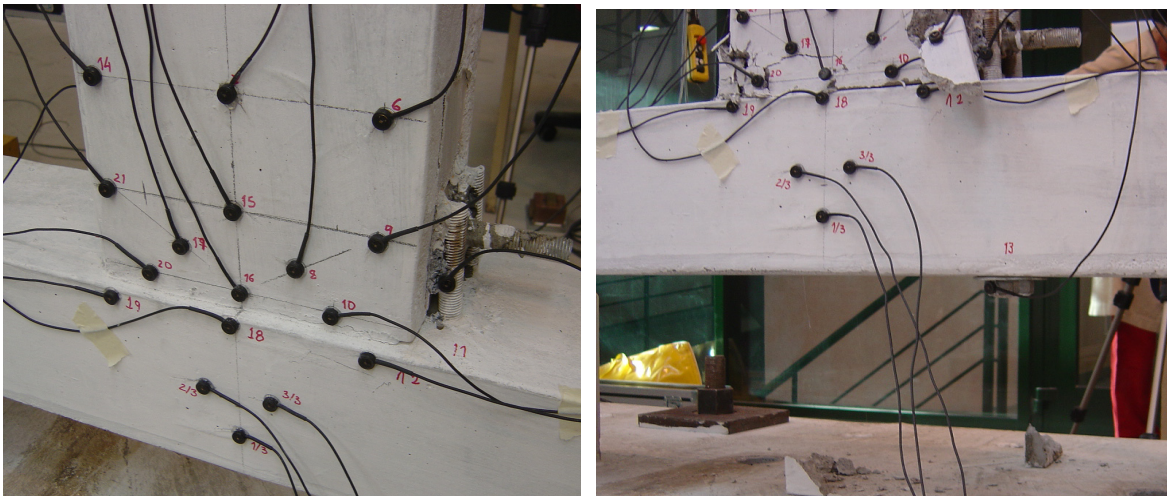

Figure C.14: Beam-Column Tests – Typical led layout.

C.8 Specimen V1

Figure C.15: Specimen V1 – Initial crack pattern.

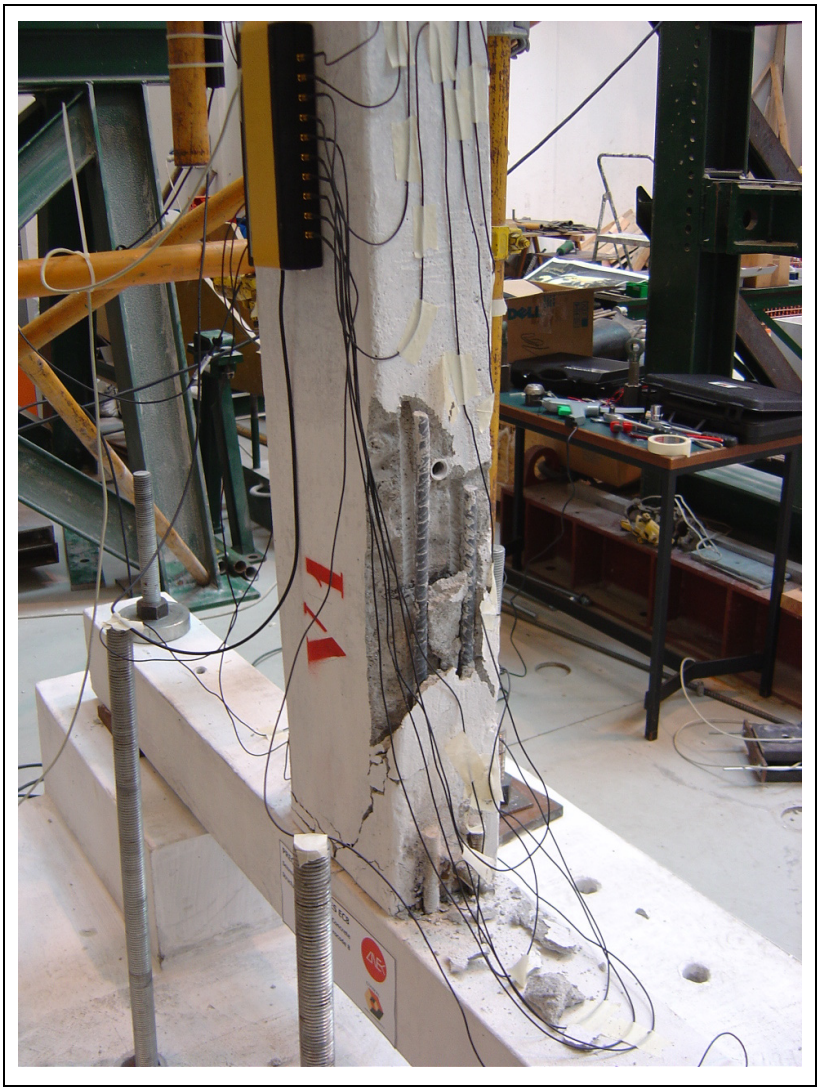

Figure C.16: Specimen V1 – Cover spalling due to non-confined reinforcements.

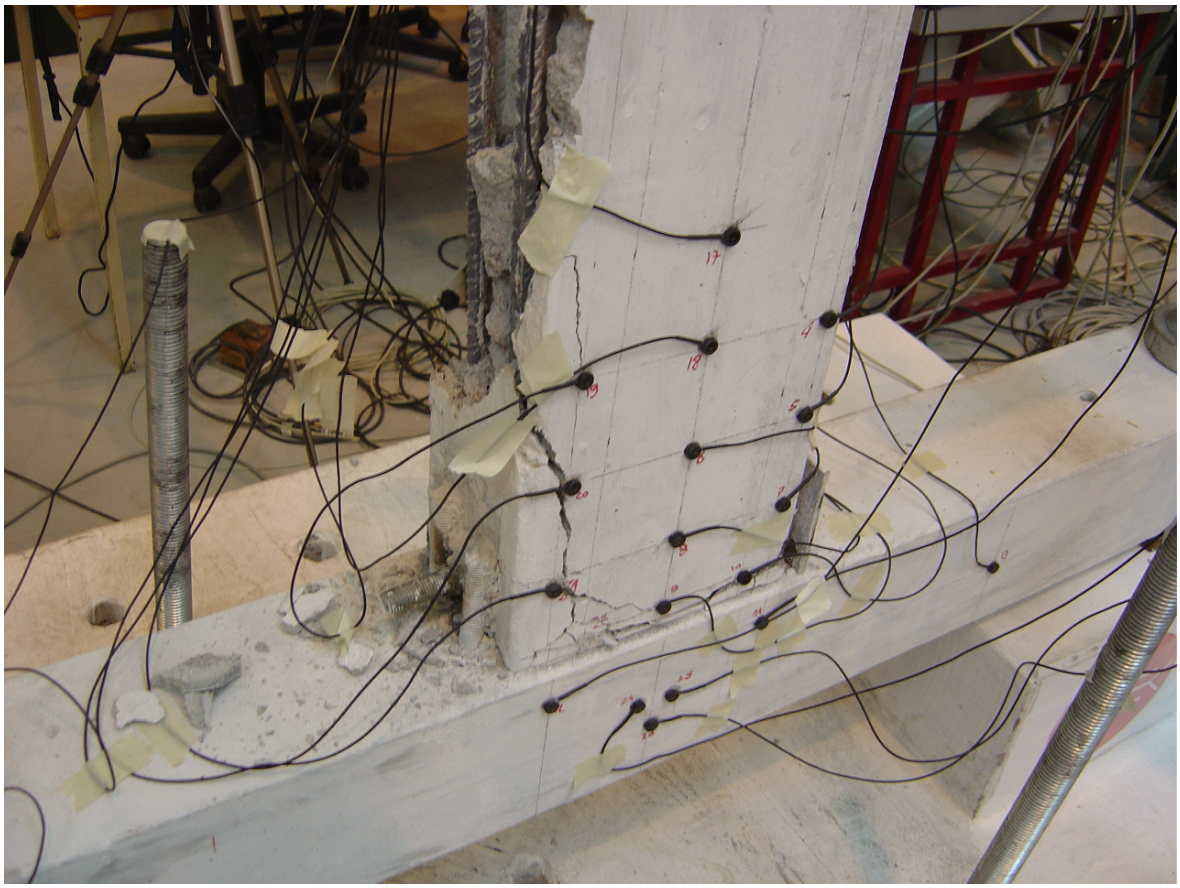

Figure C.17: Specimen V1 – Global view (during the test).

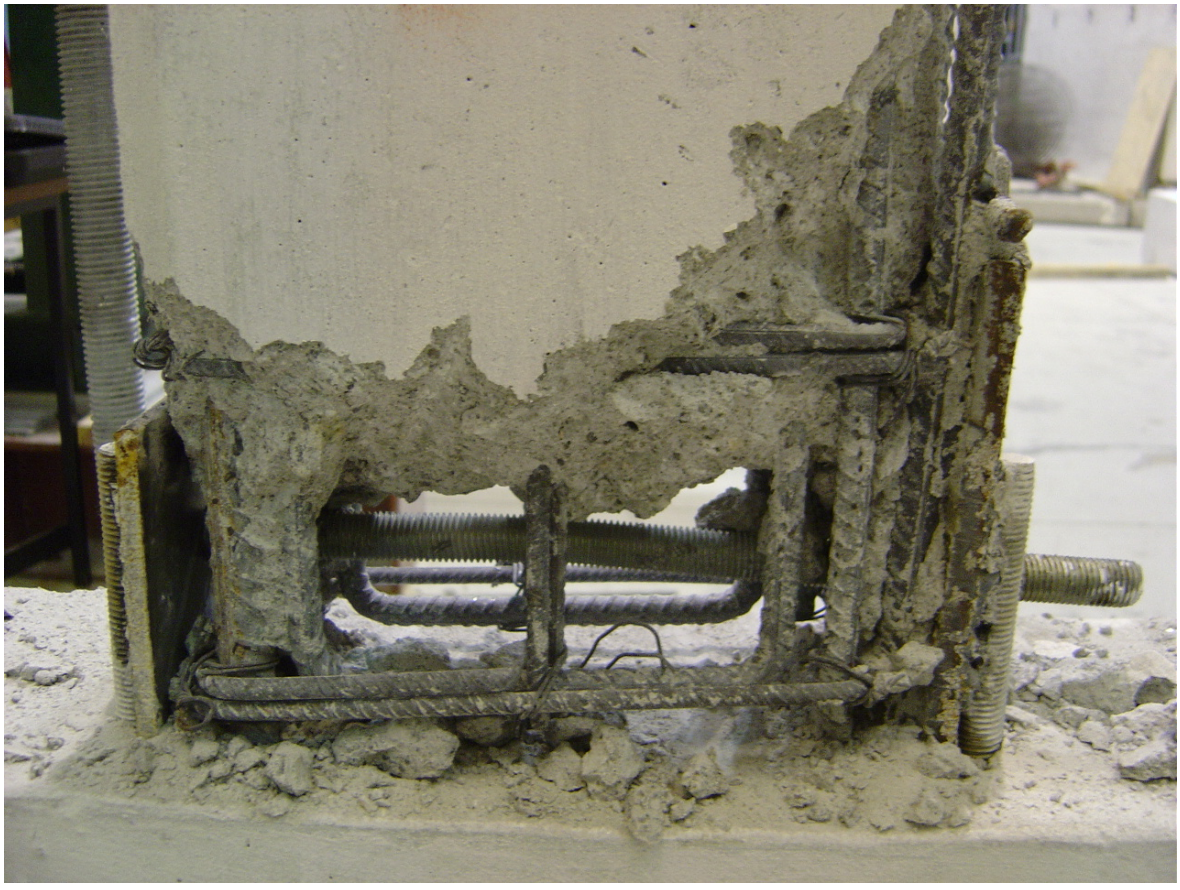

Figure C.18: Specimen V1 – Reinforcing steel inspection.

C.9 Specimen V2

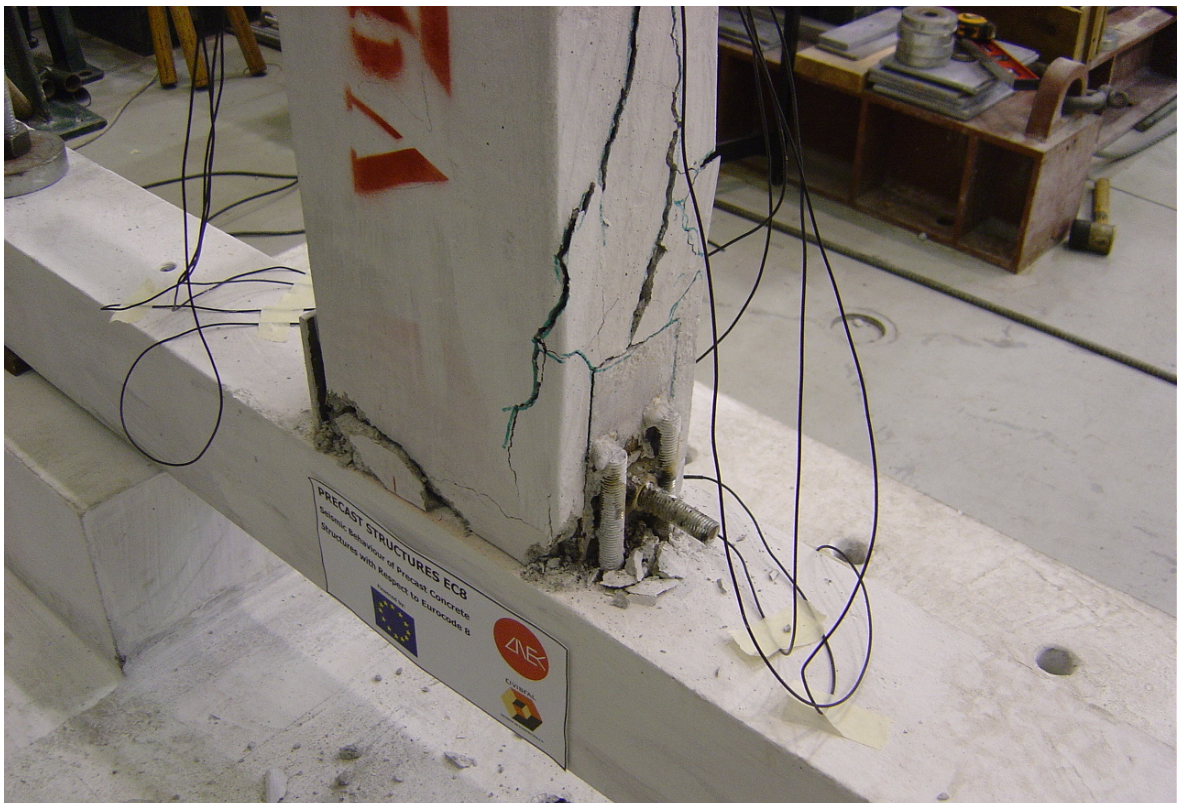

Figure C.19: Specimen V2 – Evolution of the cracks pattern.

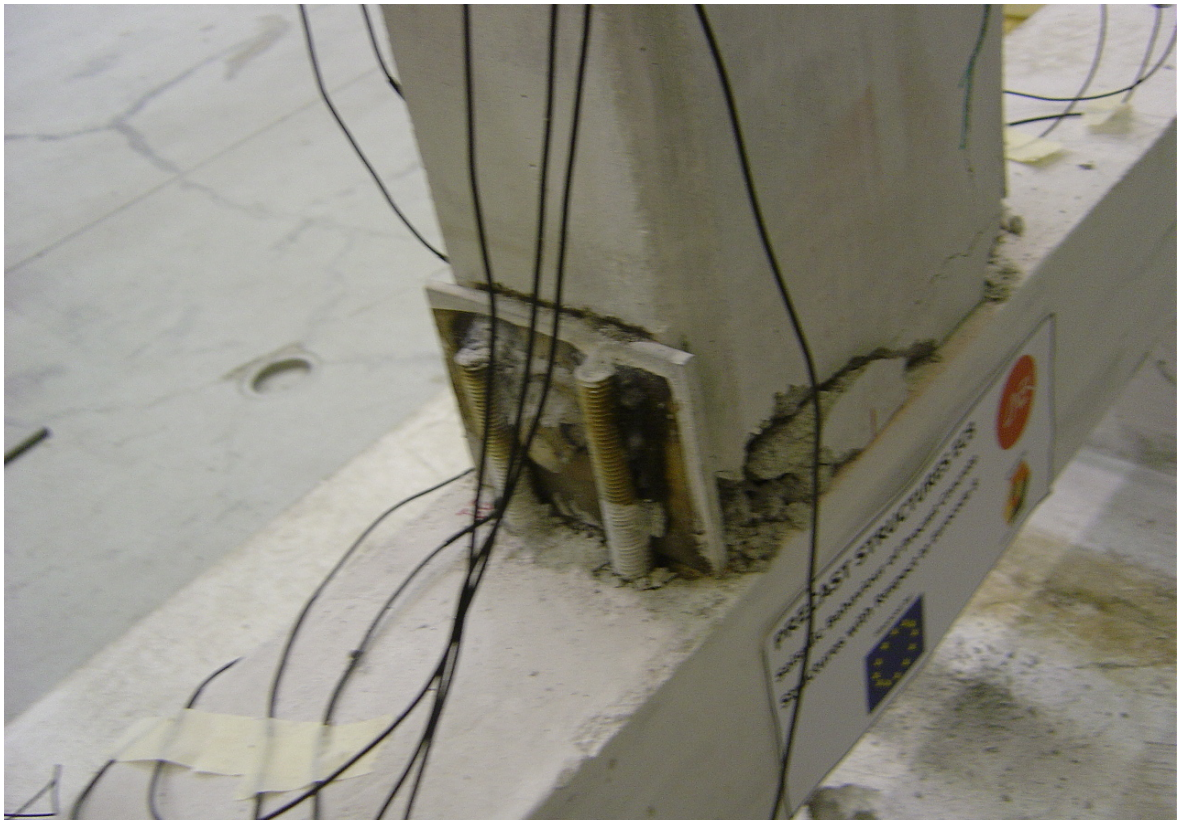

Figure C.20: Specimen V2 – Detail of the plate-beam relative displacements.

Figure C.21: Specimen V2 – Detail of the most damaged zone.

Figure C.22: Specimen V2 – Detail of the bolt's response.

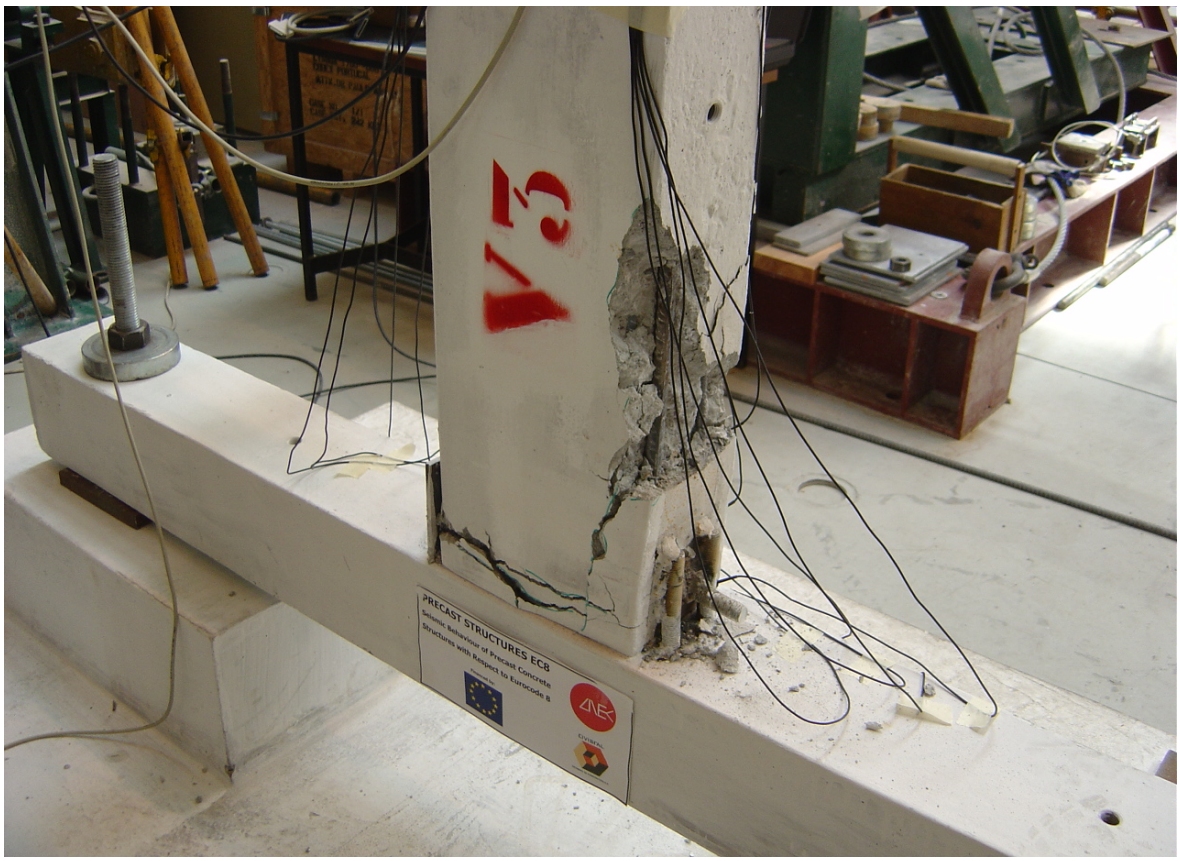

Figure C.23: Specimen V3 – General view (during the test).

Figure C.24: Specimen V3 – Detail of the plate-beam relative displacements.

C.11 Specimen V4

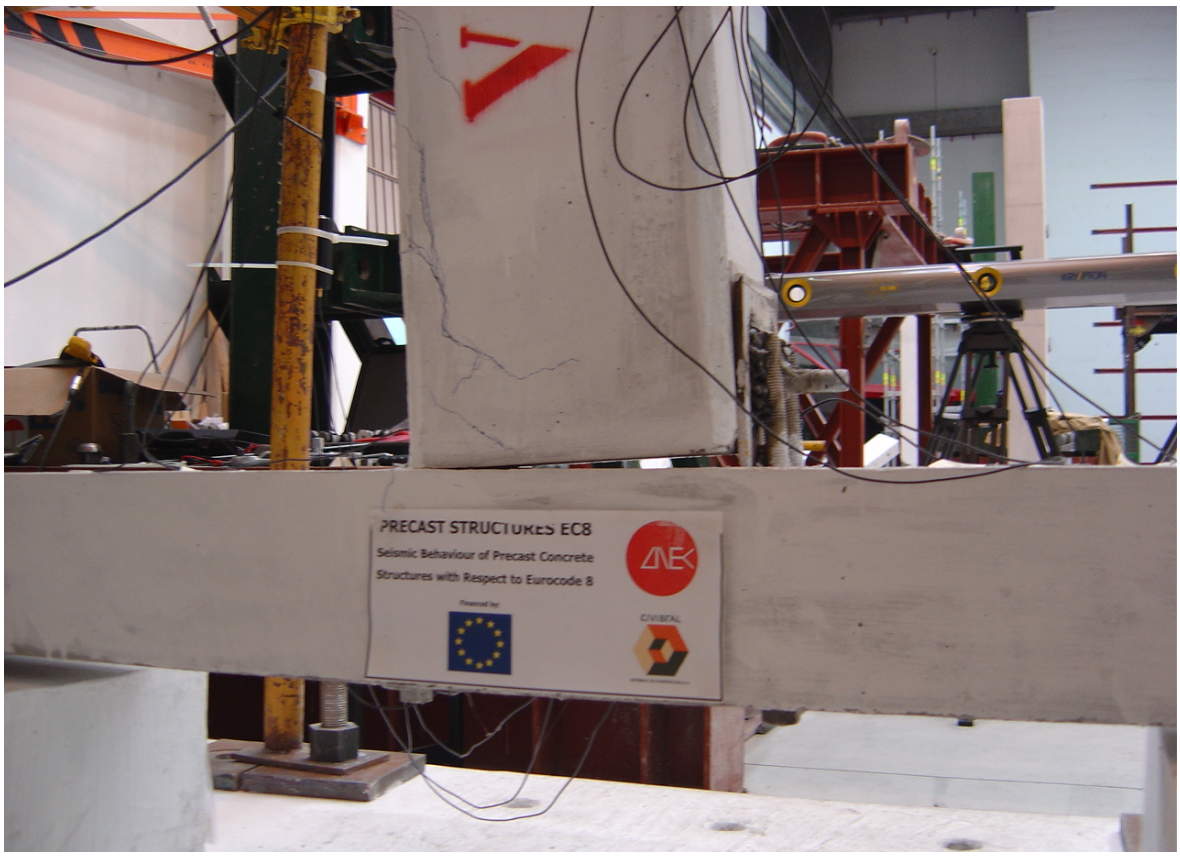

Figure C.25: Specimen V4 – Detail of large gap between the column and the beam.

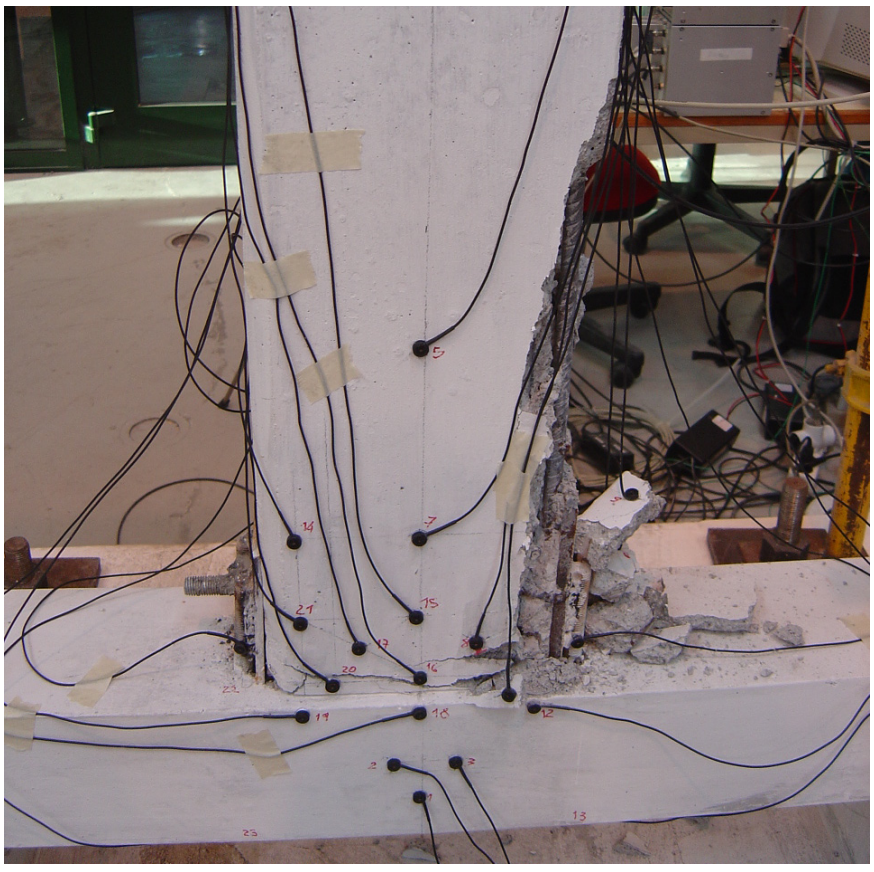

Figure C.26: Specimen V4 – General view (after the test).

C.12 Specimen V5

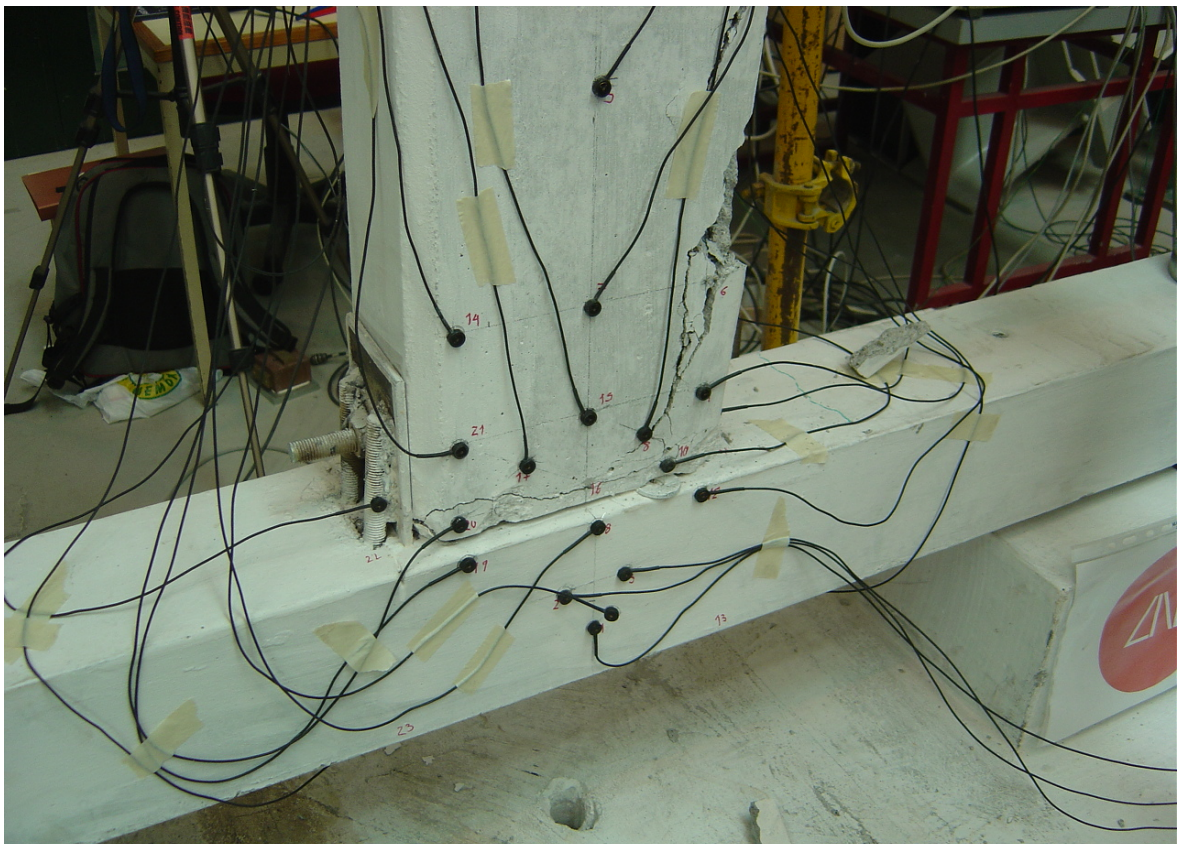

Figure C.27: Specimen V5 – General view (after the test).

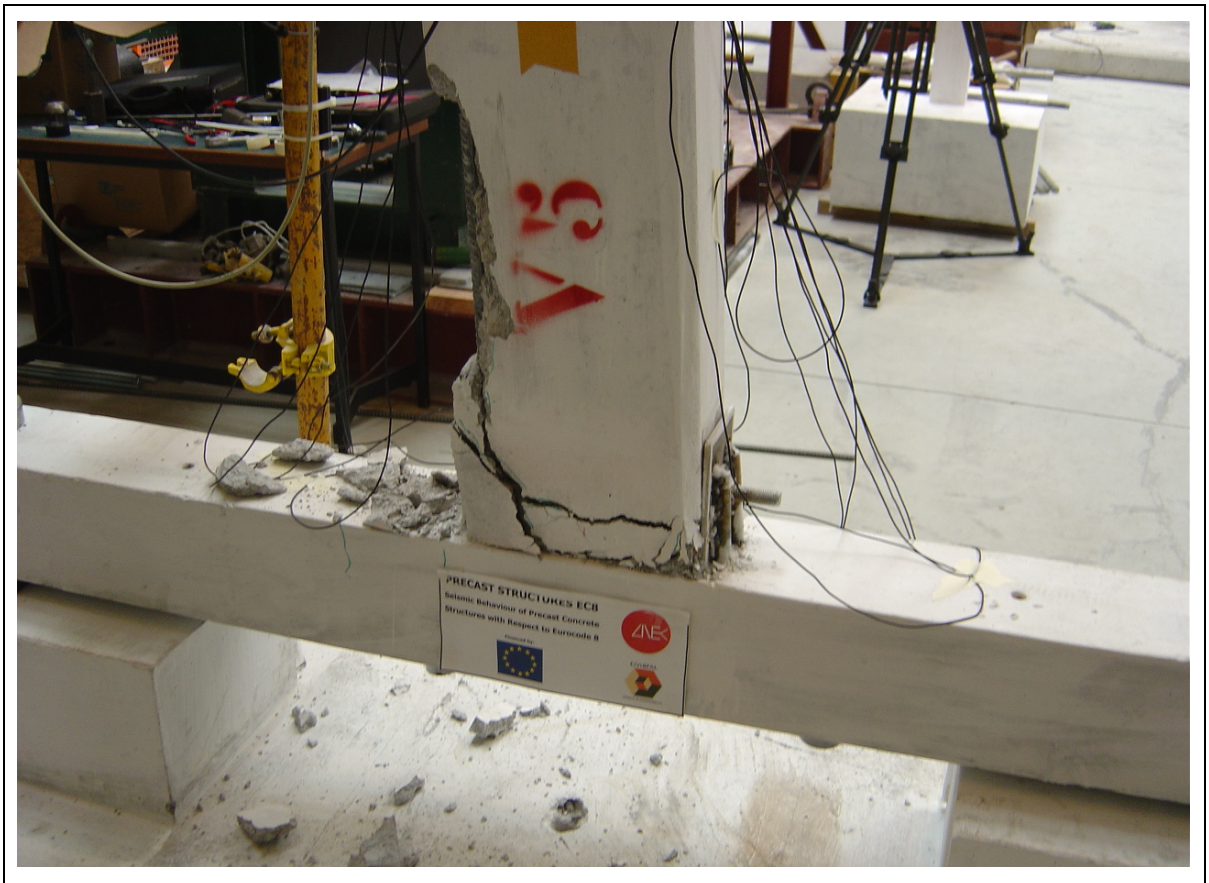

Figure C.28: Specimen V5 – General view of the most damaged zone.

C.13 Specimen VL1

Figure C.29: Specimen VL1 – View of the initial damage.

Figure C.30: Specimen VL1 – Detail of the hollow box/beam interaction.

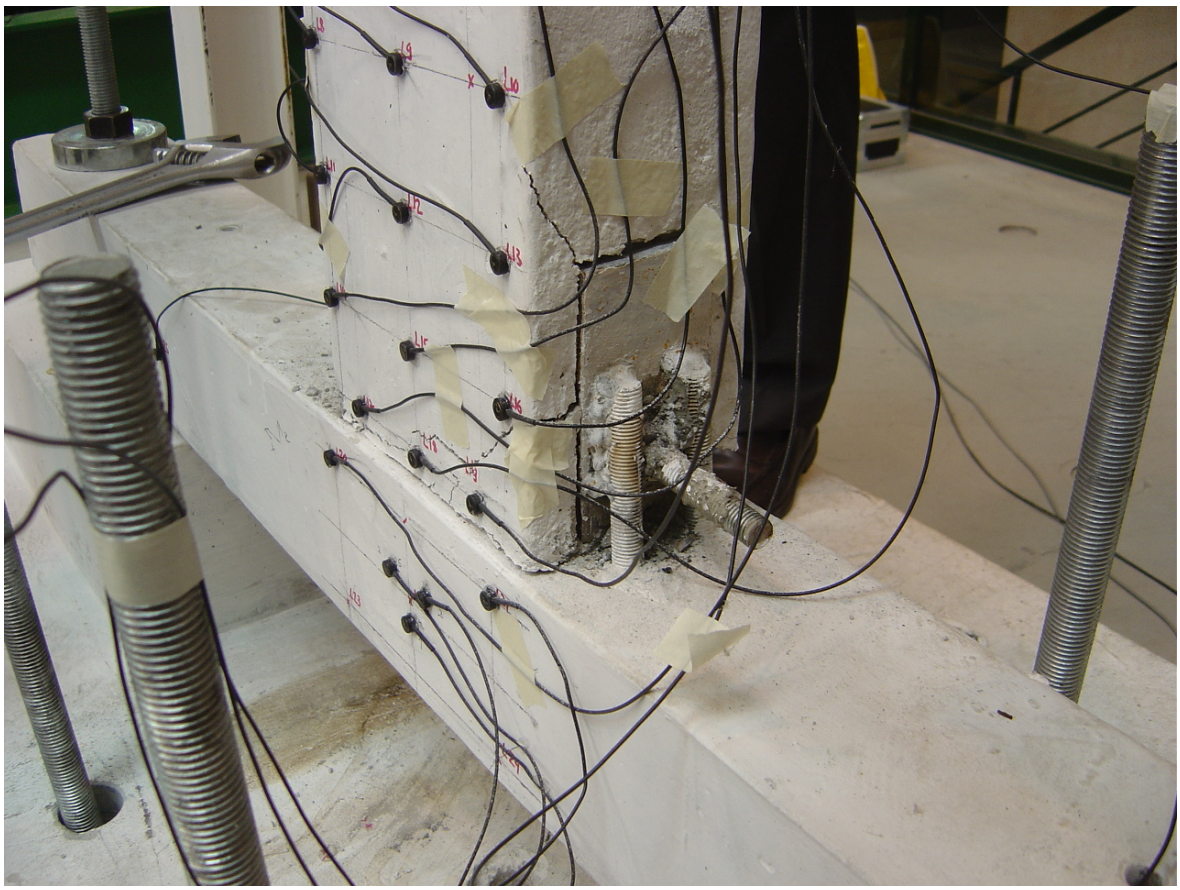

Figure C.31: Specimen VL1 – Detail of the plate-beam relative displacements.

Figure C.32: Specimen VL1 – Reinforcing steel inspection.

C.14 Specimen VL2

Figure C.33: Specimen VL2 – Detail of the hollow box/beam interaction.

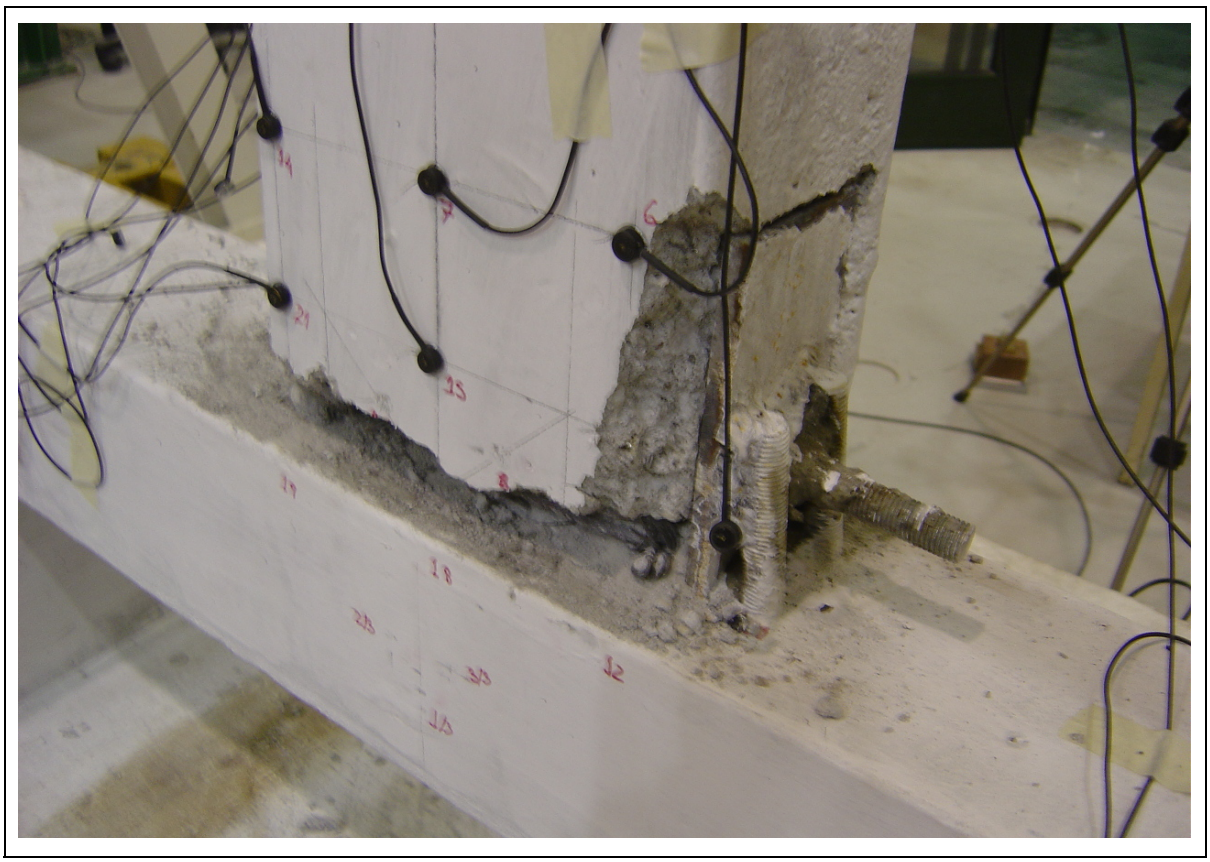

Figure C.34: Specimen VL2 – Detail of the plate-beam relative displacements.

C.15 Specimen VL3

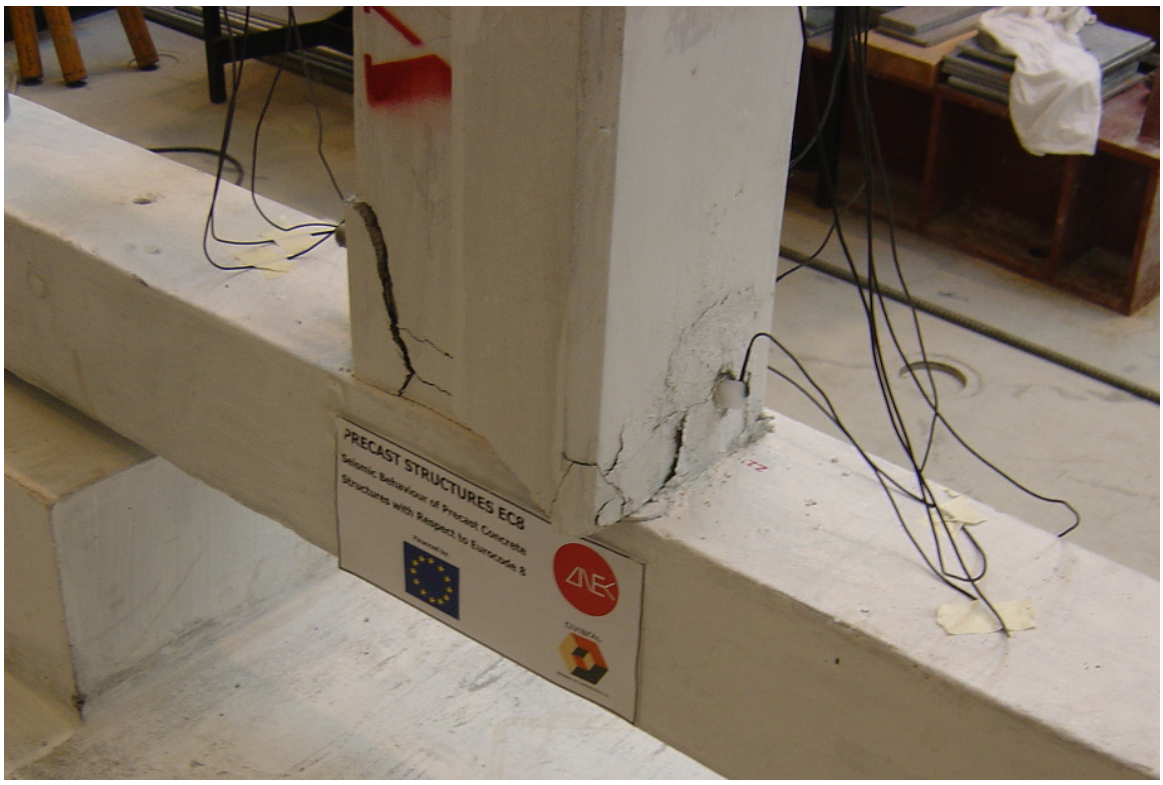

Figure C.35: Specimen VL3 – Initial damage pattern.

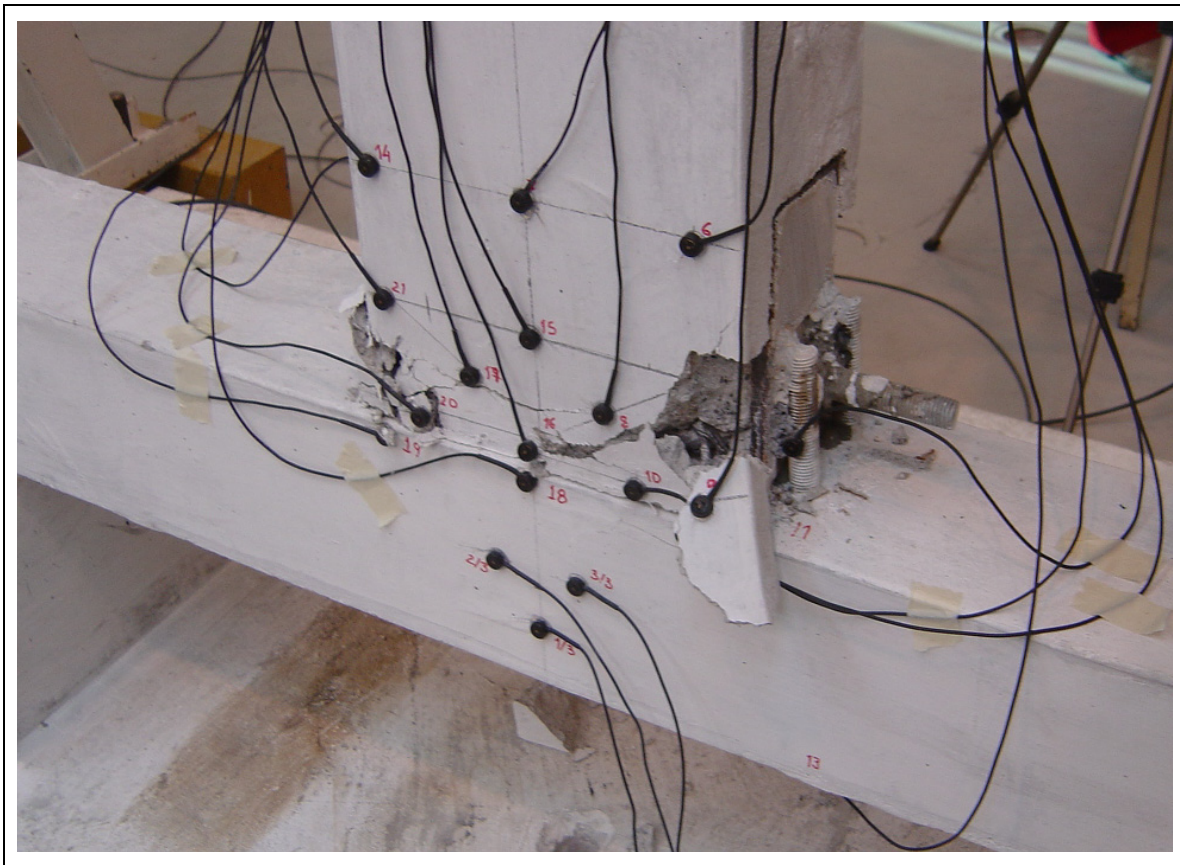

Figure C.36: Specimen VL3 – General view of the most damage zone.

C.16 Specimen VL4

Figure C.37: Specimen VL4 – Detail of the initial damage.

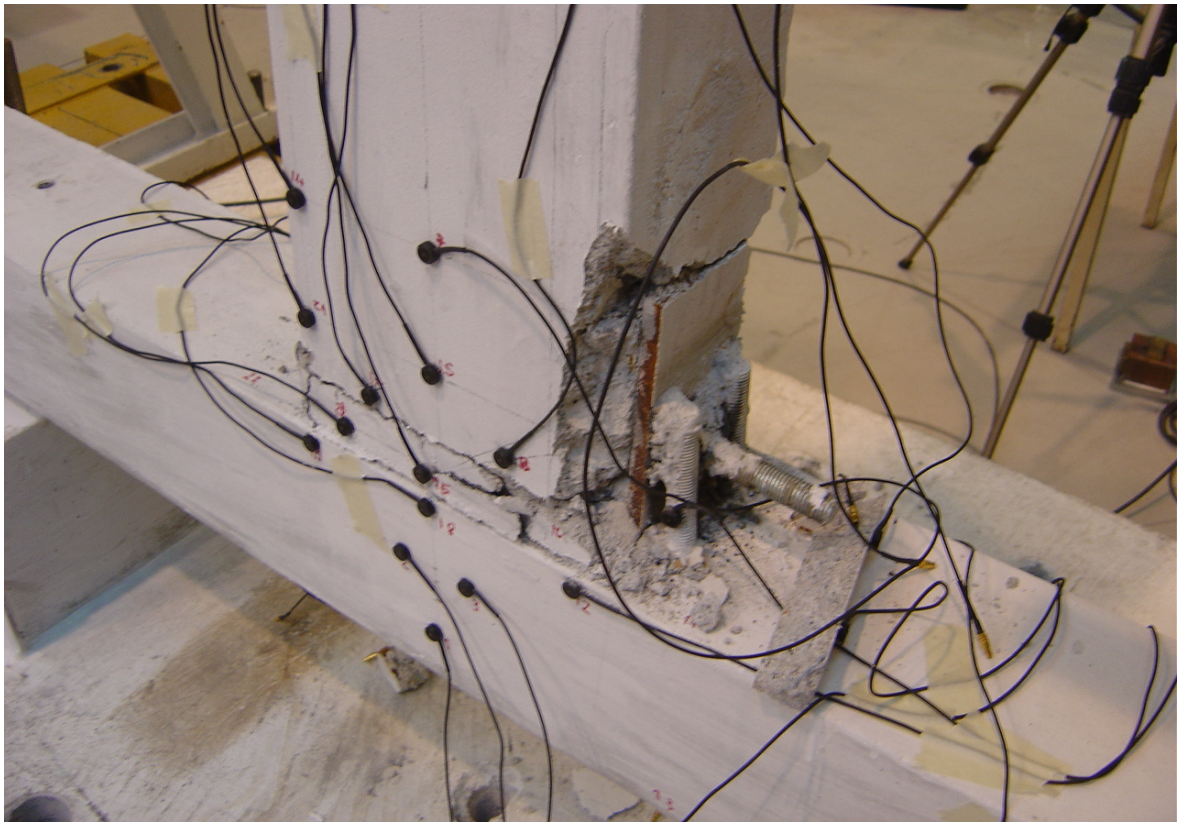

Figure C.38: Specimen VL4 – General view of the most damaged zone (after the test).

C.17 Specimen VL5

Figure C.39: Specimen VL5 – Detail of the initial cracking.

Figure C.40: Specimen VL5 – Detail of the plate-beam relative displacements.

ANNEX D NATURAL FREQUENCIES

Contents:

List of Figures:

D.1 Specimen P1

Channels: P1-Acc1-Column Mid Span-Ambient;

Frames: Nº20; Overlap=0.00%; Nº points per frame=6000;

Window:None ; Decimate Factor: 1;

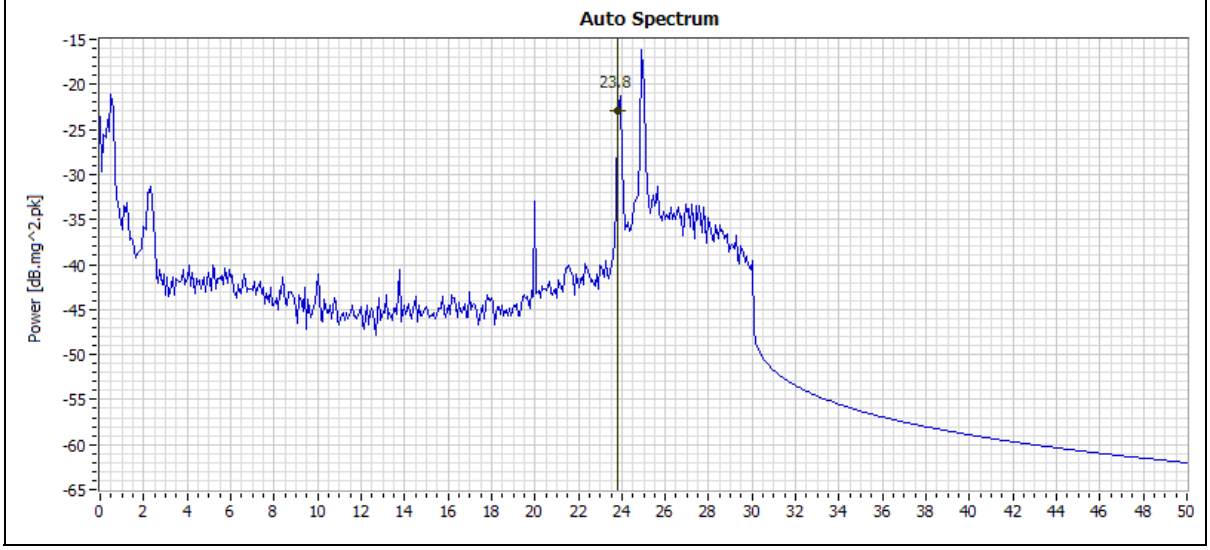

Figure D-1: Specimen P1 – Fundamental Frequency - FRF Peak Picking.

D.2 Specimen P2

Input Channels: P2-Acc2-Column Bottom;

Output Channels: P2-Acc1-Beam Mid Span;

Frames: Nº23; Overlap=0.00%; Nº points per frame=2609;

Window:None ; Decimate Factor: 1;

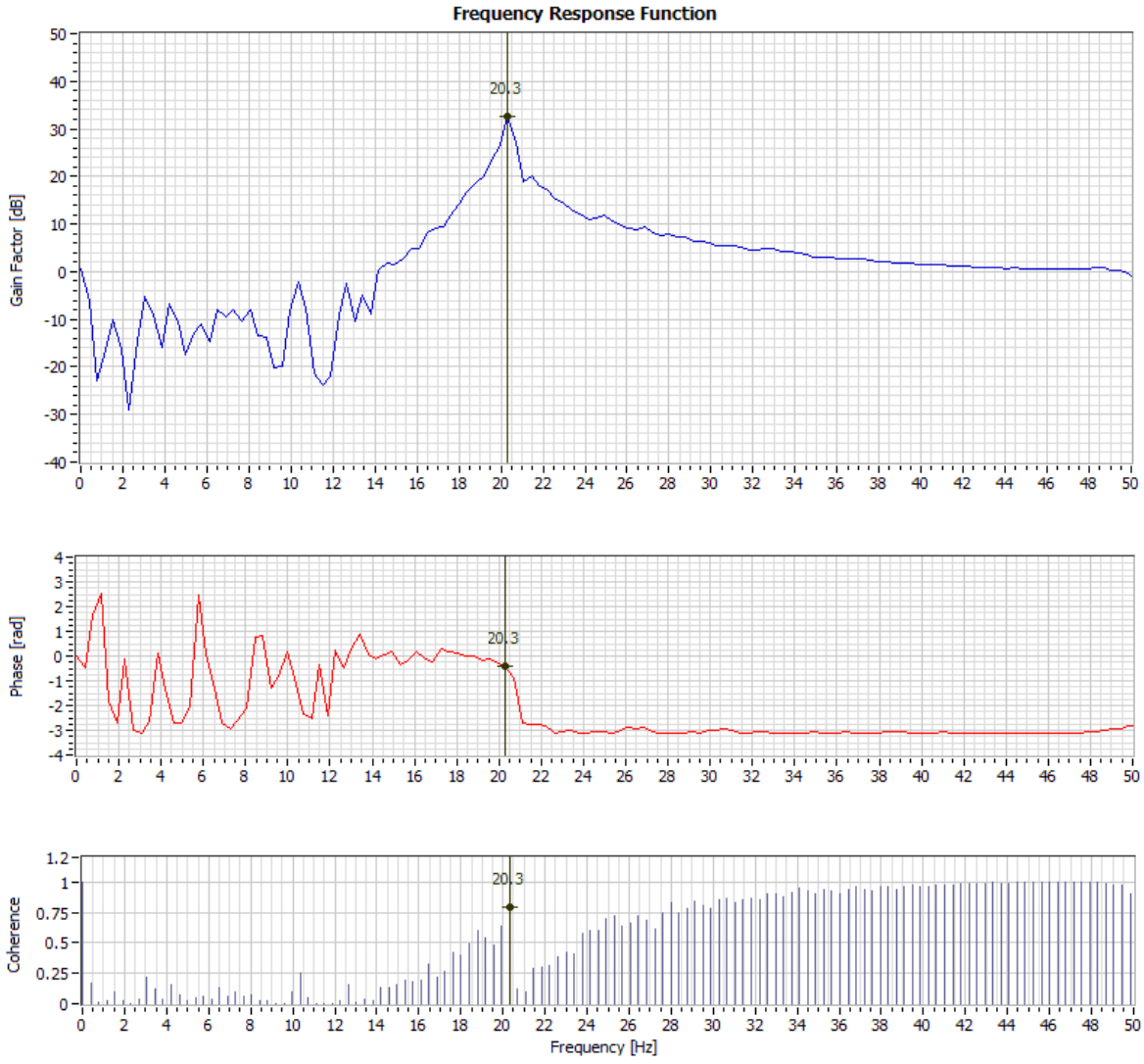

Figure D-2: Specimen P2 – Fundamental Frequency - FRF Peak Picking.

D.3 Specimen P3

Input Channels: P3-Acc2-Column Bottom;

Output Channels: P3-Acc1-Beam Mid Span;

Frames: Nº31; Overlap=0.00%; Nº points per frame=1935;

Window:None ; Decimate Factor: 1;

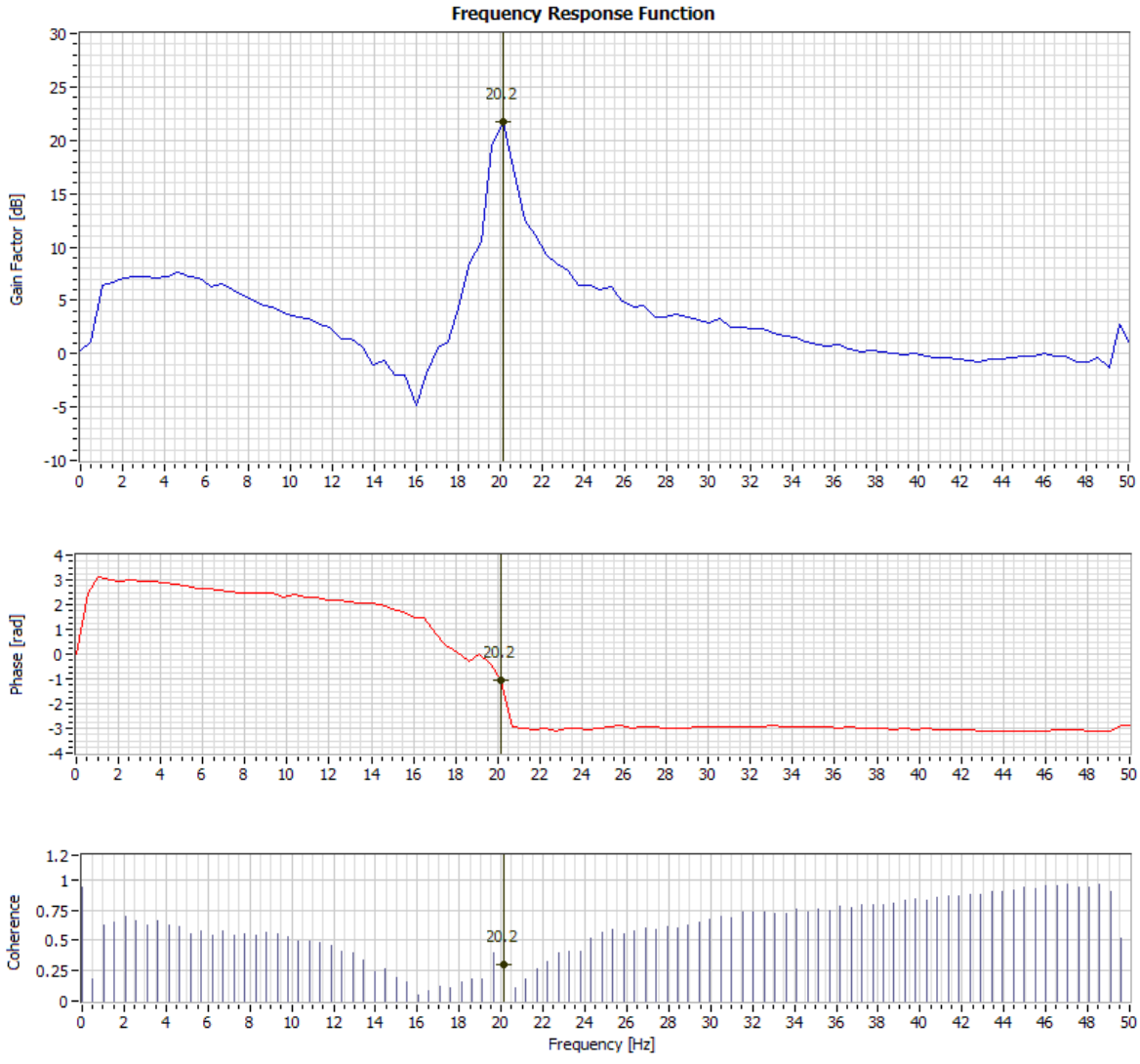

Figure D-3: Specimen P3 – Fundamental Frequency - FRF Peak Picking..

D.4 Specimen P4

Input Channels: P4-Acc2-Column Bottom;

Output Channels: P4-Acc1-Beam Mid Span;

Frames: Nº37; Overlap=0.00%; Nº points per frame=1622;

Window:None ; Decimate Factor: 1;

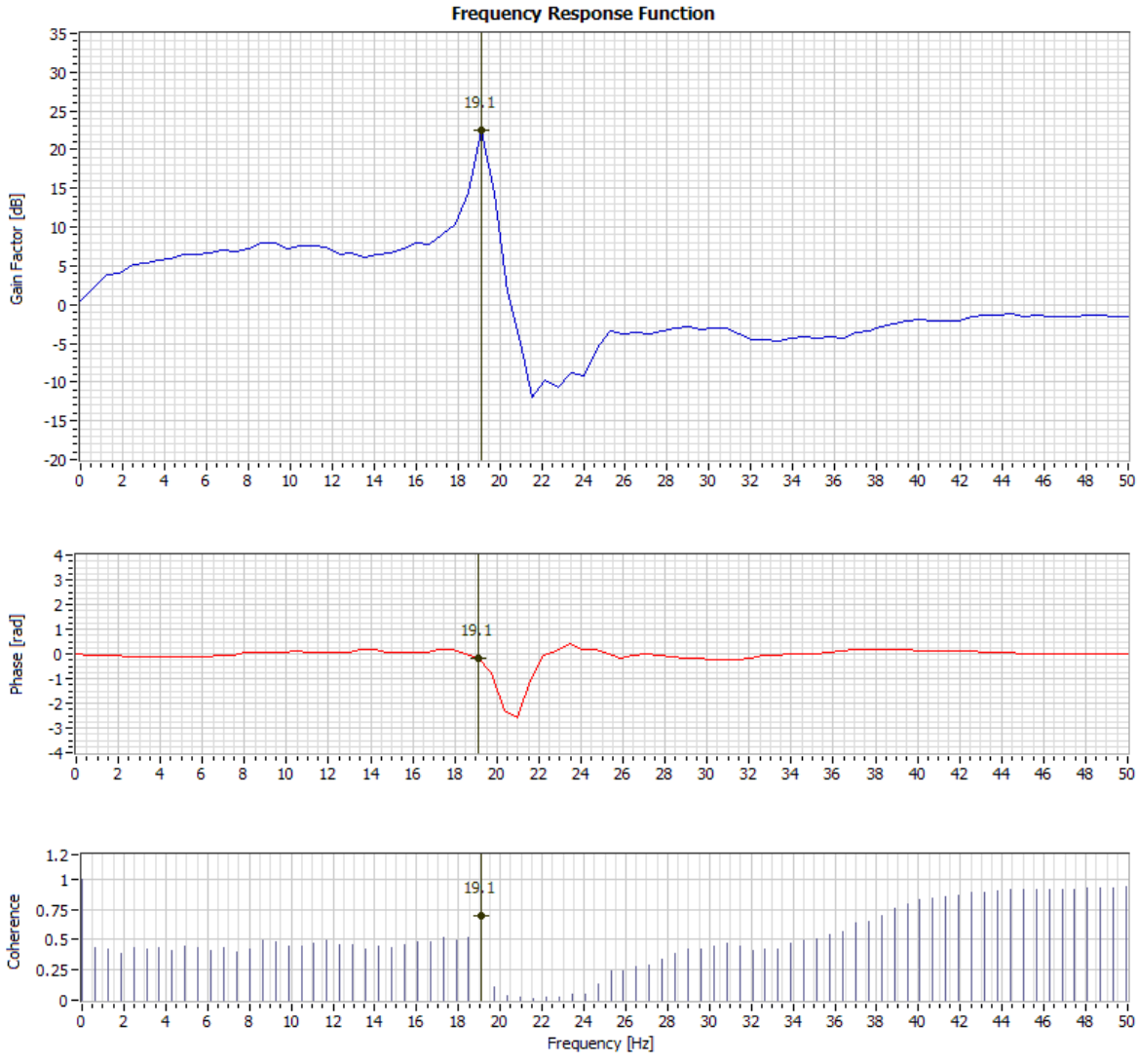

Figure D-4: Specimen P4 – Fundamental Frequency - FRF Peak Picking..

D.5 Specimen V1

Output Channels: V1-Acc1-Column Mid Span;V1-Acc1-Column Mid Span 2;

Frames: Nº100; Overlap=0.00%; Nº points per frame=1440;

Window:None ; Decimate Factor: 1;

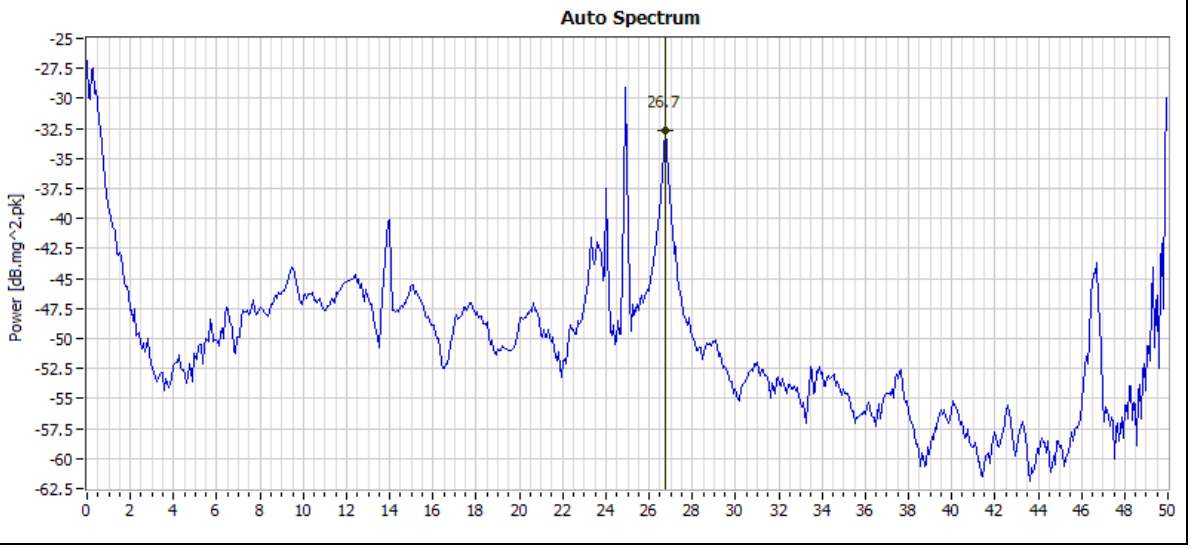

Figure D-5: Specimen V1 – Fundamental Frequency - FRF Peak Picking.

D.6 Specimen V2

Input Channels: V2-Acc2-Column Bottom;

Output Channels: V2-Acc1-Beam Mid Span;

Frames: Nº16; Overlap=0.00%; Nº points per frame=250;

Window:None ; Decimate Factor: 1;

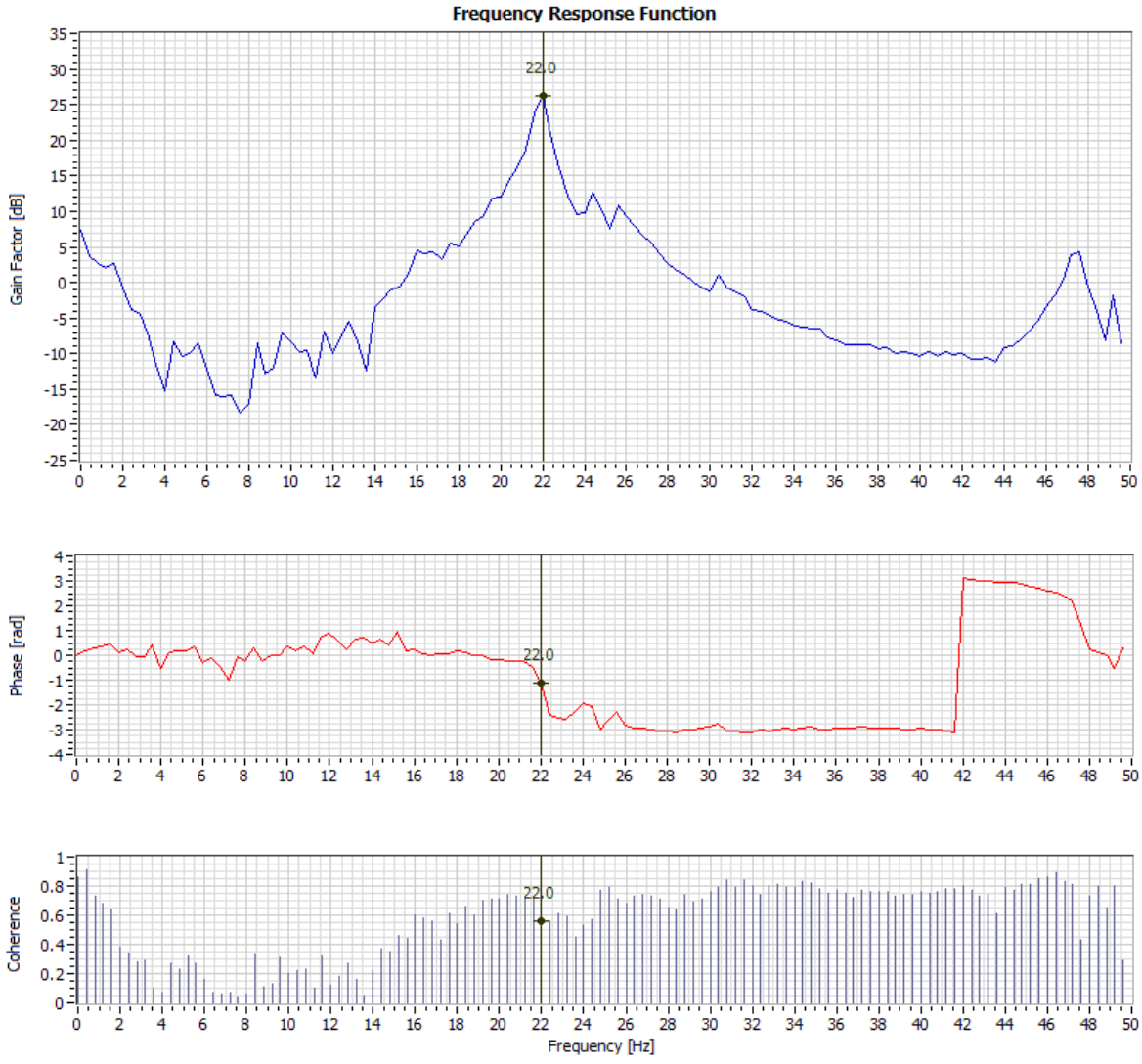

Figure D-6: Specimen V2 – Fundamental Frequency - FRF Peak Picking.

D.7 Specimen V3

Input Channels: V3-Acc2-Column Bottom;

Output Channels: V3-Acc1-Beam Mid Span;

Frames: Nº17; Overlap=0.00%; Nº points per frame=3529;

Window:None ; Decimate Factor: 1;

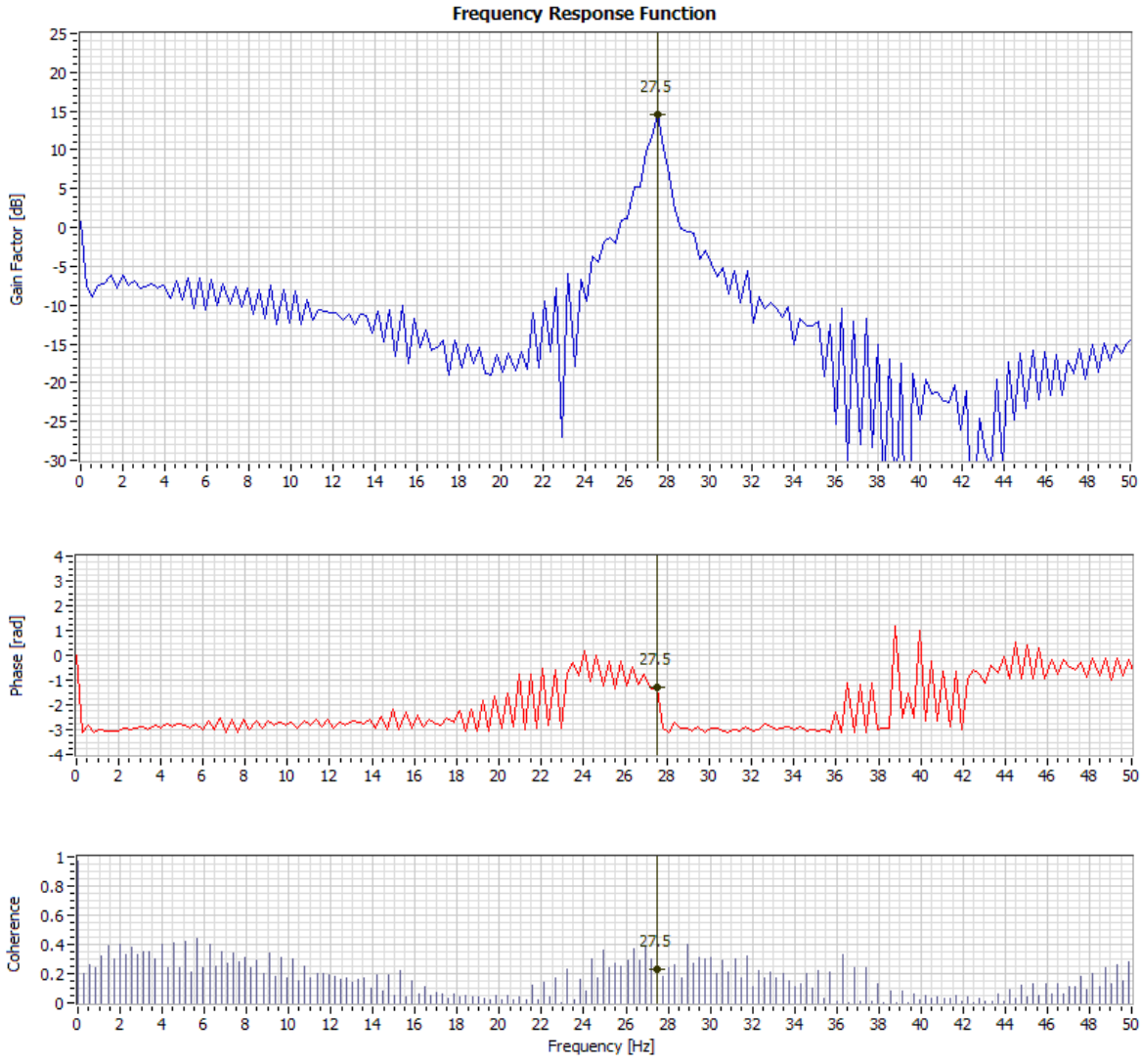

Figure D-7: Specimen V3 – Fundamental Frequency - FRF Peak Picking.

D.8 Specimen V4

Input Channels: V4-Acc2-Column Bottom;

Output Channels: V4-Acc1-Beam Mid Span;

Frames: Nº35; Overlap=0.00%; Nº points per frame=1714;

Window:None ; Decimate Factor: 1;

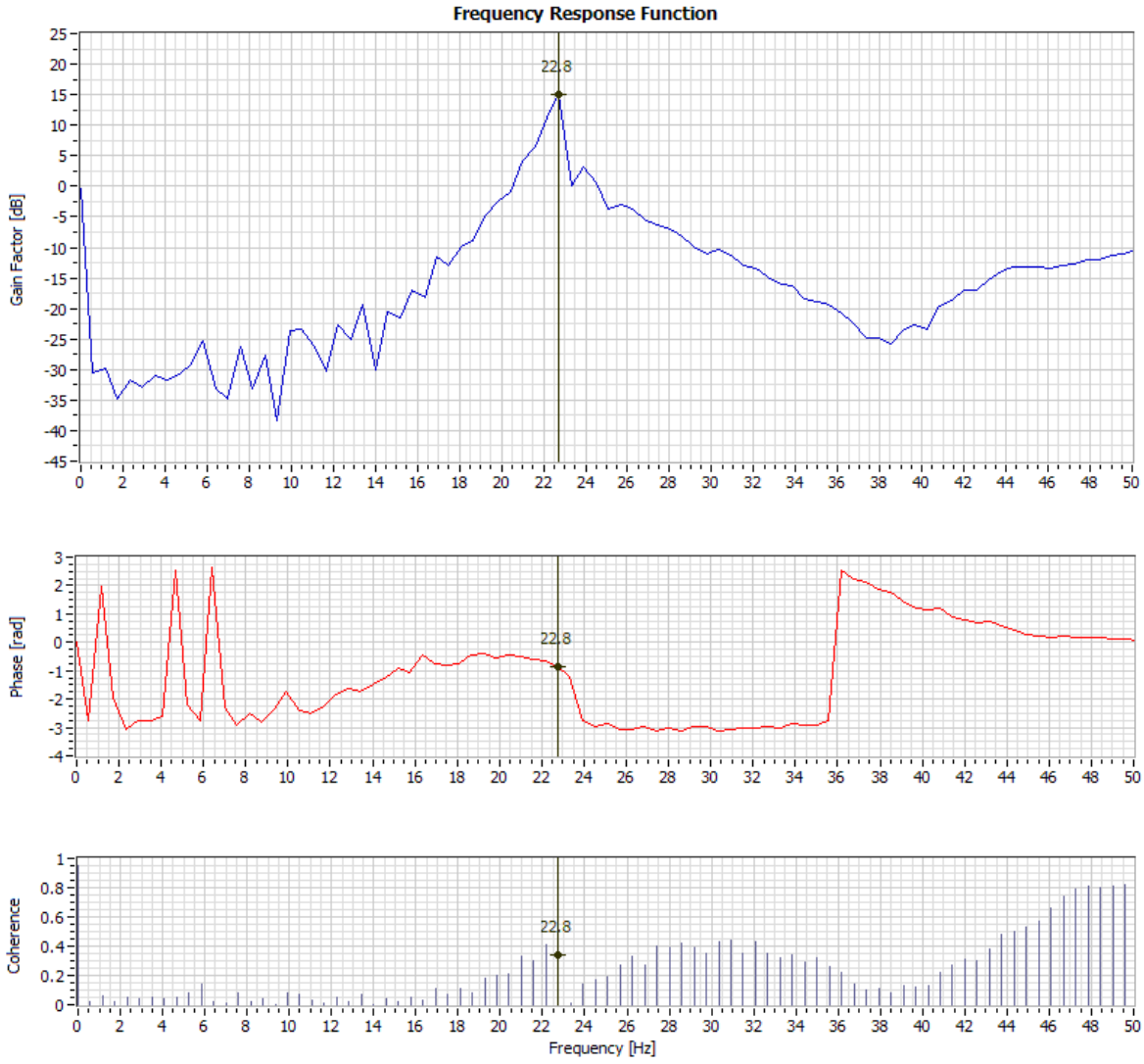

Figure D-8: Specimen V4 – Fundamental Frequency - FRF Peak Picking.

D.9 Specimen V5

Input Channels: V5-Acc2-Column Bottom;

Output Channels: V5-Acc1-Beam Mid Span;

Frames: Nº23; Overlap=5.00%; Nº points per frame=2740;

Window:None ; Decimate Factor: 1;

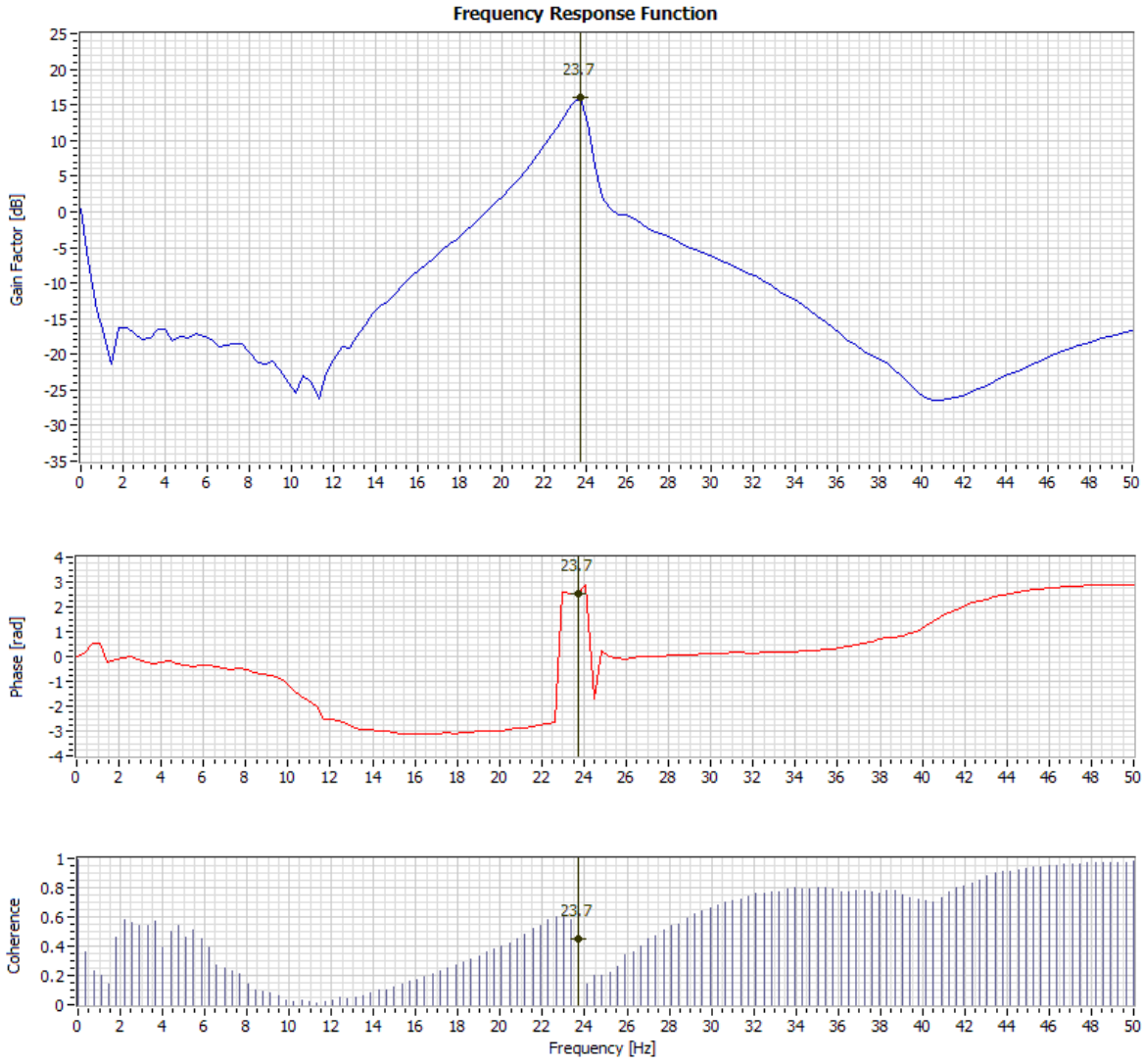

Figure D-9: Specimen V5 – Fundamental Frequency - FRF Peak Picking.

D.10 Specimen VL1

Output Channels: VL1-Acc1-Column Mid Span;

Frames: Nº13; Overlap=0.00%; Nº points per frame=1846;

Window:None ; Decimate Factor: 1;

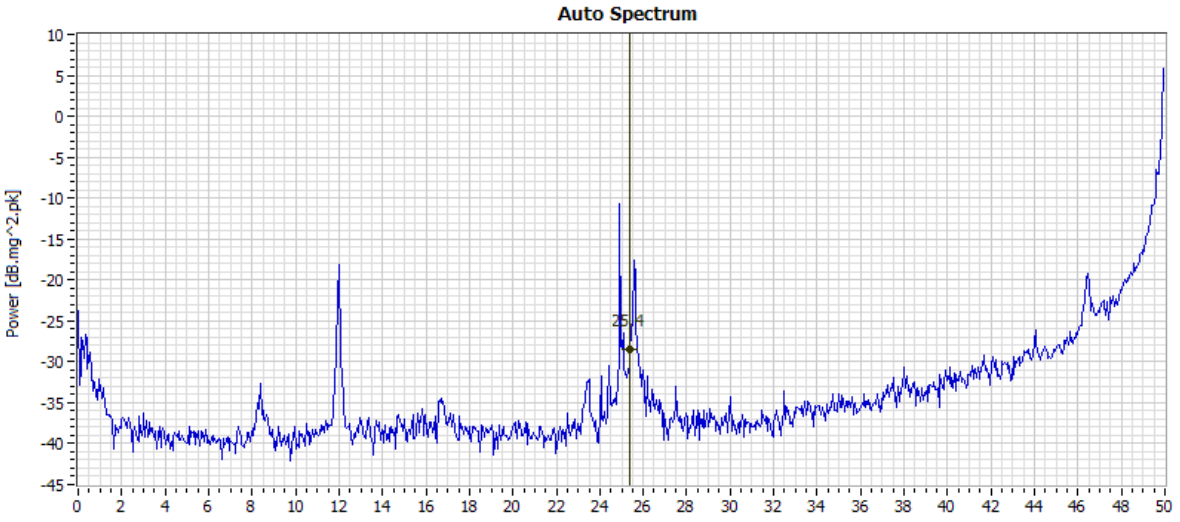

Figure D-10: Specimen VL1 – Fundamental Frequency - FRF Peak Picking.

D.11 Specimen VL2

Input Channels: VL2-Acc2-Column Bottom;

Output Channels: VL2-Acc1-Beam Mid Span;

Frames: Nº31; Overlap=0.00%; Nº points per frame=194;

Window:None ; Decimate Factor: 1;

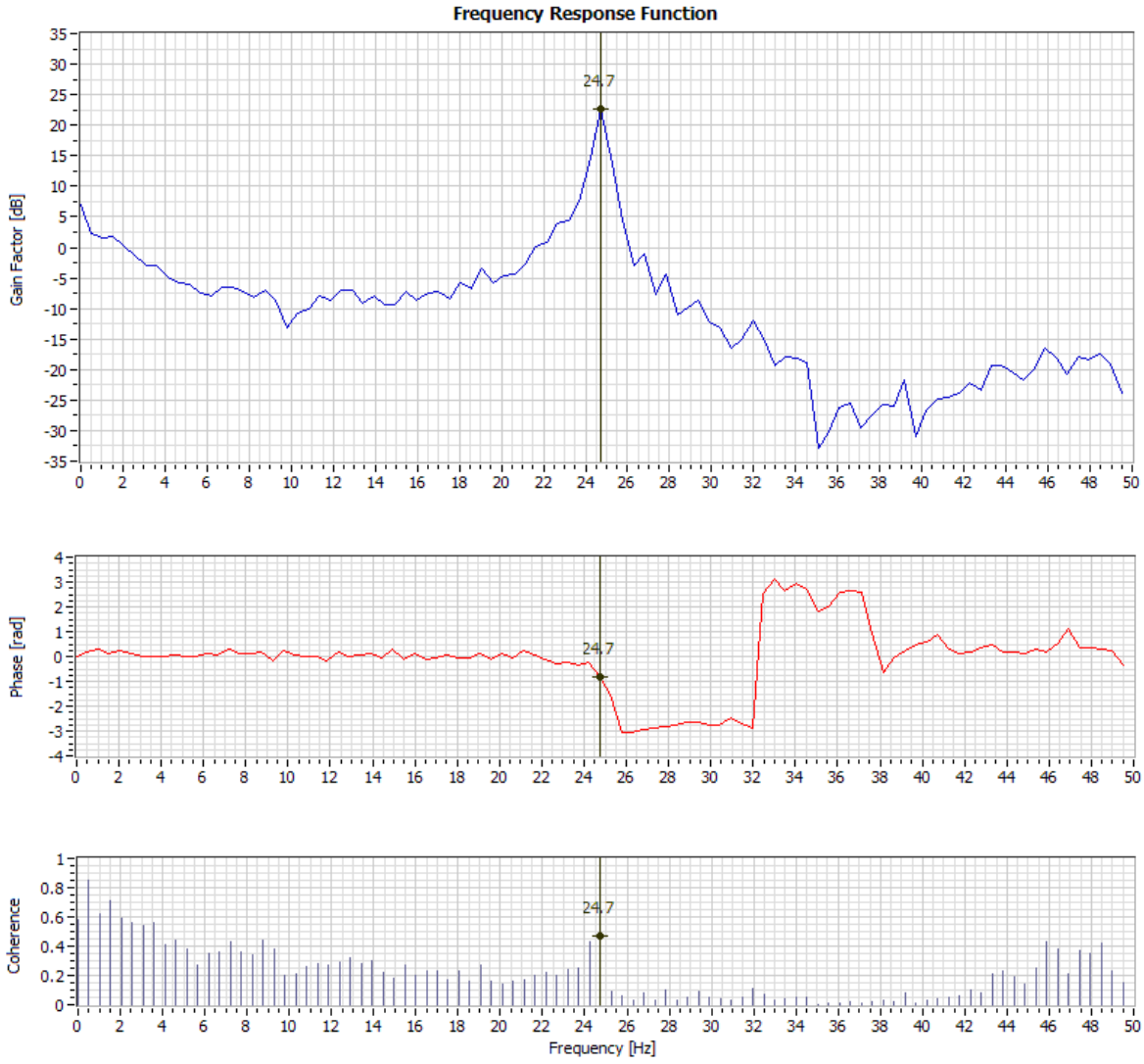

Figure D-11: Specimen VL2 – Fundamental Frequency - FRF Peak Picking.

D.12 Specimen VL3

Input Channels: VL3-Acc2-Column Bottom;

Output Channels: VL3-Acc1-Beam Mid Span;

Frames: Nº31; Overlap=0.00%; Nº points per frame=1935;

Window:None ; Decimate Factor: 1;

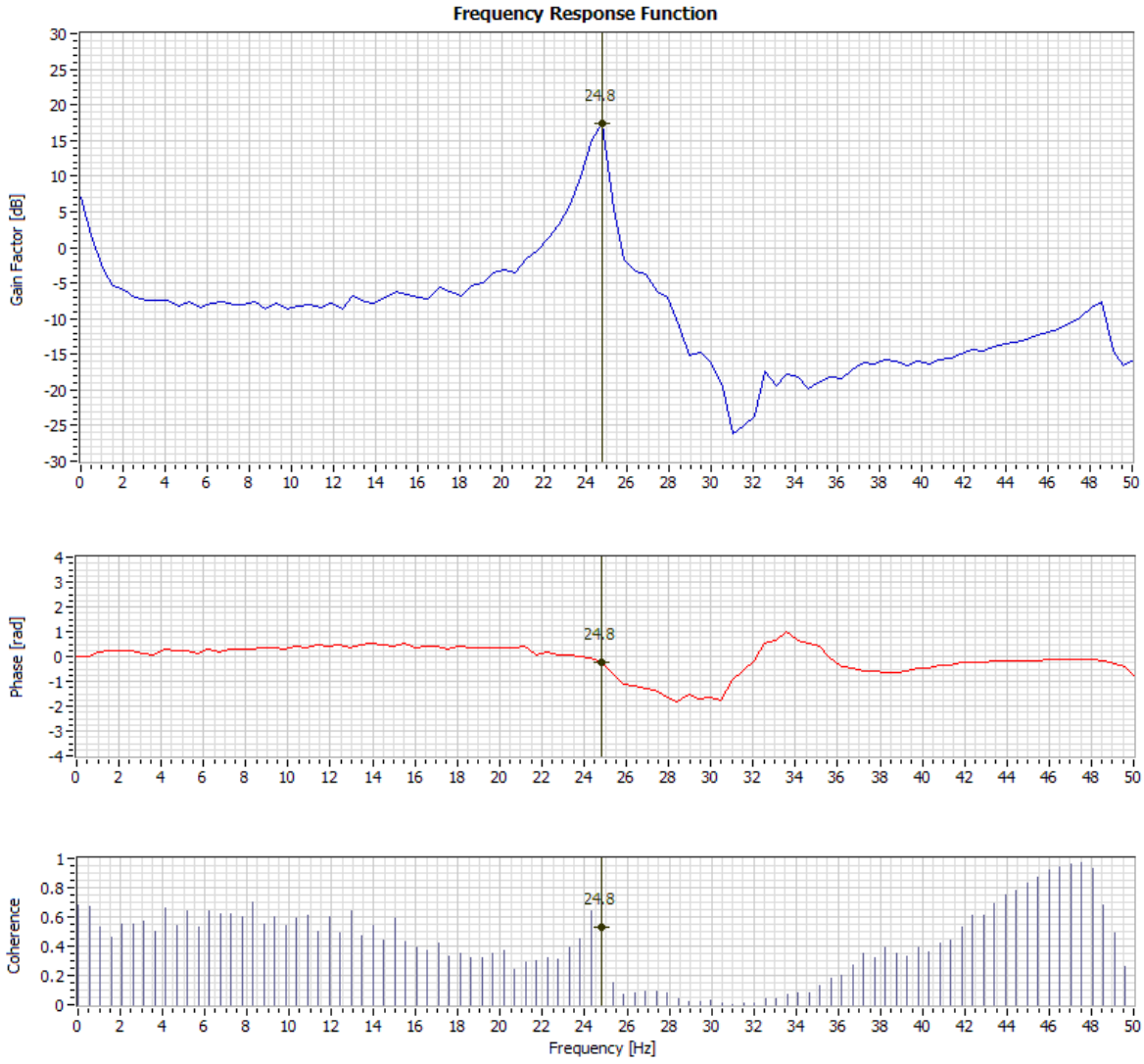

Figure D-12: Specimen VL3 – Fundamental Frequency - FRF Peak Picking.

D.13 Specimen VL4

Input Channels: VL4-Acc2-Column Bottom;

Output Channels: VL4-Acc1-Beam Mid Span;

Frames: Nº32; Overlap=0.00%; Nº points per frame=188;

Window:None ; Decimate Factor: 1;

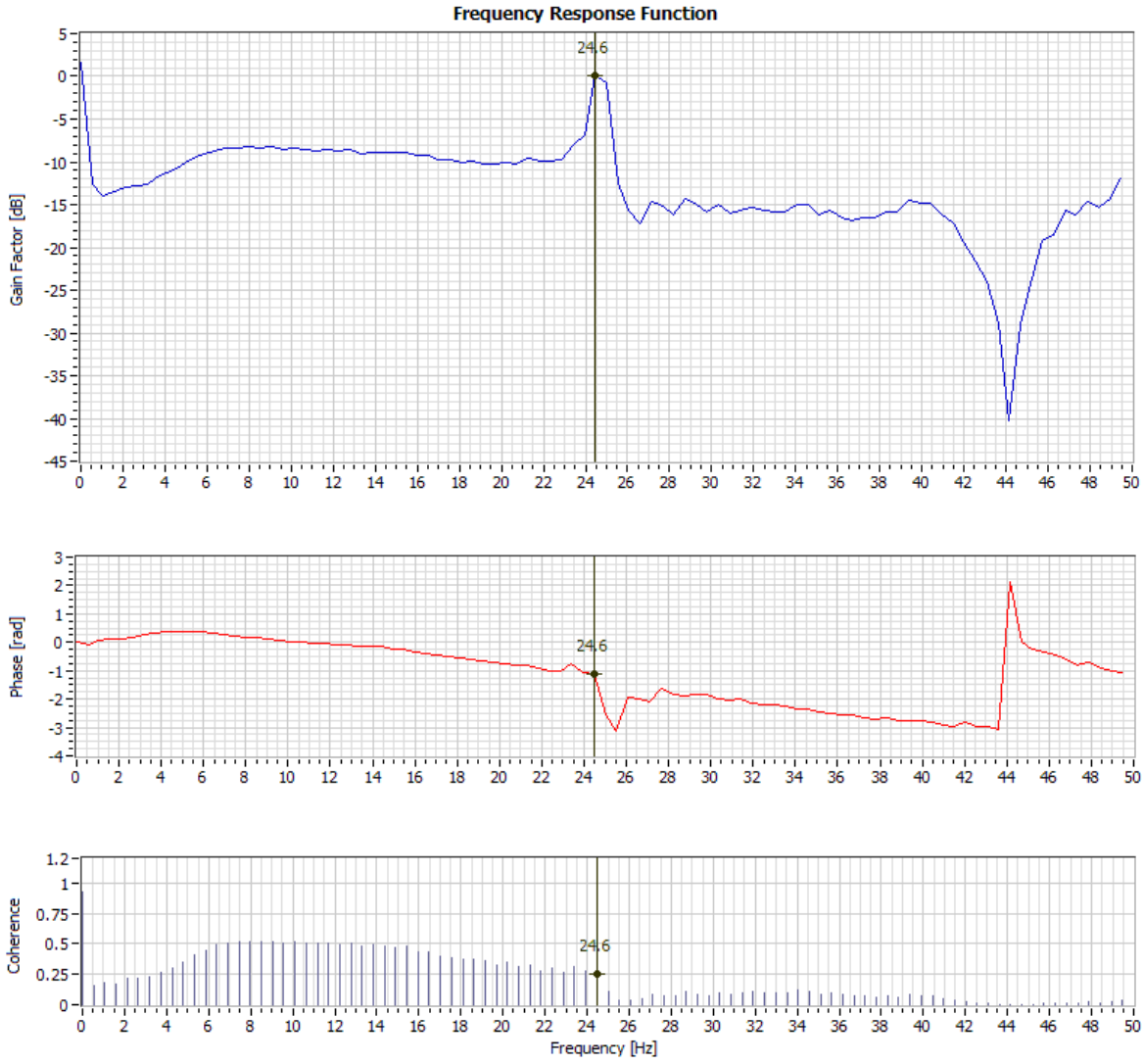

Figure D-13: Specimen VL4 – Fundamental Frequency - FRF Peak Picking.

D.14 Specimen VL5

Input Channels: VL5-Acc2-Column Bottom;

Output Channels: VL5-Acc1-Beam Mid Span;

Frames: Nº28; Overlap=0.00%; Nº points per frame=2143;

Window:None ; Decimate Factor: 1;

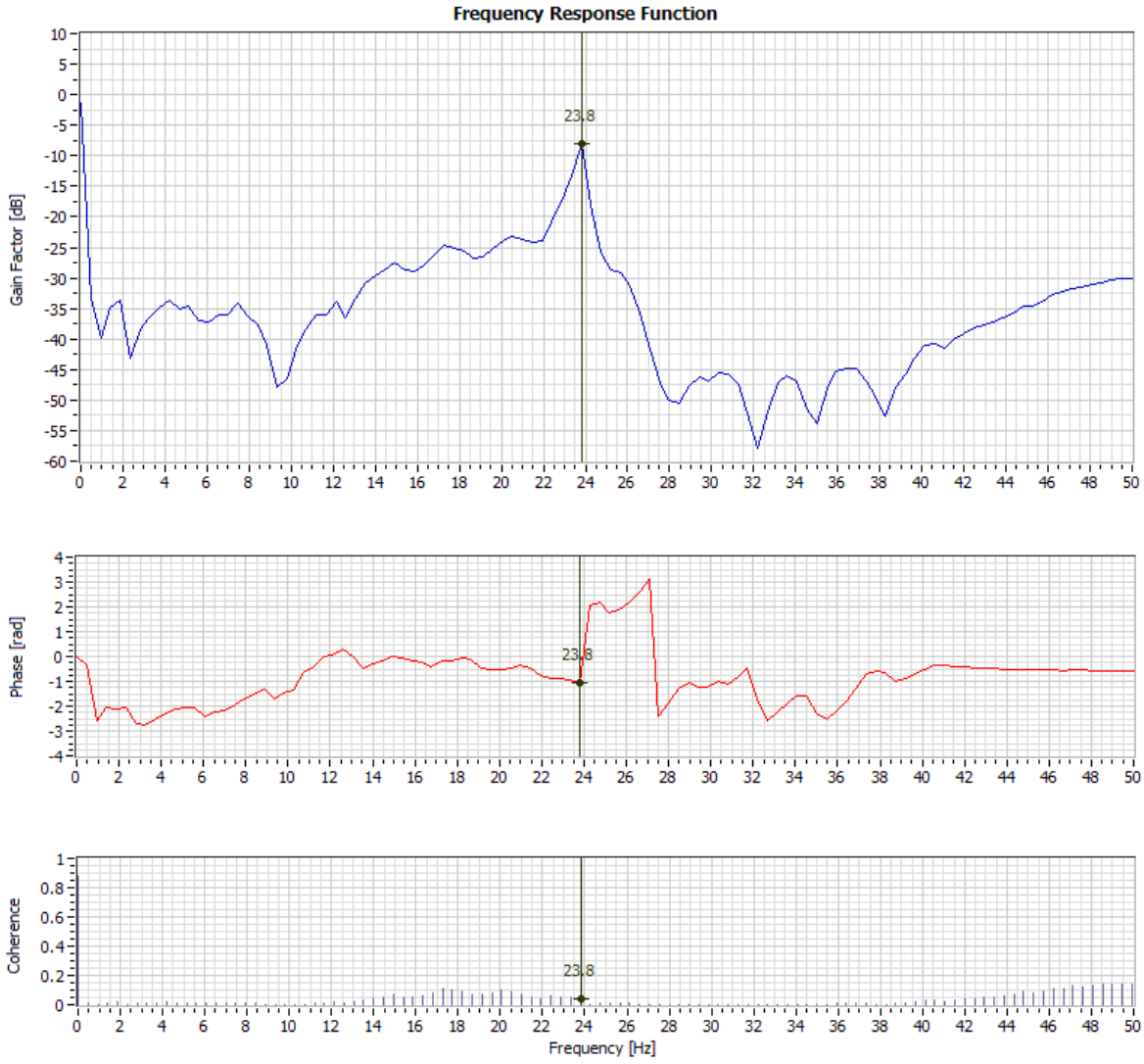

Figure D-14: Specimen VL5 – Fundamental Frequency - FRF Peak Picking.

ANNEX E GLOBAL FORCES AND DISPLACEMENTS

Contents:

List of Figures:

E.1 Specimen P1

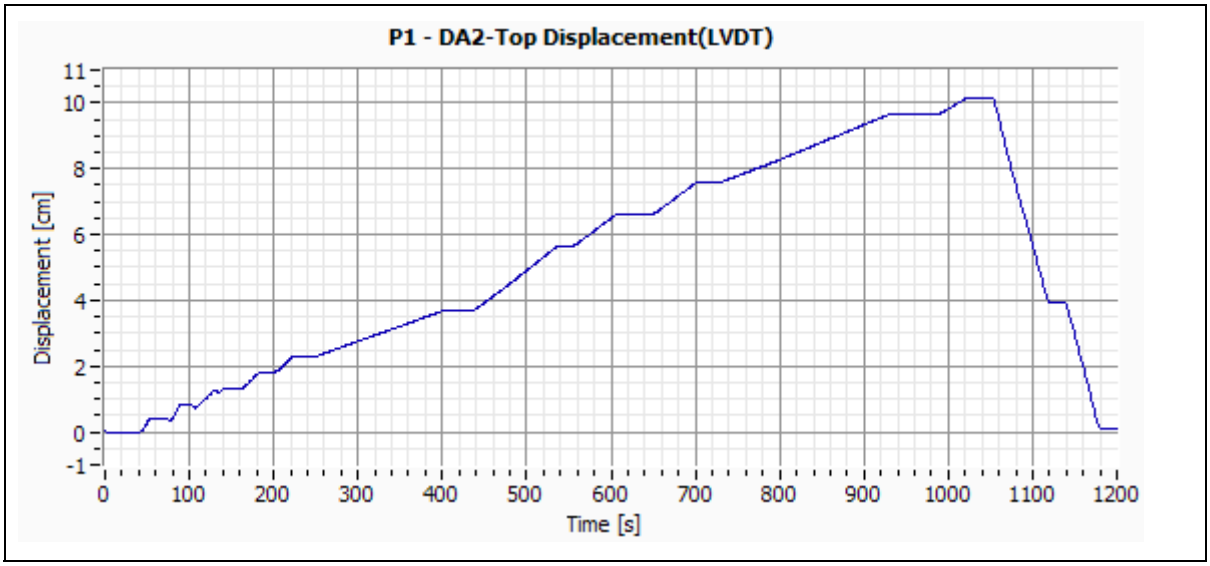

Figure E-1:– Specimen P1-DA2 Top Displacement.

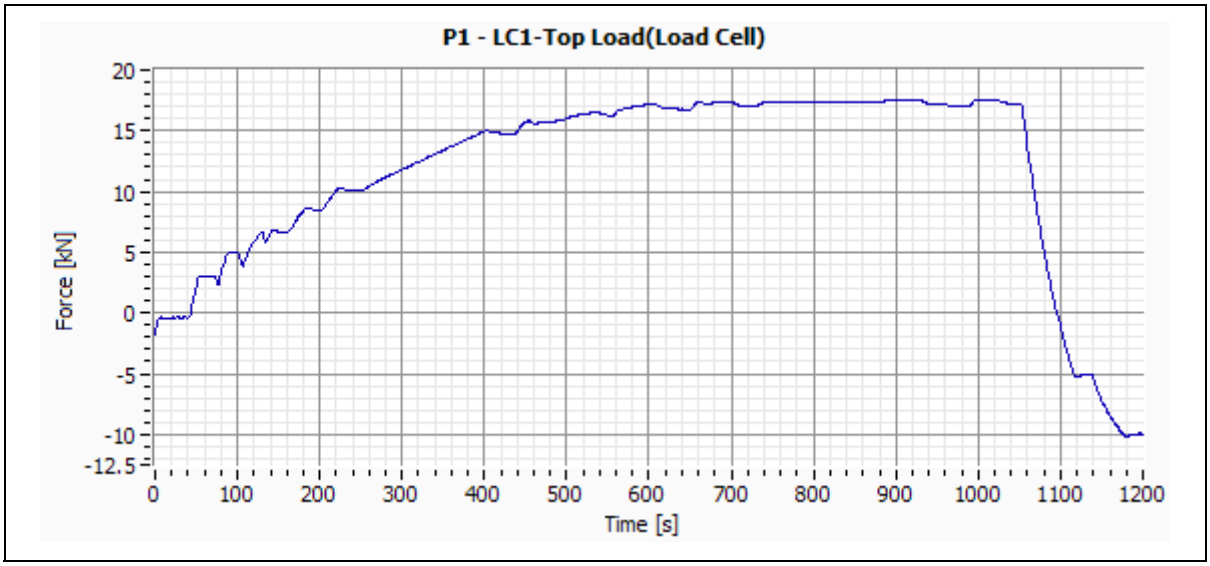

Figure E-2:– Specimen P1-LC1 Top Load.

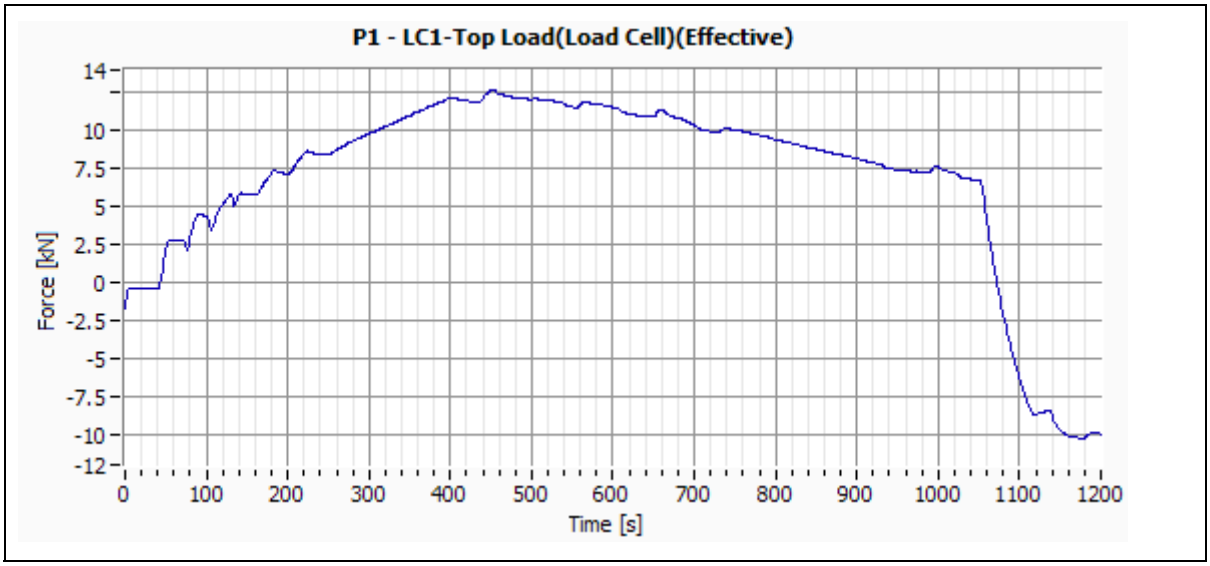

Figure E-3:– Specimen P1-LC1 Top Load (Effective).

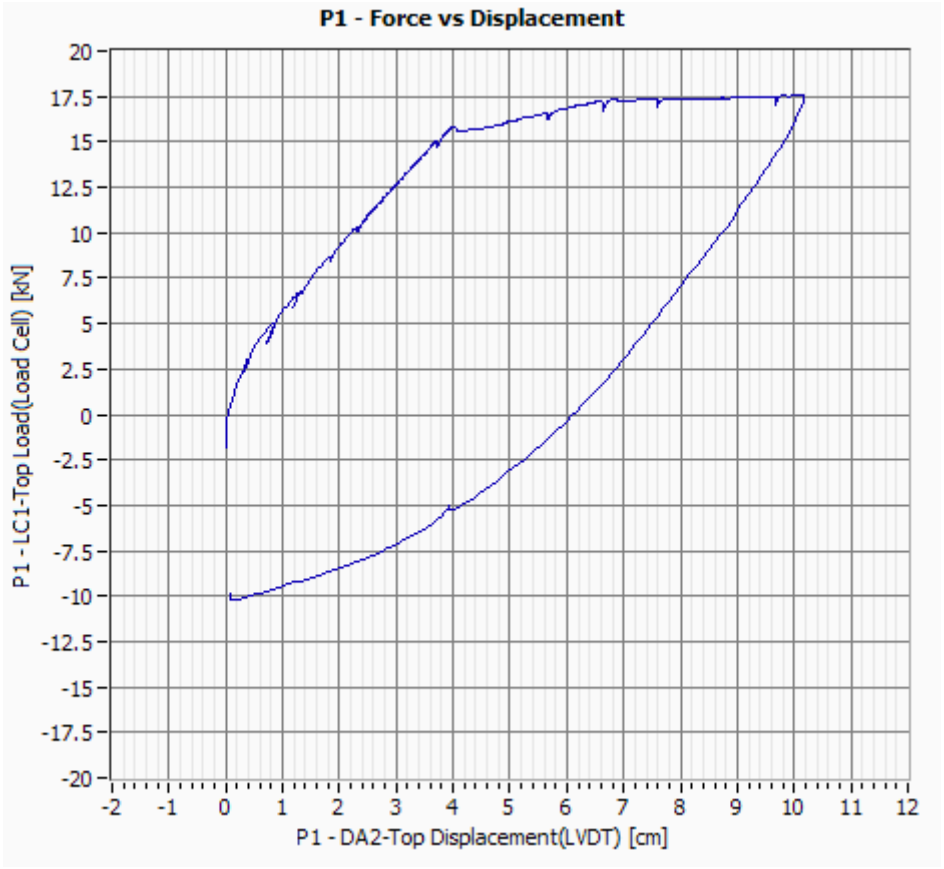

Figure E-4:– Specimen P1-Force vs. Displacement.

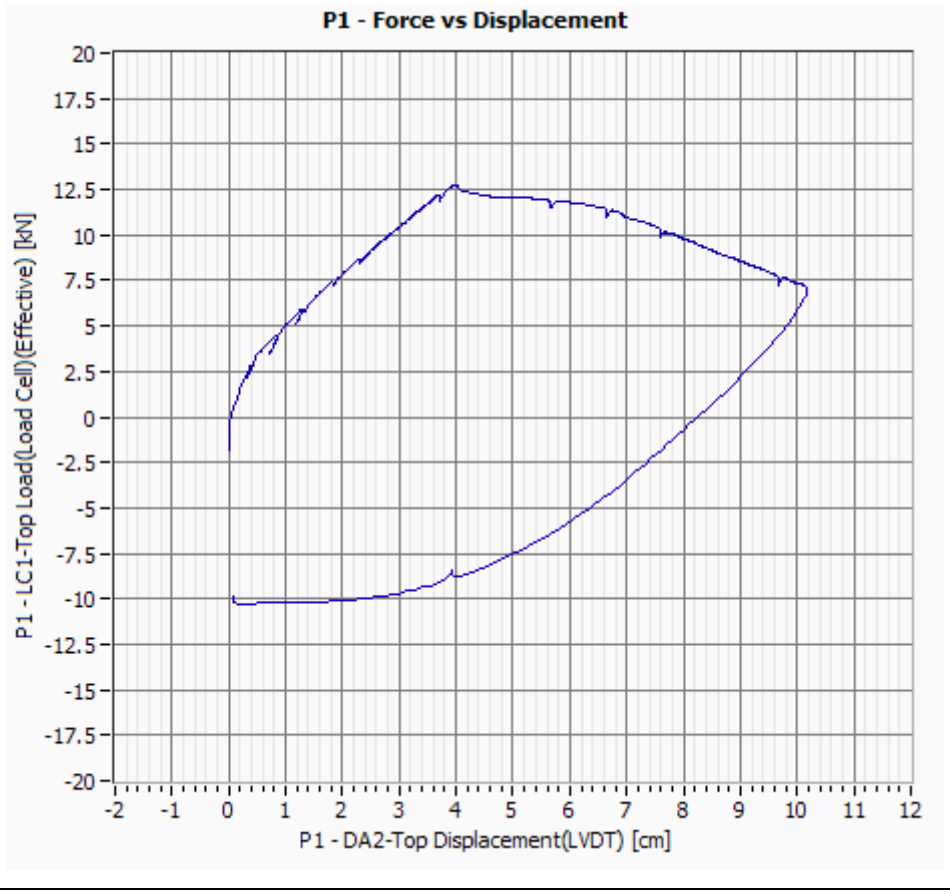

Figure E-5:– Specimen P1-Force (Effective) vs. Displacement.

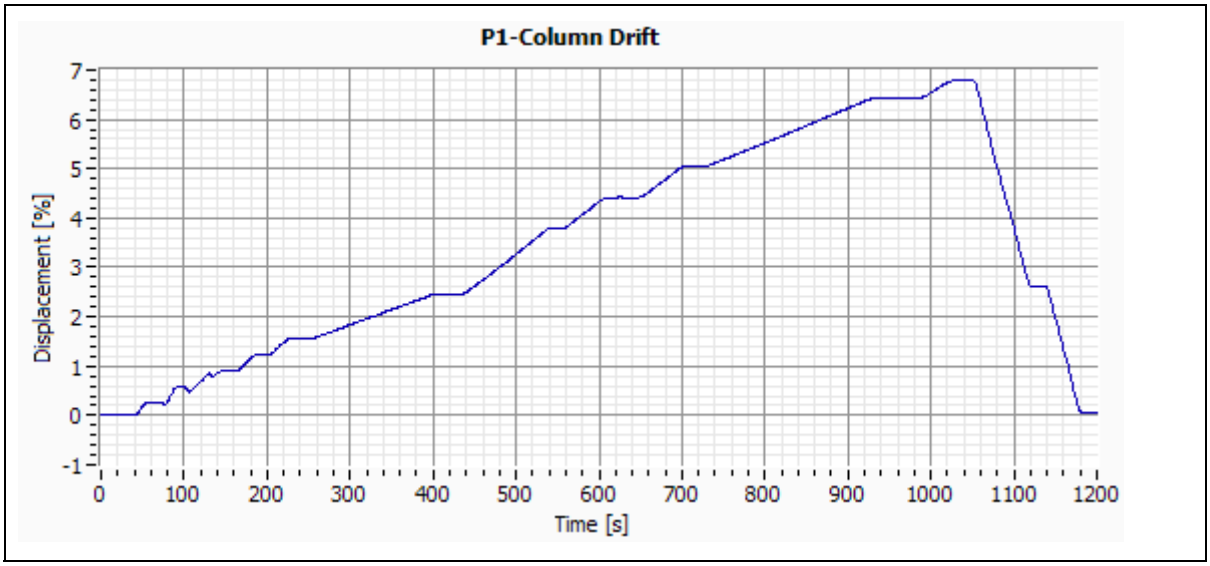

Figure E-6:– Specimen P1-Column Drift.

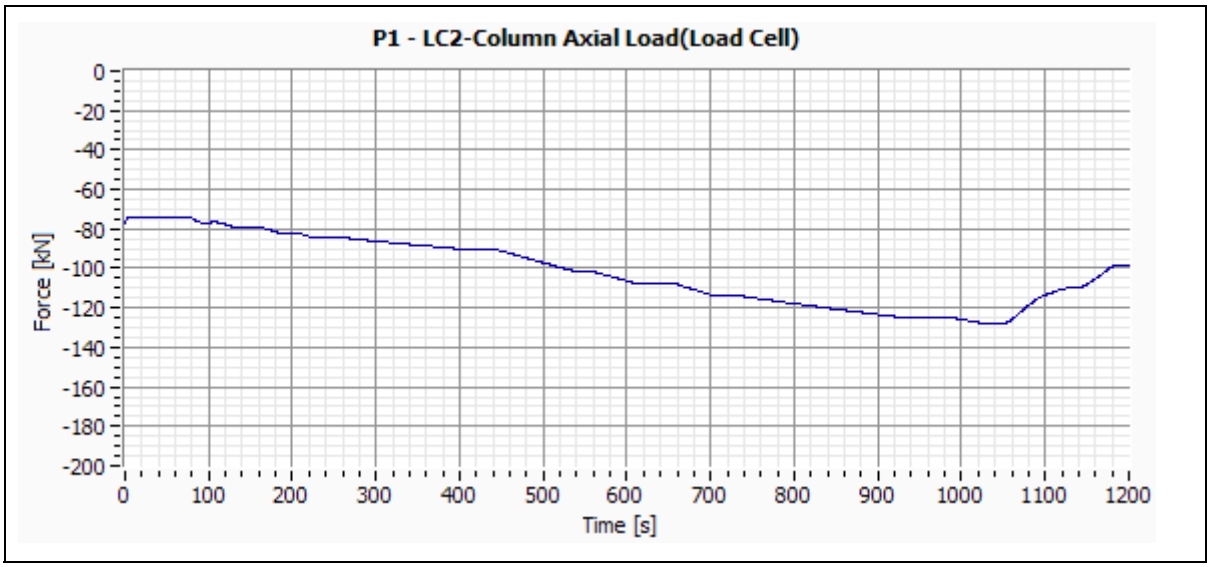

Figure E-7:– Specimen P1-Column Axial Load.

E.2 Specimen P2

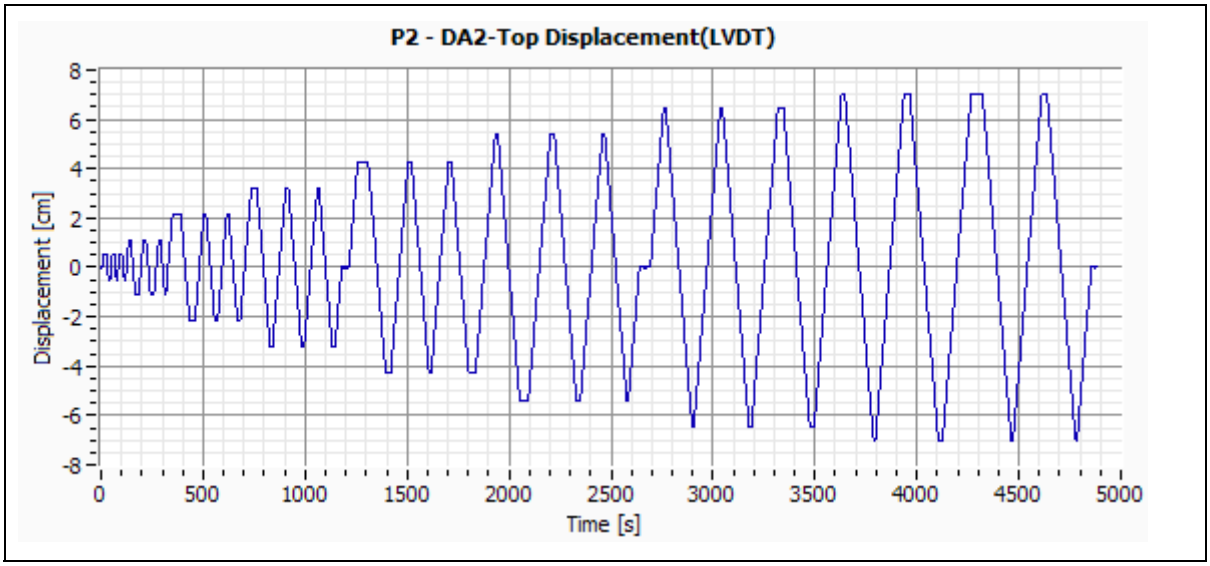

Figure E-8:– Specimen P2-DA2 Top Displacement.

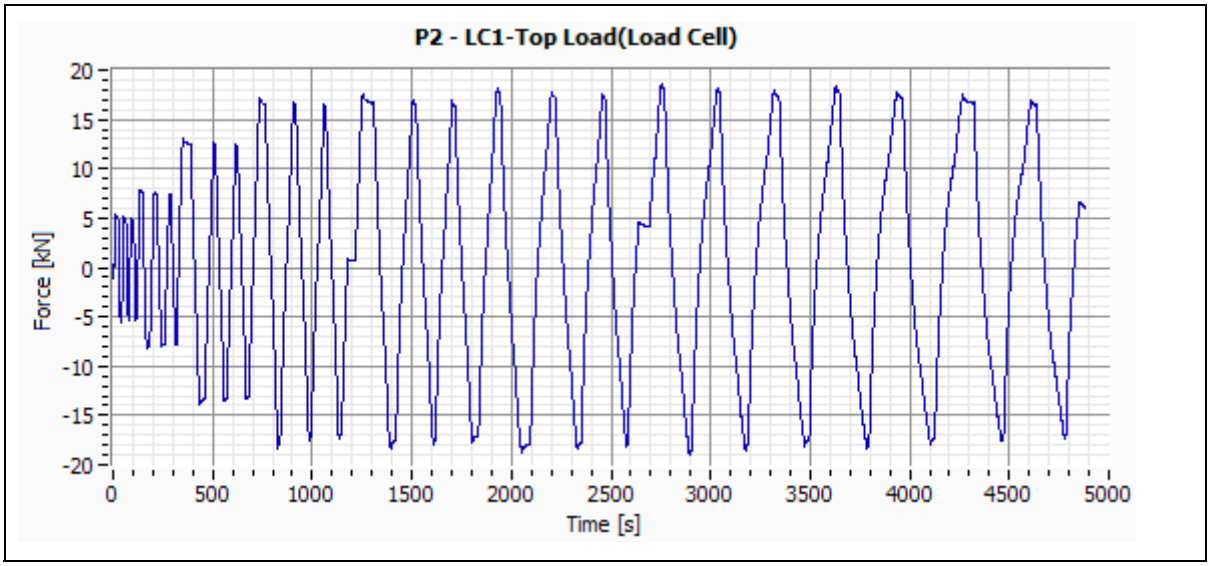

Figure E-9:– Specimen P2-LC1 Top Load.

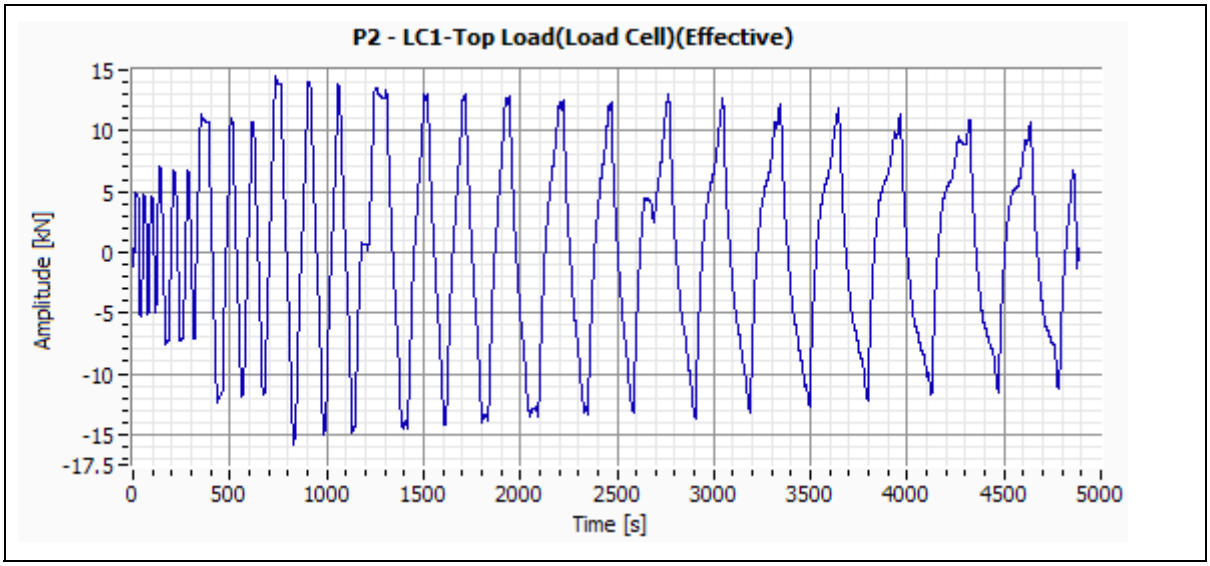

Figure E-10:– Specimen P2-LC1 Top Load (Effective).

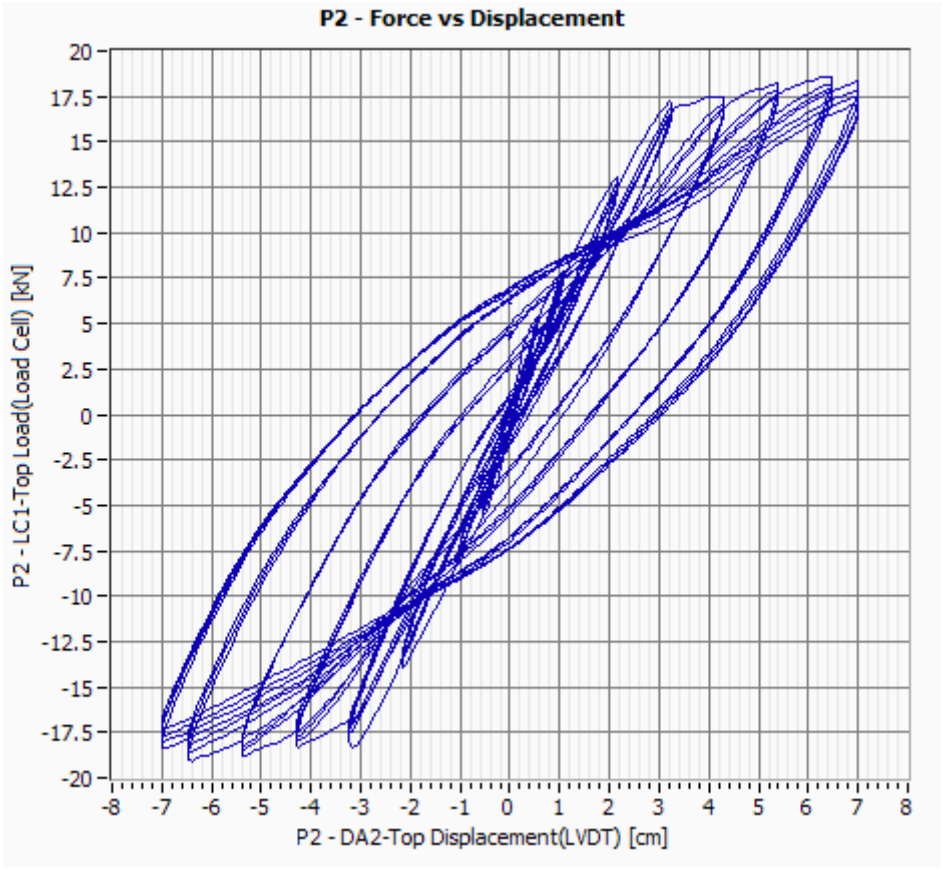

Figure E-11:– Specimen P2-Force vs. Displacement.

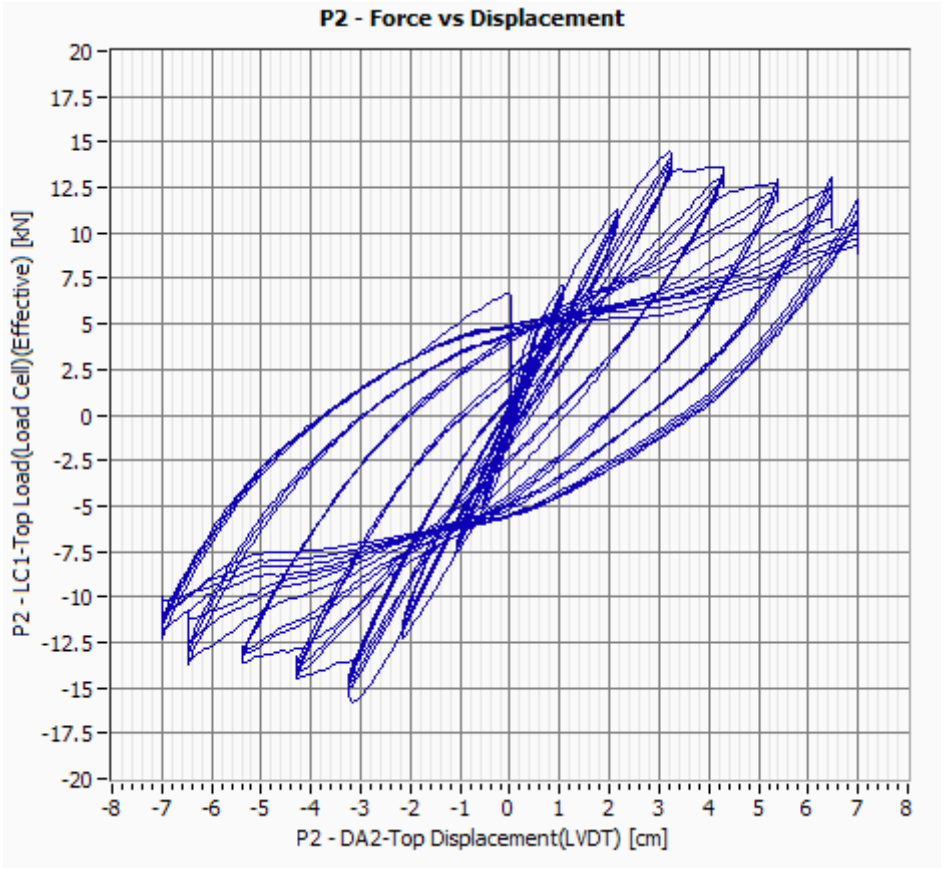

Figure E-12:– Specimen P2-Force (Effective) vs. Displacement.

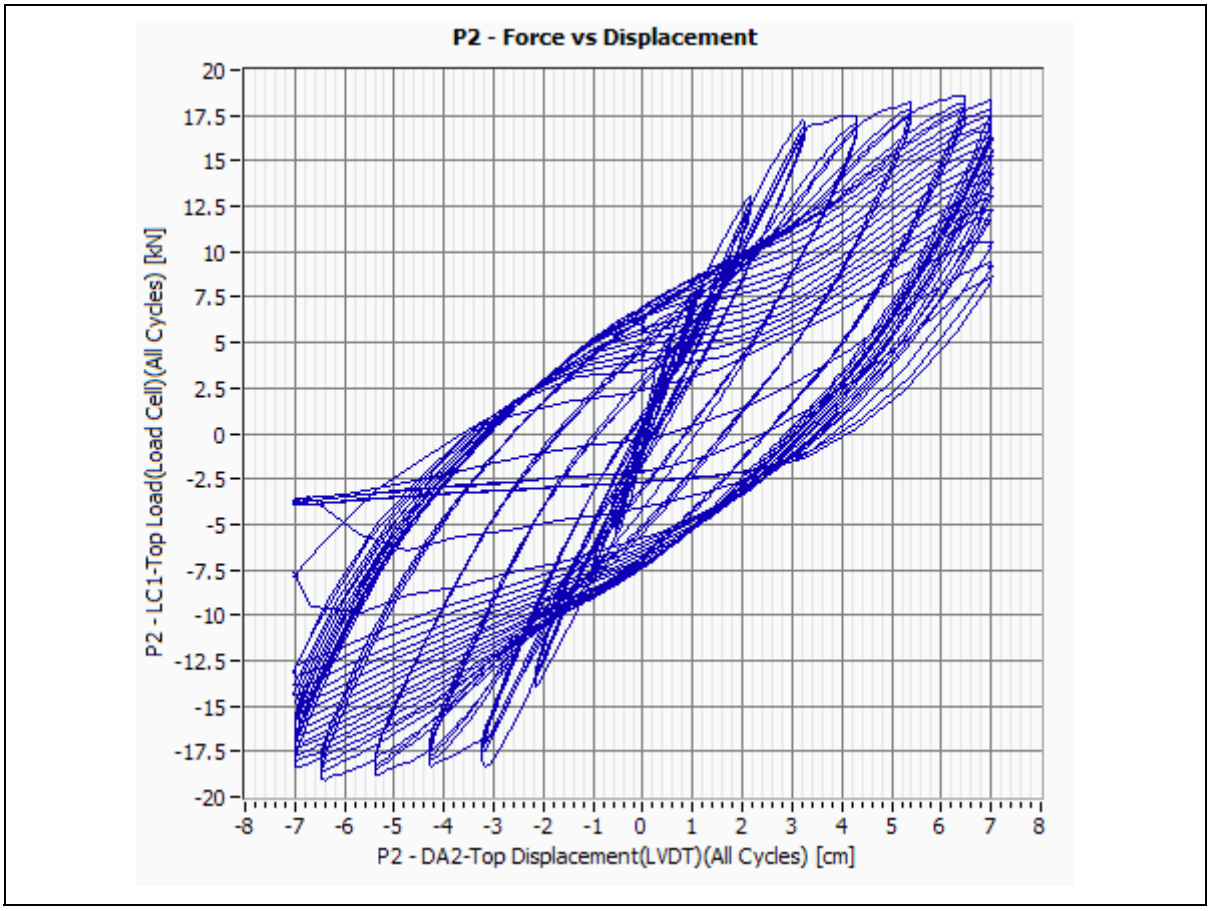

Figure E-13:– Specimen P2-Force vs. Displacement (All Cycles).

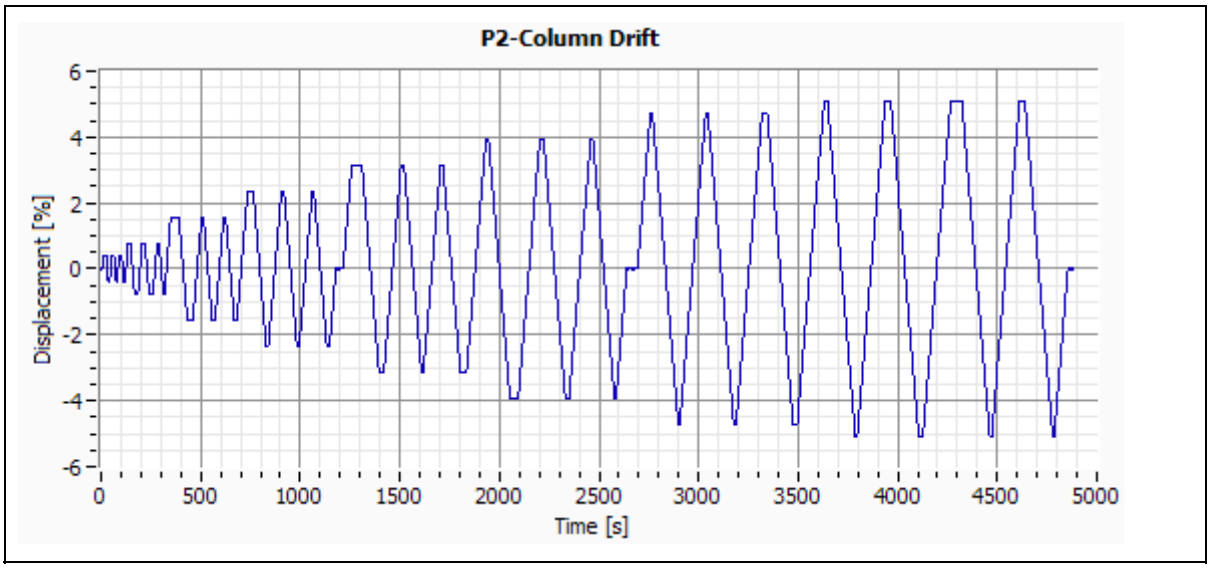

Figure E-14:– Specimen P2-Column Drift.

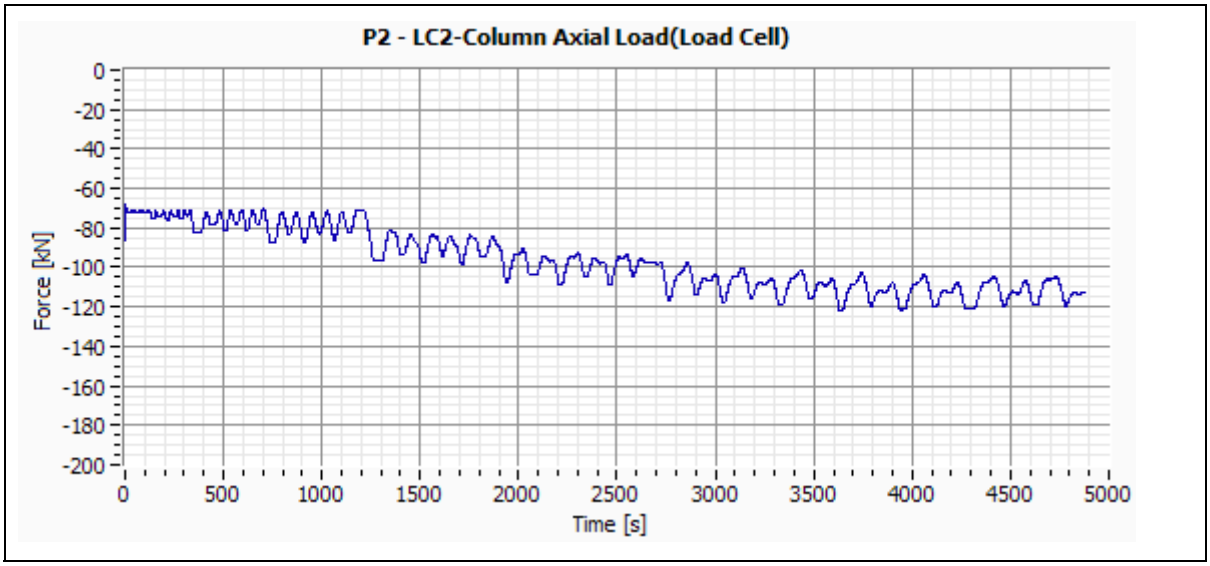

Figure E-15:– Specimen P2-Column Axial Load.

E.3 Specimen P3

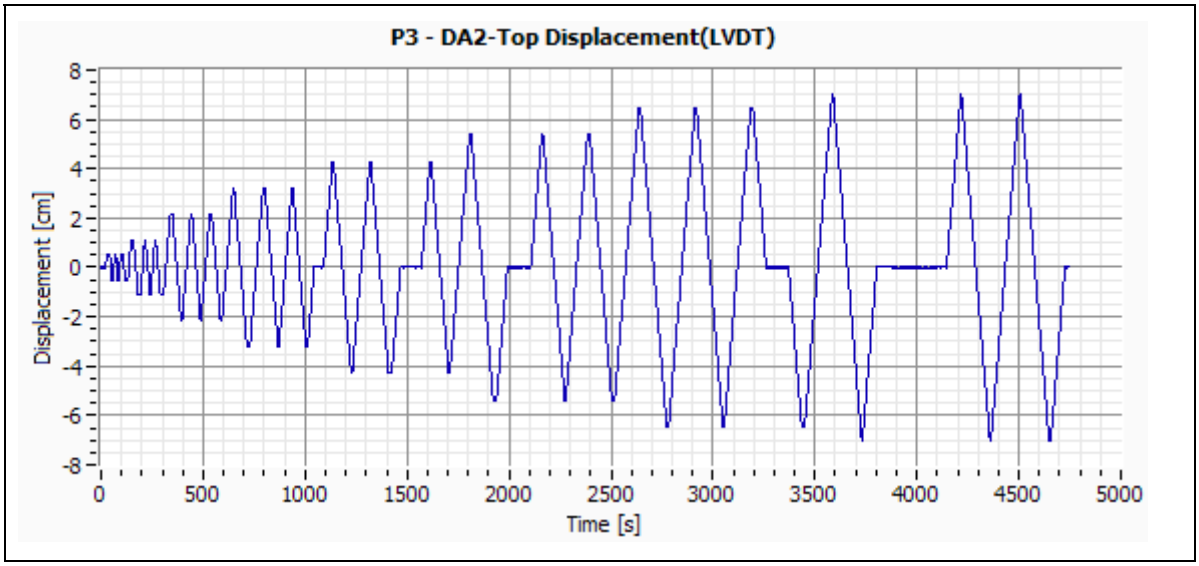

Figure E-16:– Specimen P3-DA2 Top Displacement.

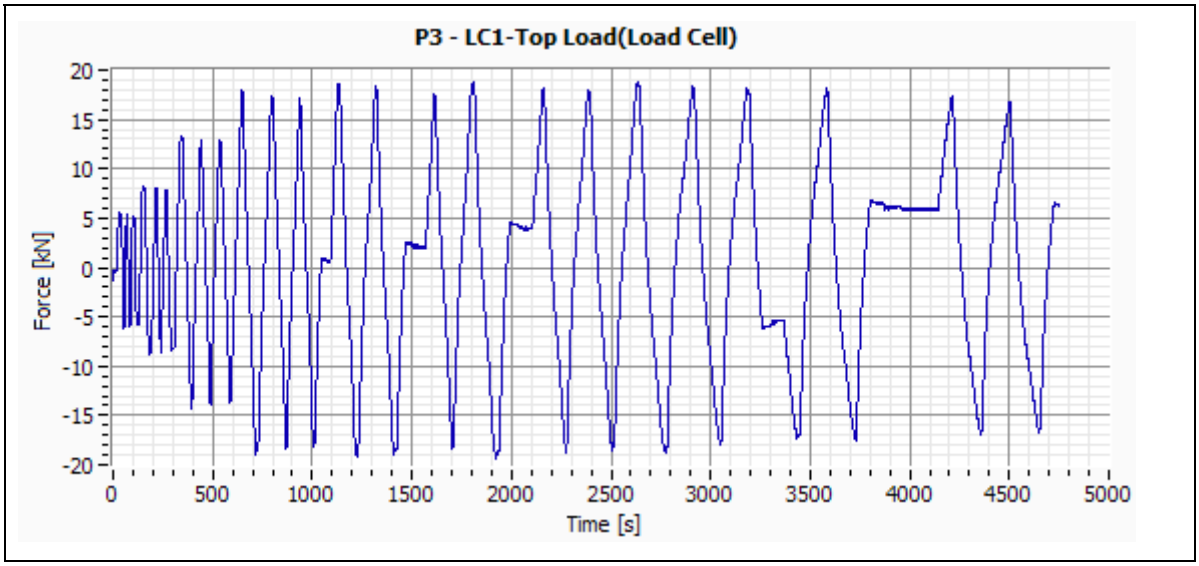

Figure E-17:– Specimen P3-LC1 Top Load.

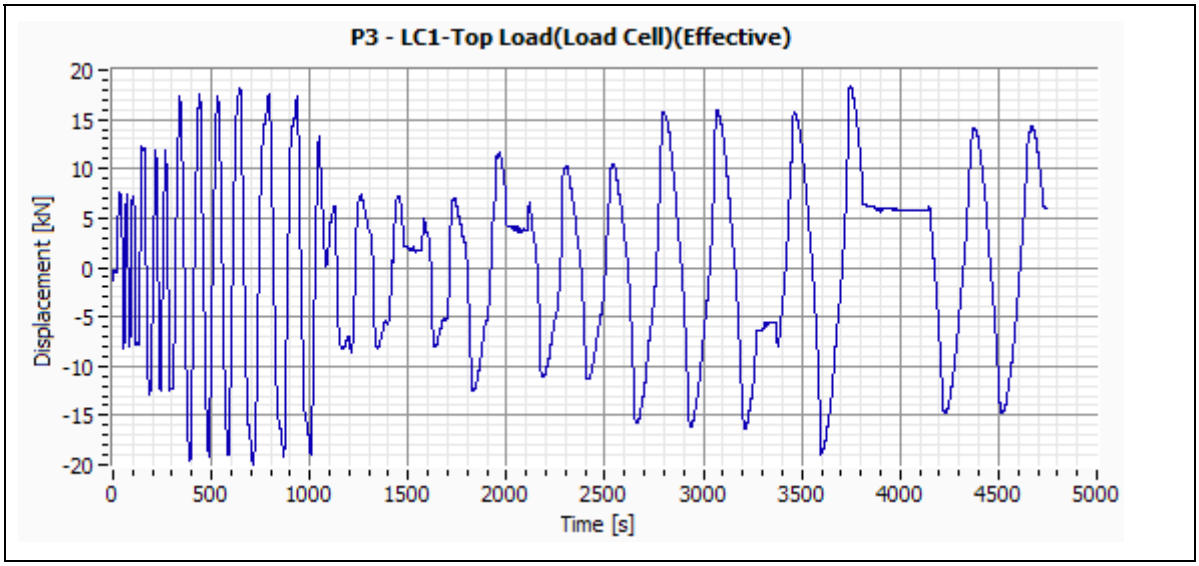

Figure E-18:– Specimen P3-LC1 Top Load (Effective).

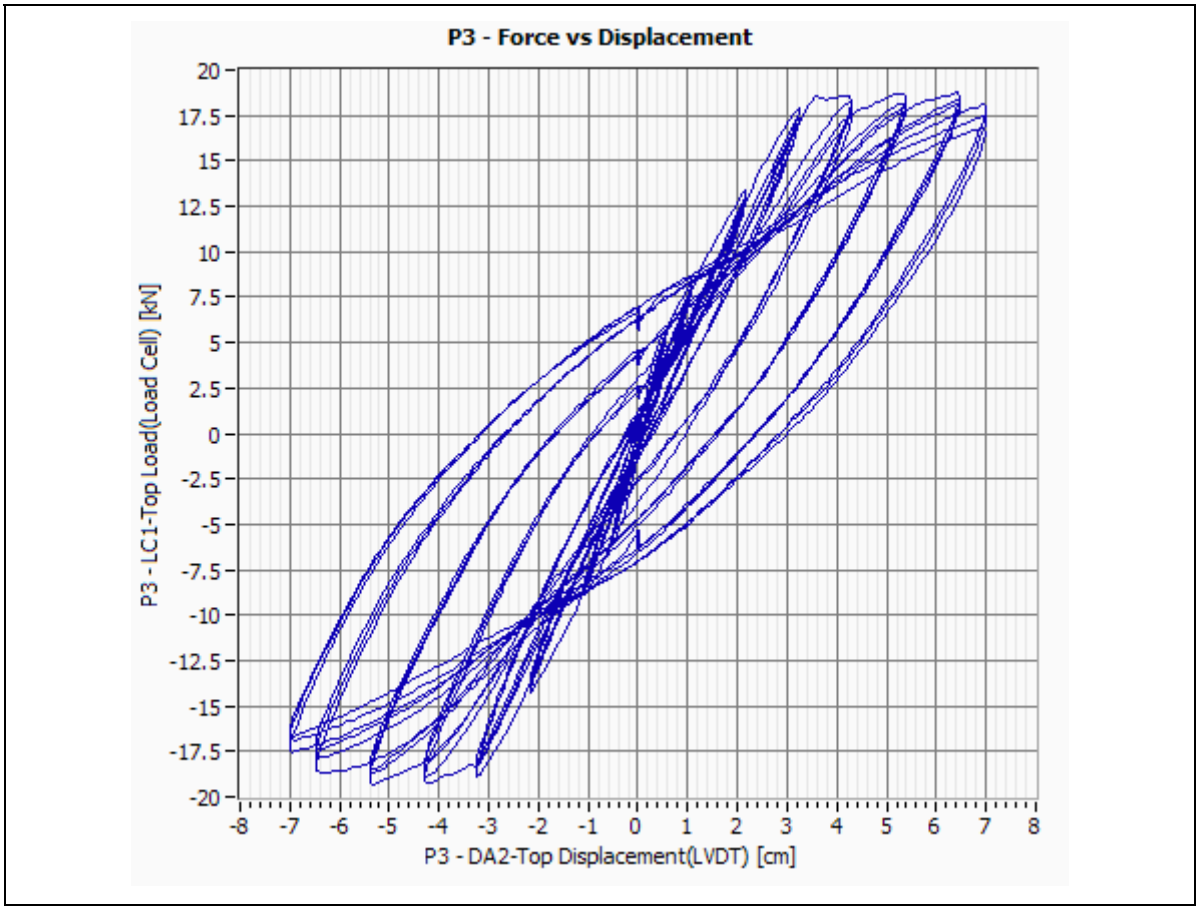

Figure E-19:– Specimen P3-Force vs. Displacement.

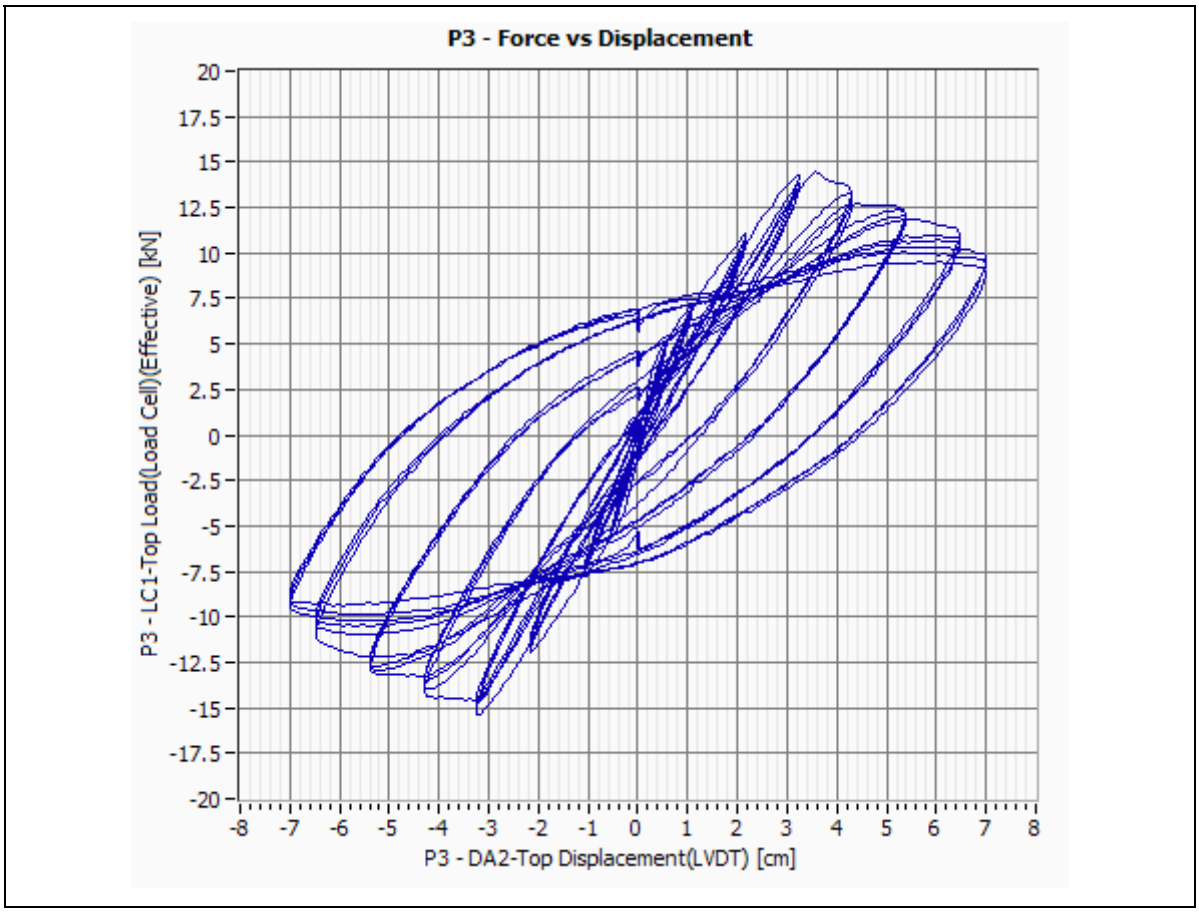

Figure E-20:– Specimen P3-Force (Effective) vs. Displacement.

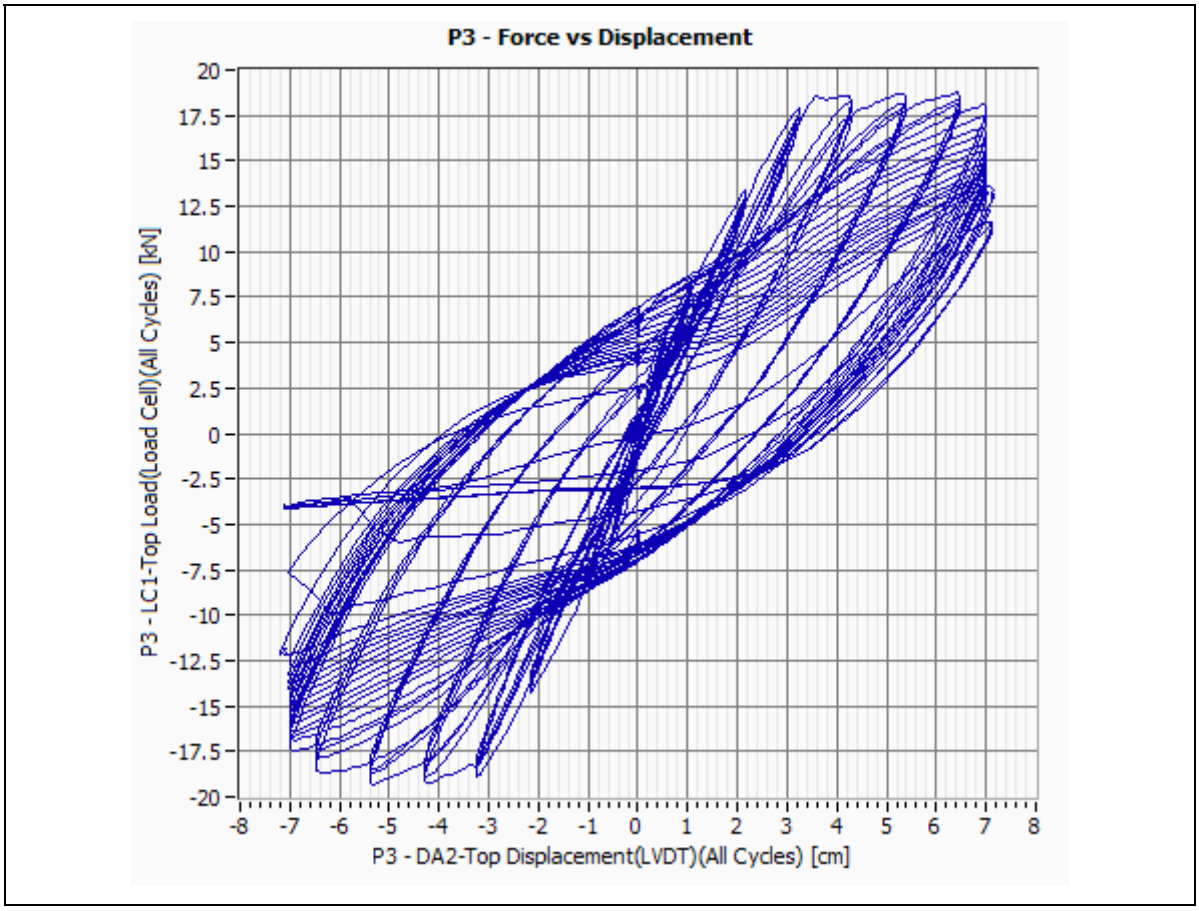

Figure E-21:– Specimen P3-Force vs. Displacement (All Cycles).

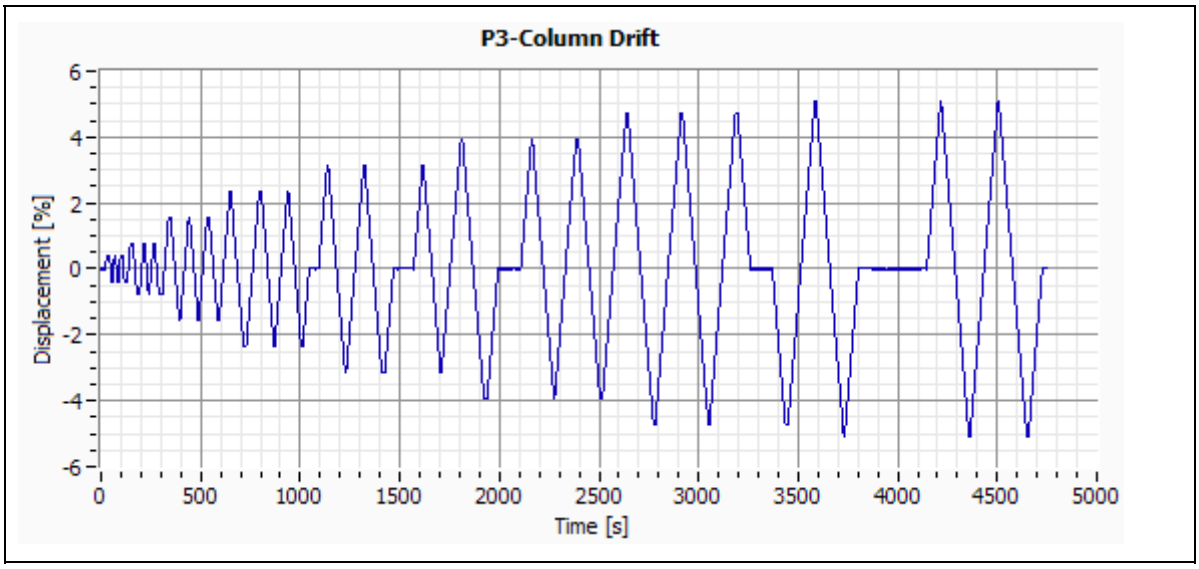

Figure E-22:– Specimen P3-Column Drift.

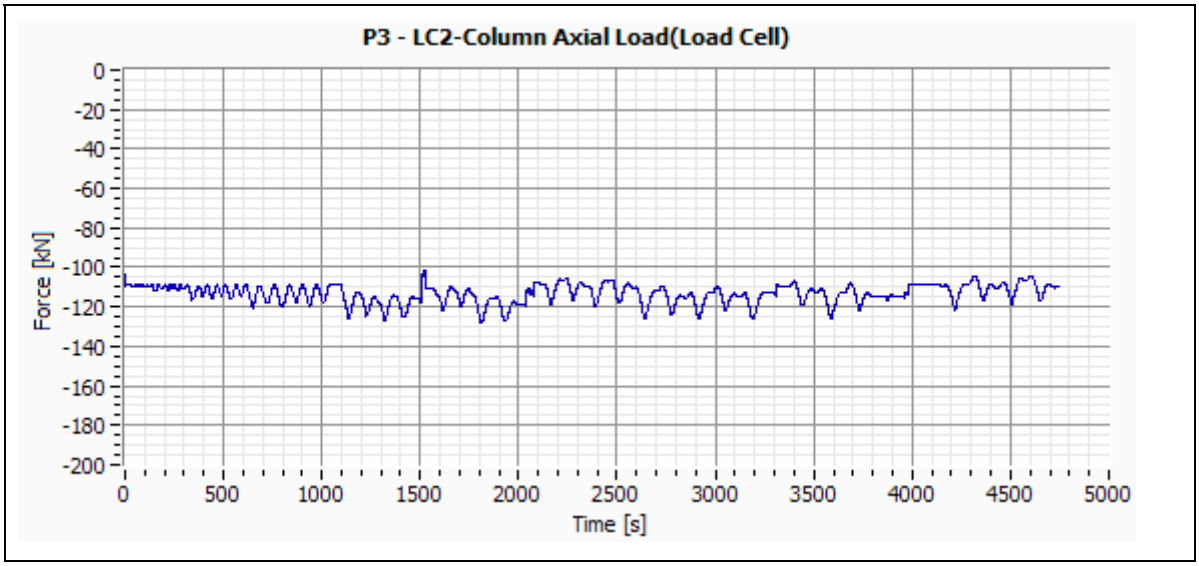

Figure E-23:– Specimen P3-Column Axial Load.

E.4 Specimen P4

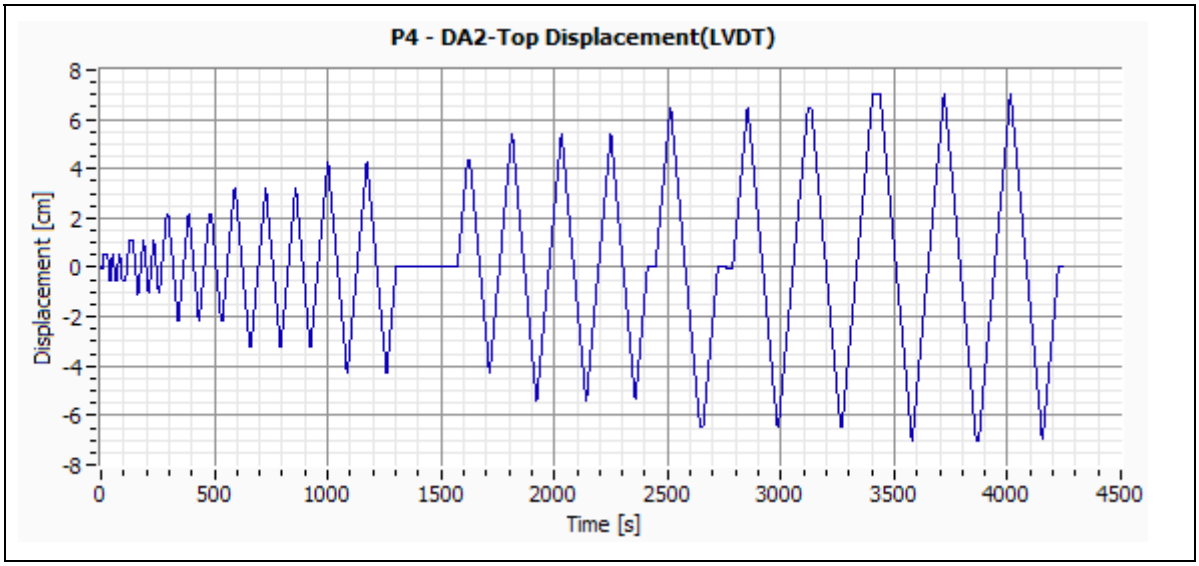

Figure E-24:– Specimen P4-DA2 Top Displacement.

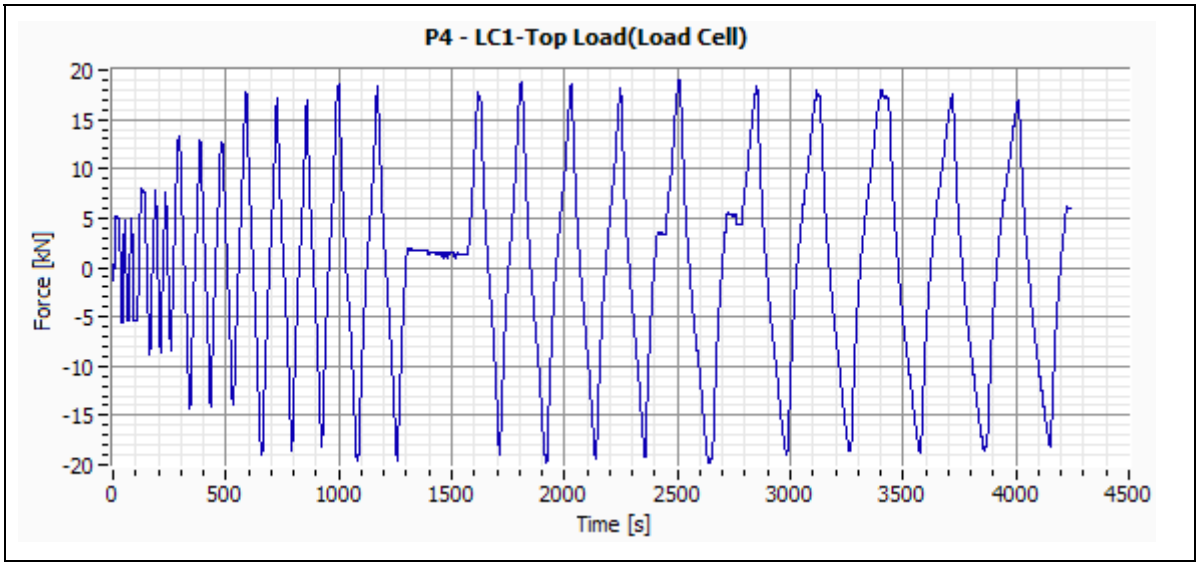

Figure E-25:– Specimen P4-LC1 Top Load.

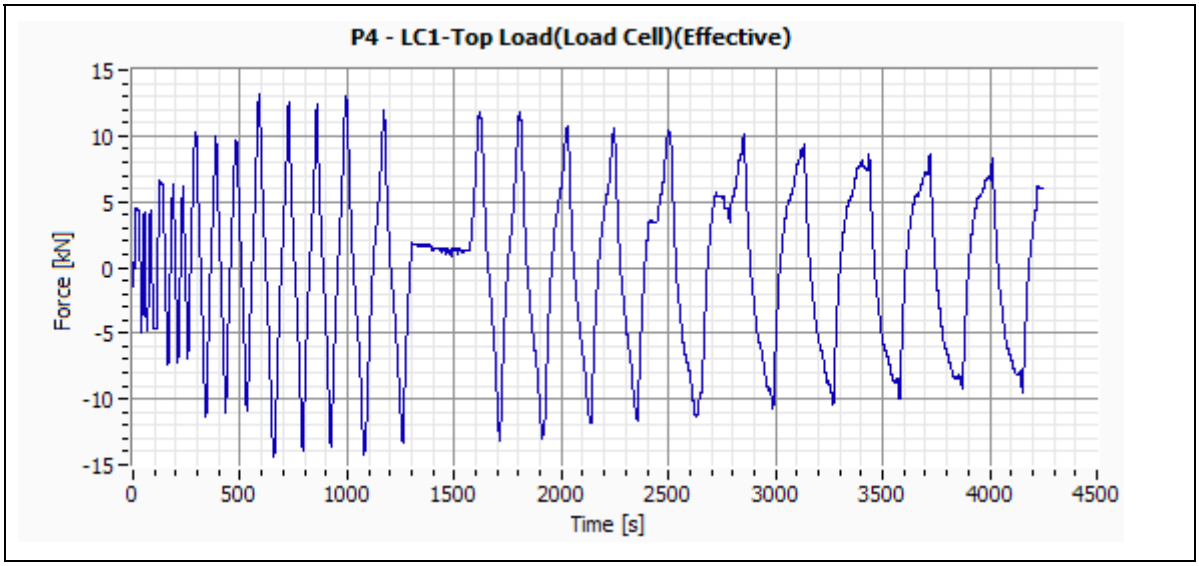

Figure E-26:– Specimen P4-LC1 Top Load (Effective).

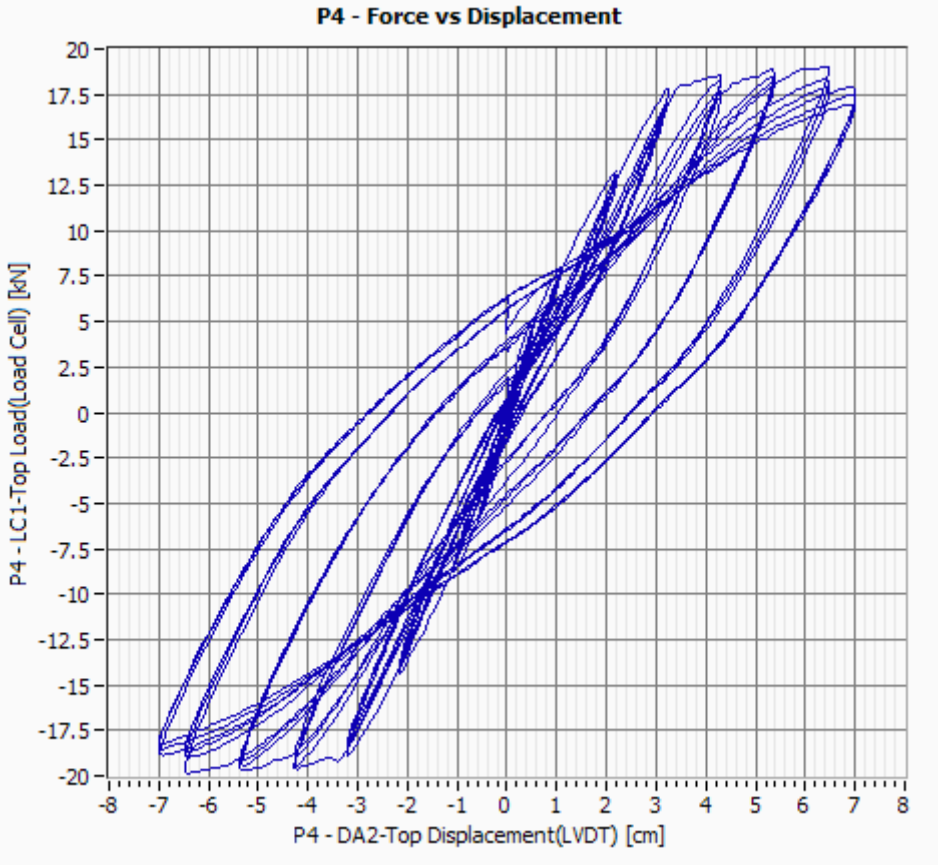

Figure E-27:– Specimen P4-Force vs. Displacement.

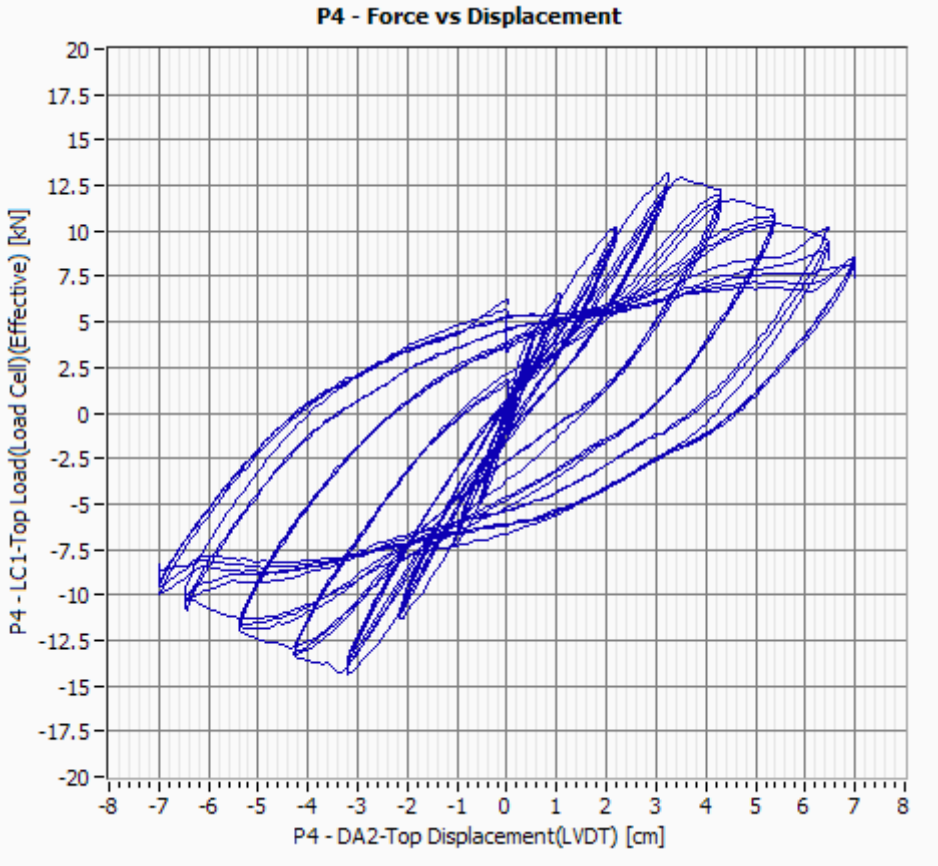

Figure E-28:– Specimen P4-Force (Effective) vs. Displacement.

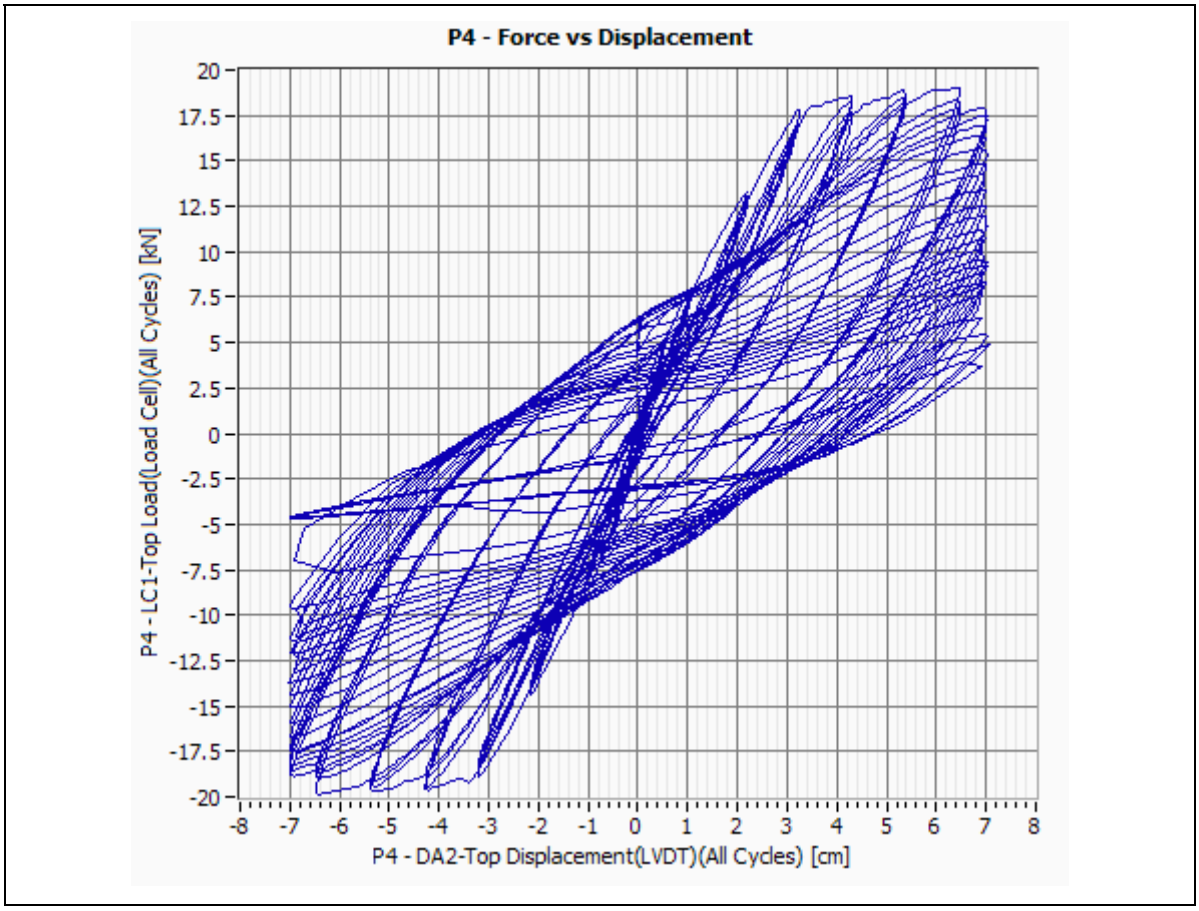

Figure E-29:– Specimen P4-Force vs. Displacement (All Cycles).

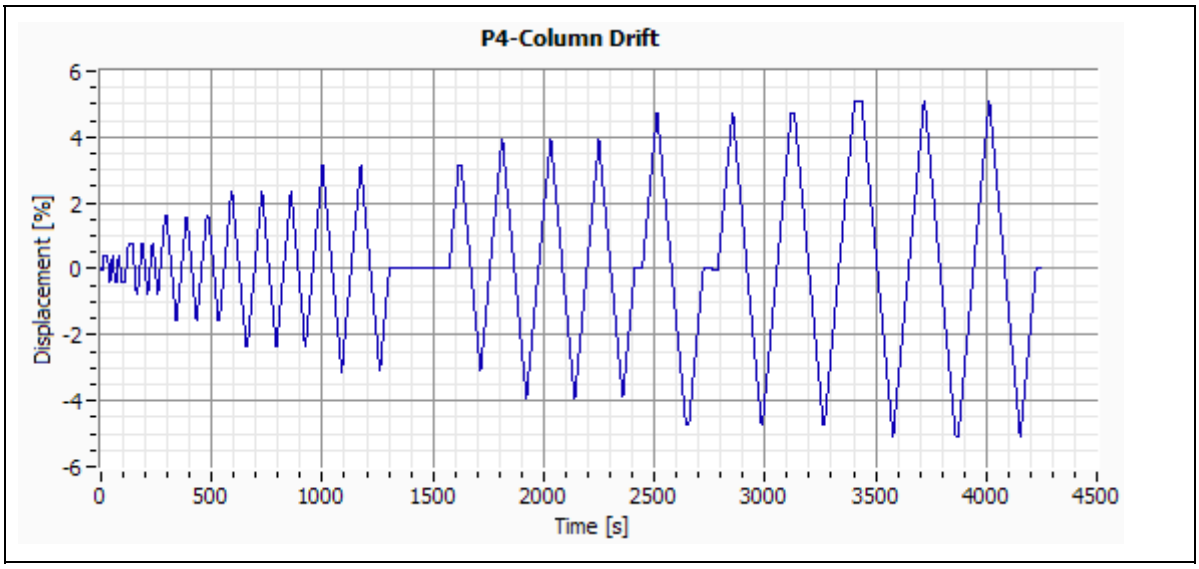

Figure E-30:– Specimen P4-Column Drift.

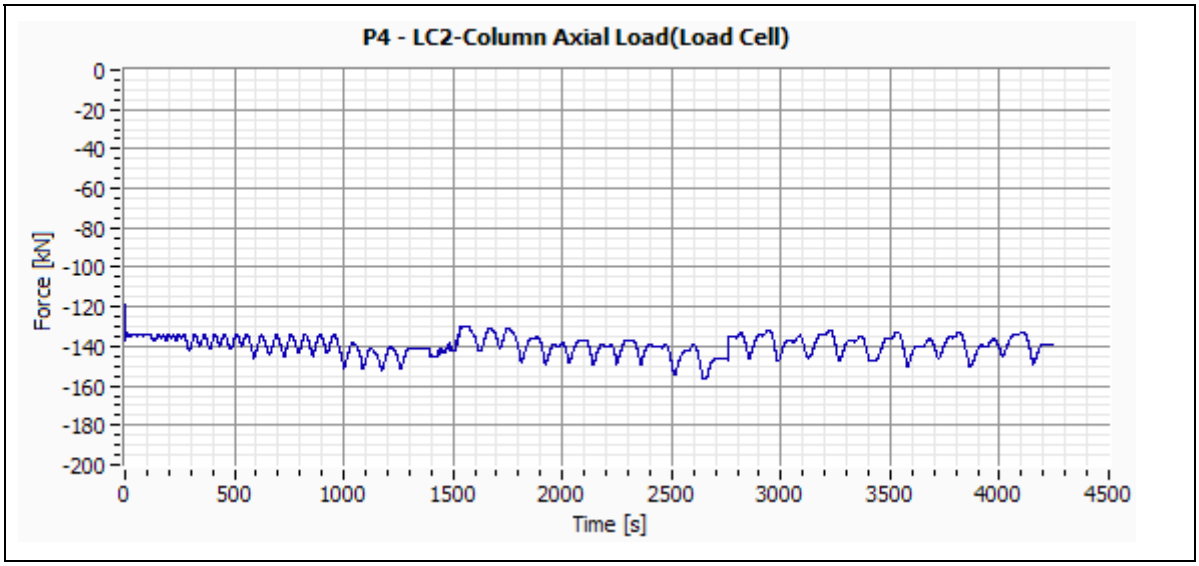

Figure E-31:– Specimen P4-Column Axial Load.

E.5 Specimen V1

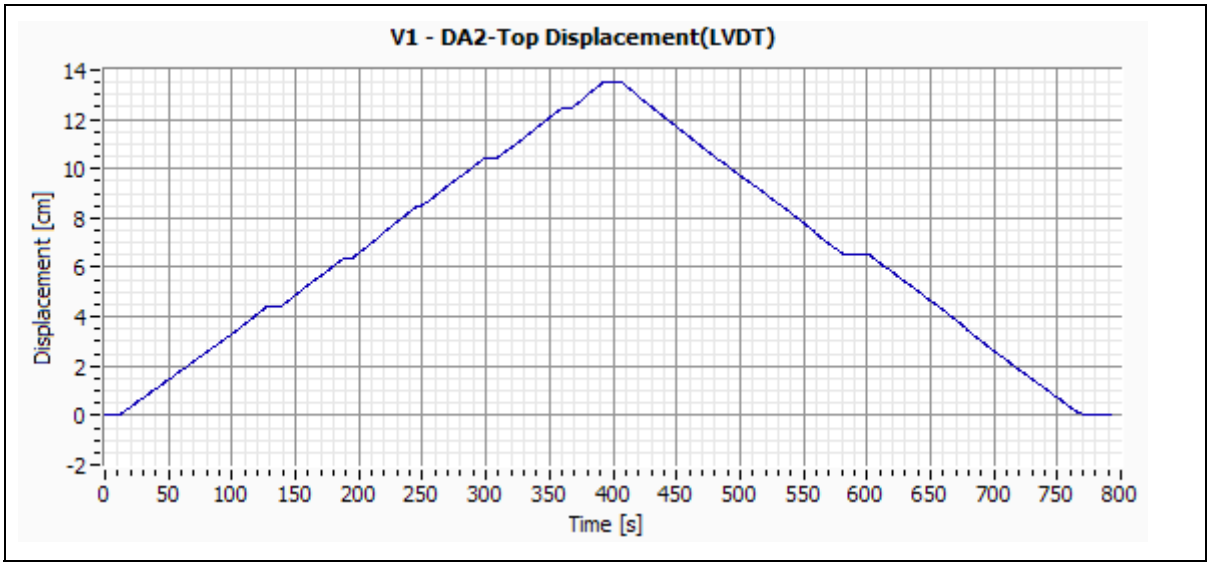

Figure E-32:– Specimen V1-DA2 Top Displacement.

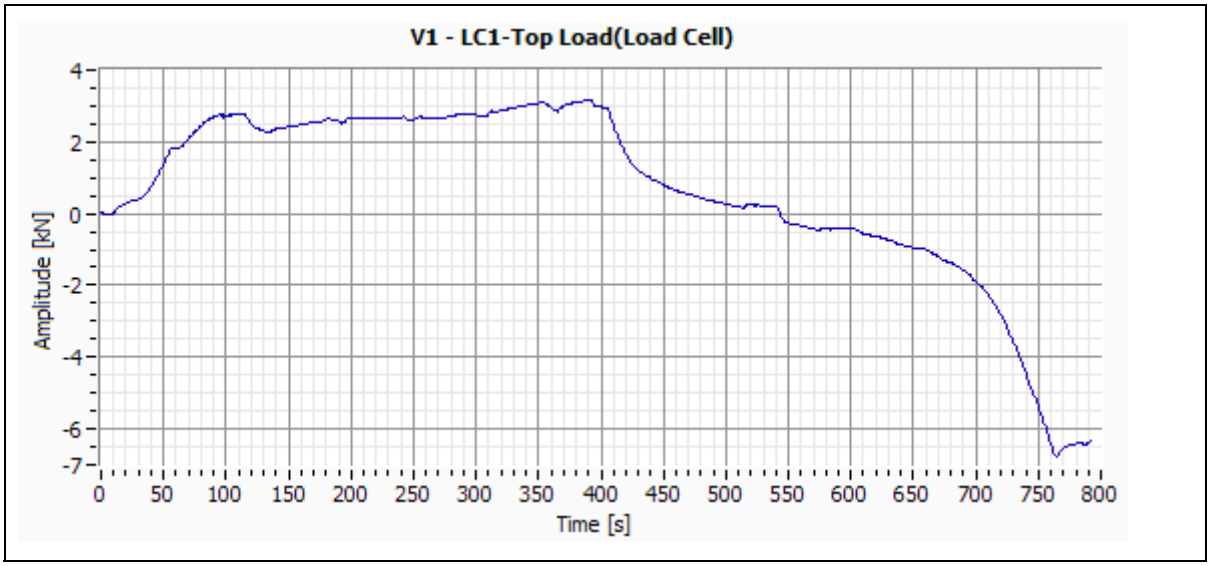

Figure E-33:– Specimen V1-LC1 Top Load.

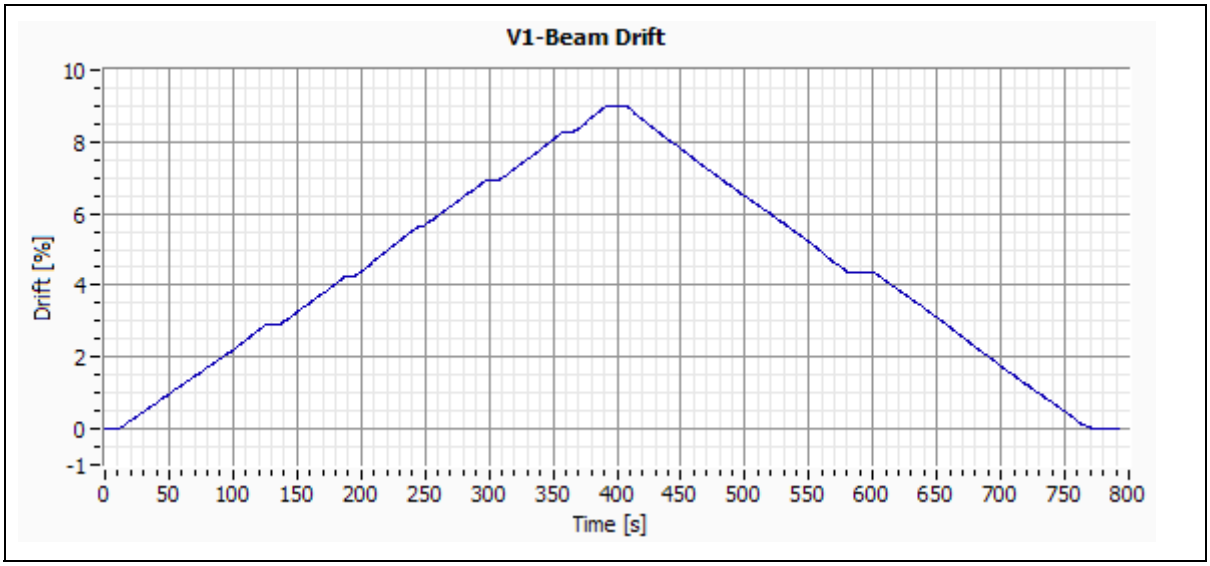

Figure E-34:– Specimen V1-Beam Drift.

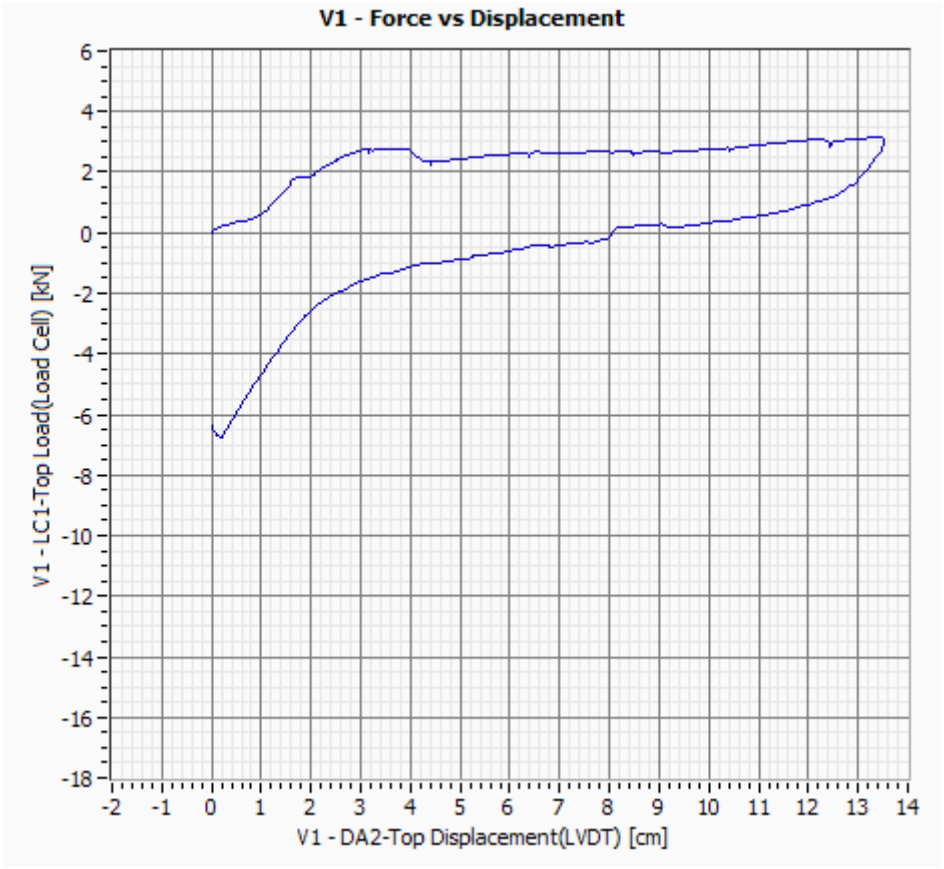

Figure E-35:– Specimen V1-Force vs. Displacement.

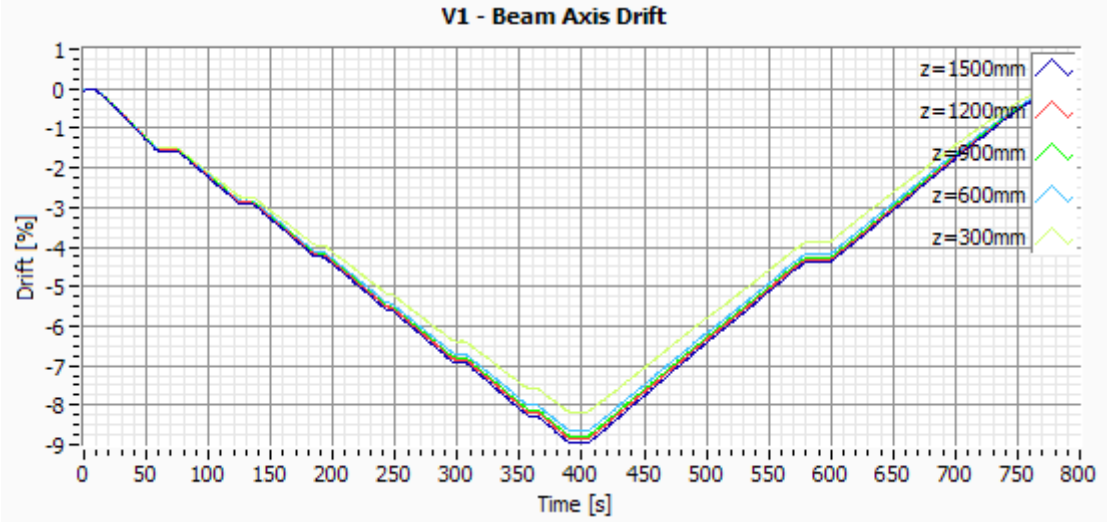

Figure E-36:– Specimen V1-Beam Axis Drift.

E.6 Specimen V2

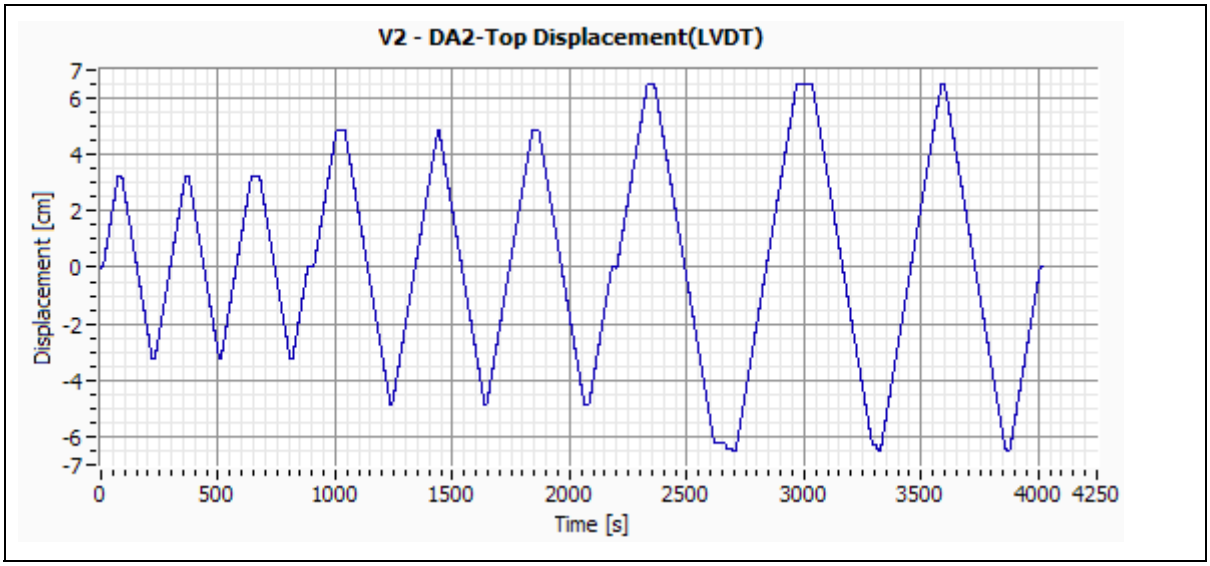

Figure E-37:– Specimen V2-DA2 Top Displacement.

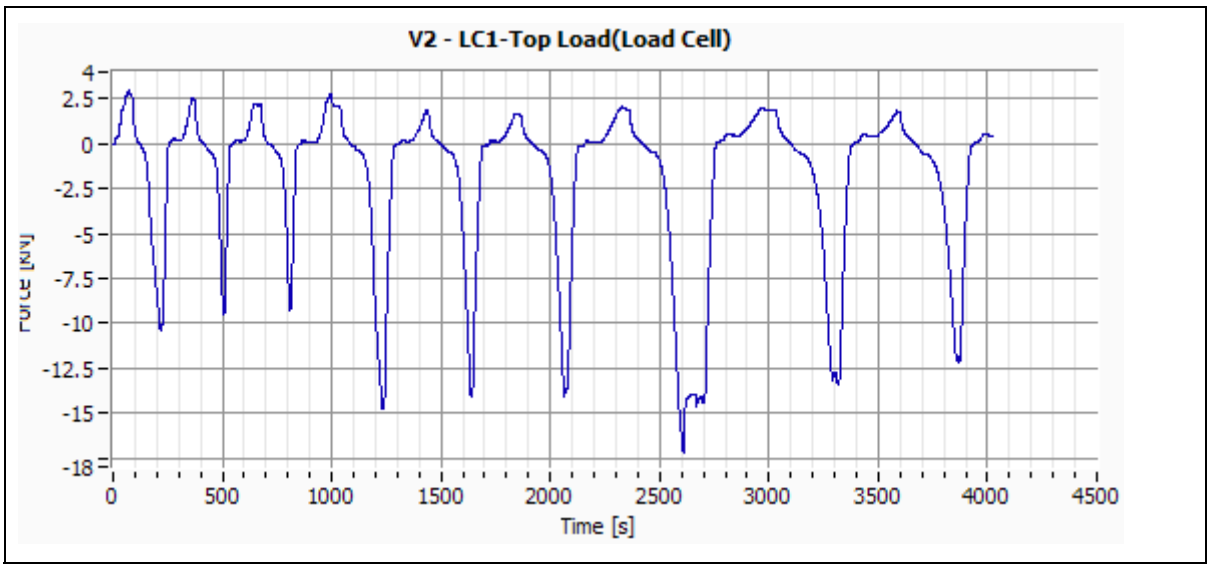

Figure E-38:– Specimen V2-LC1 Top Load.

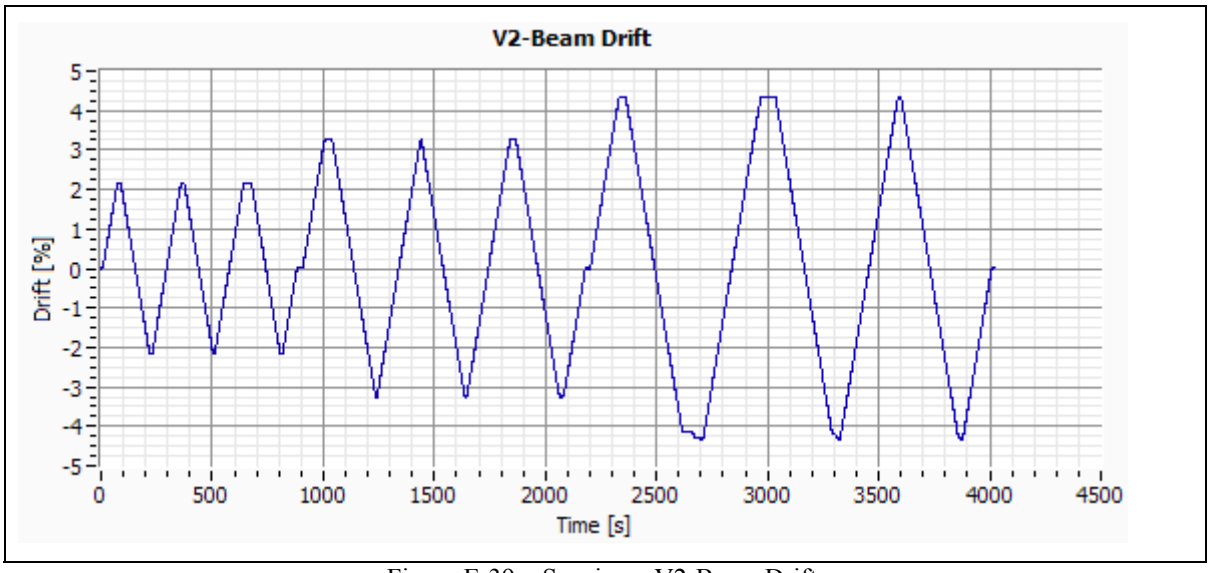

Figure E-39:– Specimen V2-Beam Drift.

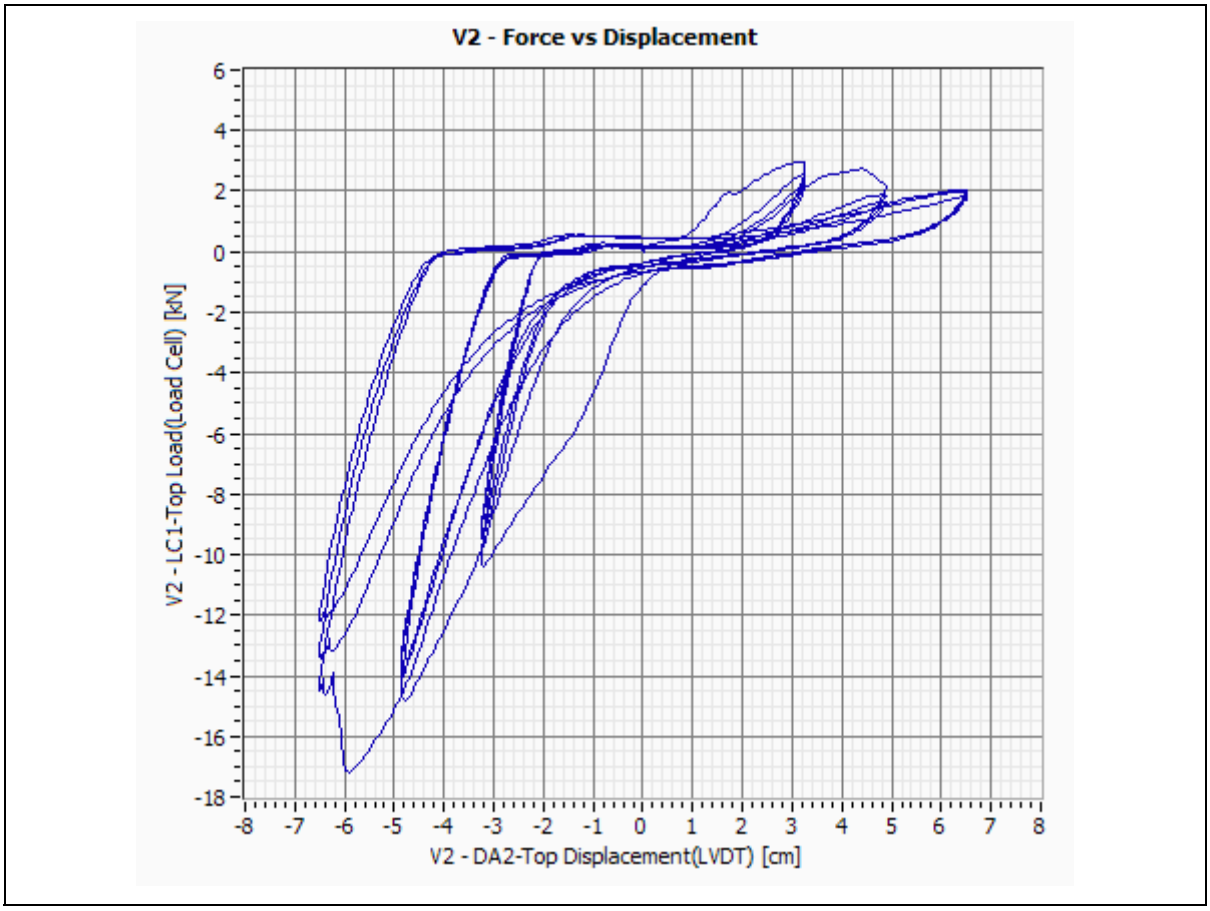

Figure E-40:– Specimen V2-Force vs. Displacement.

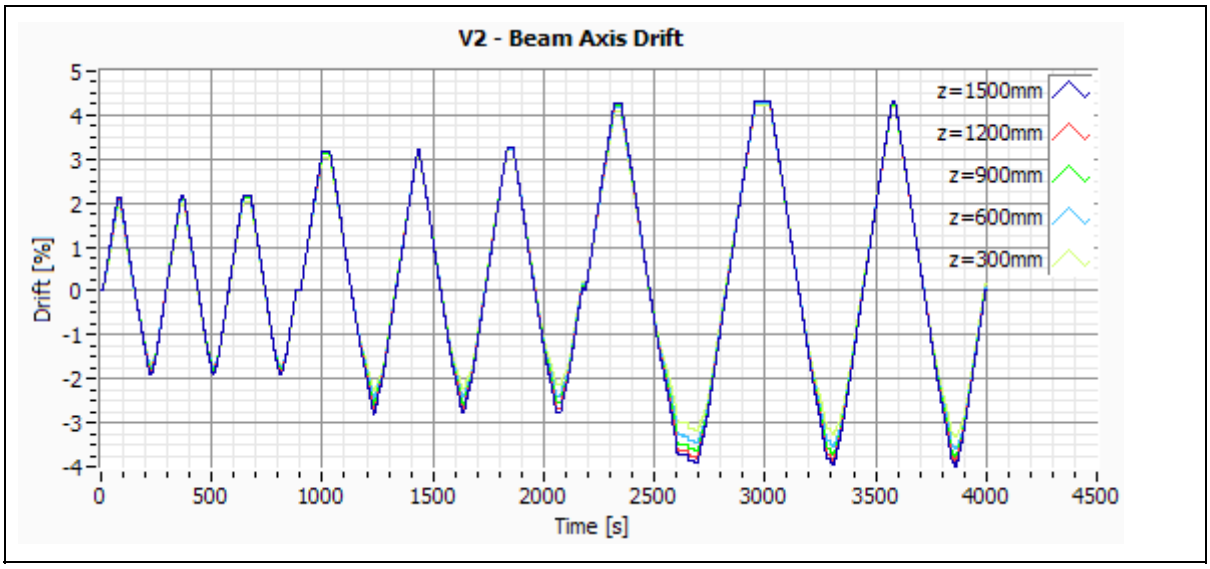

Figure E-41:– Specimen V2-Beam Axis Drift.

E.7 Specimen V3

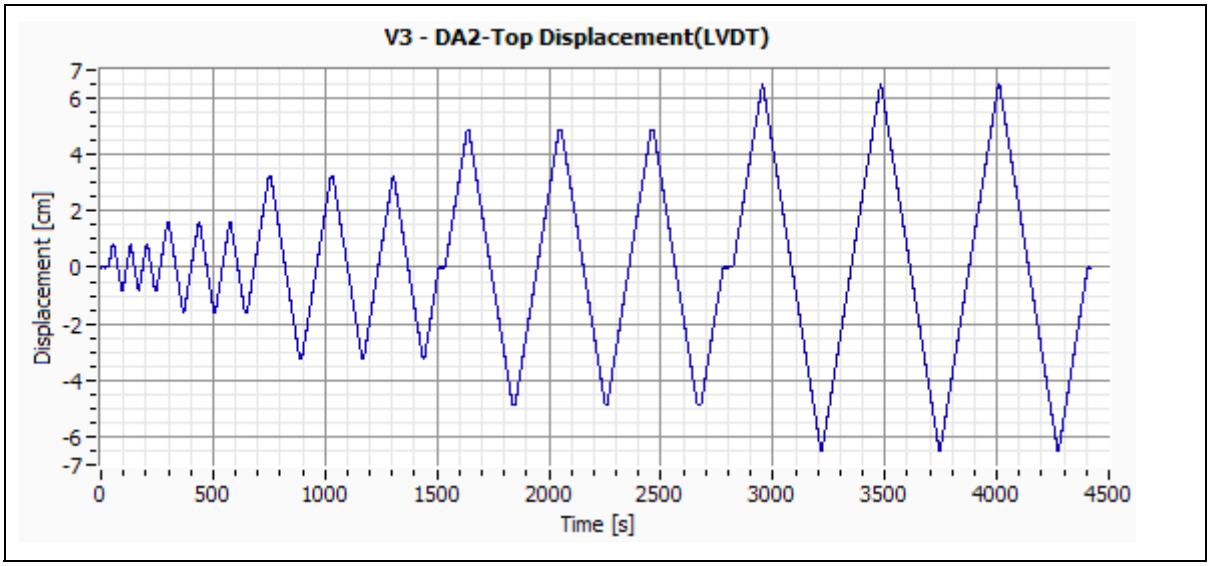

Figure E-42:– Specimen V3-DA2 Top Displacement.

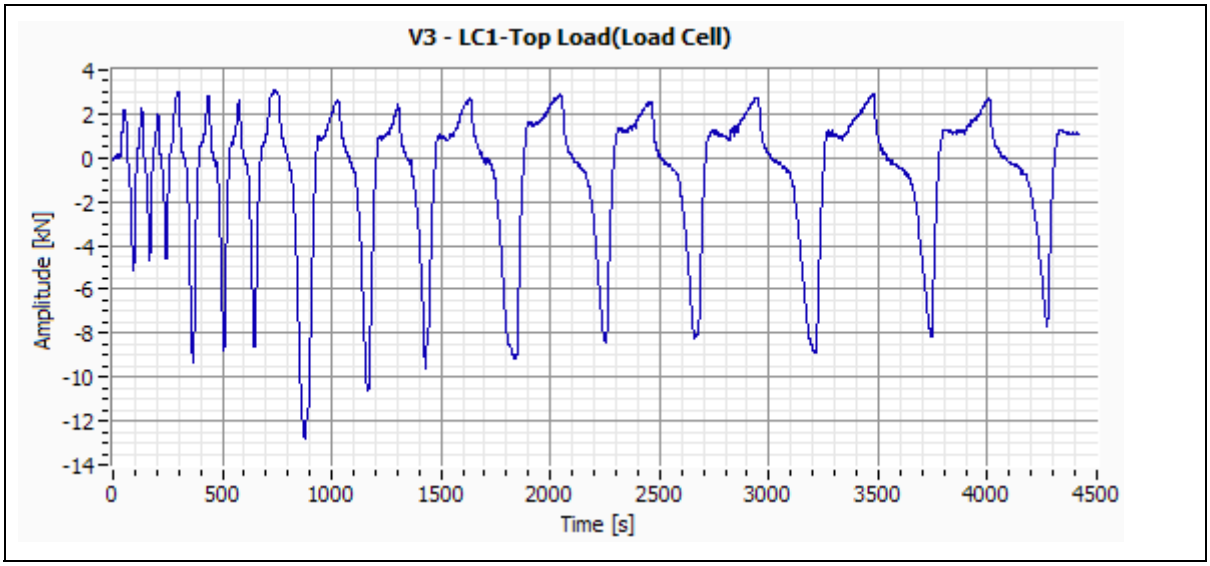

Figure E-43:– Specimen V3-LC1 Top Load.

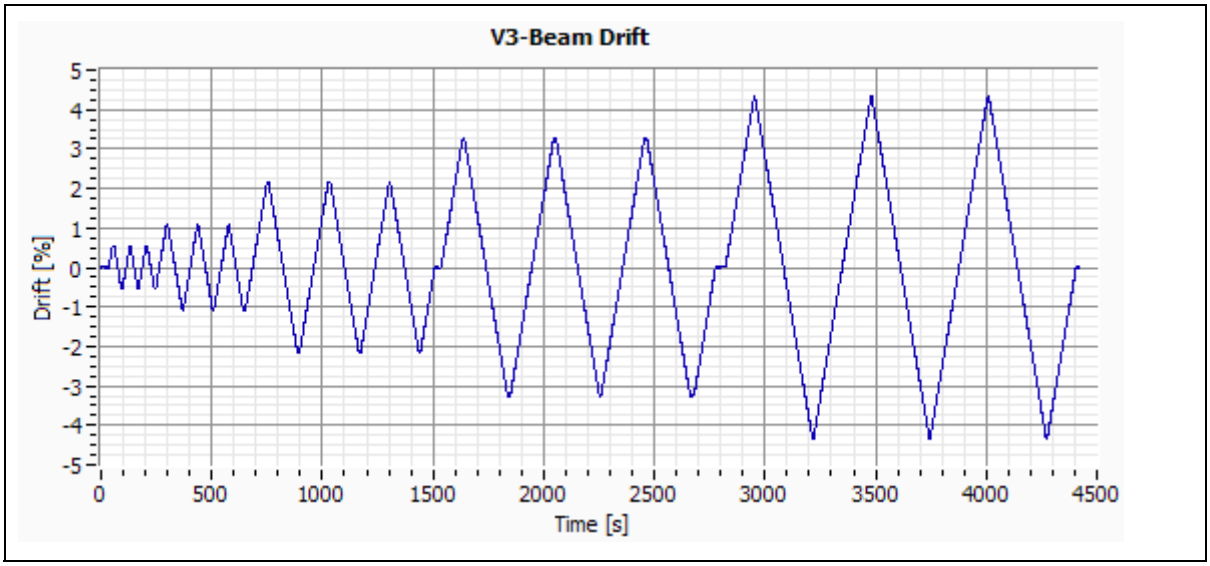

Figure E-44:– Specimen V3-Beam Drift.

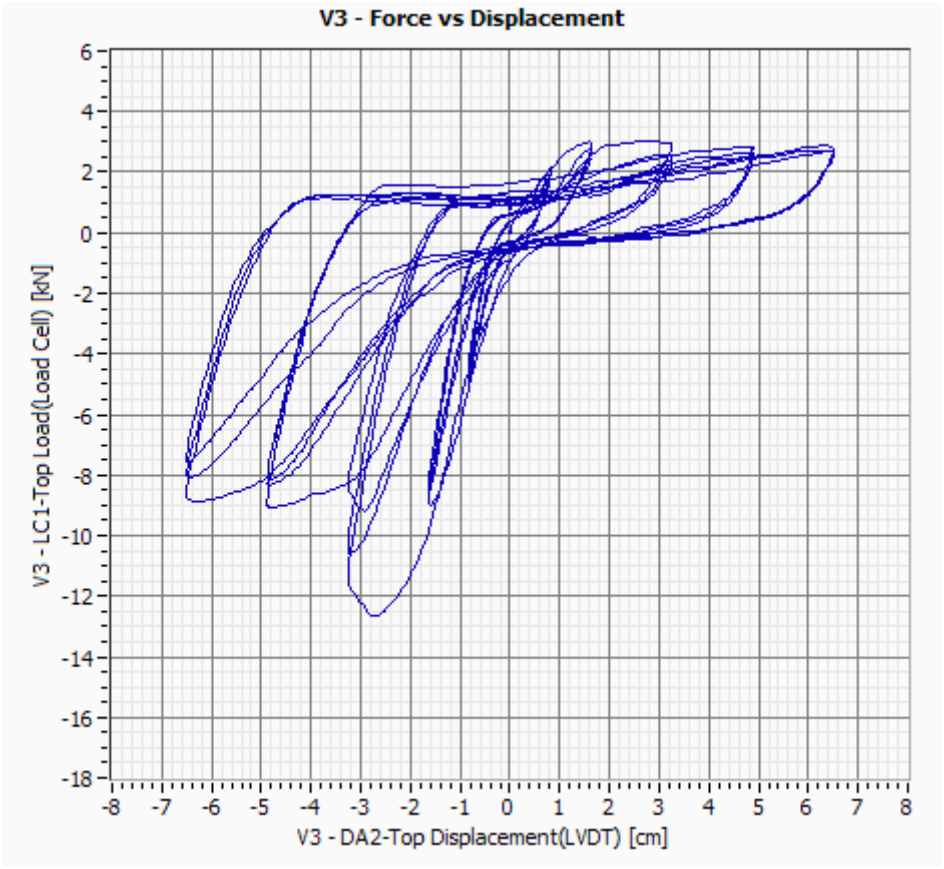

Figure E-45:– Specimen V3-Force vs. Displacement.

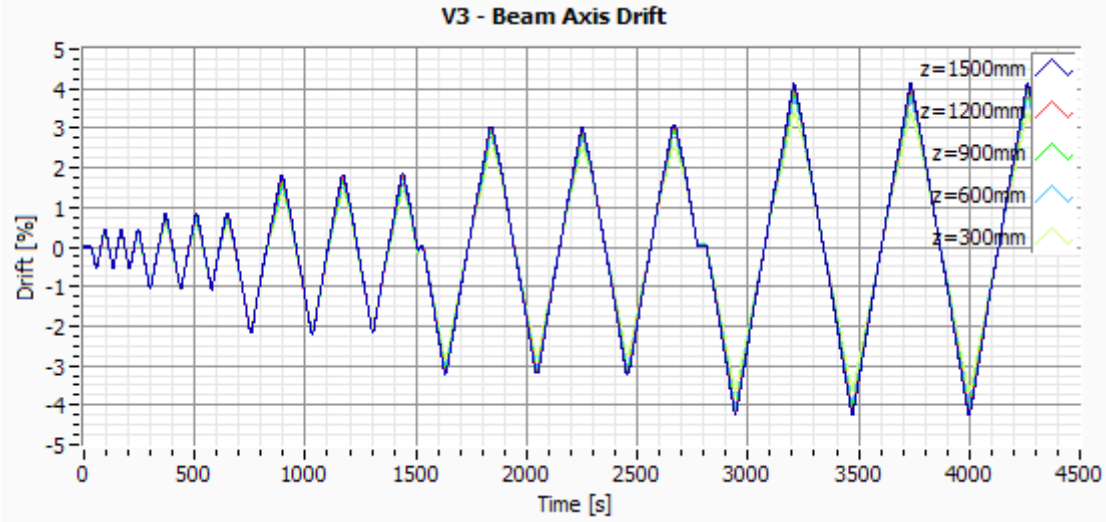

Figure E-46:– Specimen V3-Beam Axis Drift.

E.8 Specimen V4

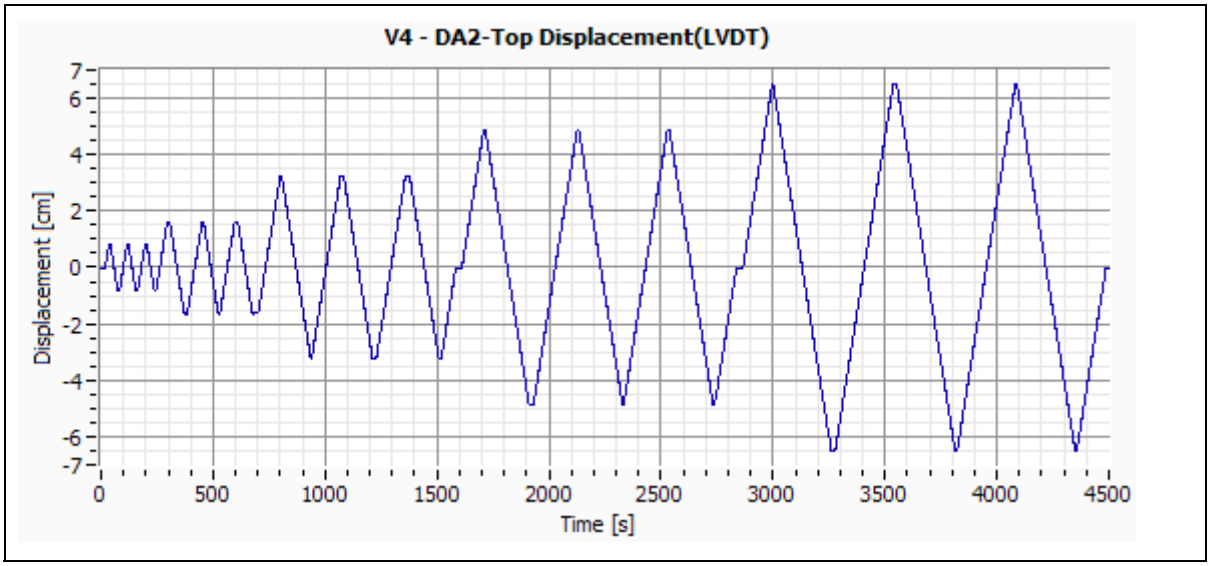

Figure E-47:– Specimen V4-DA2 Top Displacement.

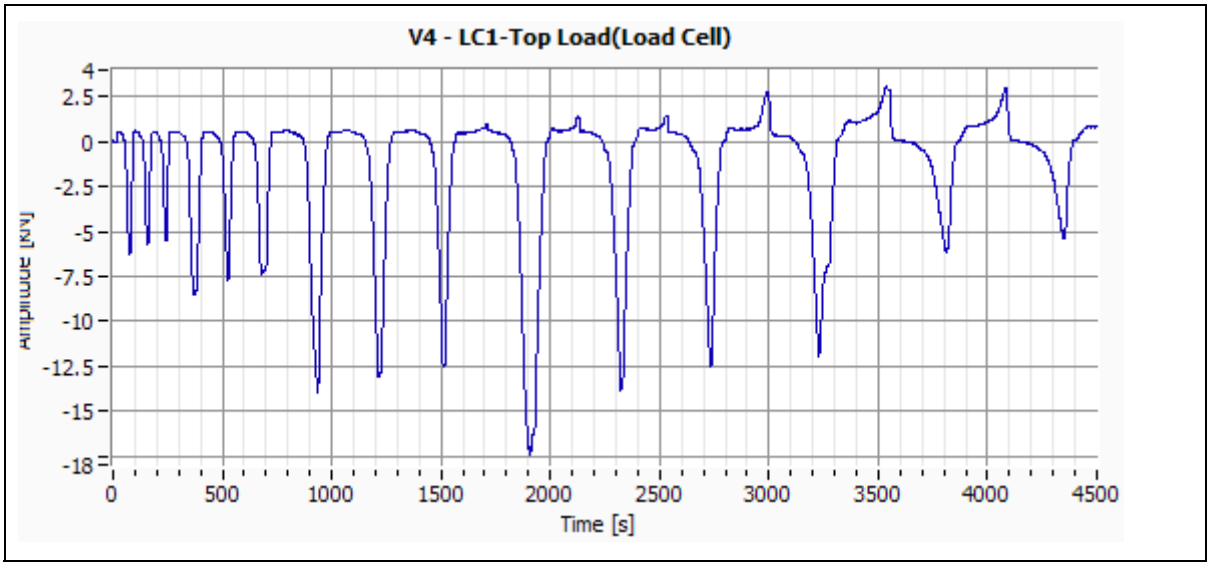

Figure E-48:– Specimen V4-LC1 Top Load.

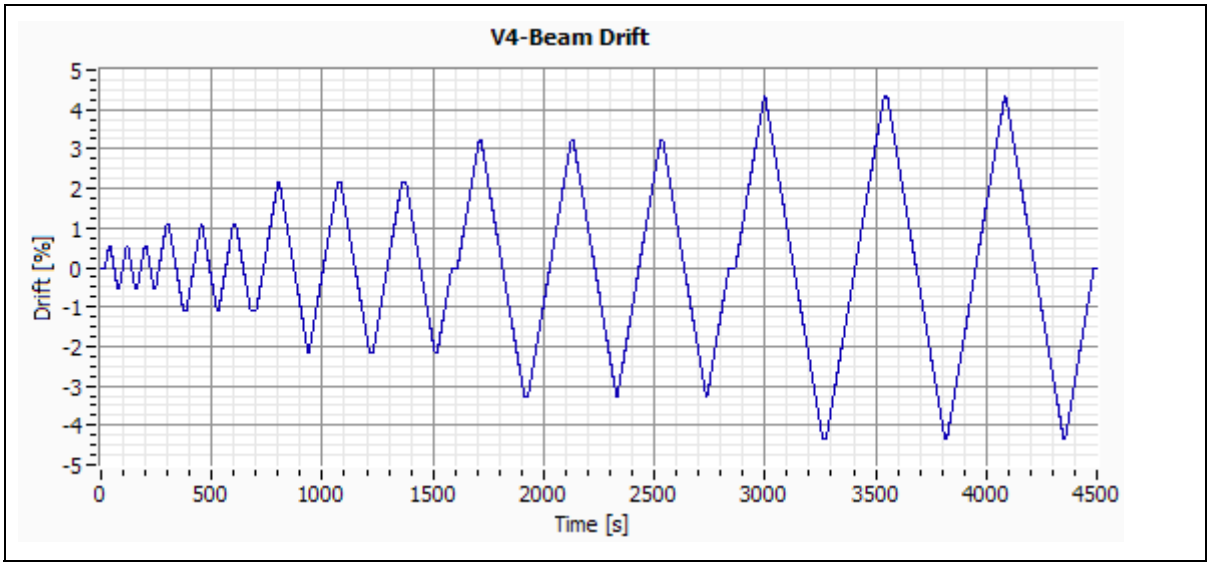

Figure E-49:– Specimen V4-Beam Drift.

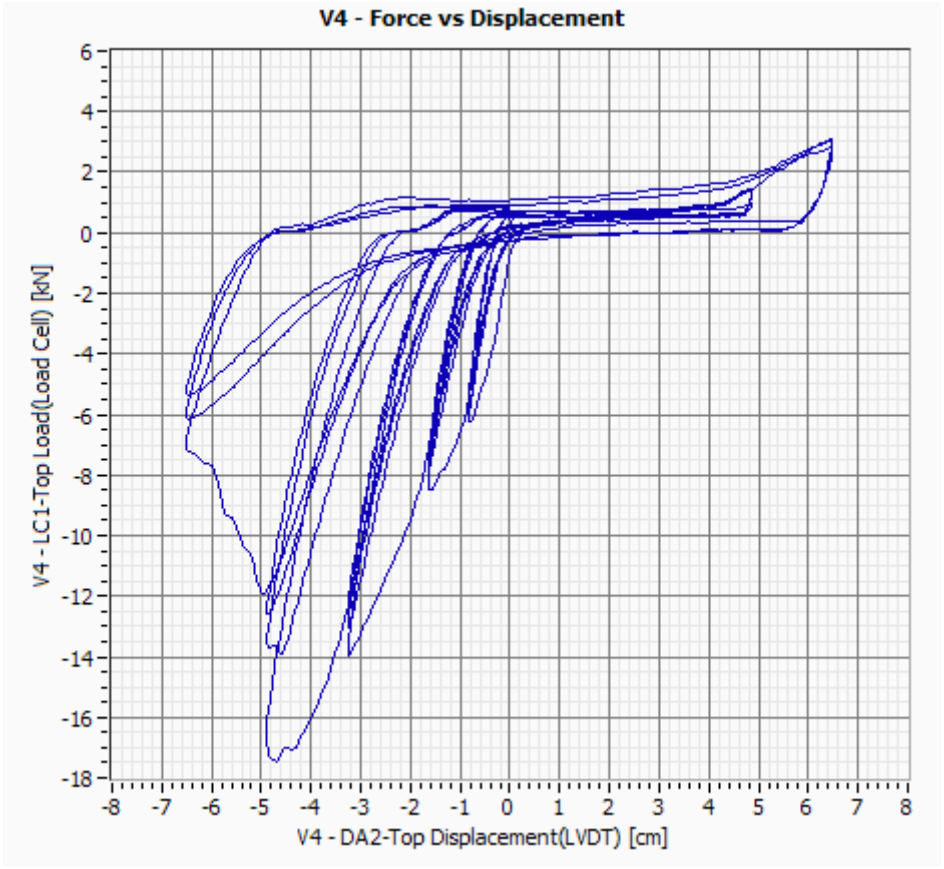

Figure E-50:– Specimen V4-Force vs. Displacement.

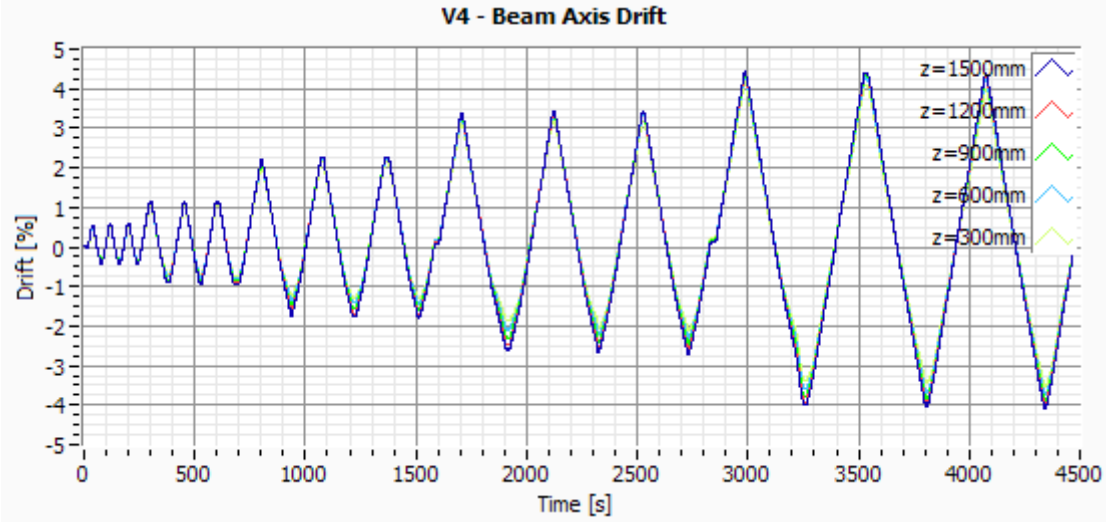

Figure E-51:– Specimen V4-Beam Axis Drift.

E.9 Specimen V5

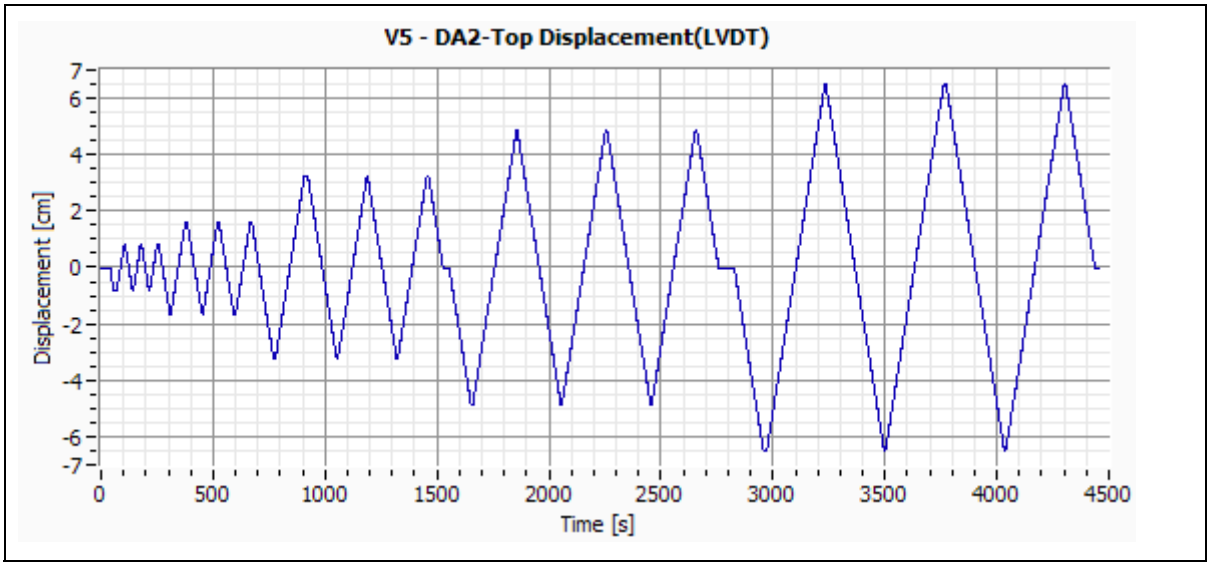

Figure E-52:– Specimen V5-DA2 Top Displacement.

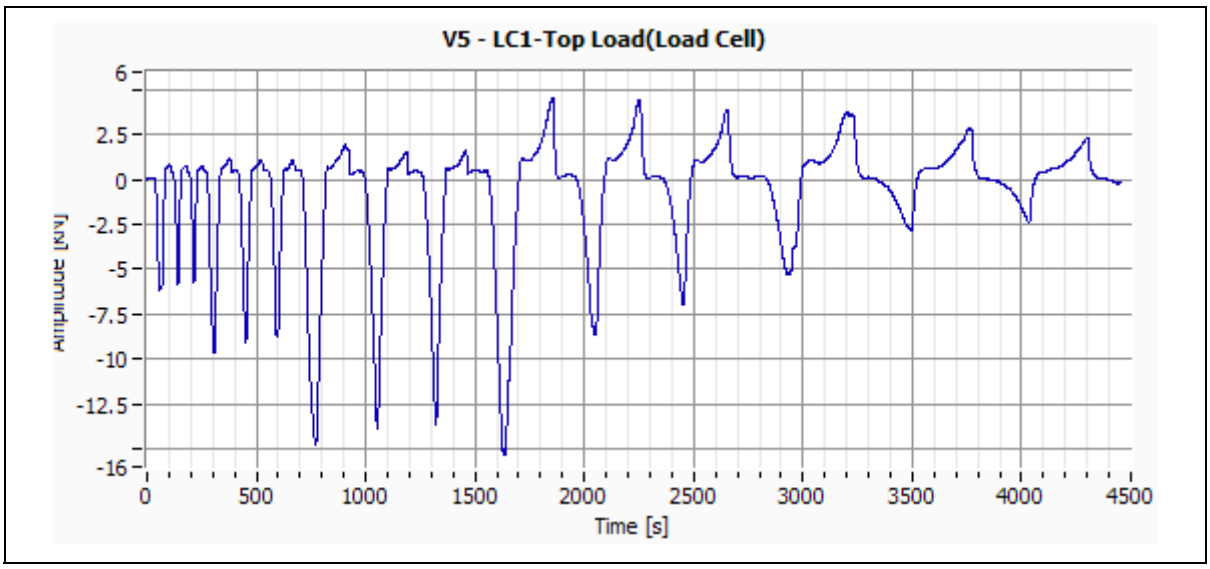

Figure E-53:– Specimen V5-LC1 Top Load.

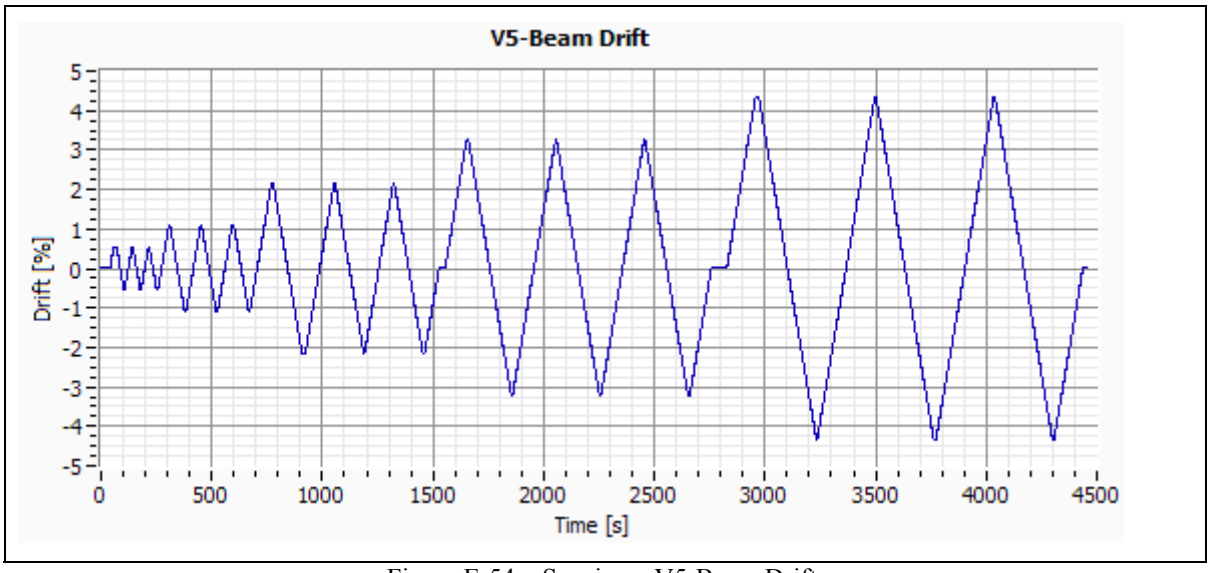

Figure E-54:– Specimen V5-Beam Drift.

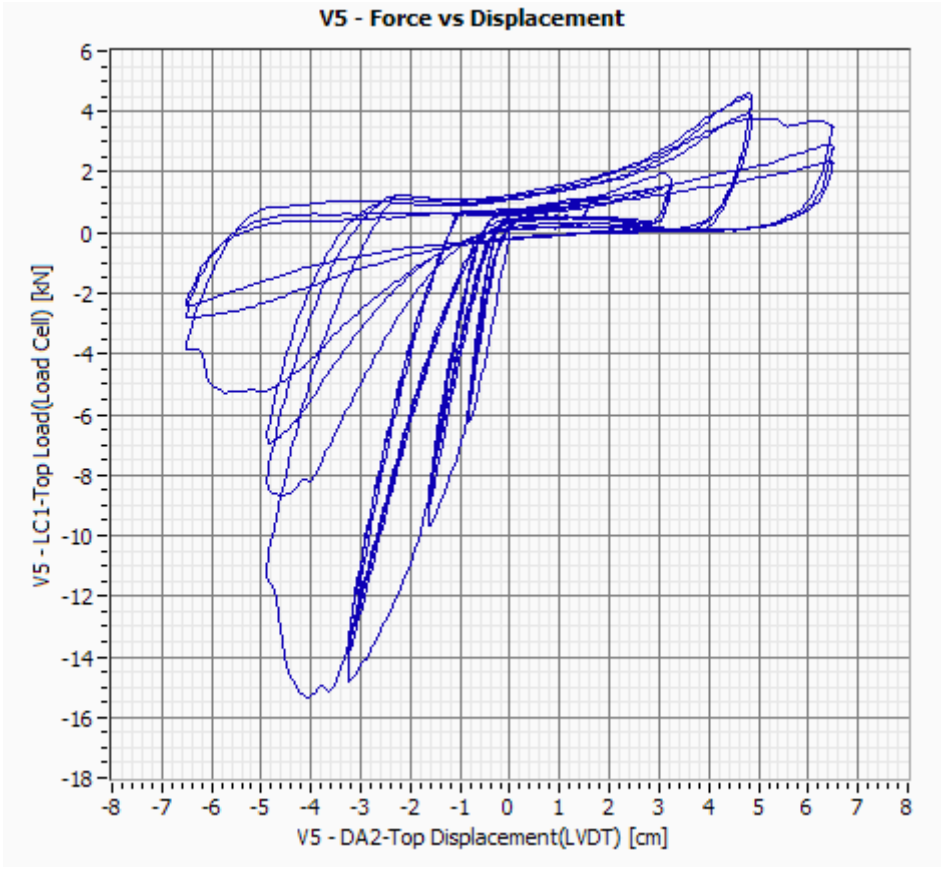

Figure E-55:– Specimen V5-Force vs. Displacement.

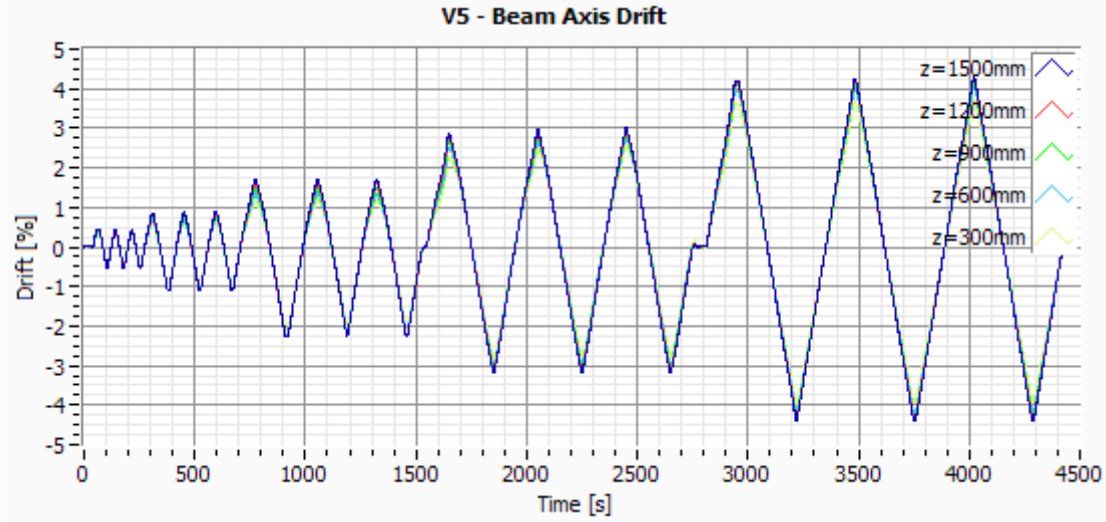

Figure E-56:– Specimen V5-Beam Axis Drift.

E.10 Specimen VL1

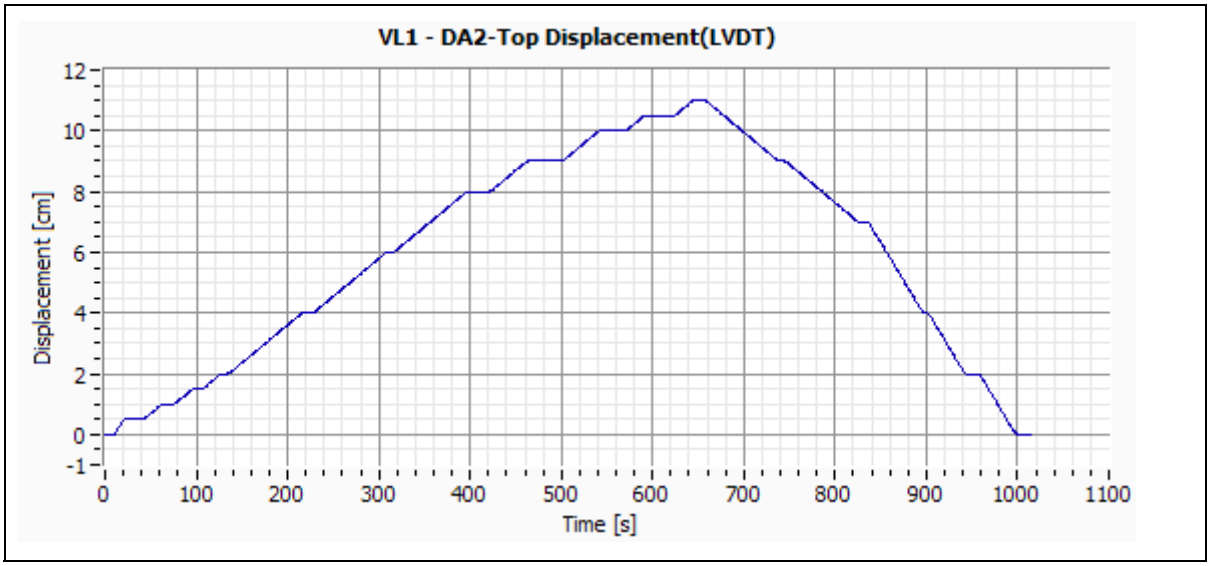

Figure E-57: – Specimen VL1-DA2 Top Displacement.

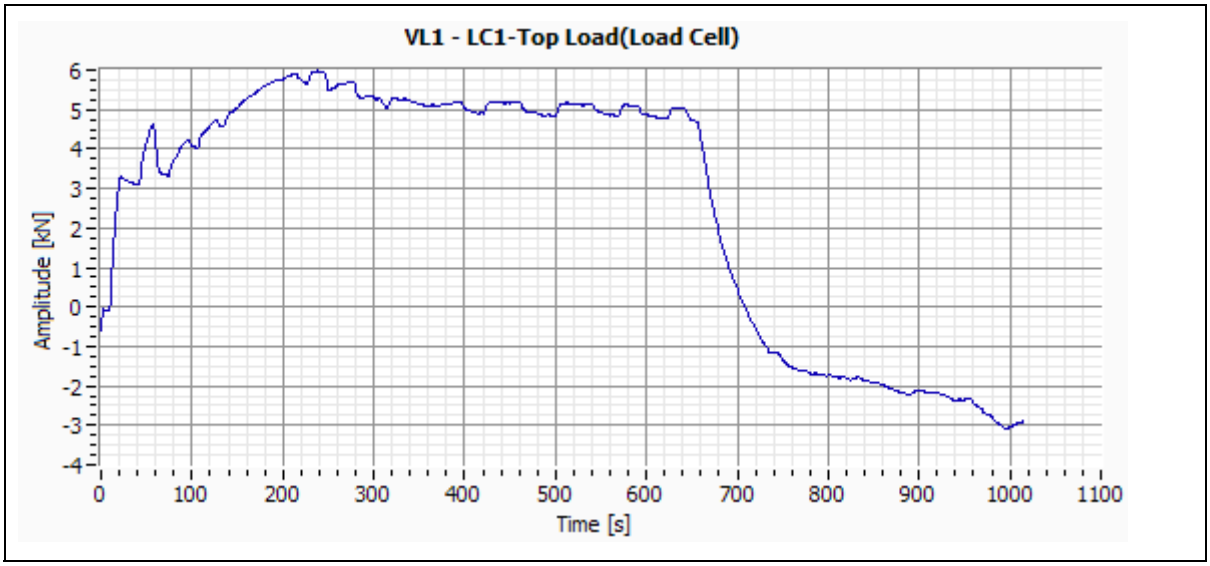

Figure E-58: – Specimen VL1-LC1 Top Load.

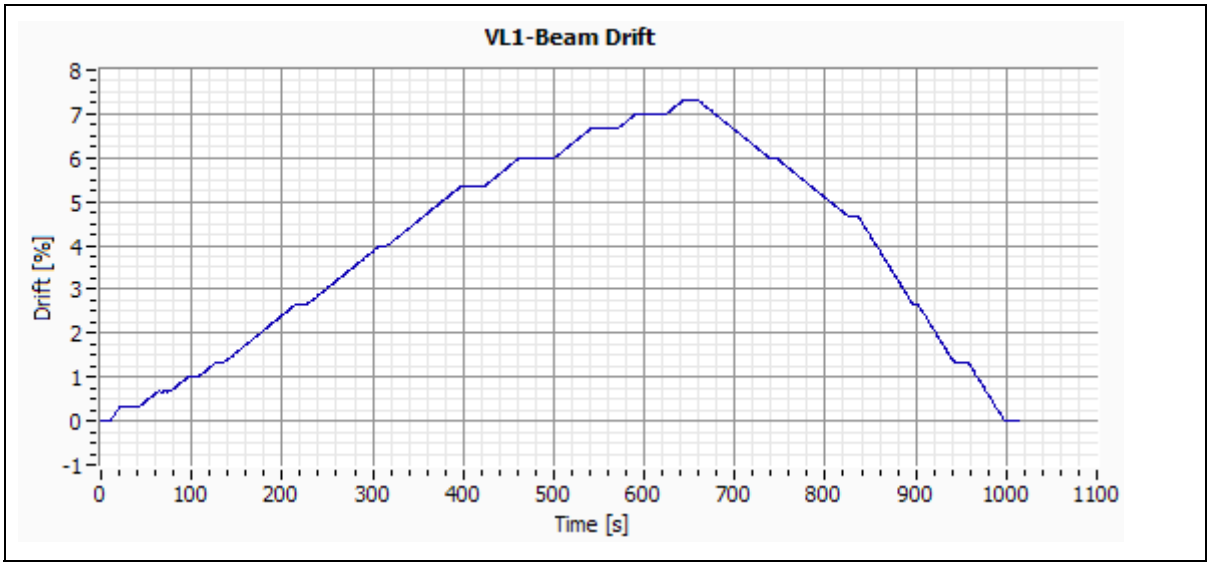

Figure E-59: – Specimen VL1-Beam Drift.

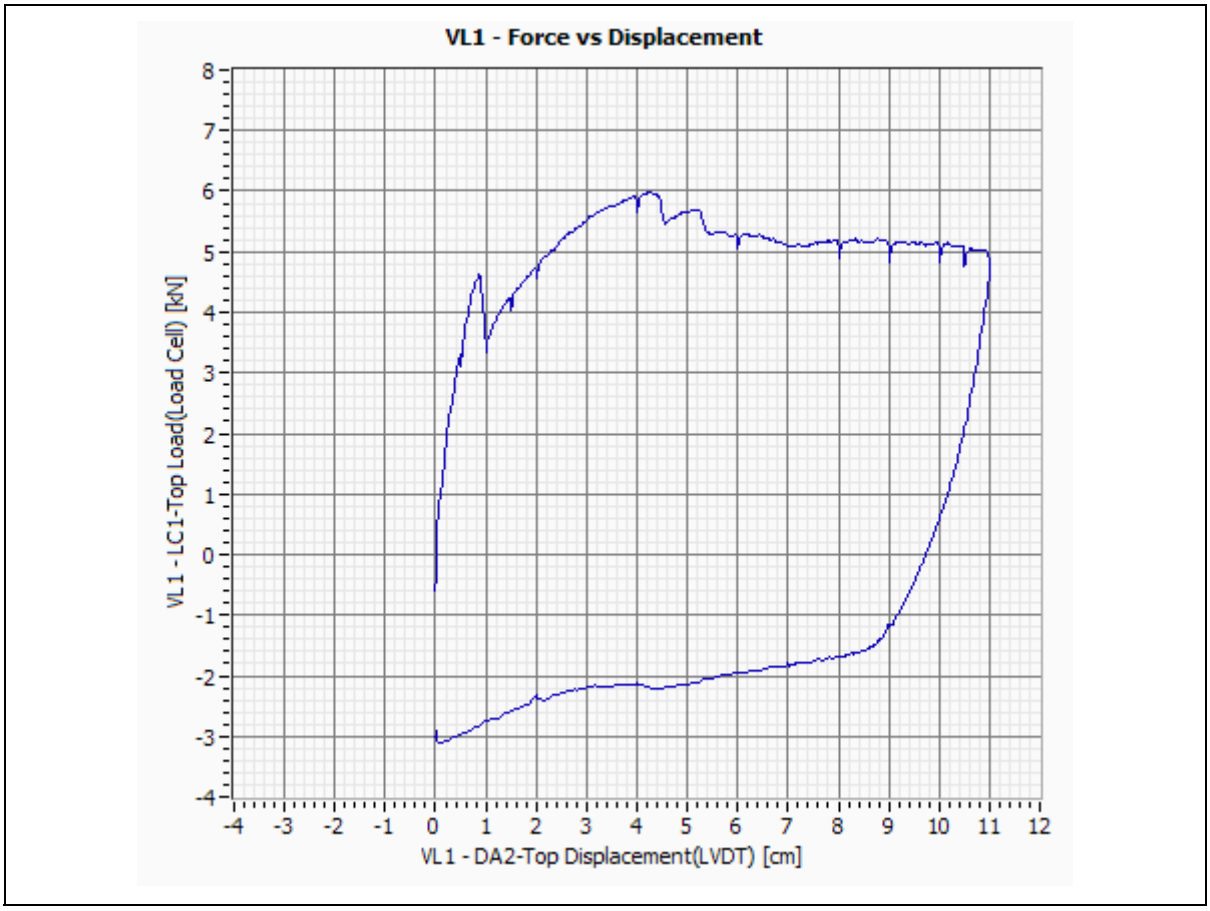

Figure E-60: – Specimen VL1-Force vs. Displacement.

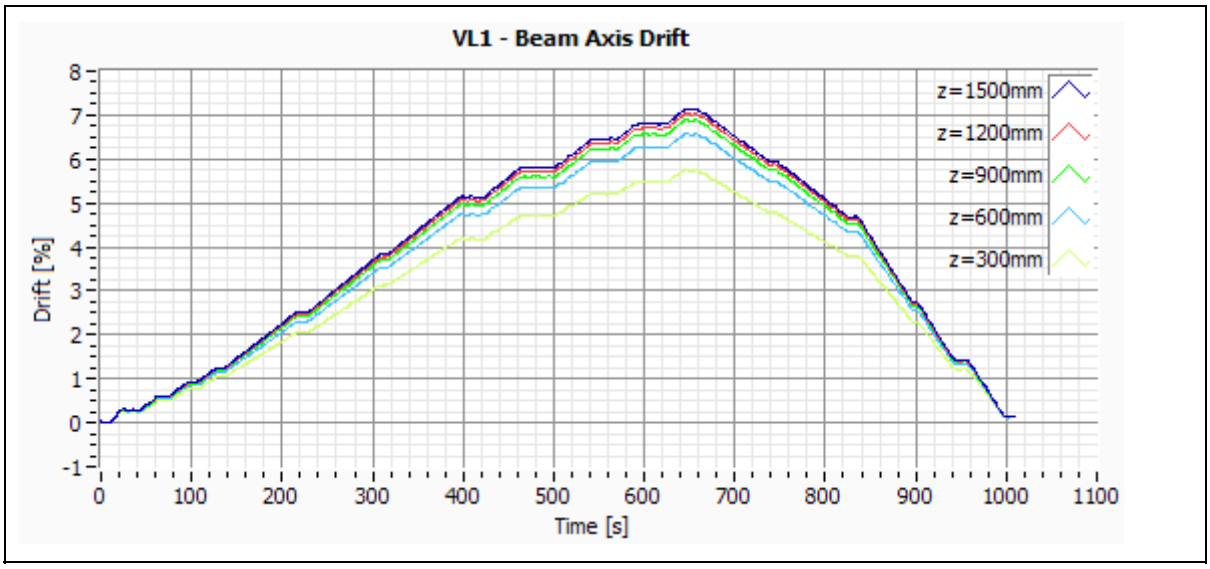

Figure E-61: – Specimen VL1-Beam Axis Drift.

E.11 Specimen VL2

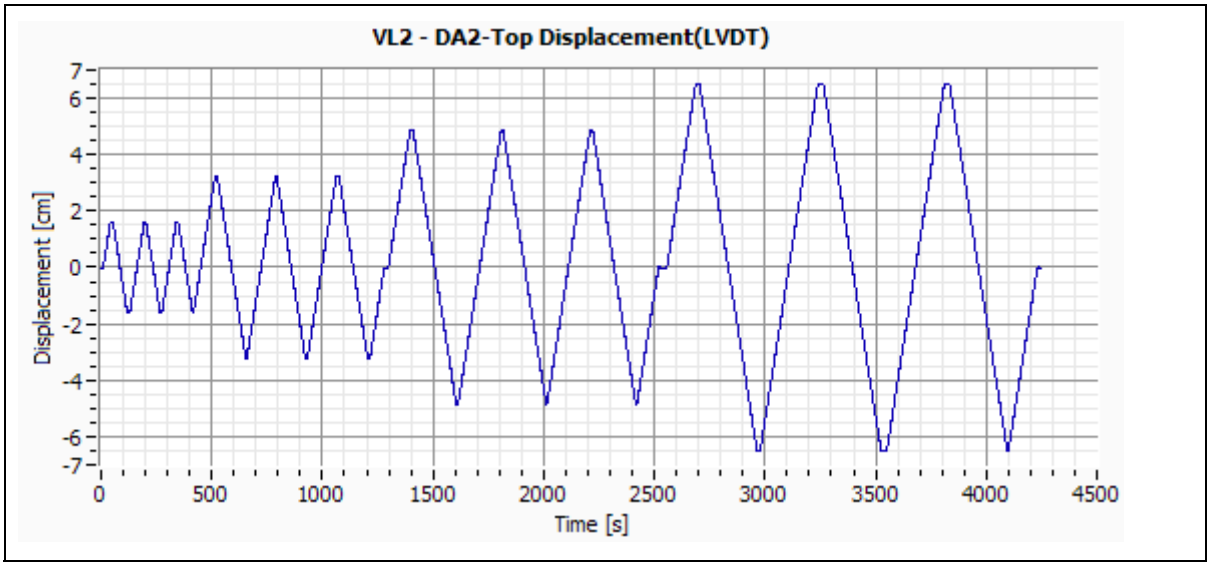

Figure E-62:– Specimen VL2-DA2 Top Displacement.

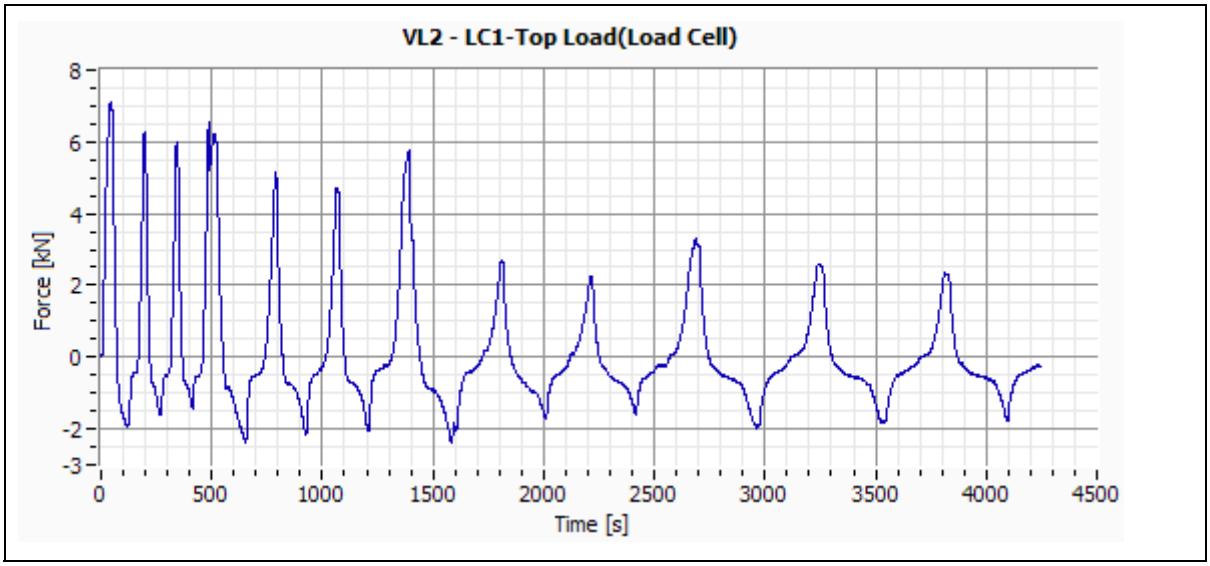

Figure E-63:– Specimen VL2-LC1 Top Load.

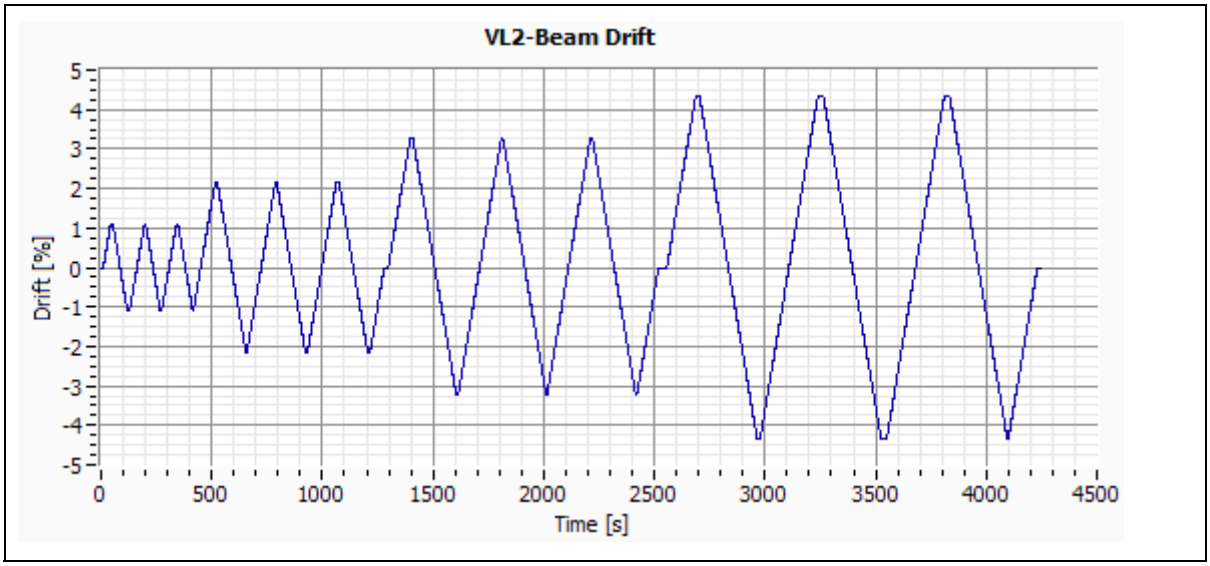

Figure E-64:– Specimen VL2-Beam Drift.

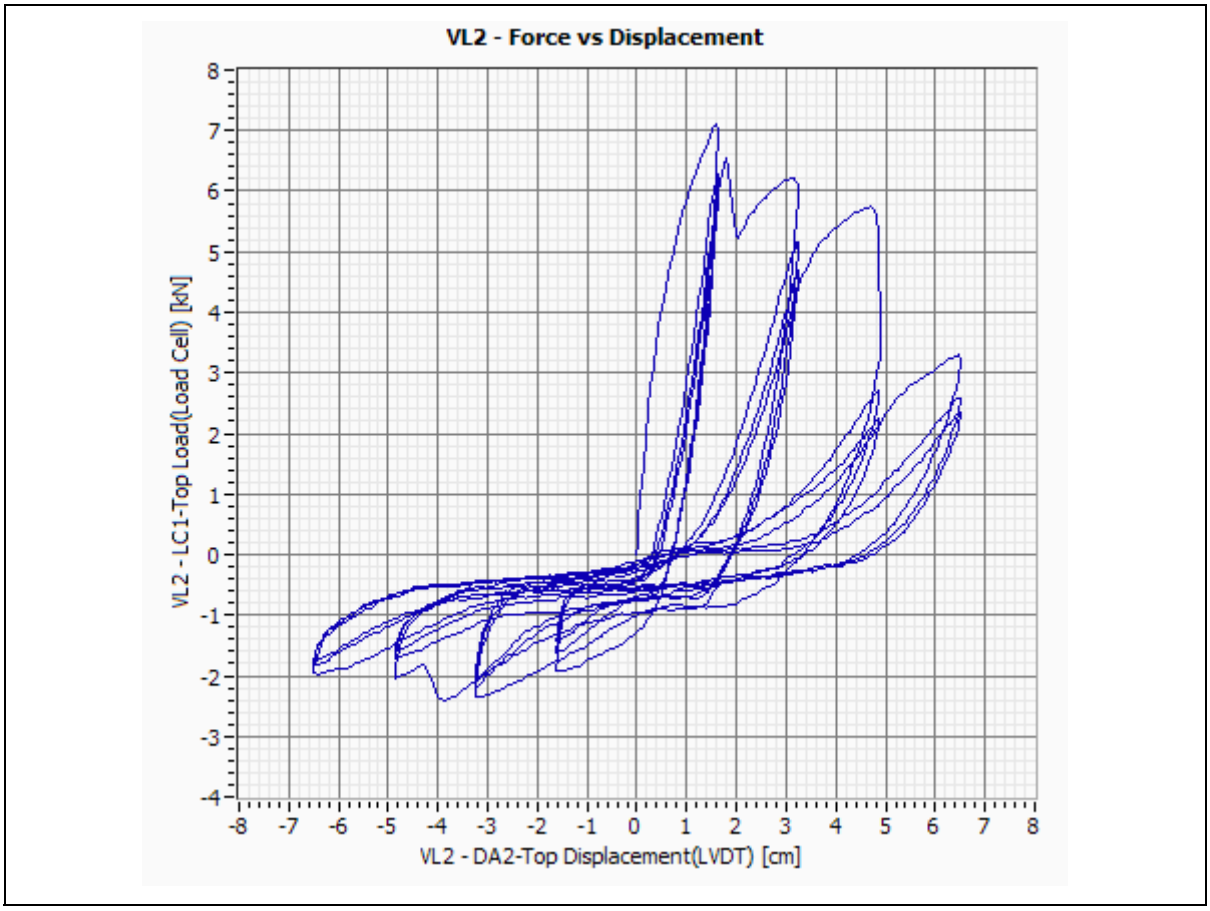

Figure E-65:– Specimen VL2-Force vs. Displacement.

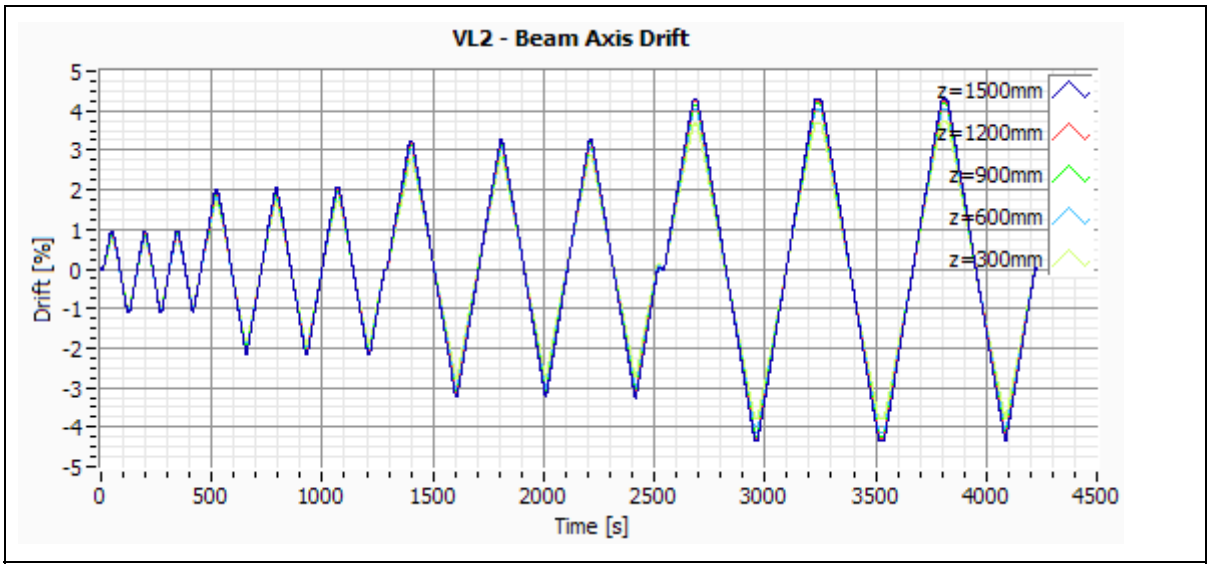

Figure E-66:– Specimen VL2-Beam Axis Drift.

E.12 Specimen VL3

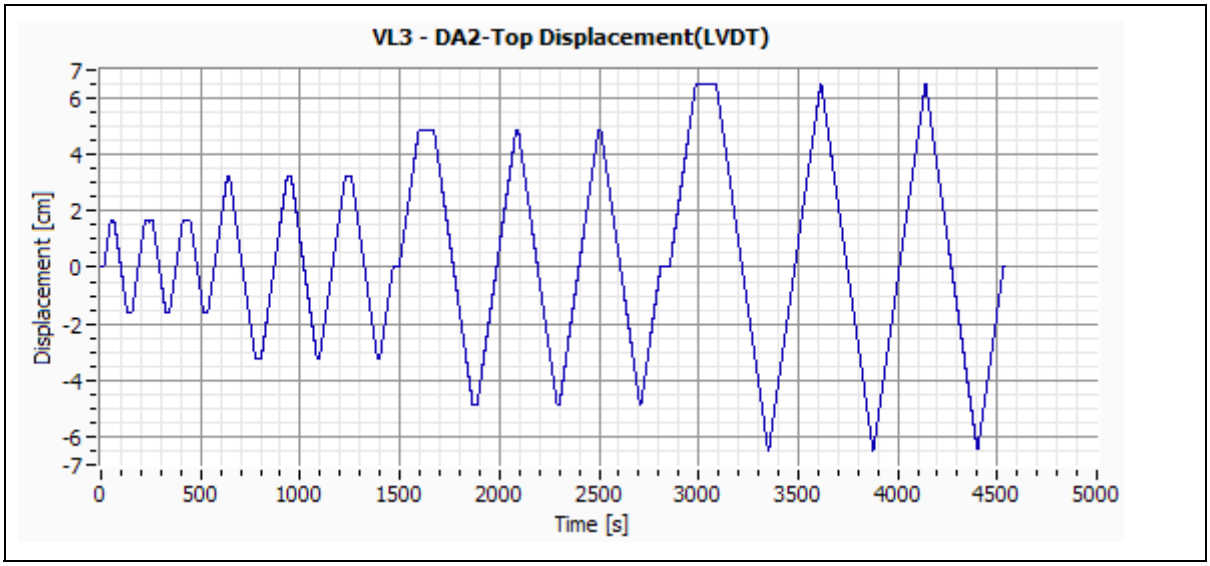

Figure E-67:– Specimen VL3-DA2 Top Displacement.

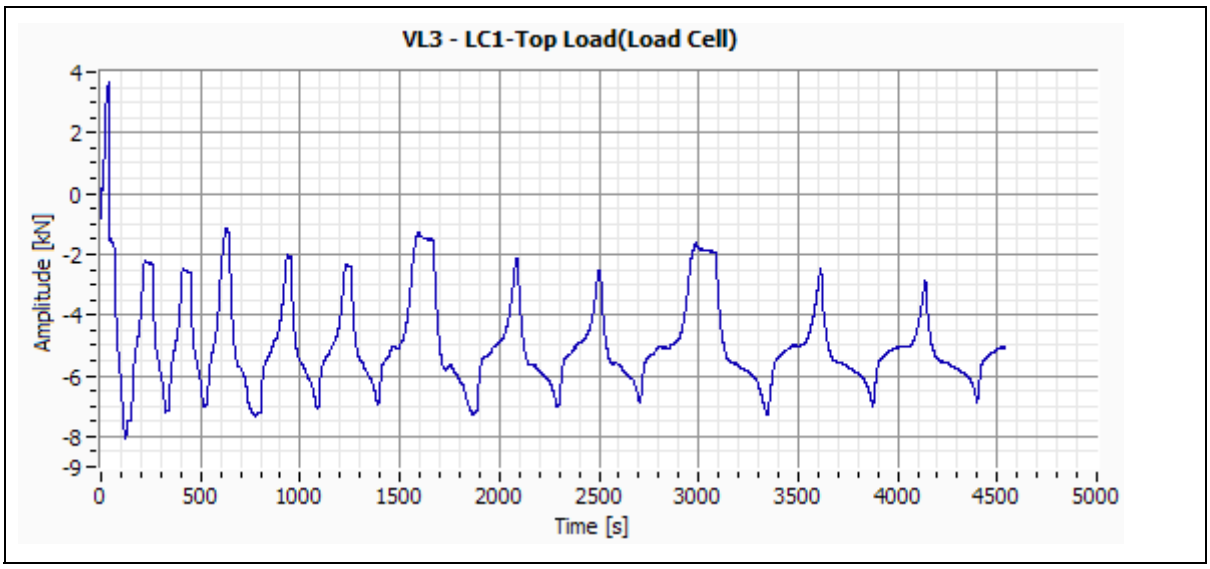

Figure E-68:– Specimen VL3-LC1 Top Load.

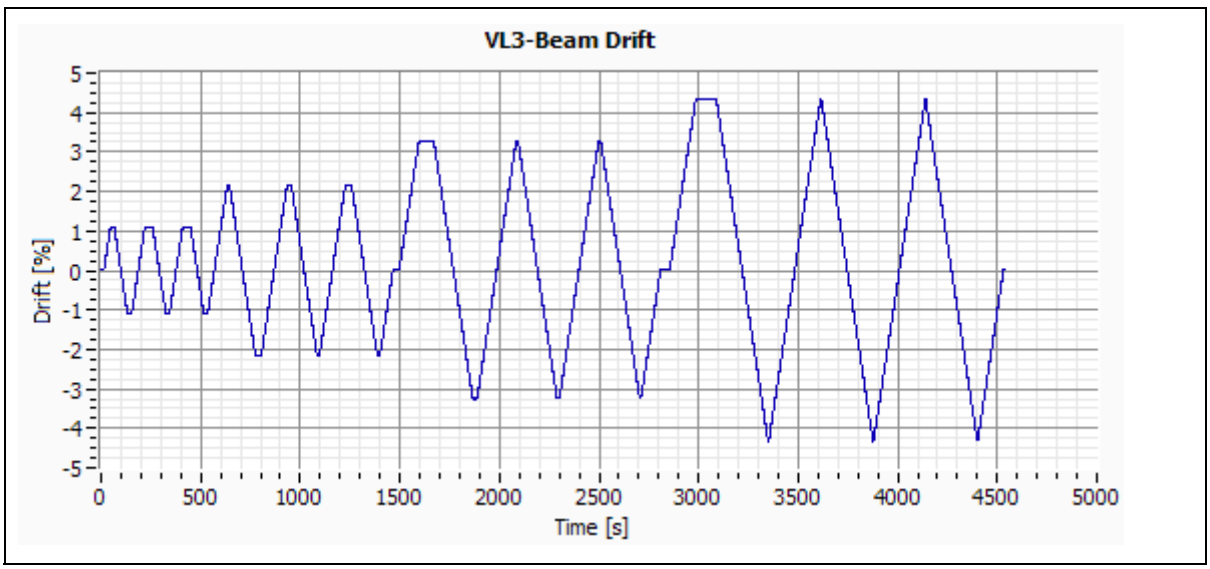

Figure E-69:– Specimen VL3-Beam Drift.

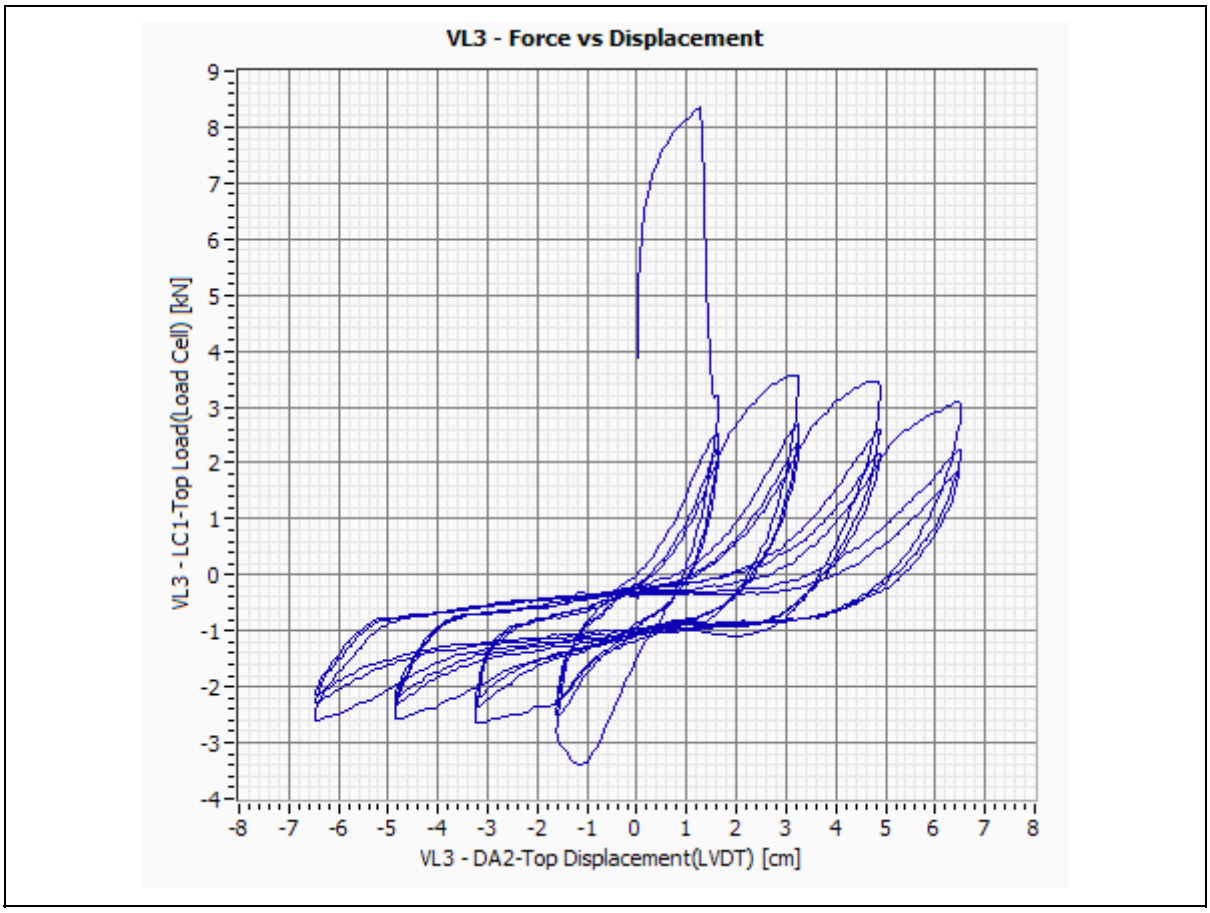

Figure E-70:– Specimen VL3-Force vs. Displacement.

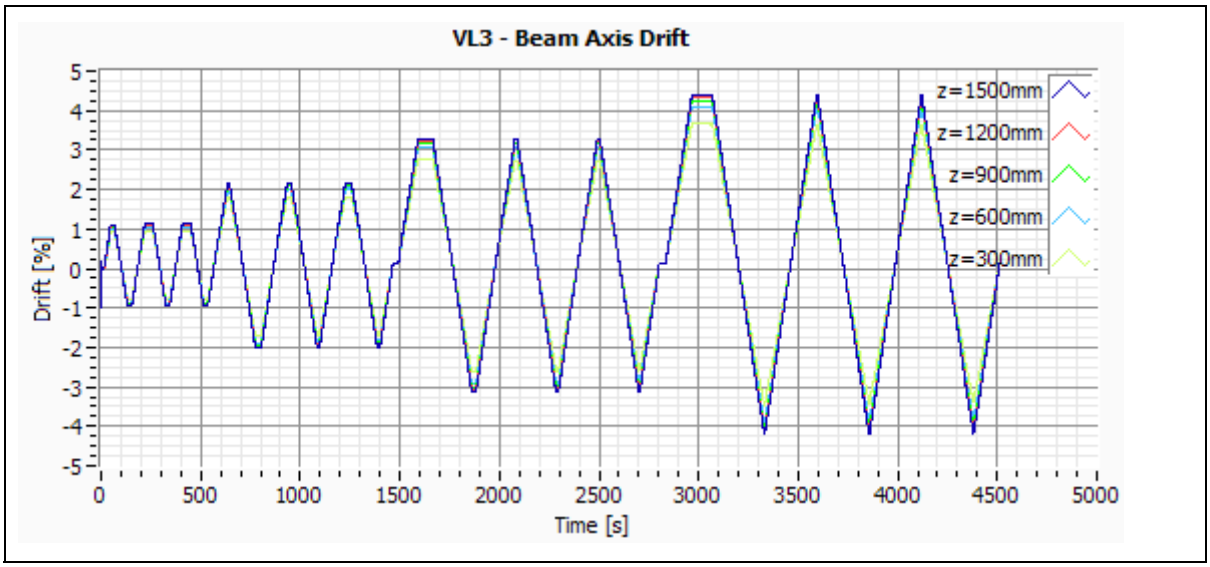

Figure E-71:– Specimen VL3-Beam Axis Drift.

E.13 Specimen VL4

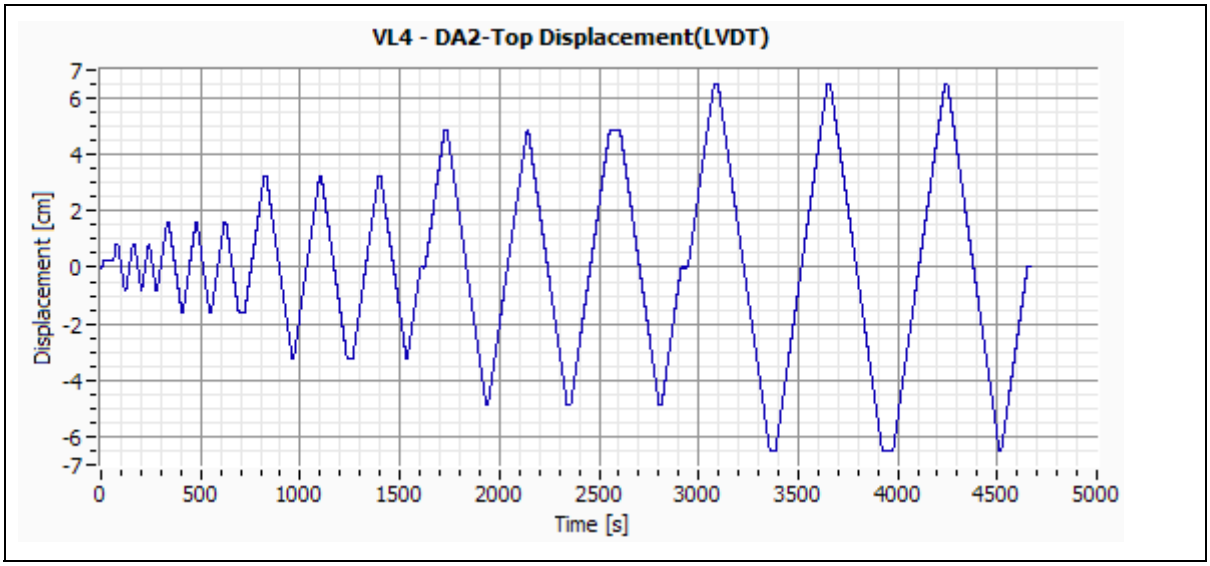

Figure E-72:– Specimen VL4-DA2 Top Displacement.

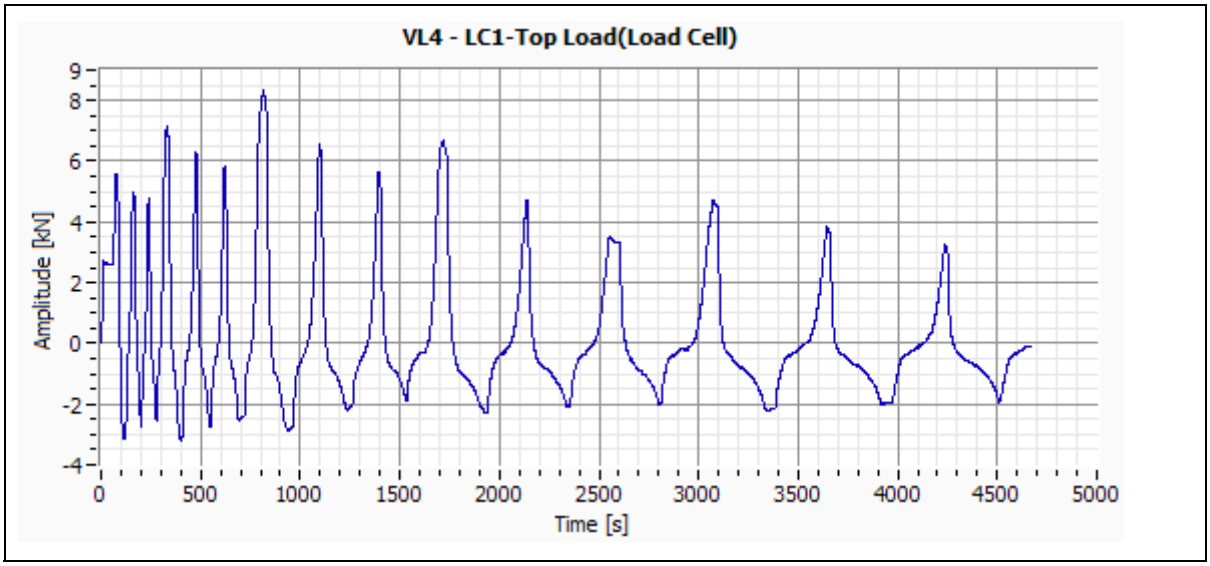

Figure E-73:– Specimen VL4-LC1 Top Load.

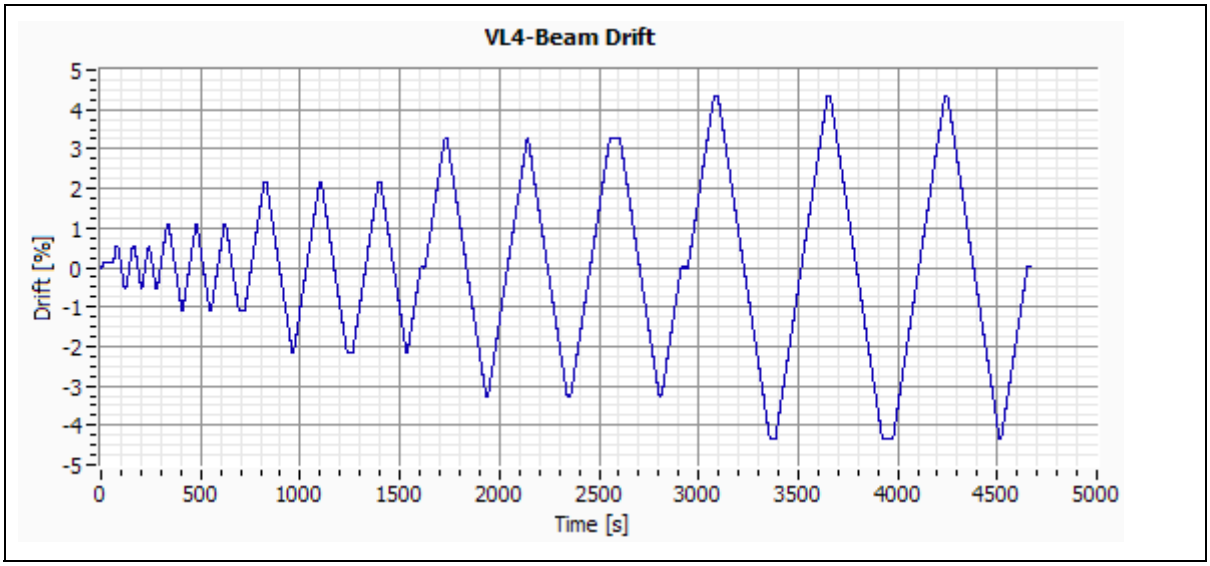

Figure E-74:– Specimen VL4-Beam Drift.

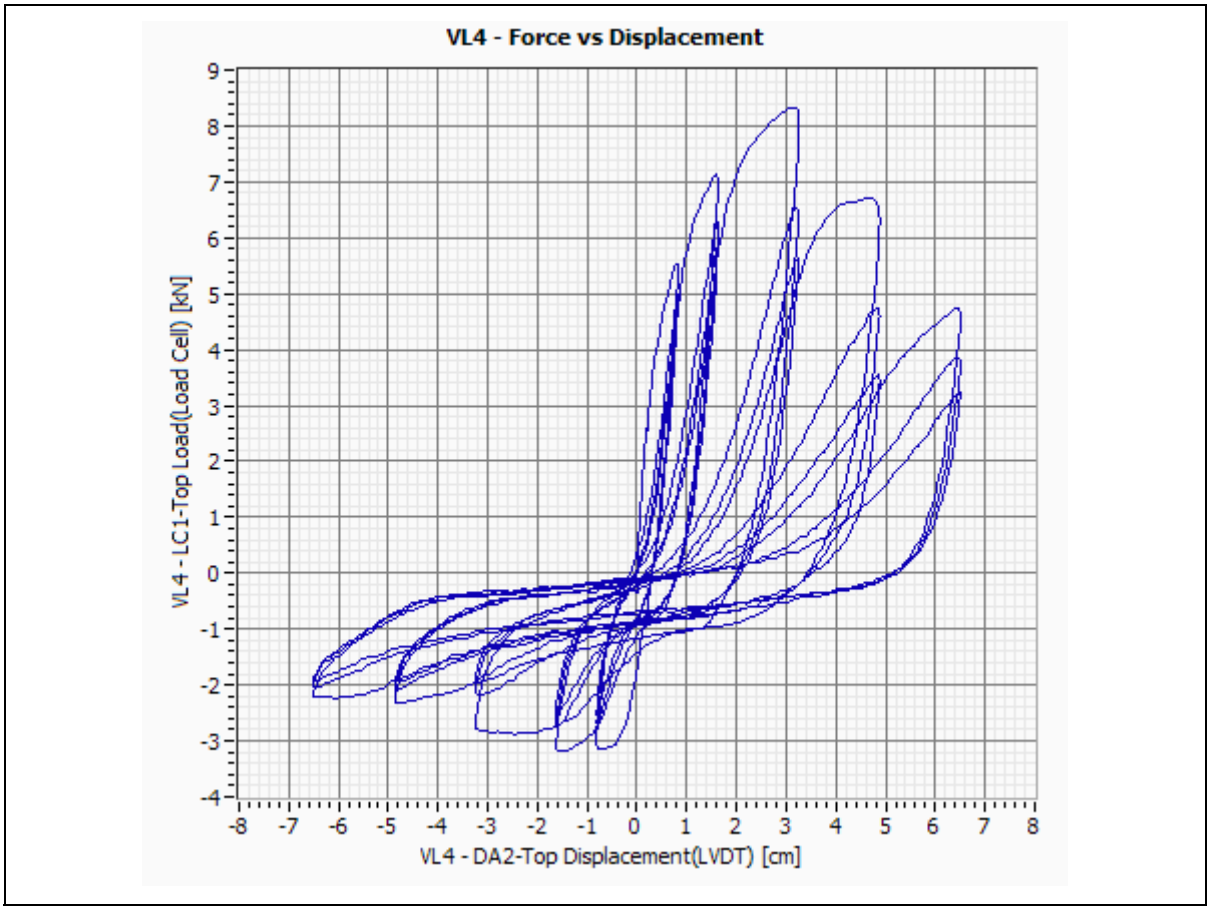

Figure E-75:– Specimen VL4-Force vs. Displacement.

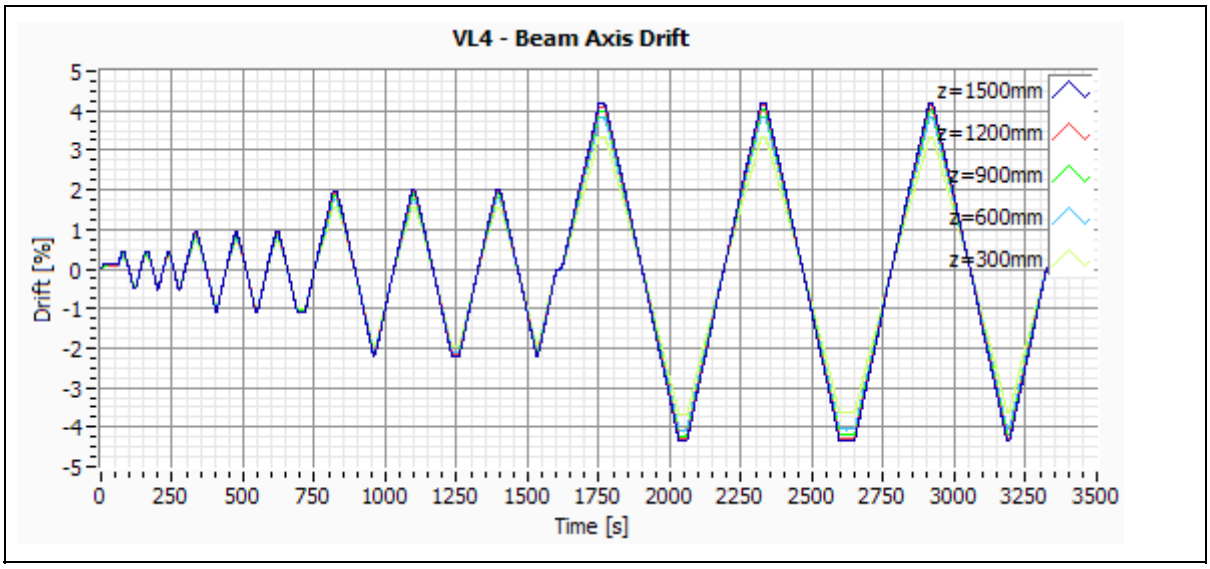

Figure E-76:– Specimen VL4-Beam Axis Drift.

E.14 Specimen VL5

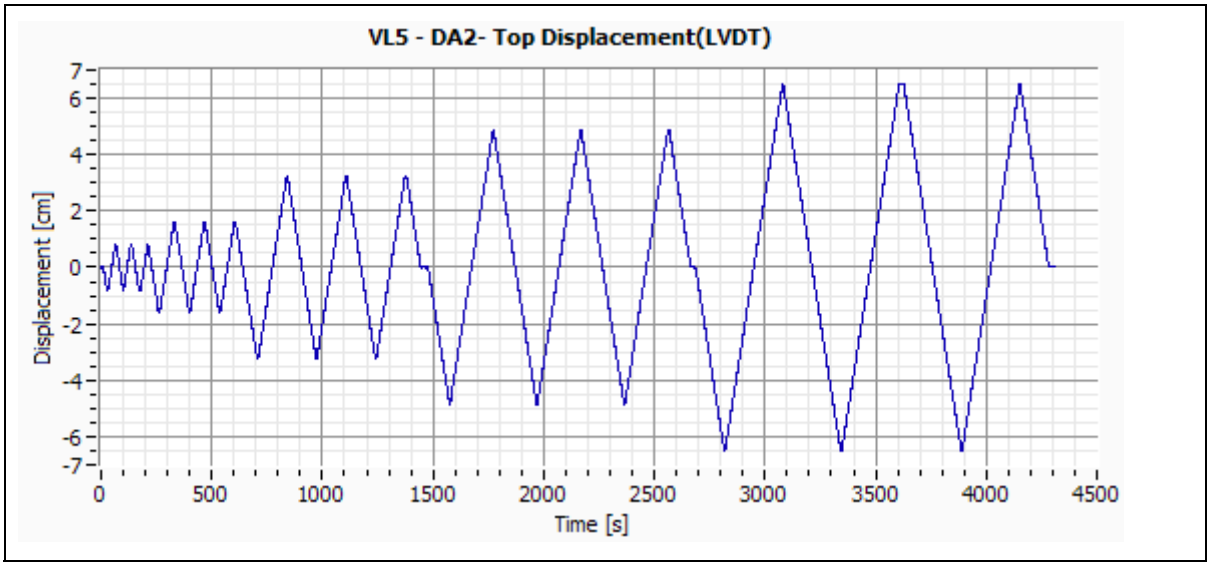

Figure E-77:– Specimen VL5-DA2 Top Displacement.

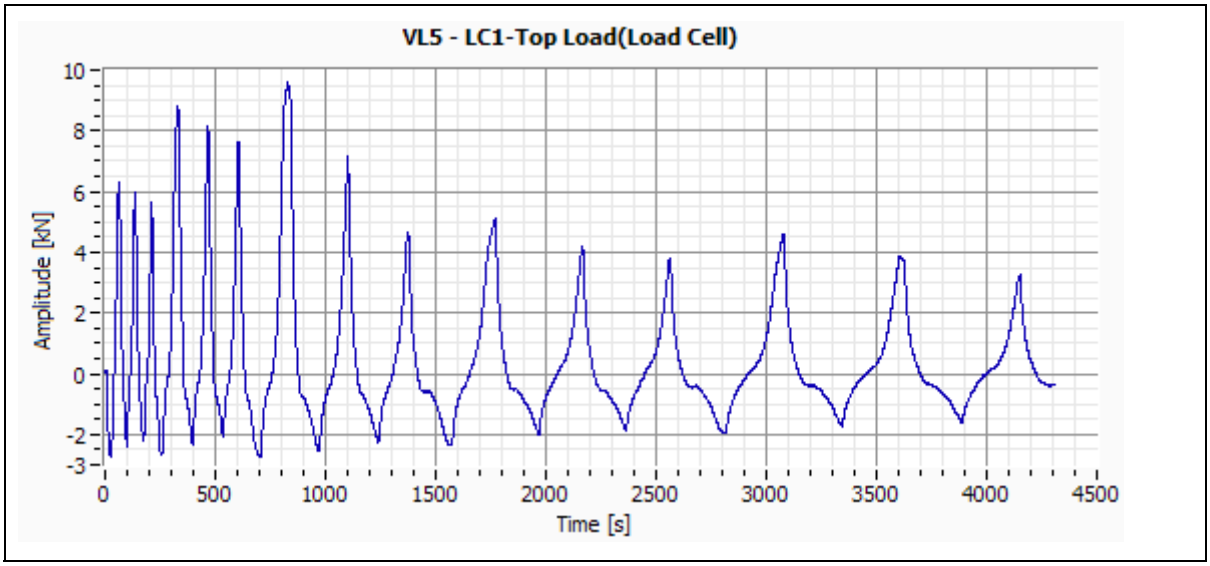

Figure E-78:– Specimen VL5-LC1 Top Load.

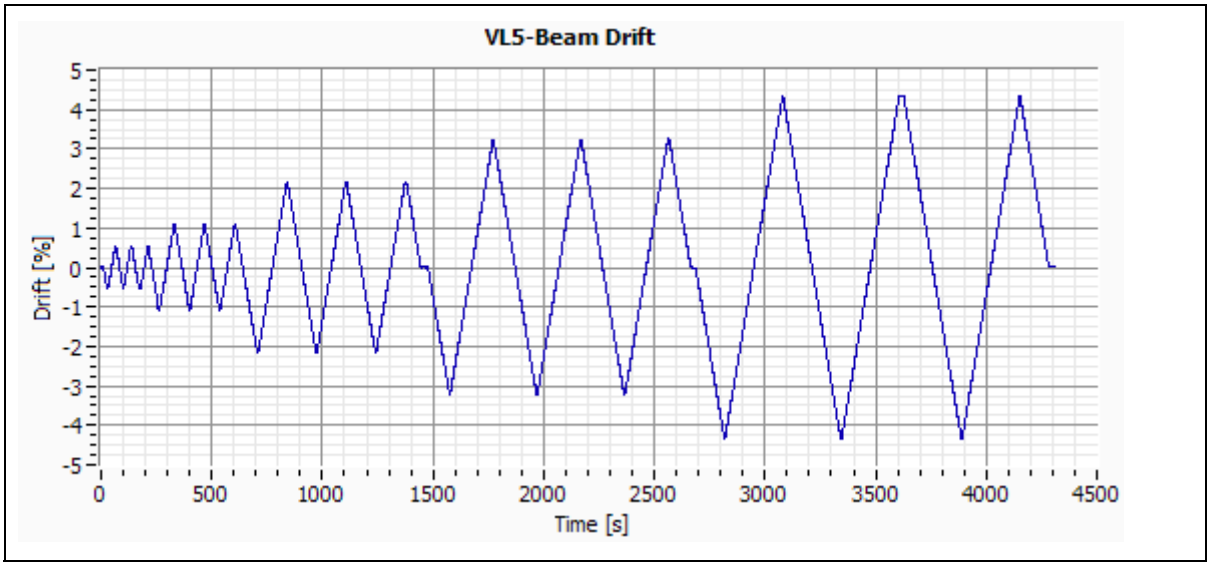

Figure E-79:– Specimen VL5-Beam Drift.

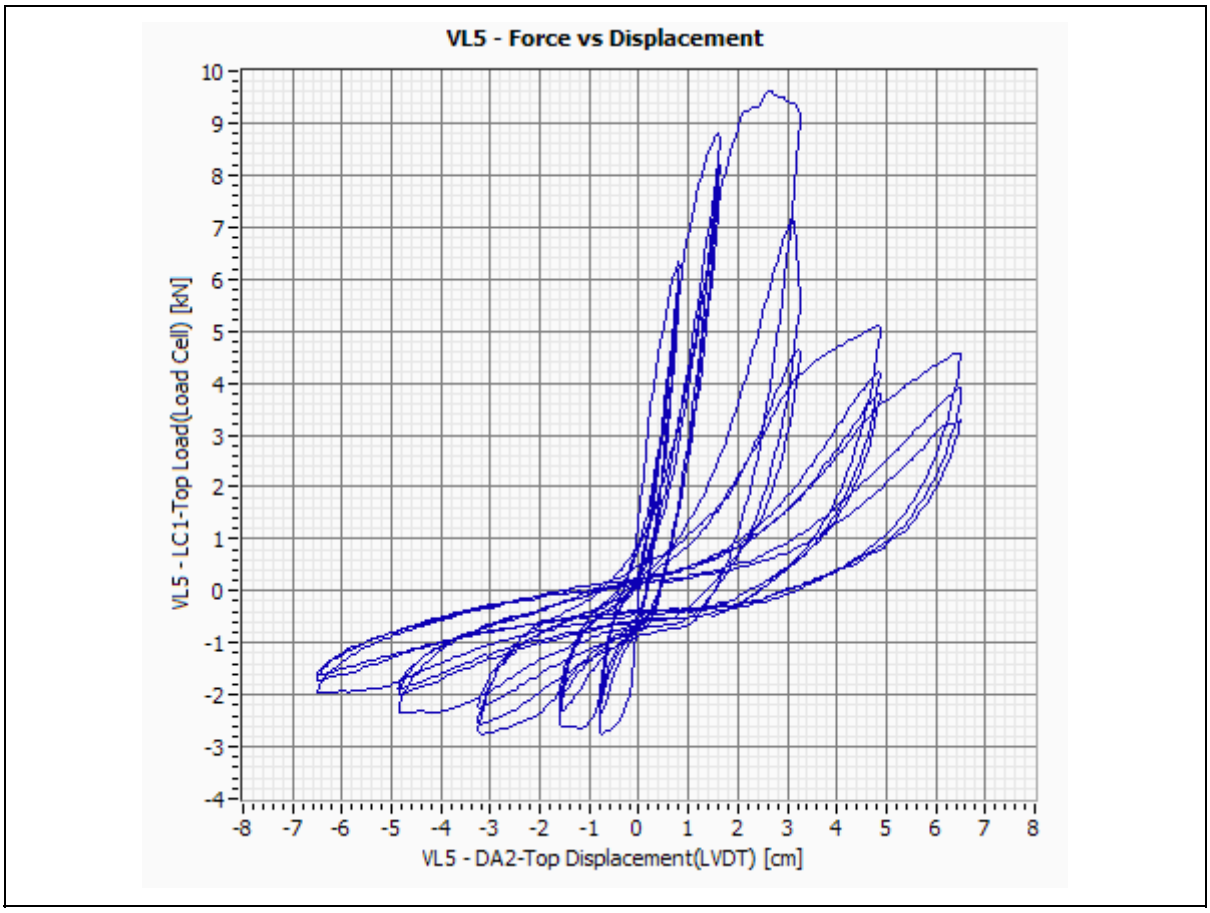

Figure E-80:– Specimen VL5-Force vs. Displacement.

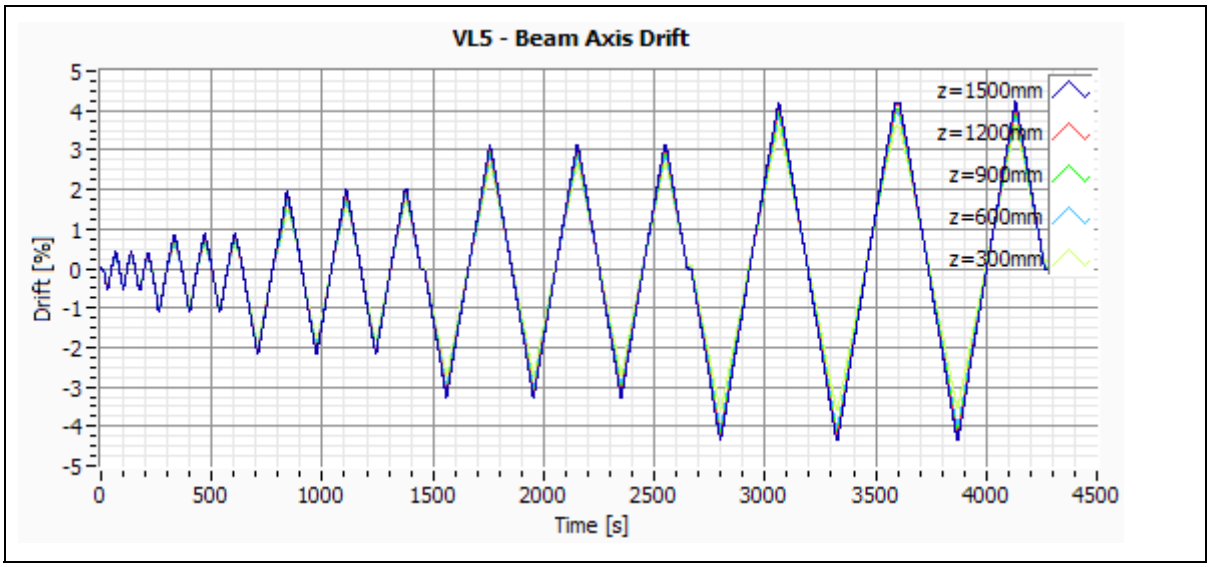

Figure E-81:– Specimen VL5-Beam Axis Drift.

ANNEX F CONNECTIONS MOMENTS AND ROTATIONS

Contents:

List of Figures:

F.1 Specimen P1

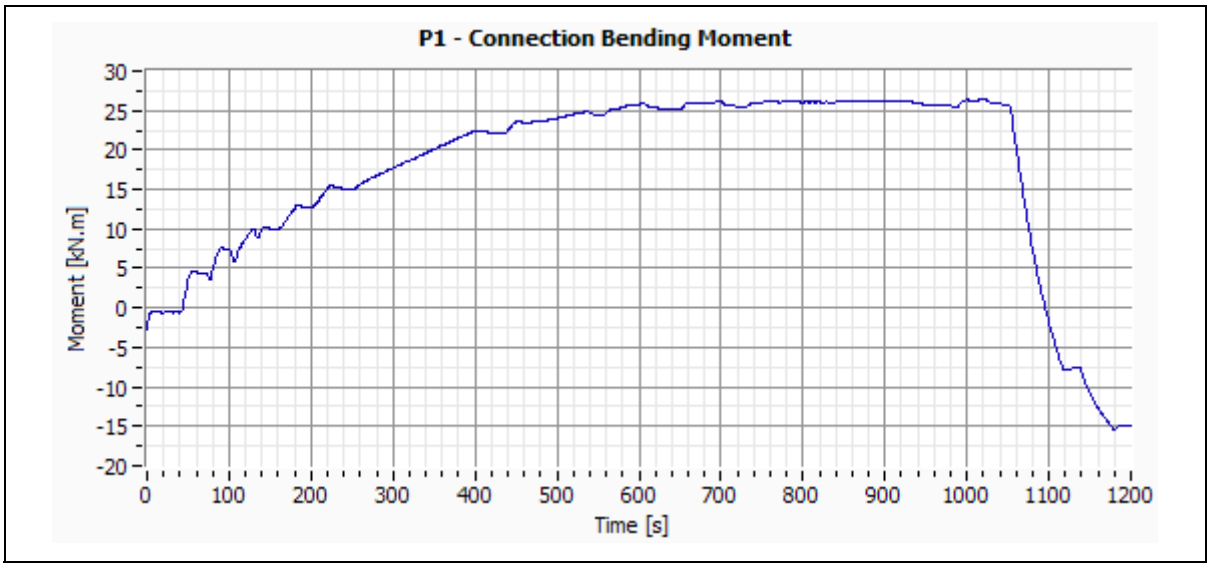

Figure F-1: Specimen P1 - Connection Bending Moment.

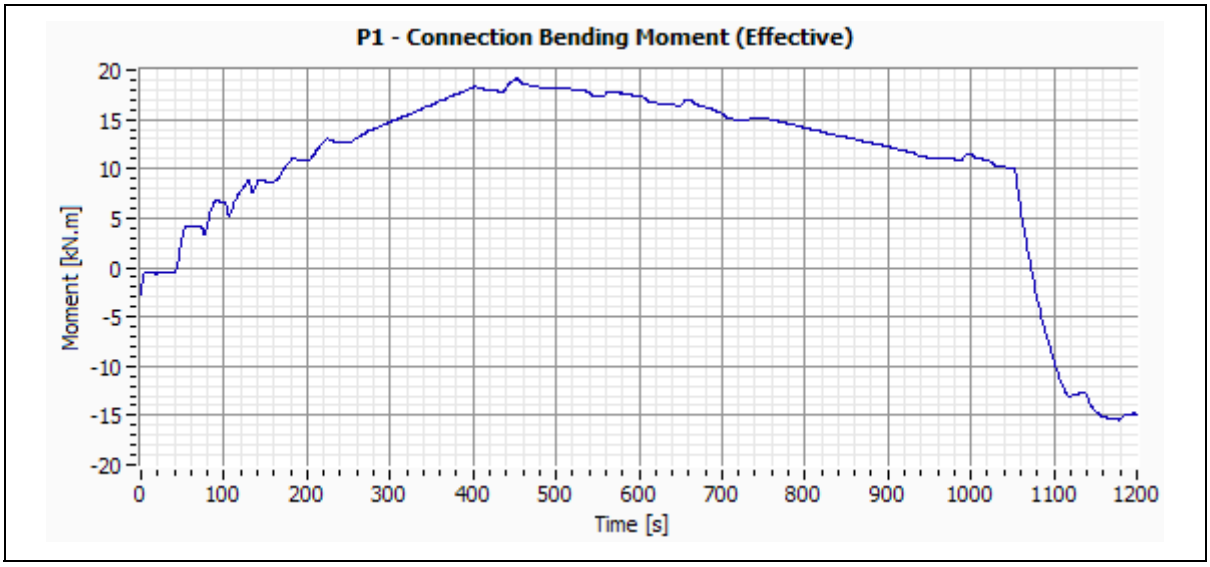

Figure F-2: Specimen P1 - Connection Bending Moment (Effective).

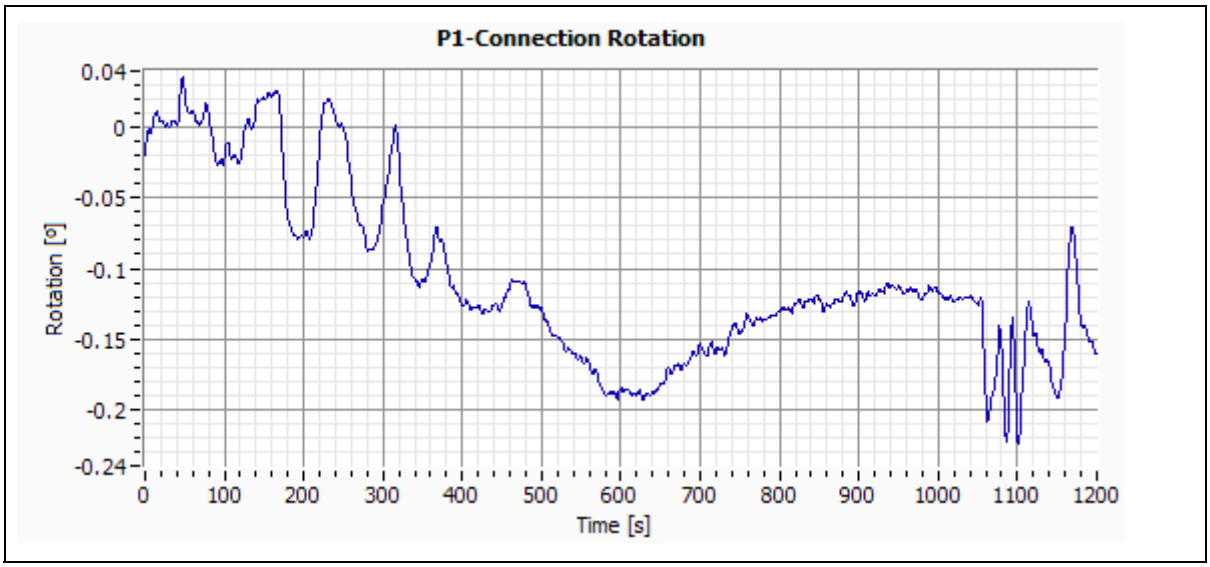

Figure F-3: Specimen P1 – Connection Rotation.

F.2 Specimen P2

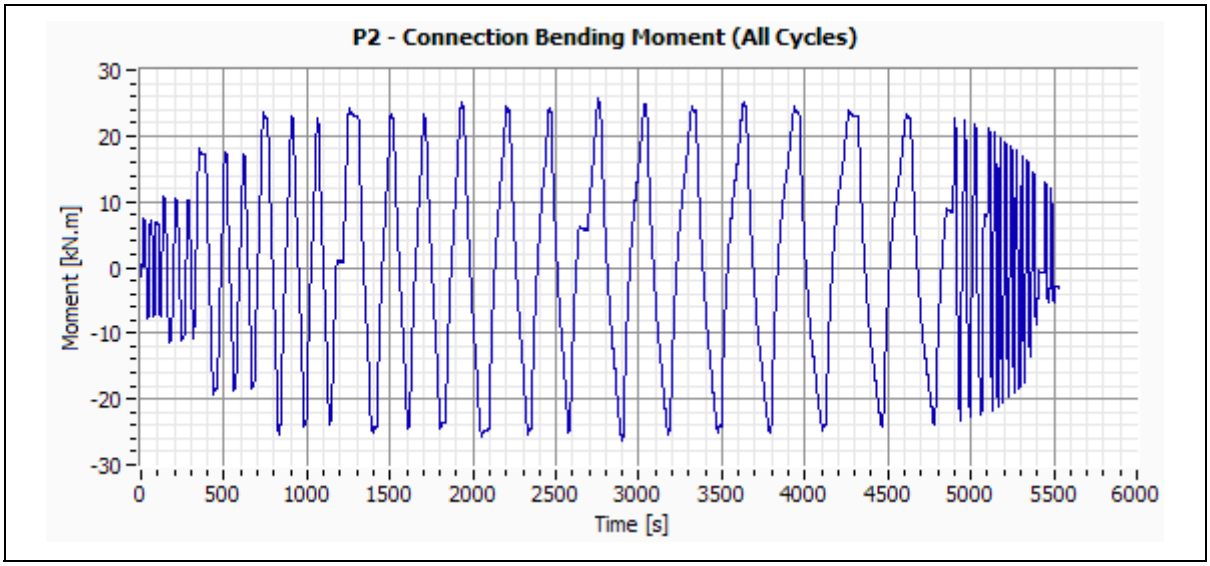

Figure F-4: Specimen P2 - Connection Bending Moment.

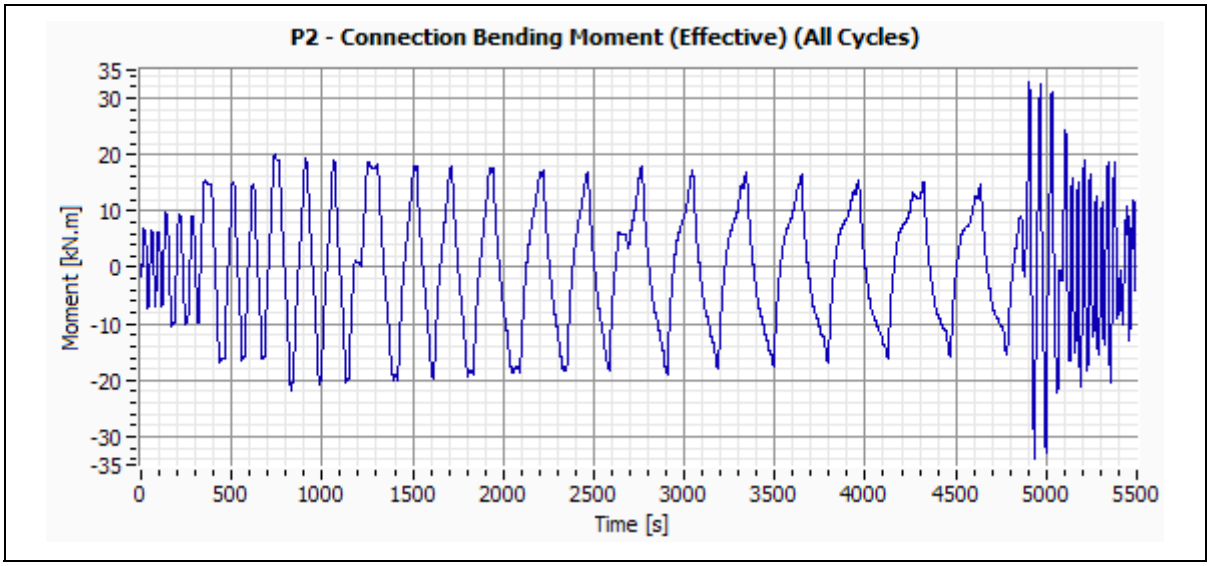

Figure F-5: Specimen P2 - Connection Bending Moment (Effective).

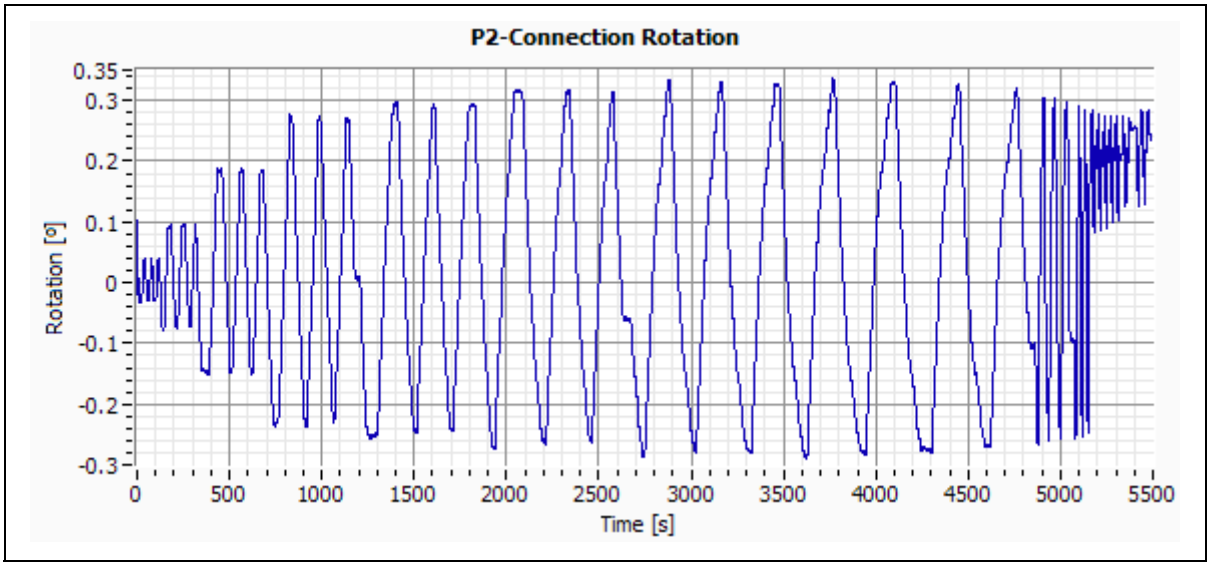

Figure F-6: Specimen P2 – Connection Rotation.

F.3 Specimen P3

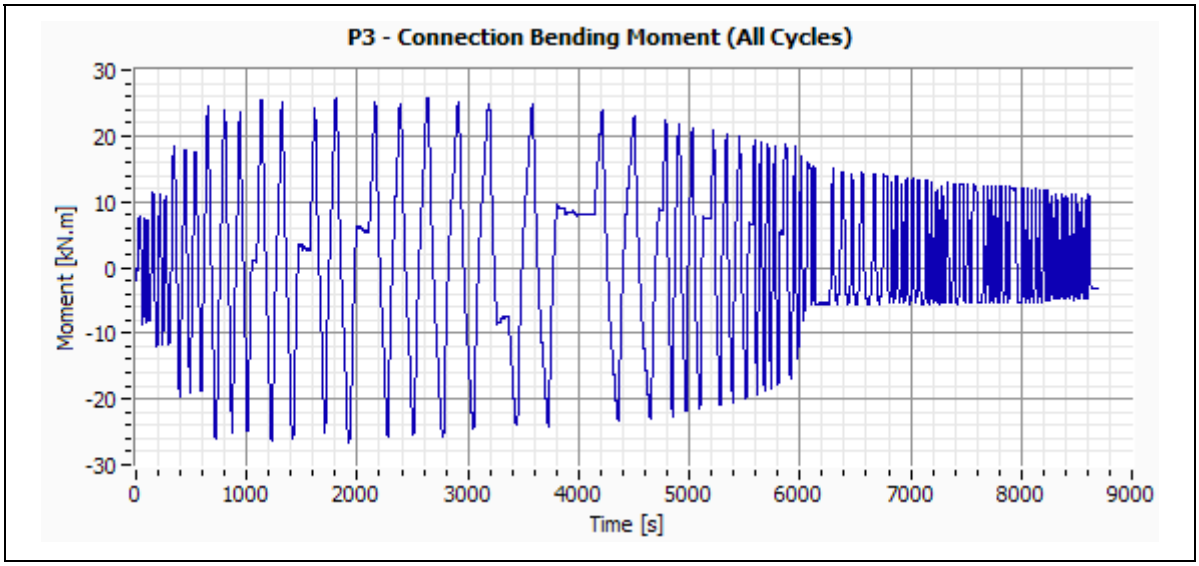

Figure F-7: Specimen P3 - Connection Bending Moment.

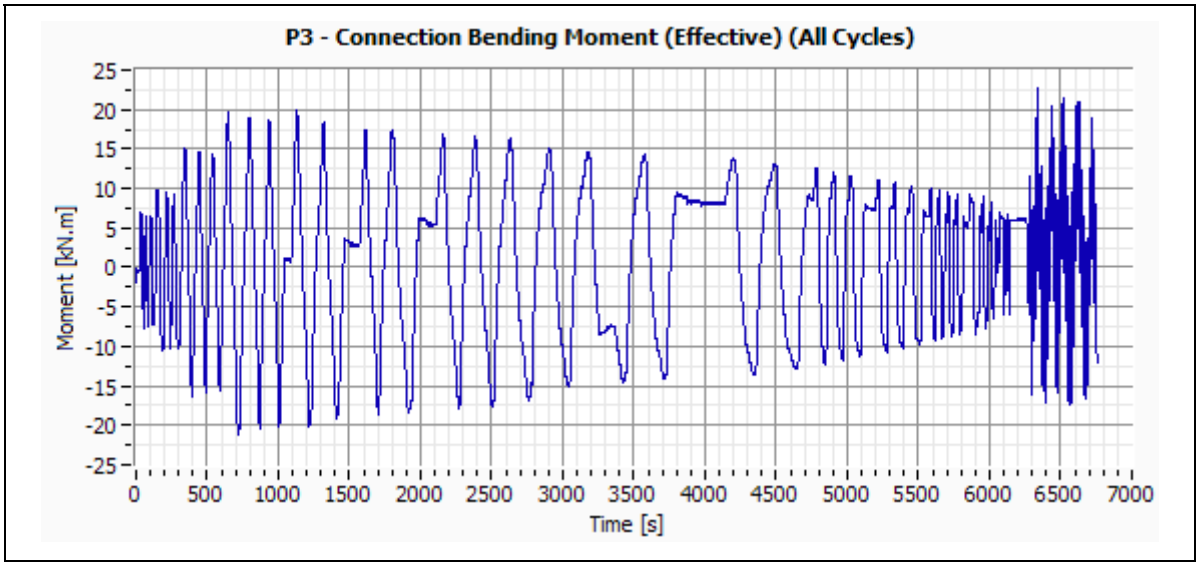

Figure F-8: Specimen P3 - Connection Bending Moment (Effective).

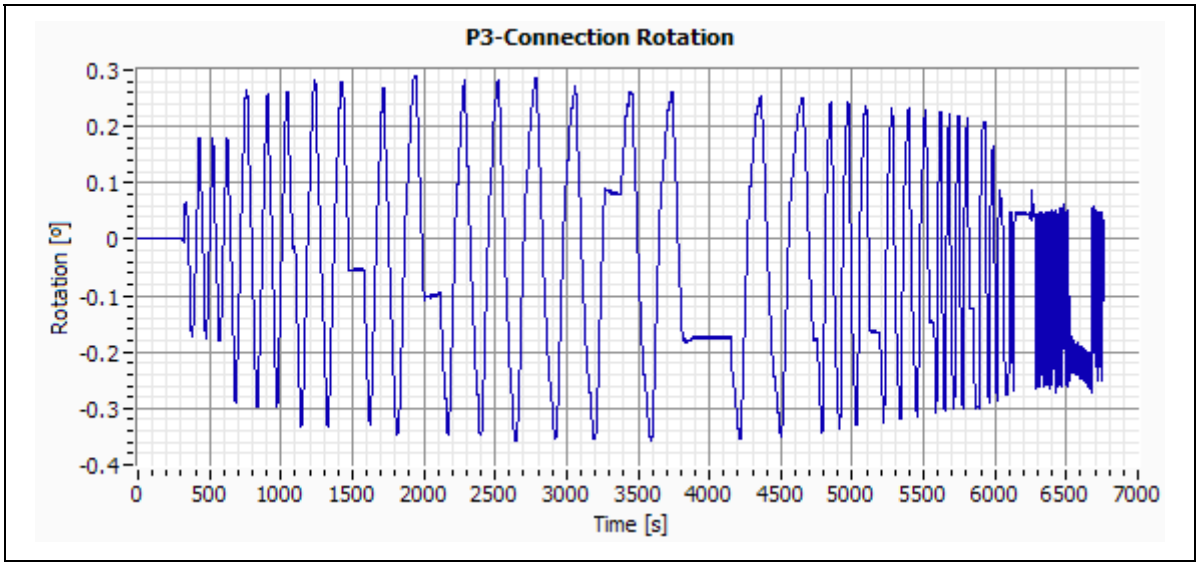

Figure F-9: Specimen P3 – Connection Rotation.

F.4 Specimen P4

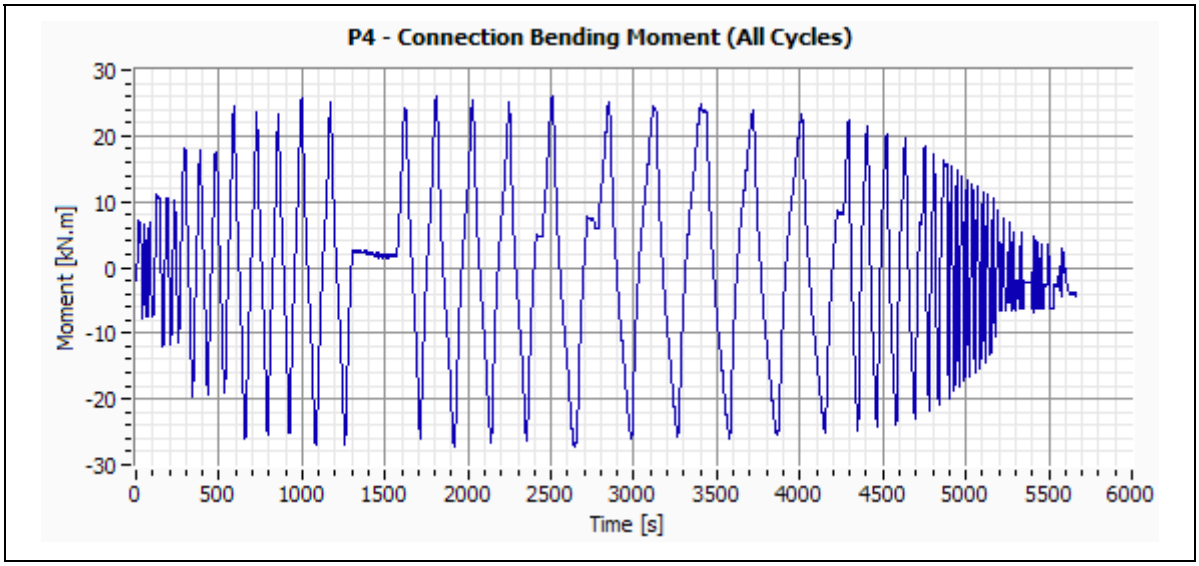

Figure F-10: Specimen P4 - Connection Bending Moment.

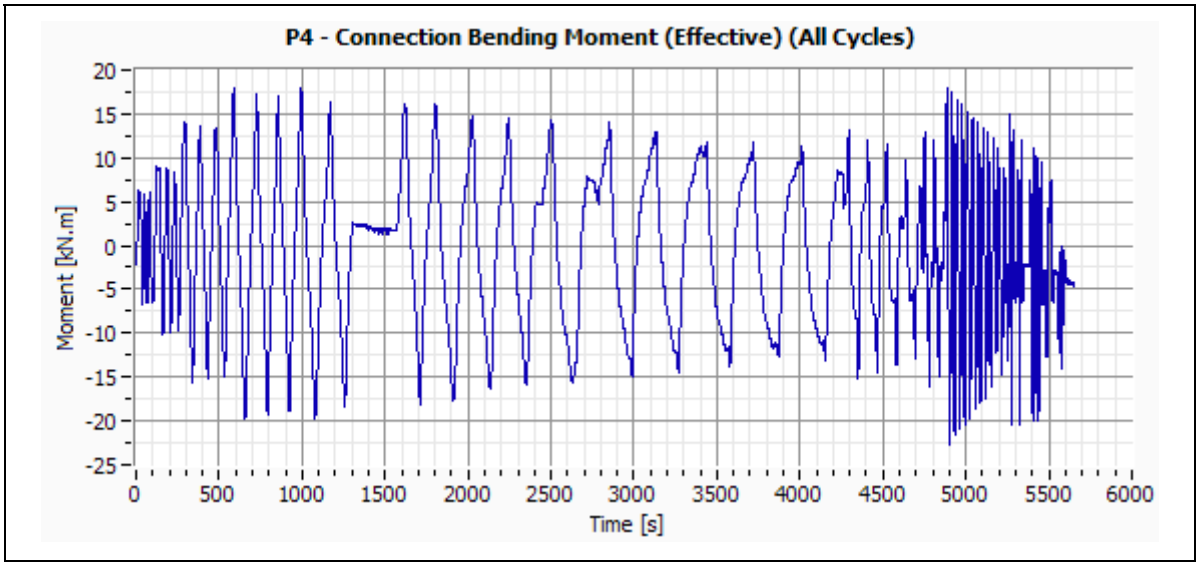

Figure F-11: Specimen P4 - Connection Bending Moment (Effective).

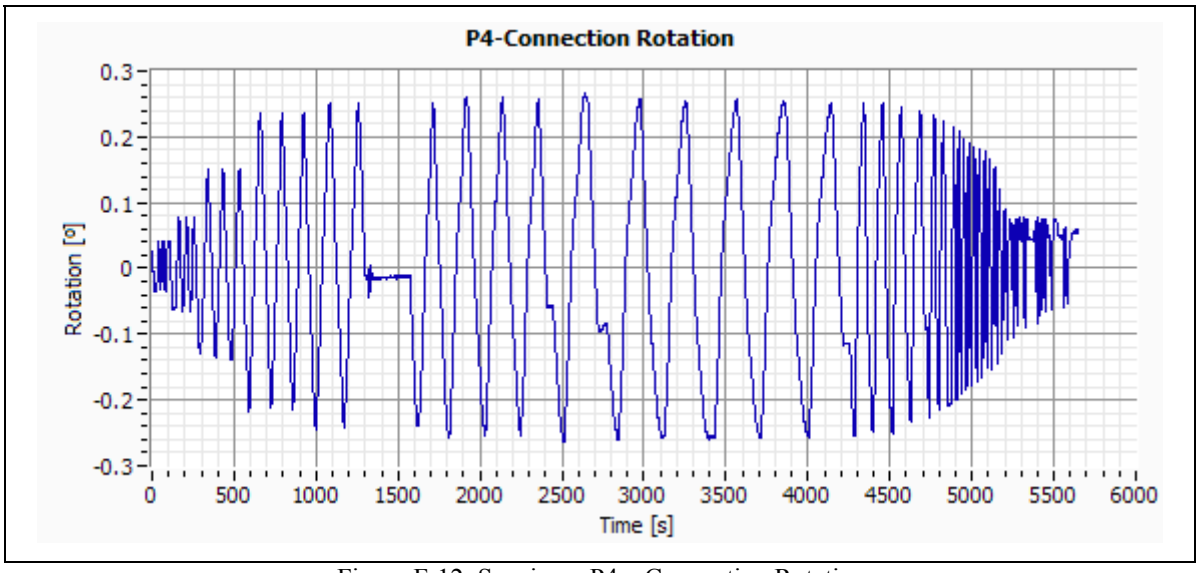

Figure F-12: Specimen P4 – Connection Rotation.

F.5 Specimen V1

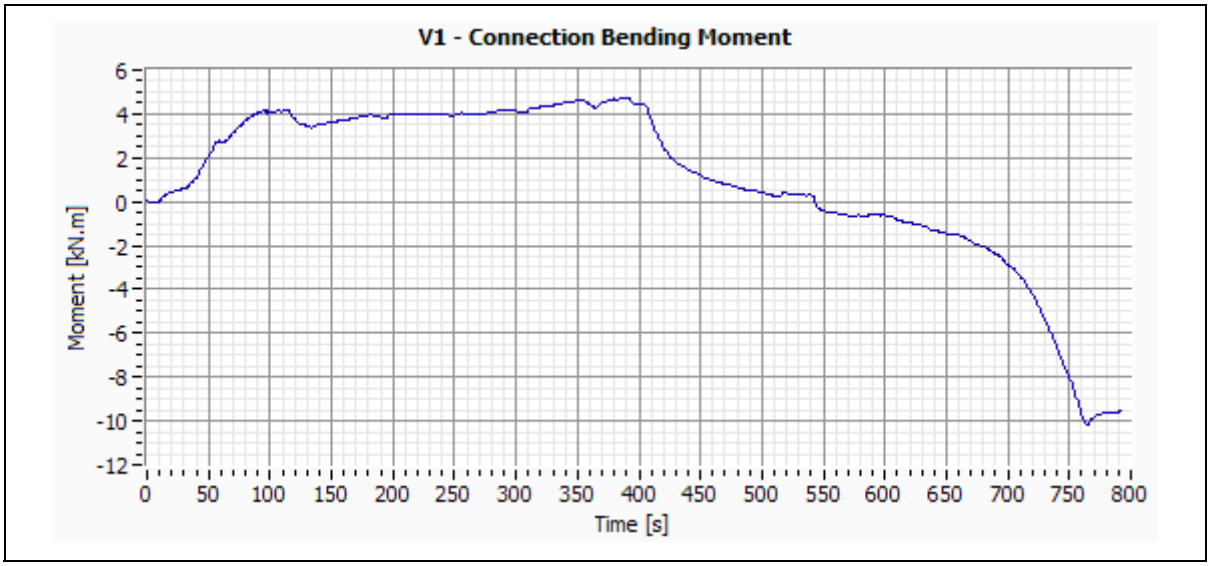

Figure F-13: Specimen V1 - Connection Bending Moment.

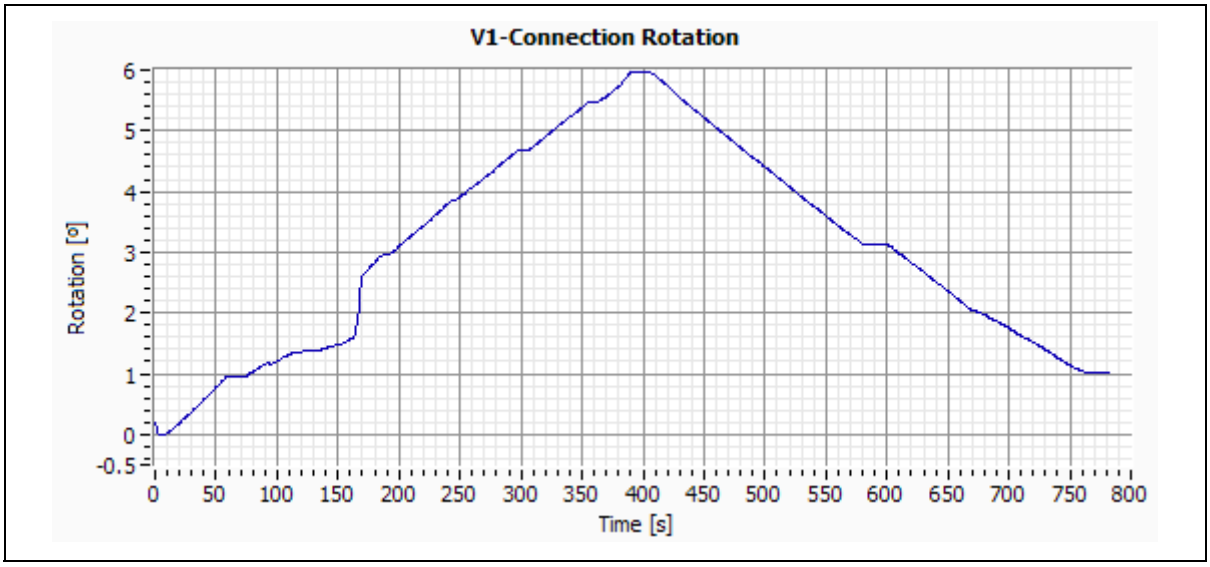

Figure F-14: Specimen V1 – Connection Rotation.

F.6 Specimen V2

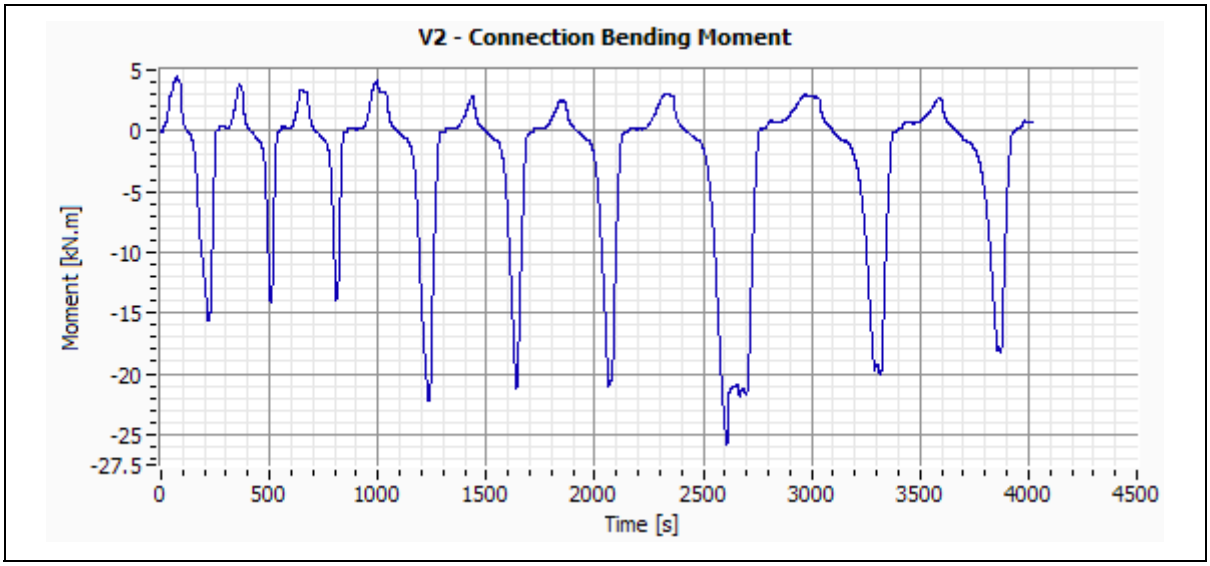

Figure F-15: Specimen V2 - Connection Bending Moment.

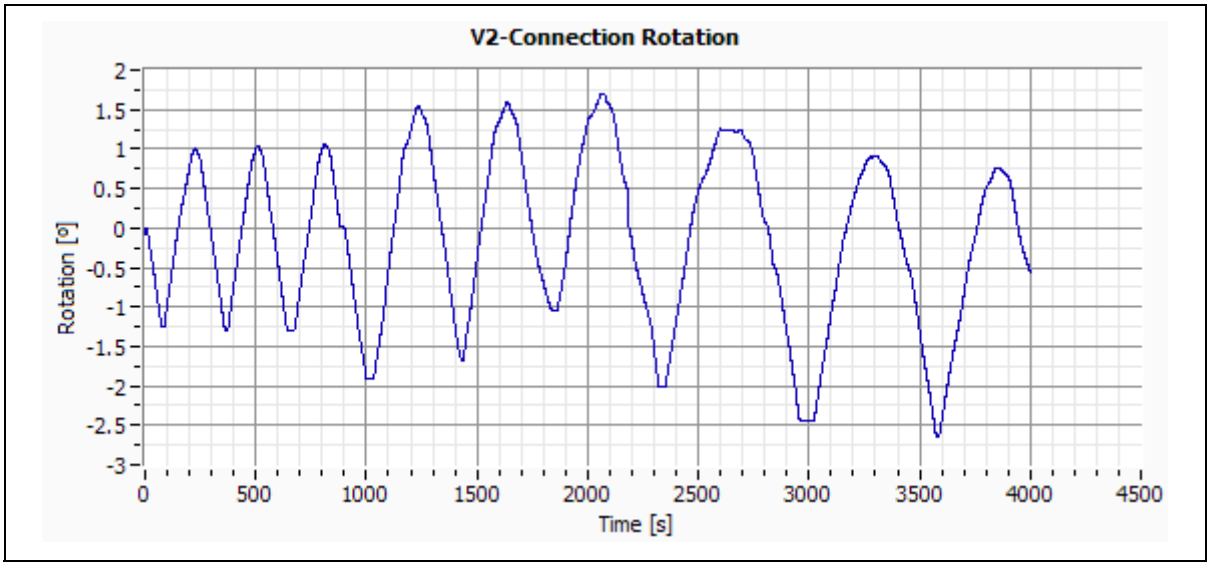

Figure F-16: Specimen V2 – Connection Rotation.

F.7 Specimen V3

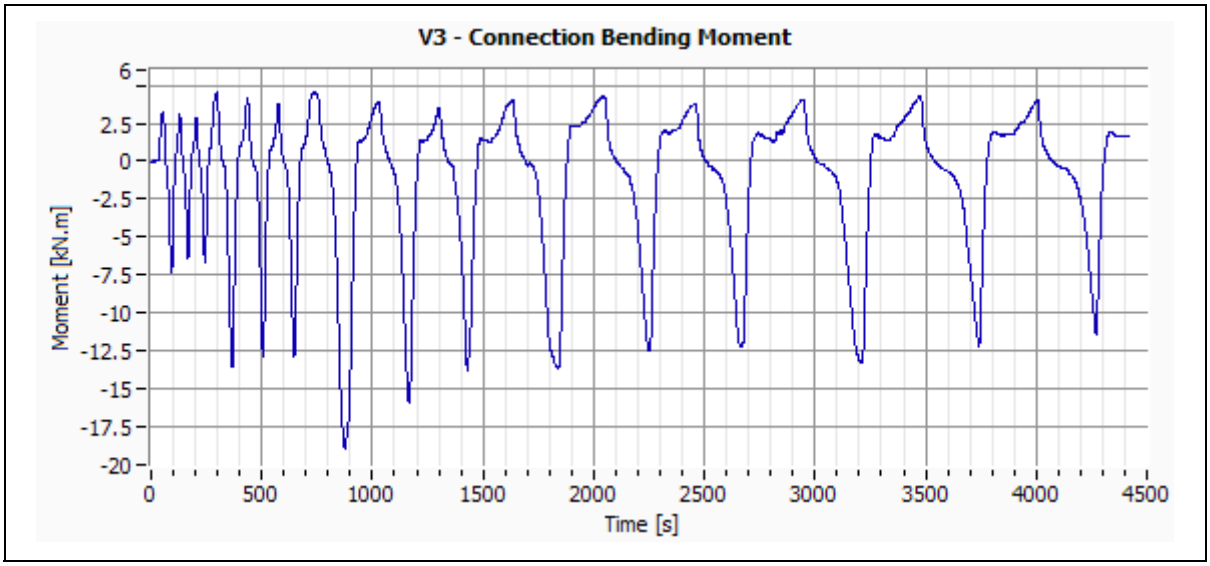

Figure F-17: Specimen V3 - Connection Bending Moment.

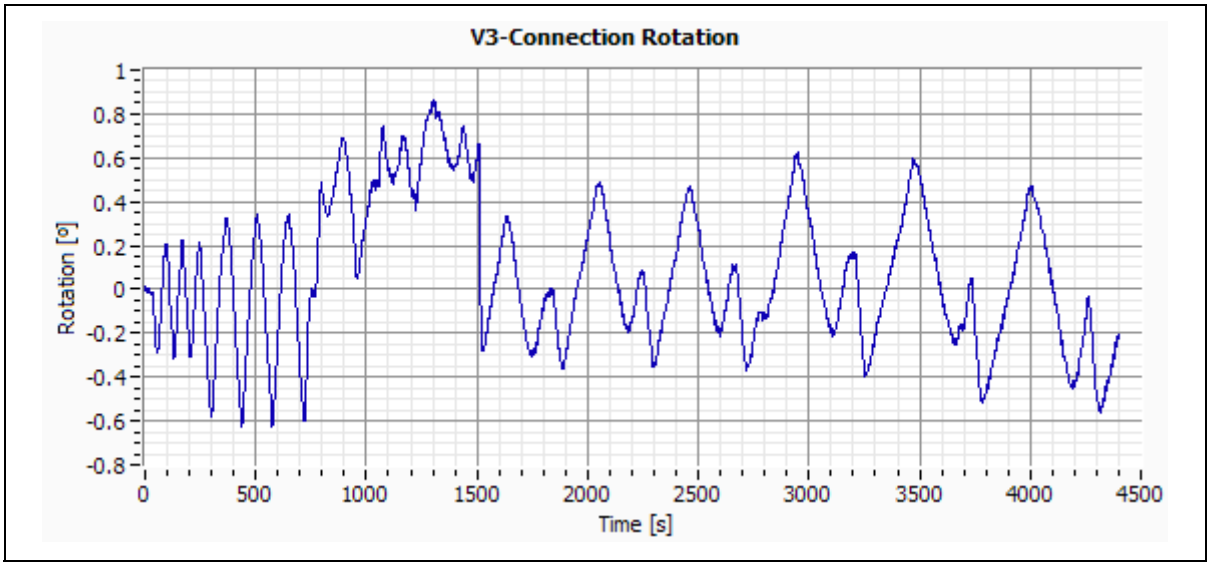

Figure F-18: Specimen V3 – Connection Rotation.

F.8 Specimen V4

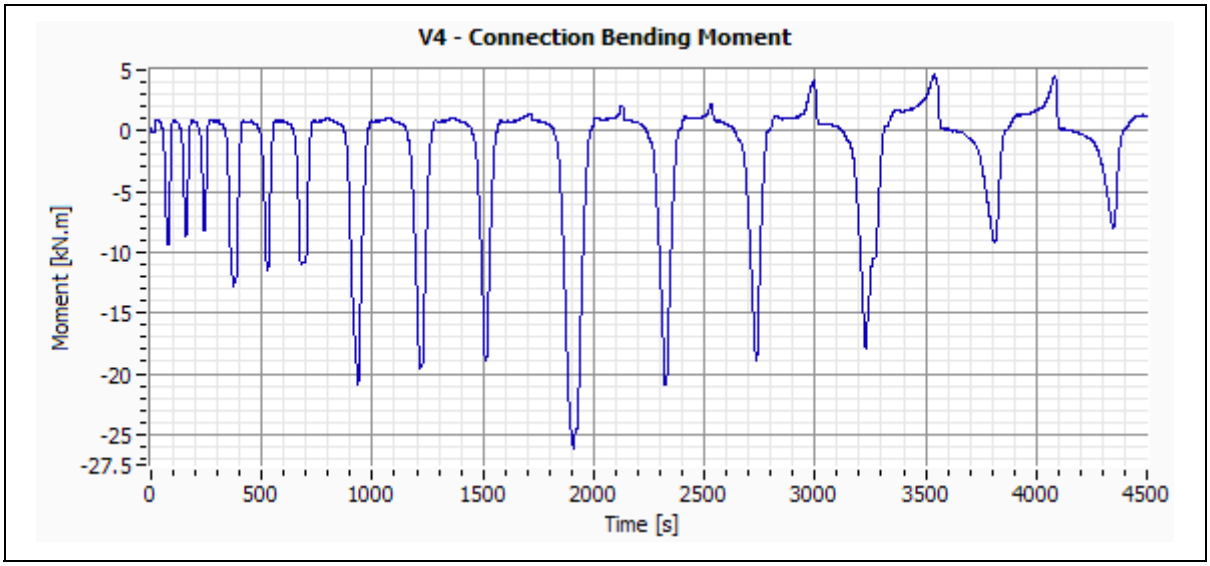

Figure F-19: Specimen V4 - Connection Bending Moment.

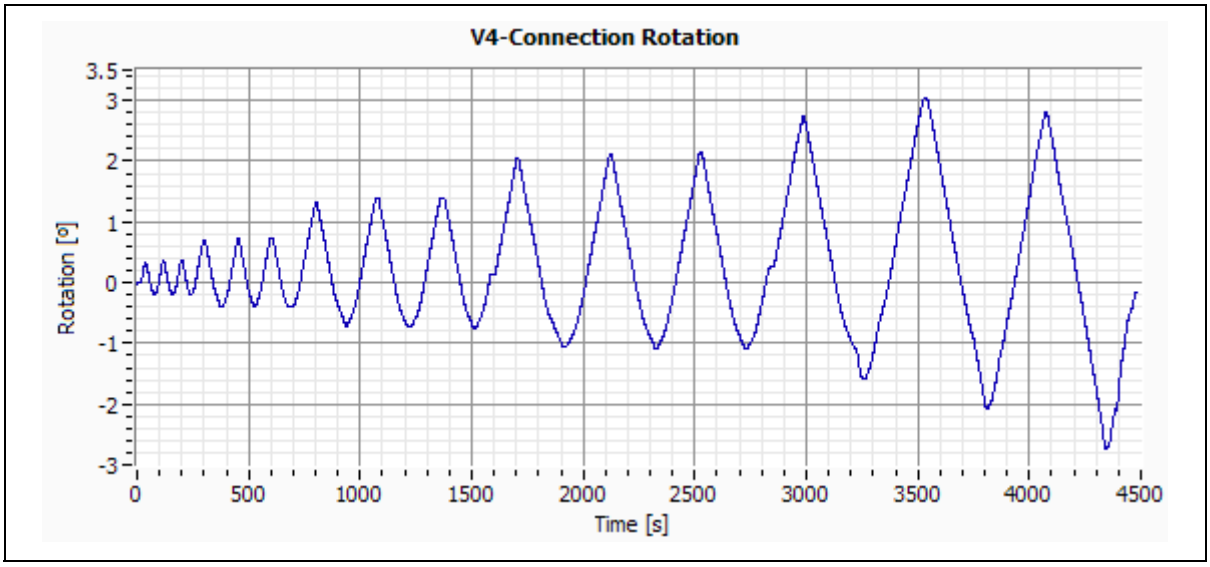

Figure F-20: Specimen V4 – Connection Rotation.

F.9 Specimen V5

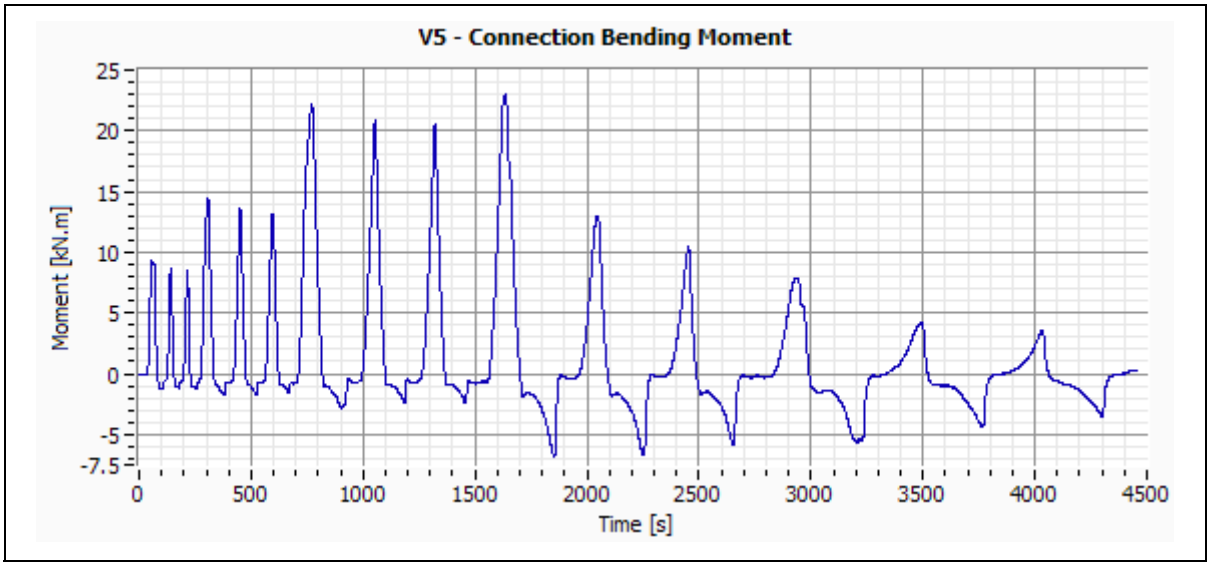

Figure F-21: Specimen V5 - Connection Bending Moment.

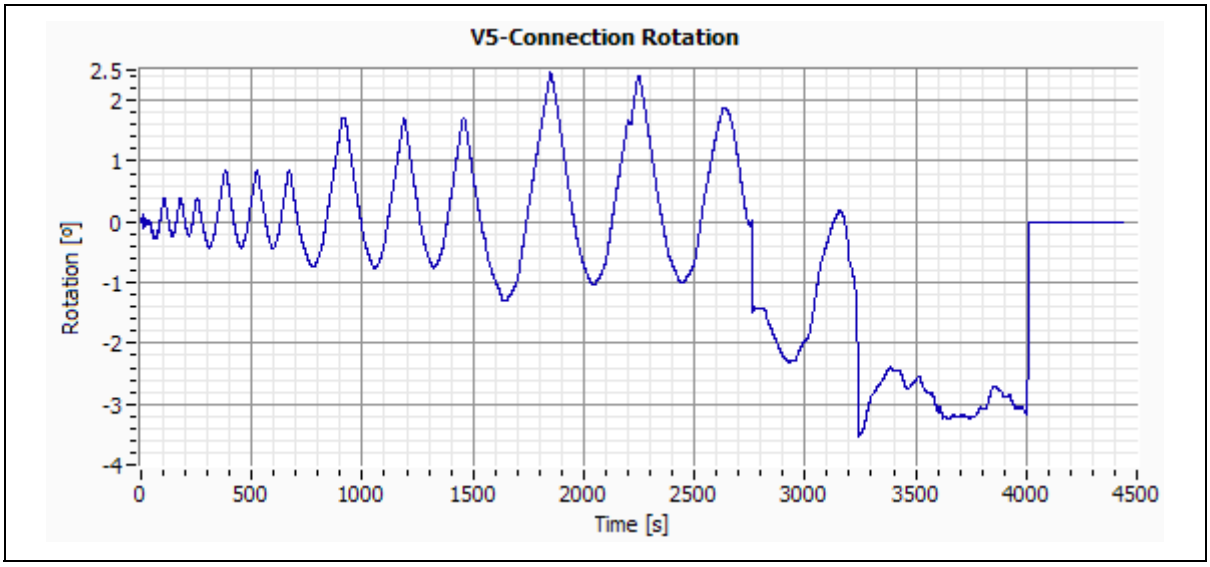

Figure F-22: Specimen V5 – Connection Rotation.

F.10 Specimen VL1

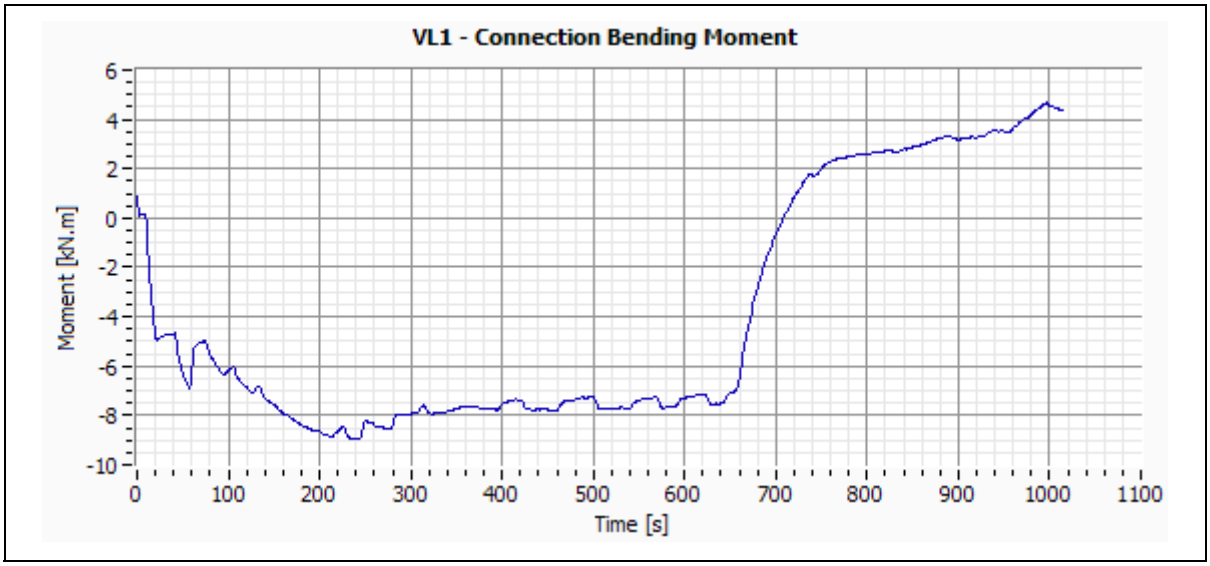

Figure F-23: Specimen VL1 - Connection Bending Moment.

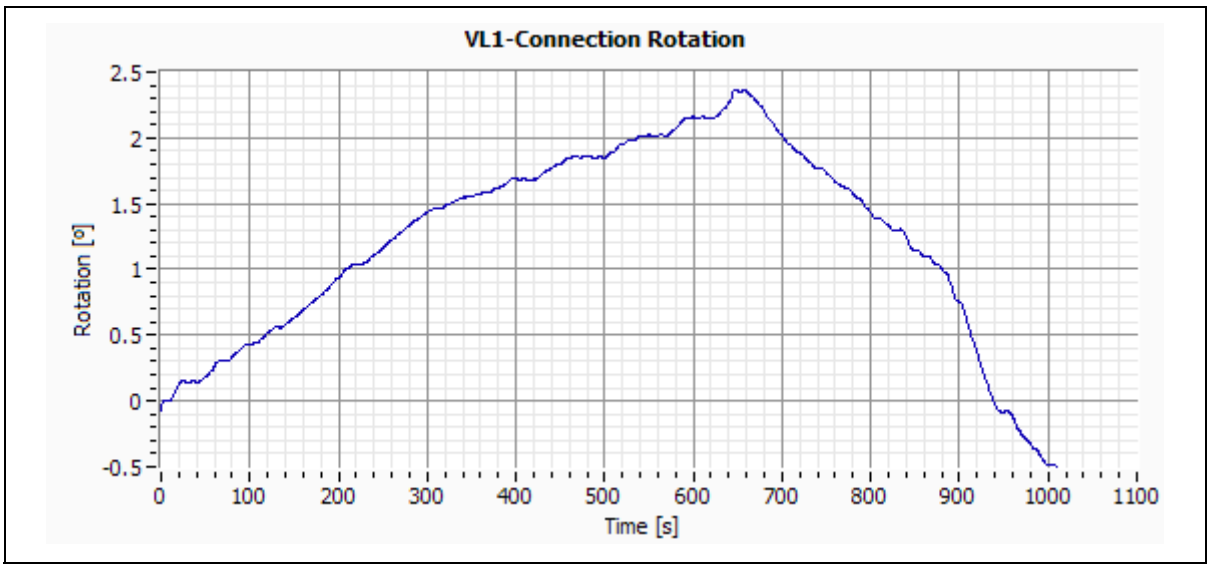

Figure F-24: Specimen VL1 – Connection Rotation.

F.11 Specimen VL2

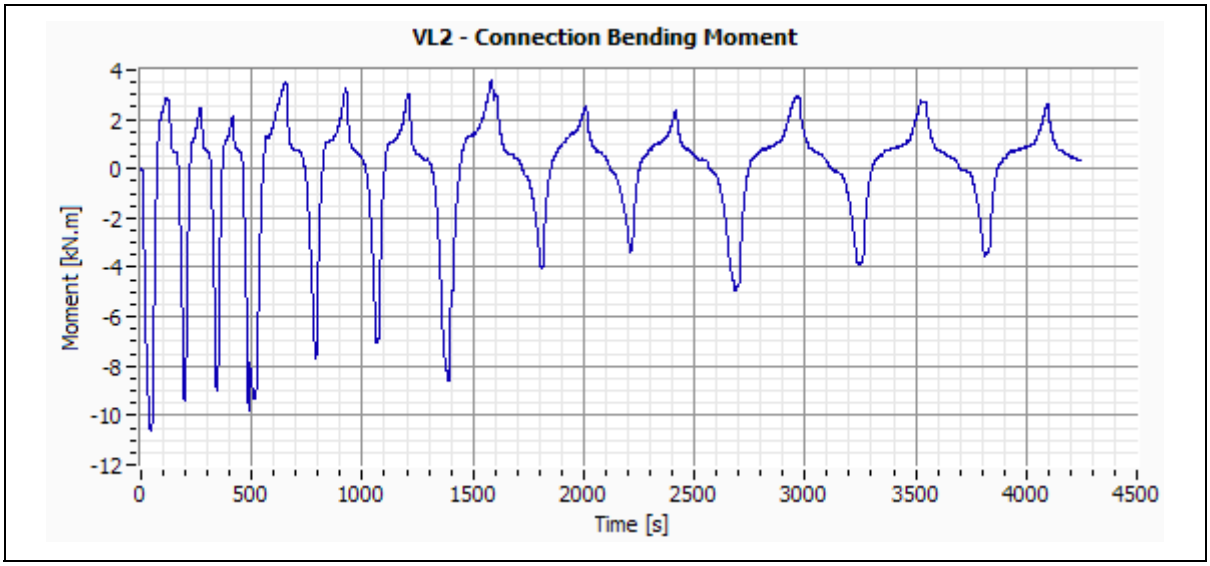

Figure F-25: Specimen VL2 - Connection Bending Moment.

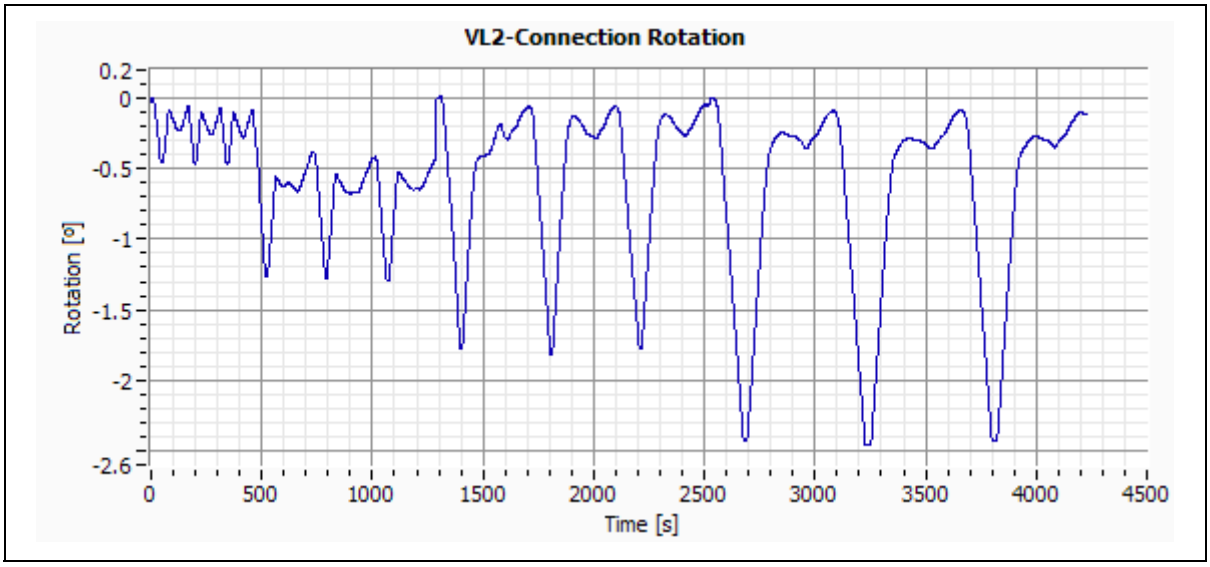

Figure F-26: Specimen VL2 – Connection Rotation.

F.12 Specimen VL3

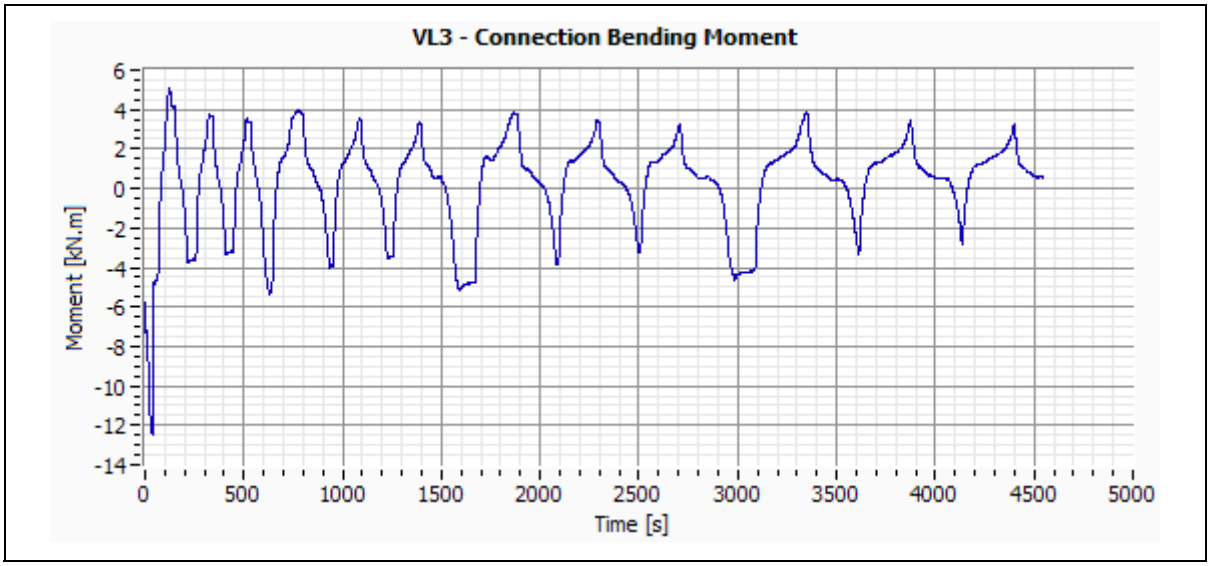

Figure F-27: Specimen VL3 - Connection Bending Moment.

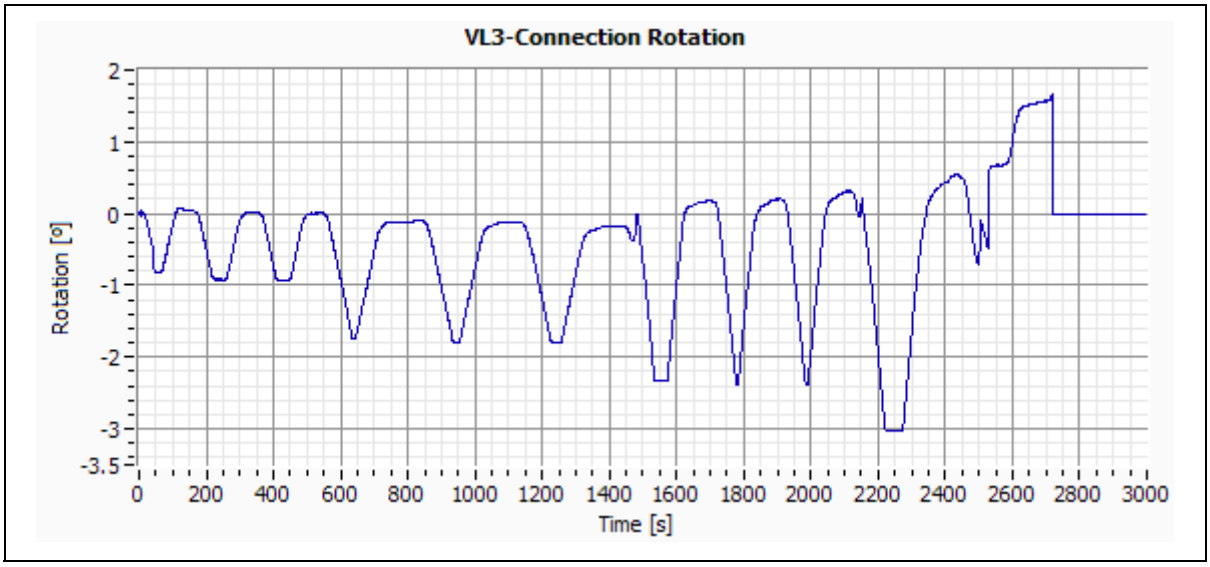

Figure F-28: Specimen VL3 – Connection Rotation.

F.13 Specimen VL4

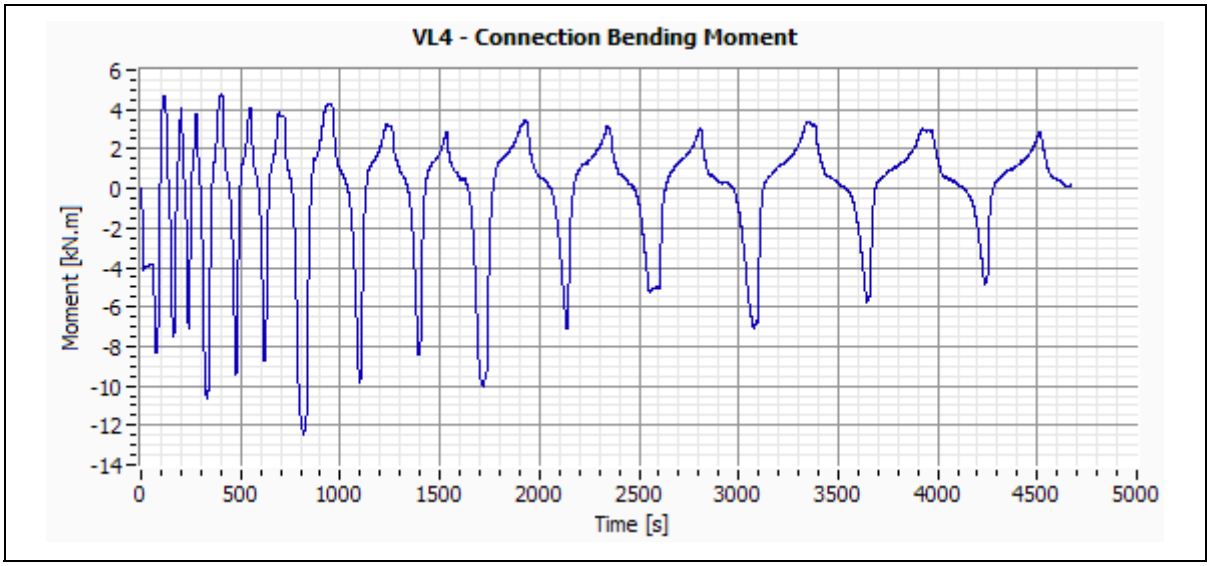

Figure F-29: Specimen VL4 - Connection Bending Moment.

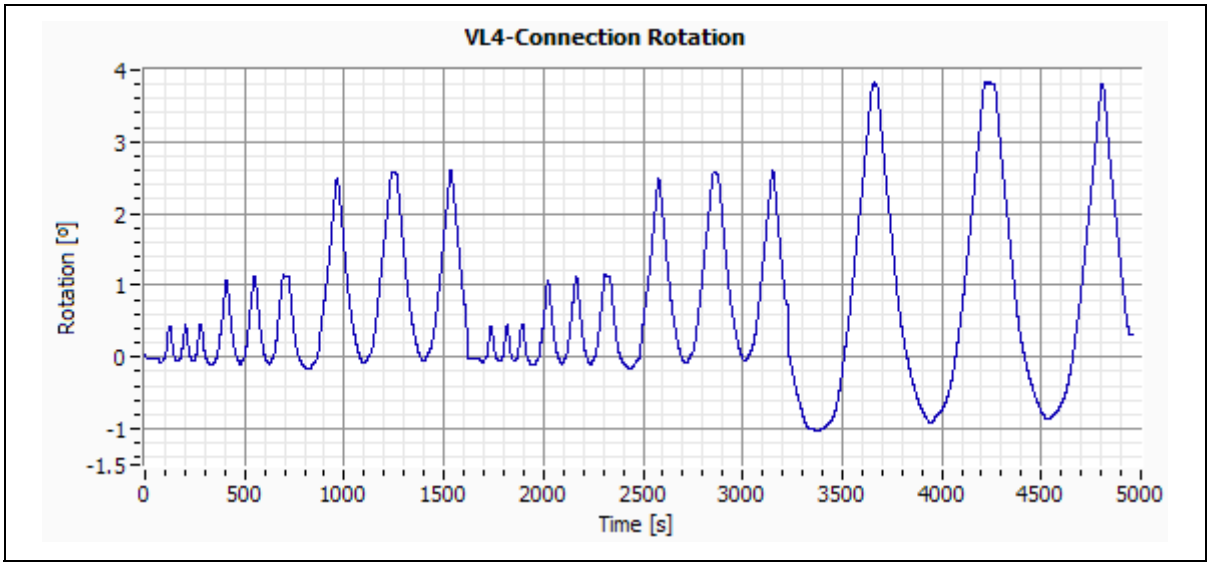

Figure F-30: Specimen VL4 – Connection Rotation.

F.14 Specimen VL5

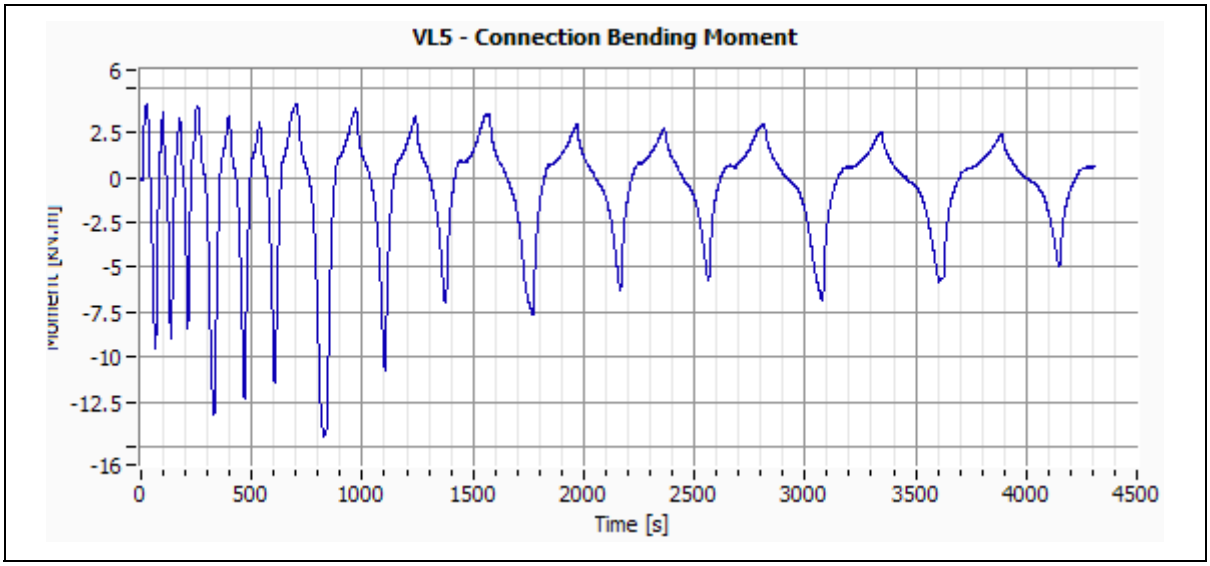

Figure F-31: Specimen VL5 - Connection Bending Moment.

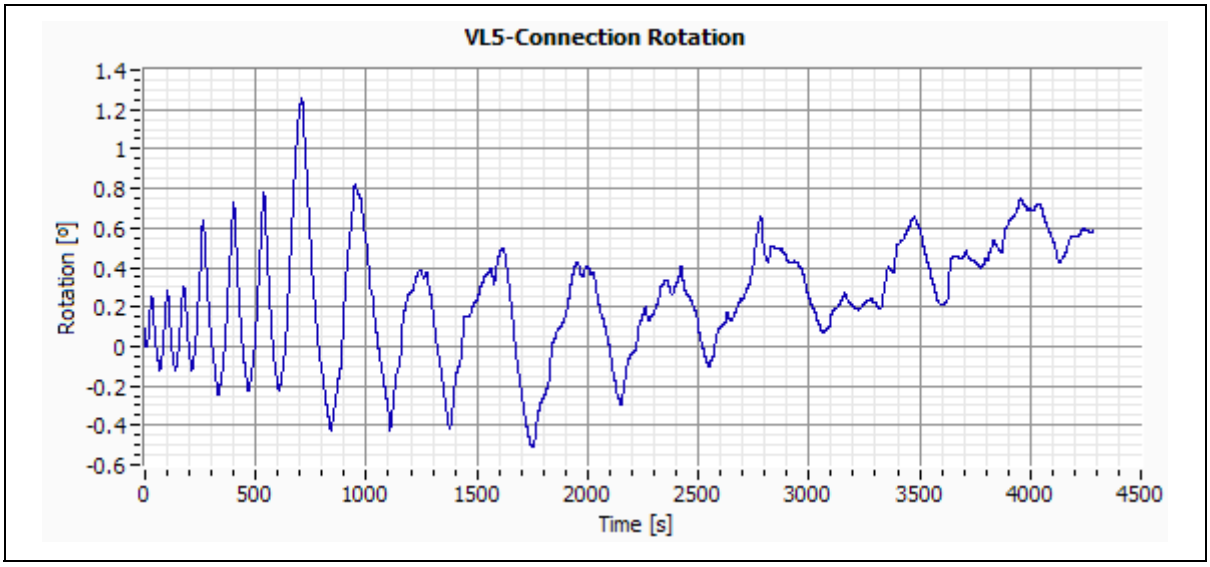

Figure F-32: Specimen VL5 – Connection Rotation.

ANNEX G LOCAL DISPLACEMENTS

Contents:

List of Figures:

G.1 Specimen P1

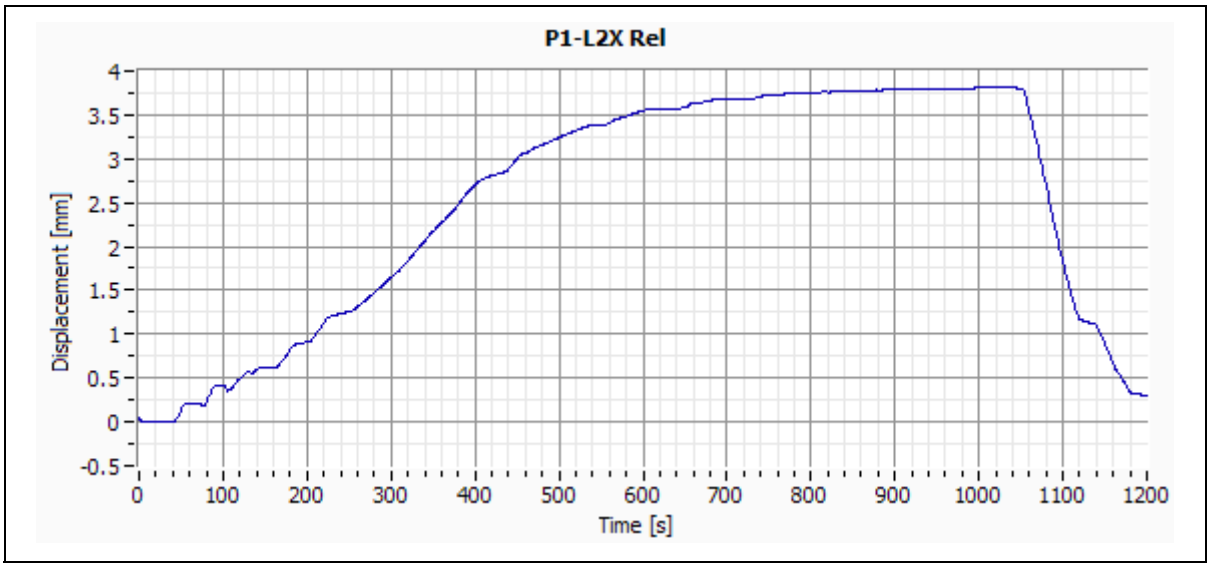

Figure G-1:– Specimen P1 – Foundation Relative Displacement – X Direction.

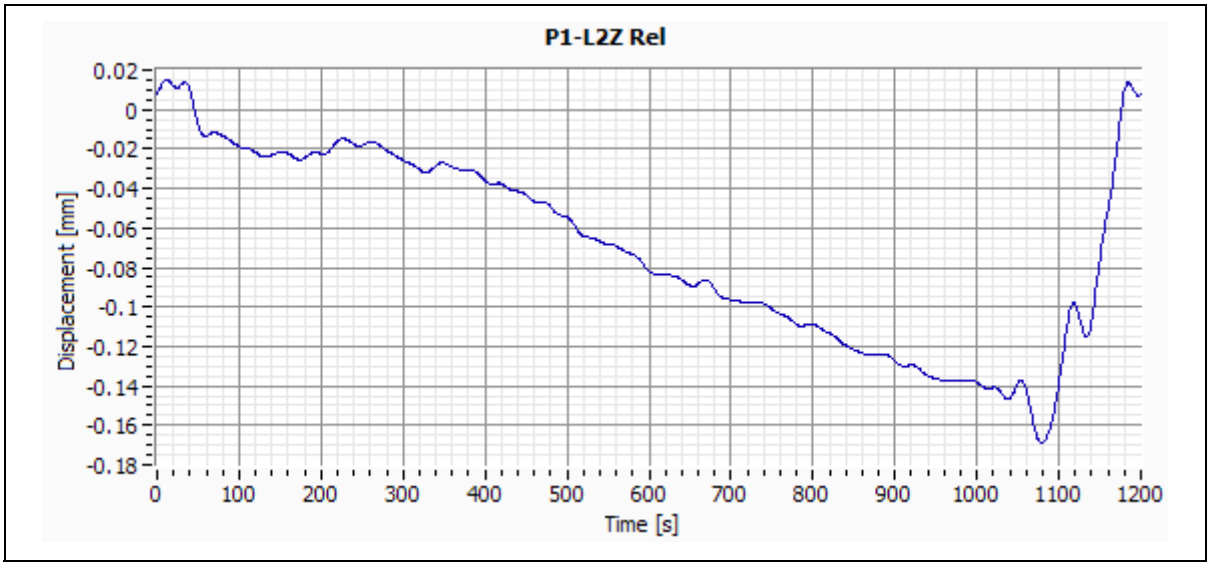

Figure G-2:– Specimen P1 – Foundation Relative Displacement – Z Direction.

G.2 Specimen P2

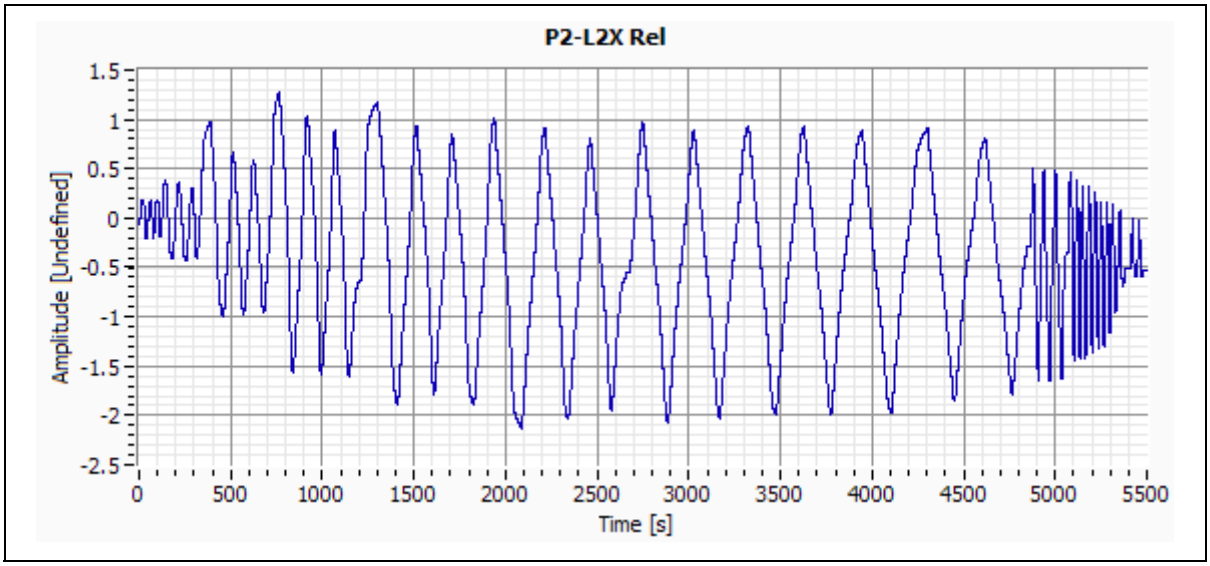

Figure G-3:– Specimen P2 – Foundation Relative Displacement – X Direction.

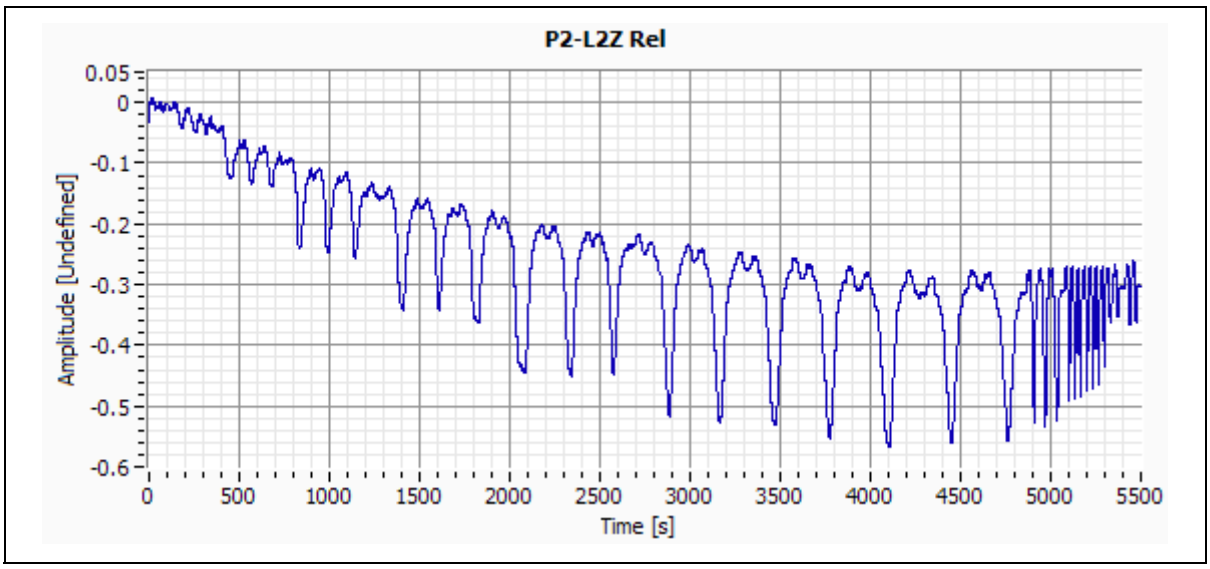

Figure G-4:– Specimen P2 – Foundation Relative Displacement – Z Direction.

G.3 Specimen P3

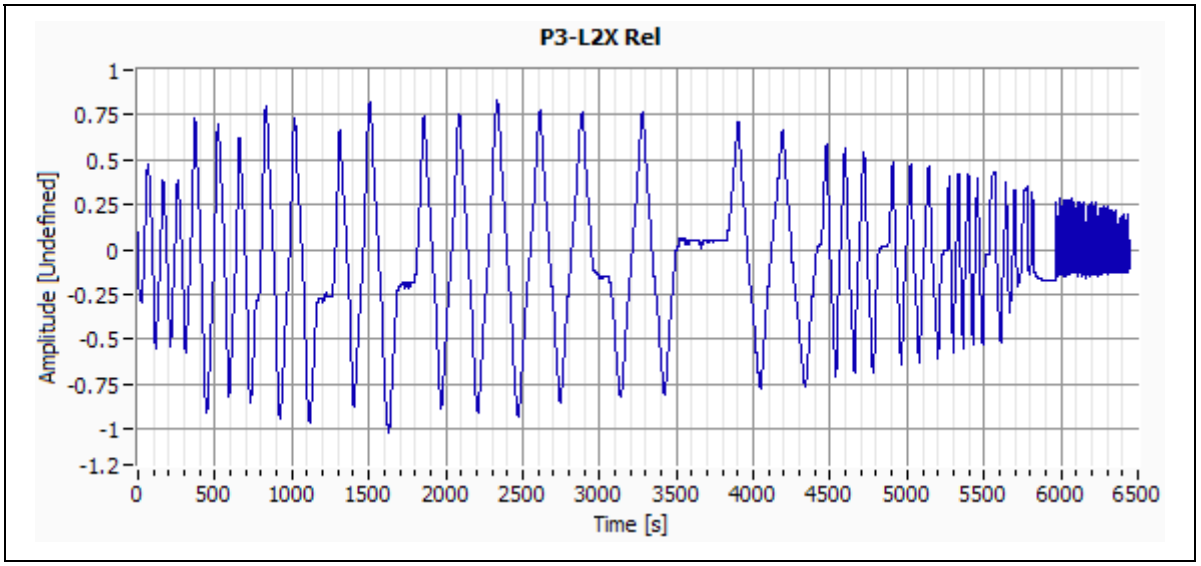

Figure G-5:– Specimen P3 – Foundation Relative Displacement – X Direction.

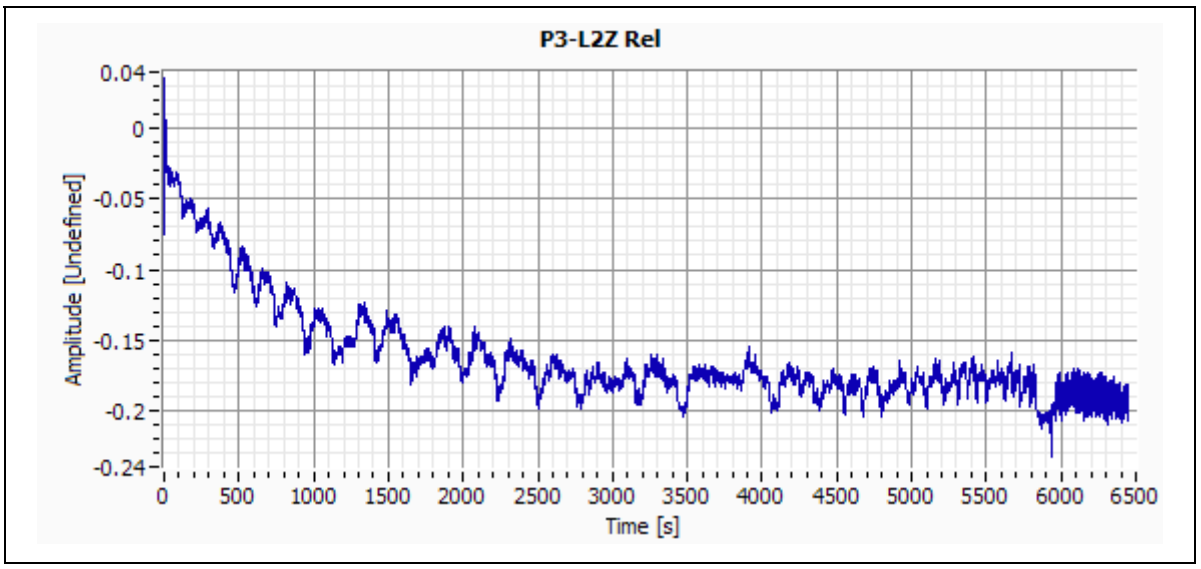

Figure G-6:– Specimen P3 – Foundation Relative Displacement – Z Direction.

G.4 Specimen P4

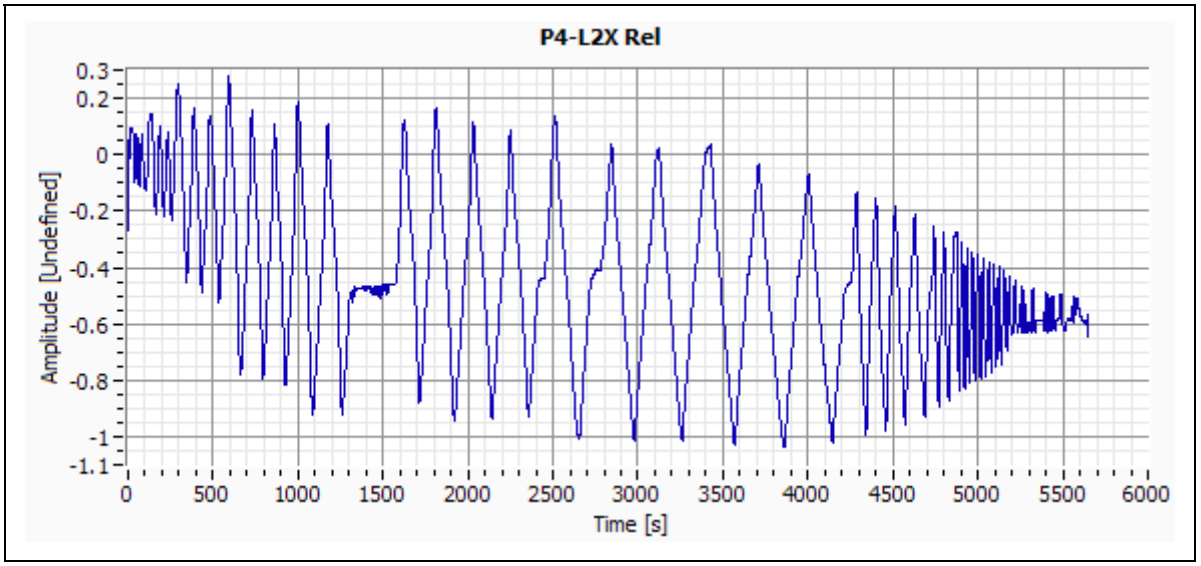

Figure G-7:– Specimen P4 – Foundation Relative Displacement – X Direction.

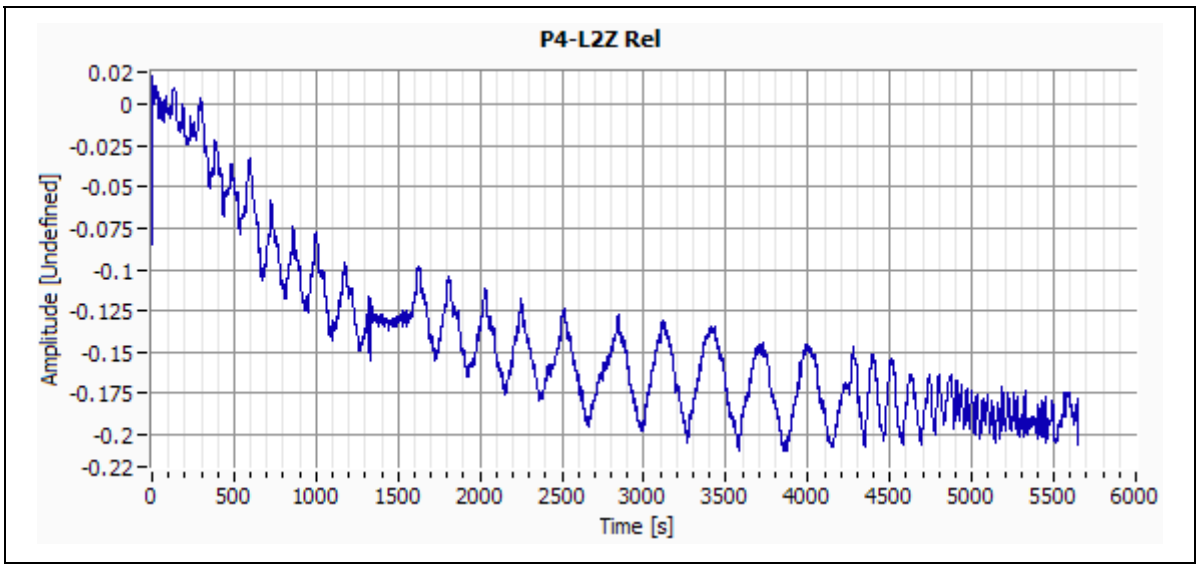

Figure G-8:– Specimen P4 – Foundation Relative Displacement – Z Direction.

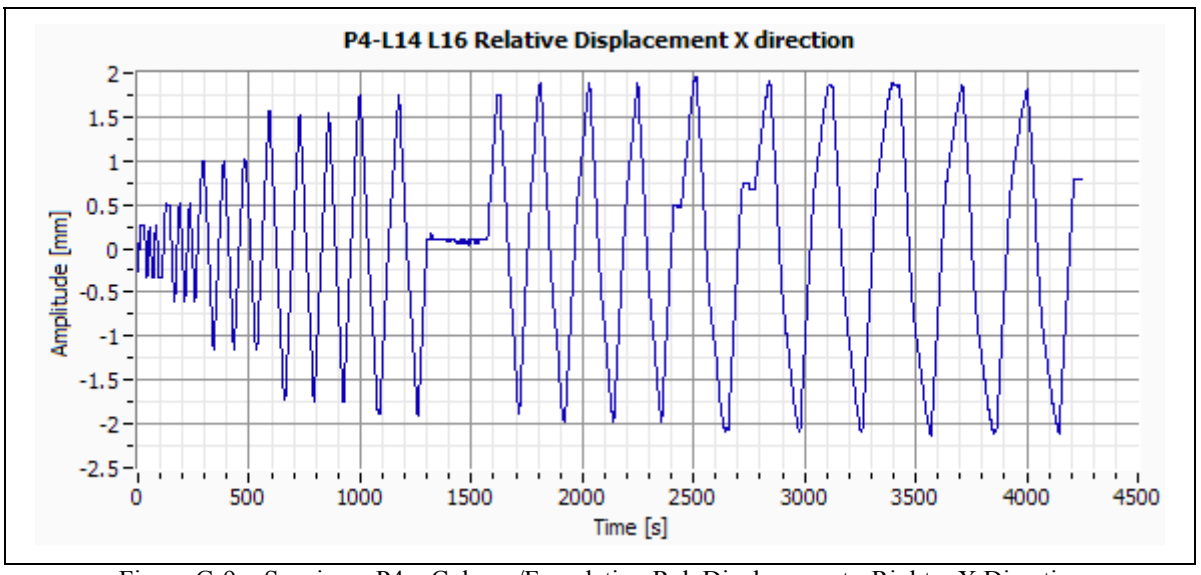

Figure G-9:– Specimen P4 – Column/Foundation Rel. Displacement - Right – X Direction.

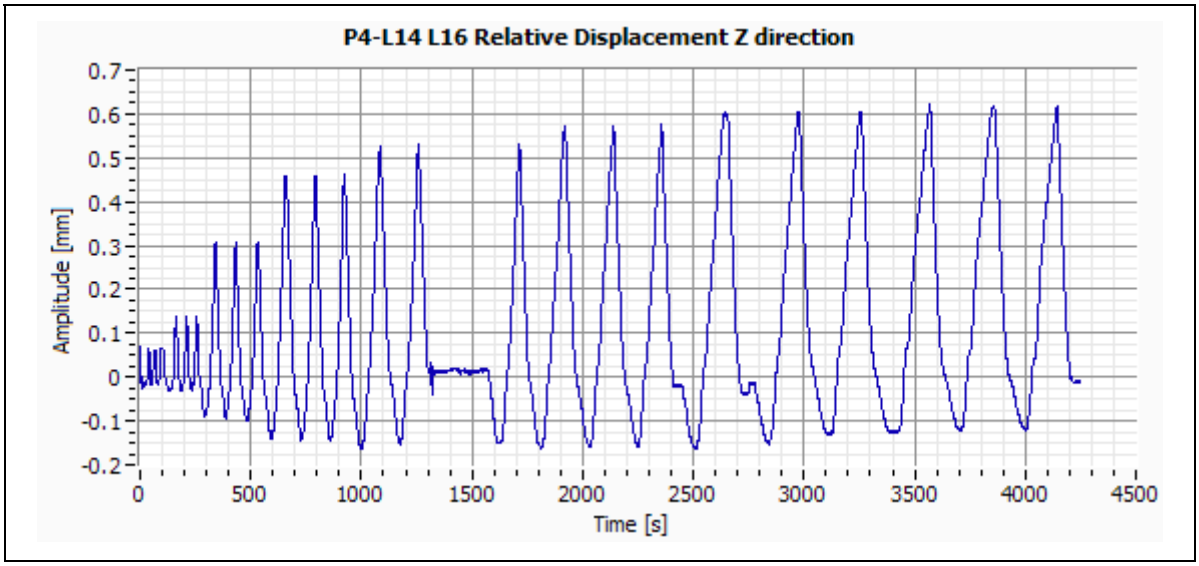

Figure G-10:– Specimen P4 – Column/Foundation Rel. Displacement - Right – Z Direction.

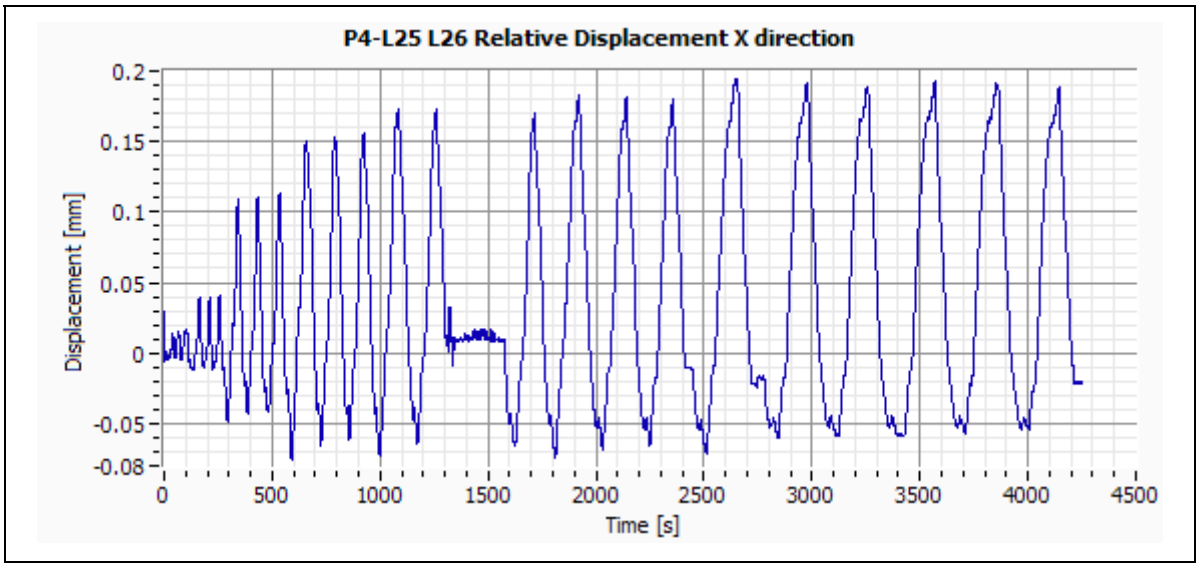

Figure G-11:– Specimen P4 – Column/Foundation Rel. Displacement - Left – X Direction.

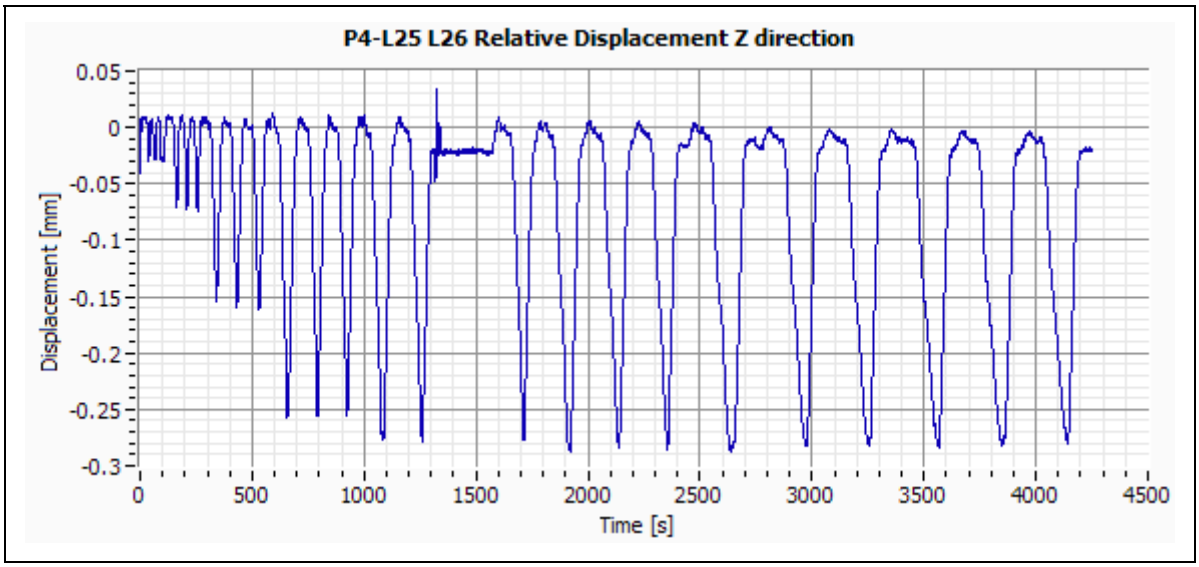

Figure G-12:– Specimen P4 – Column/Foundation Rel. Displacement - Left – Z Direction.

G.5 Specimen V1

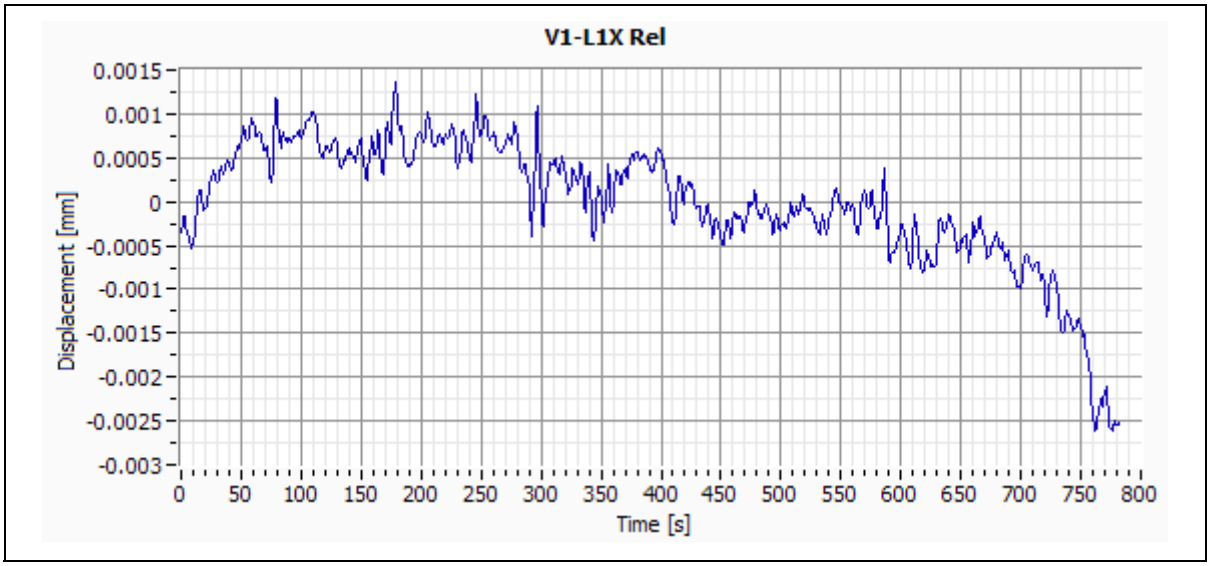

Figure G-13:– Specimen V1 – Column Central Point Relative Displacement – X Direction.

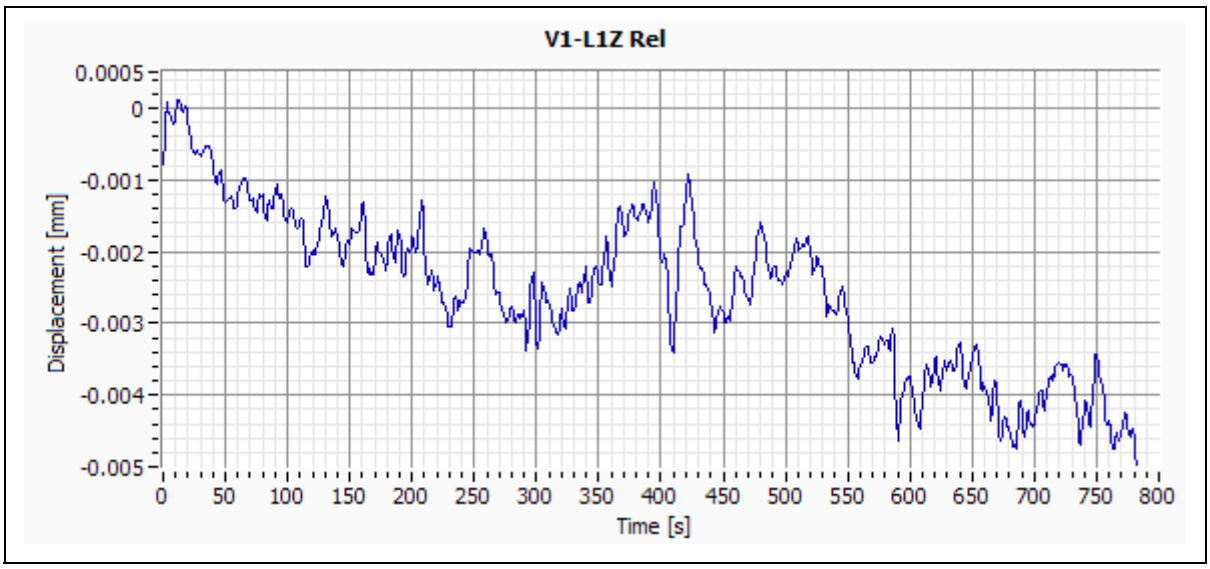

Figure G-14:– Specimen V1 – Column Central Point Relative Displacement – Z Direction.

G.6 Specimen V2

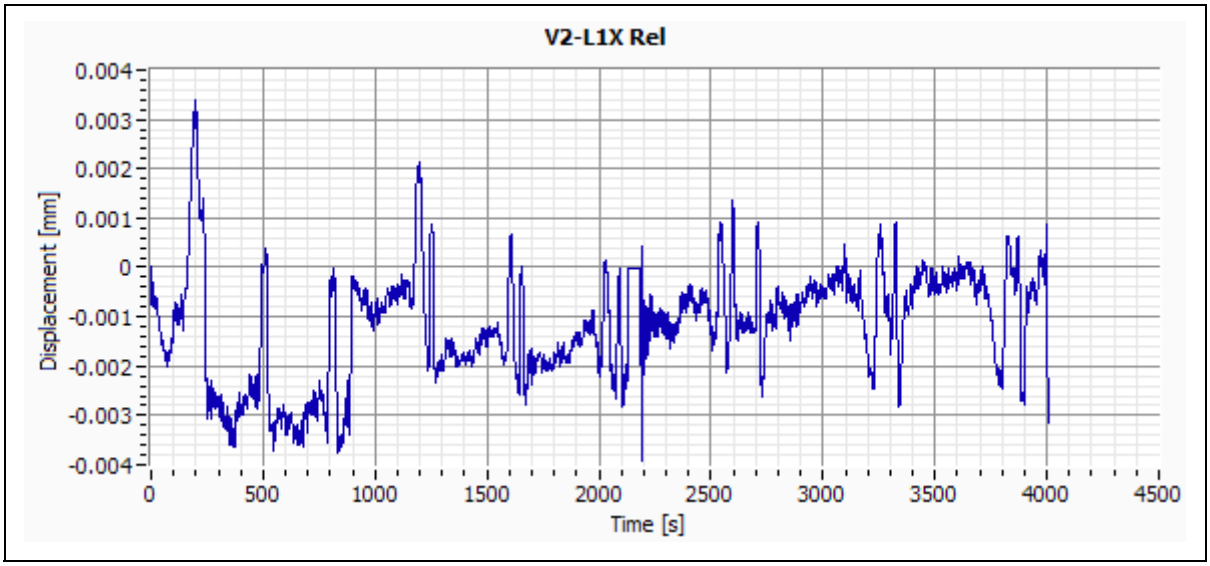

Figure G-15:– Specimen V2 – Column Central Point Relative Displacement – X Direction.

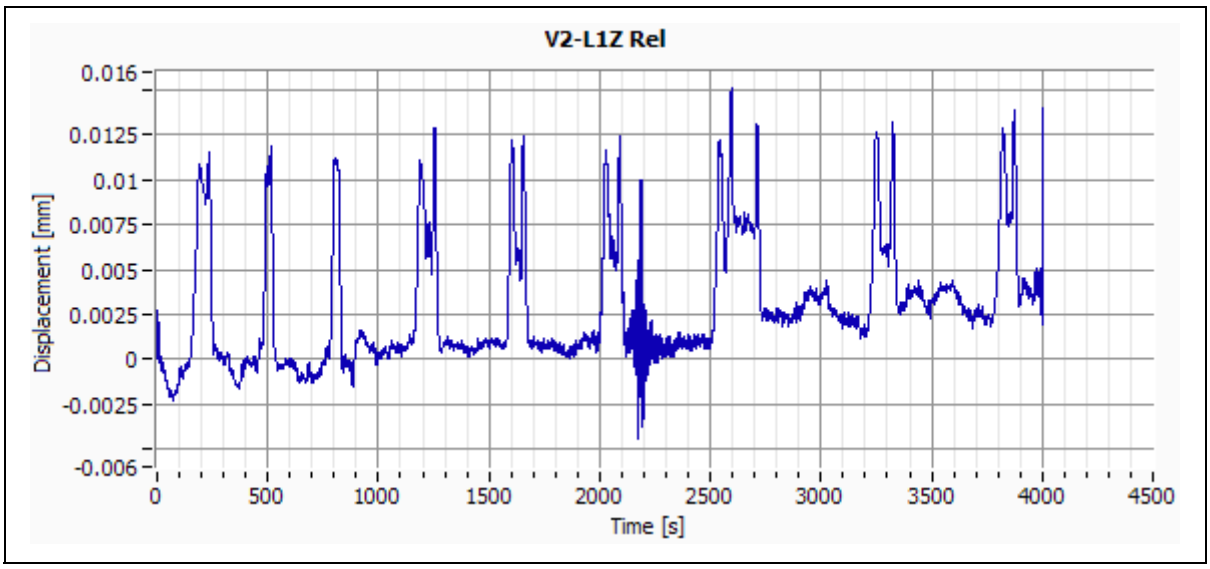

Figure G-16:– Specimen V2 – Column Central Point Relative Displacement – Z Direction.

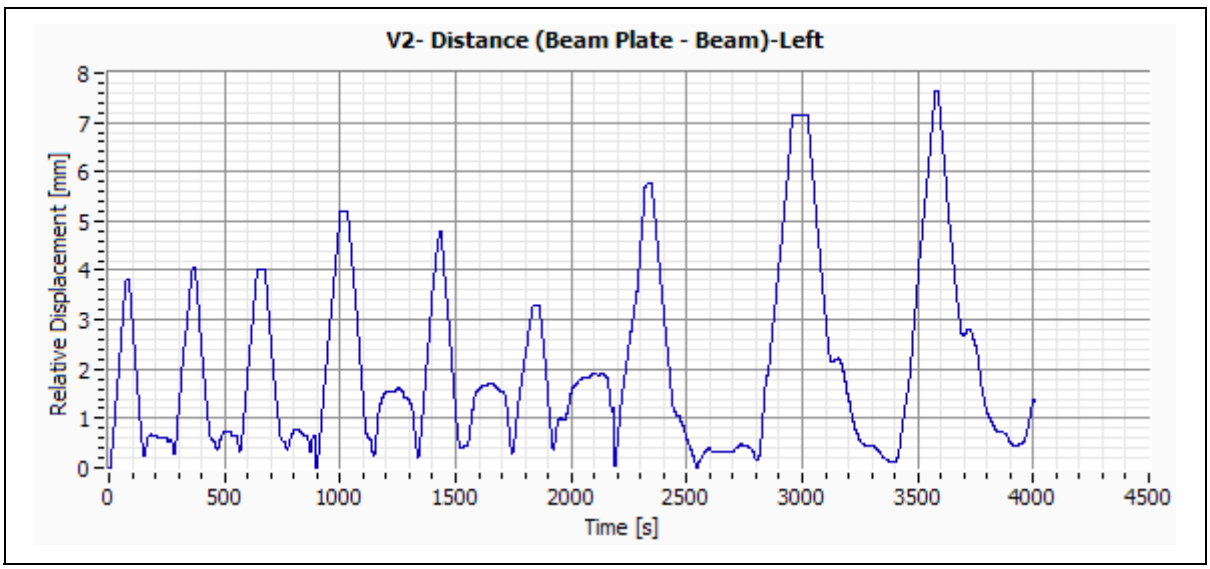

Figure G-17:– Specimen V2 – Distance (Beam Plate – Beam) – Left.

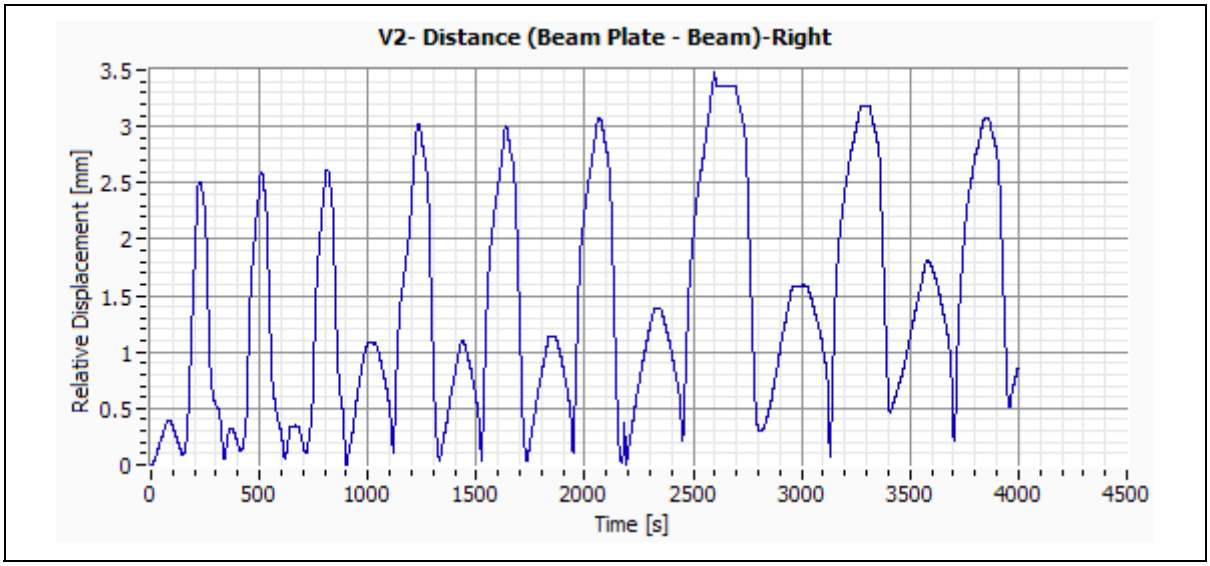

Figure G-18:– Specimen V2 – Distance (Beam Plate – Beam) – Right.

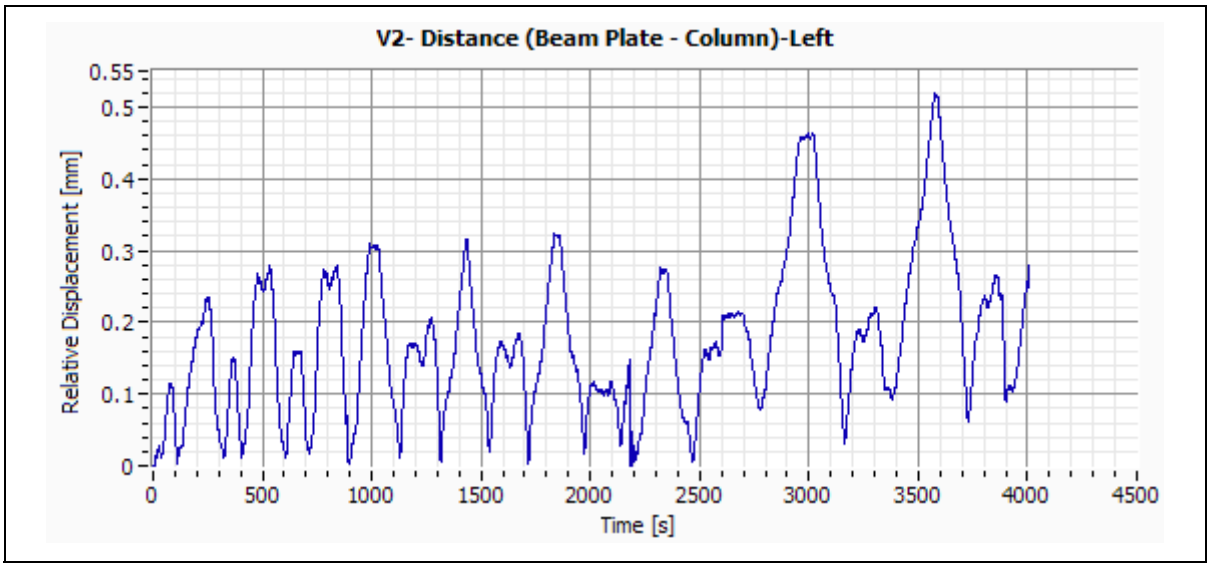

Figure G-19:– Specimen V2 – Distance (Beam Plate – Column) – Left.

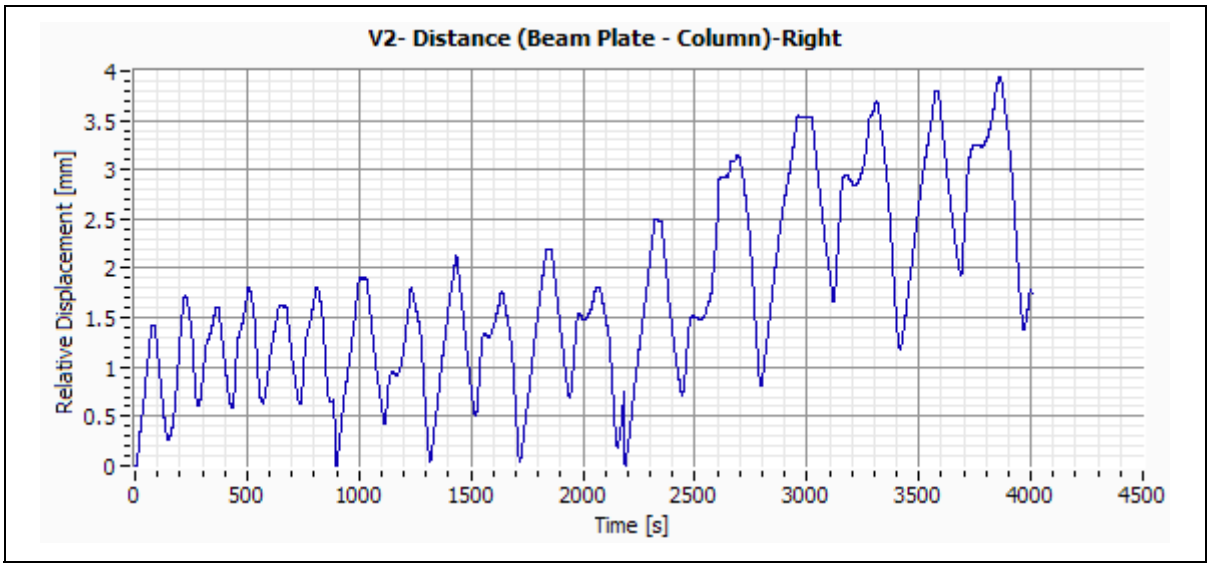

Figure G-20:– Specimen V2 – Distance (Beam Plate – Column) – Right.

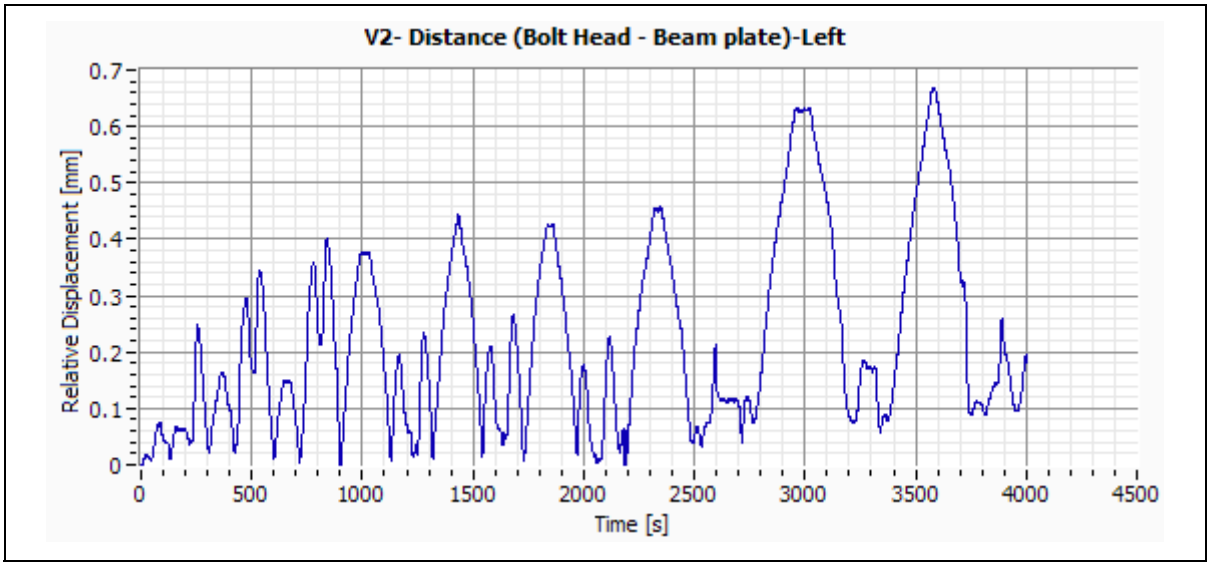

Figure G-21:– Specimen V2 – Distance (Bolt Head – Beam Plate) – Left.

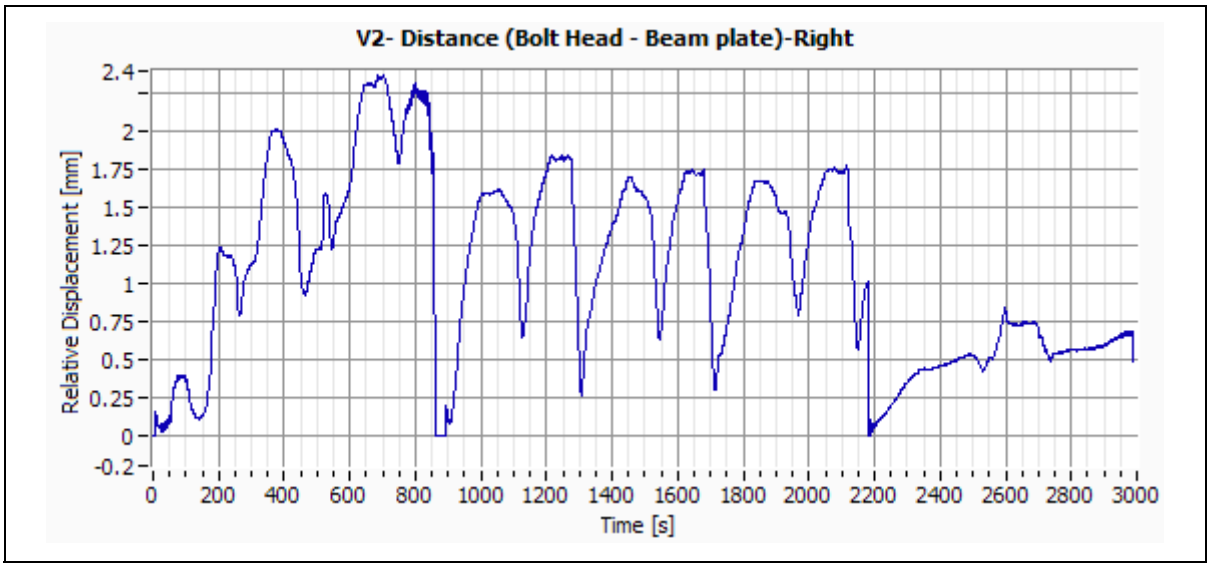

Figure G-22:– Specimen V2 – Distance (Bolt Head – Beam Plate) – Right.

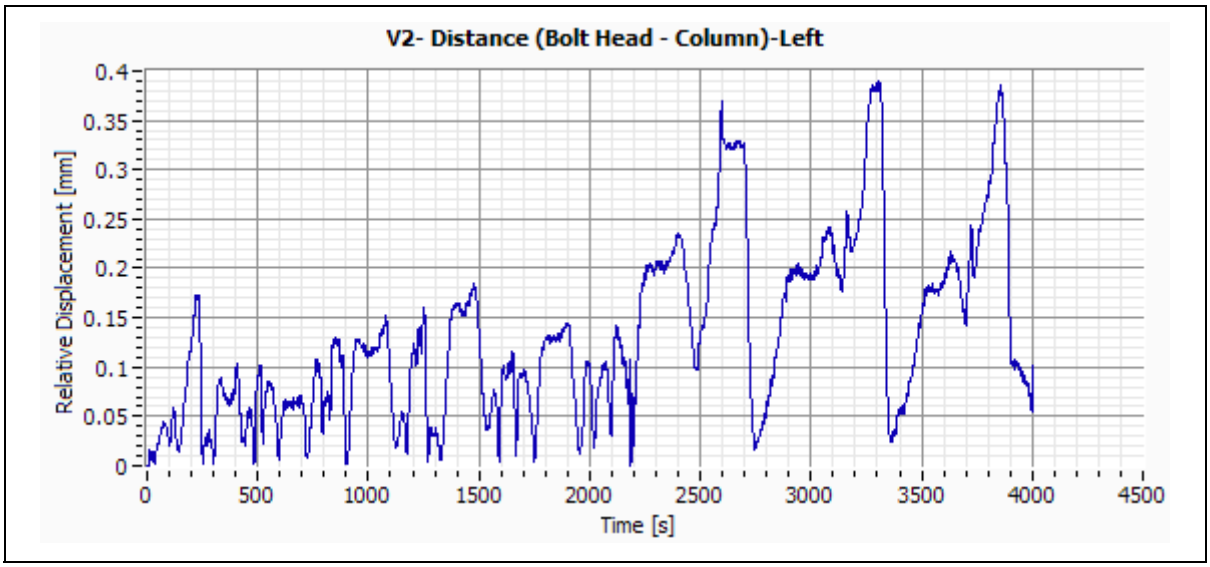

Figure G-23:– Specimen V2 – Distance (Bolt Head – Column) – Left.

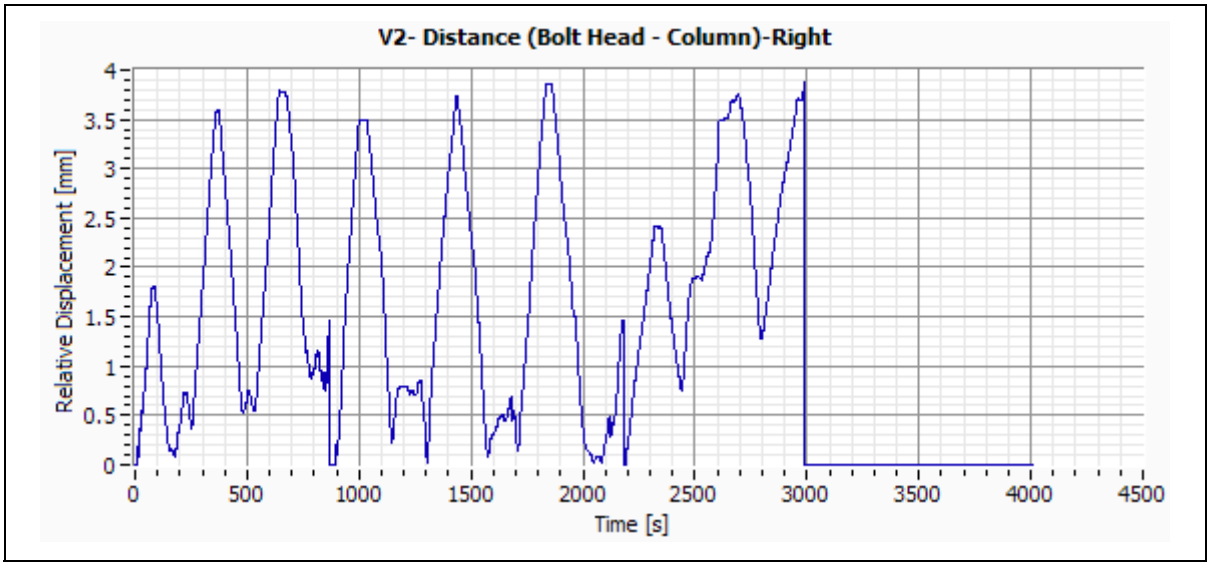

Figure G-24:– Specimen V2 – Distance (Bolt Head – Column) – Right.

G.7 Specimen V3

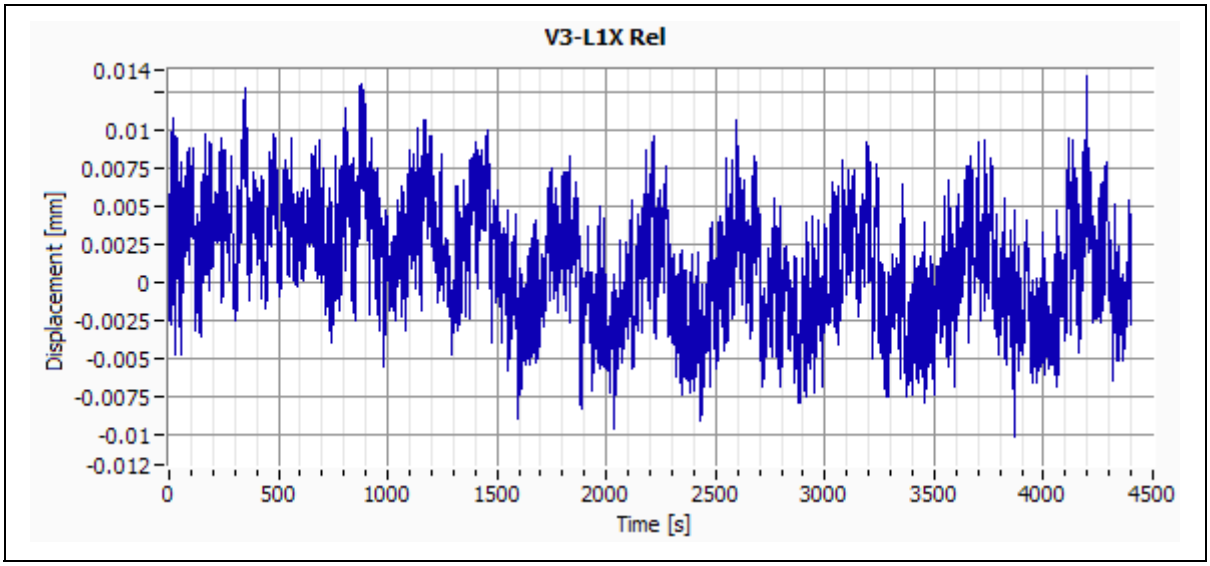

Figure G-25:– Specimen V3 – Column Central Point Relative Displacement – X Direction.

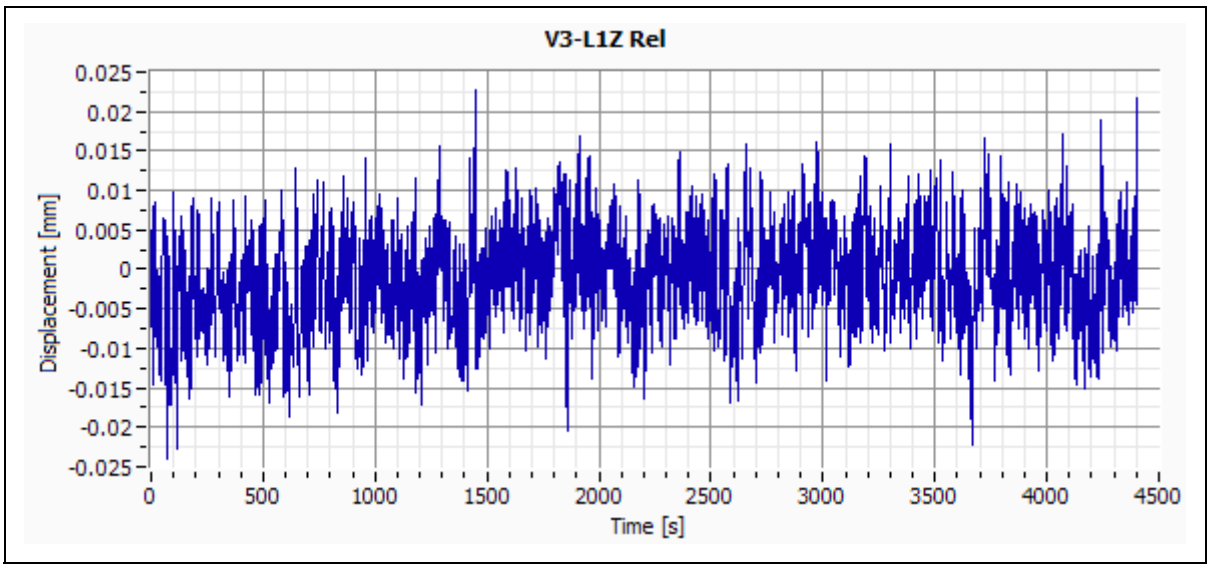

Figure G-26:– Specimen V3 – Column Central Point Relative Displacement – Z Direction.

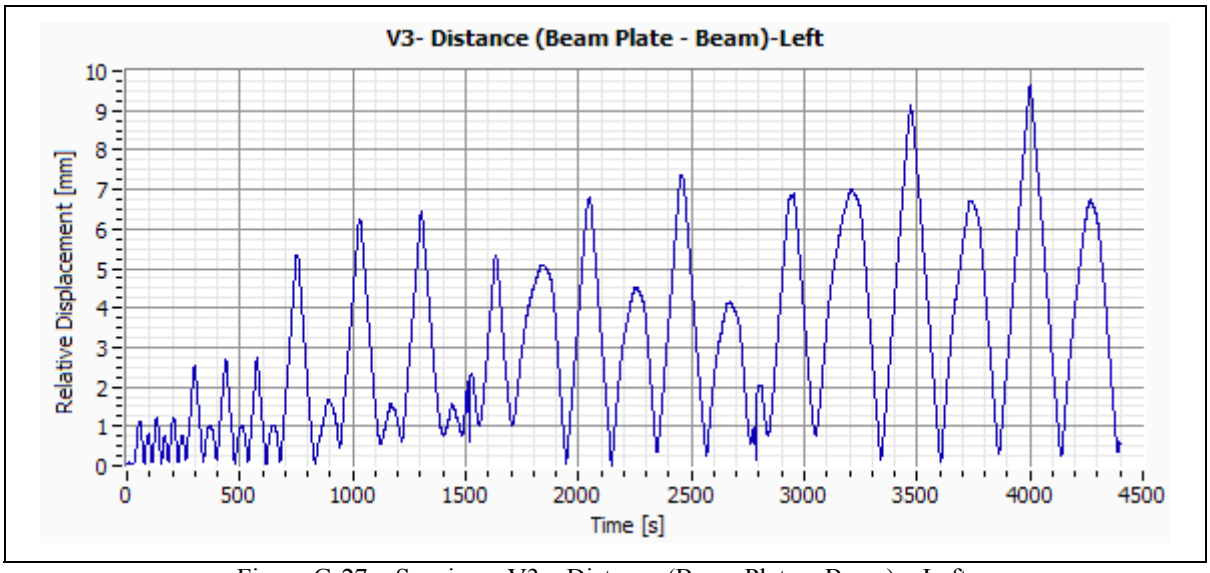

Figure G-27:– Specimen V3 – Distance (Beam Plate – Beam) – Left.

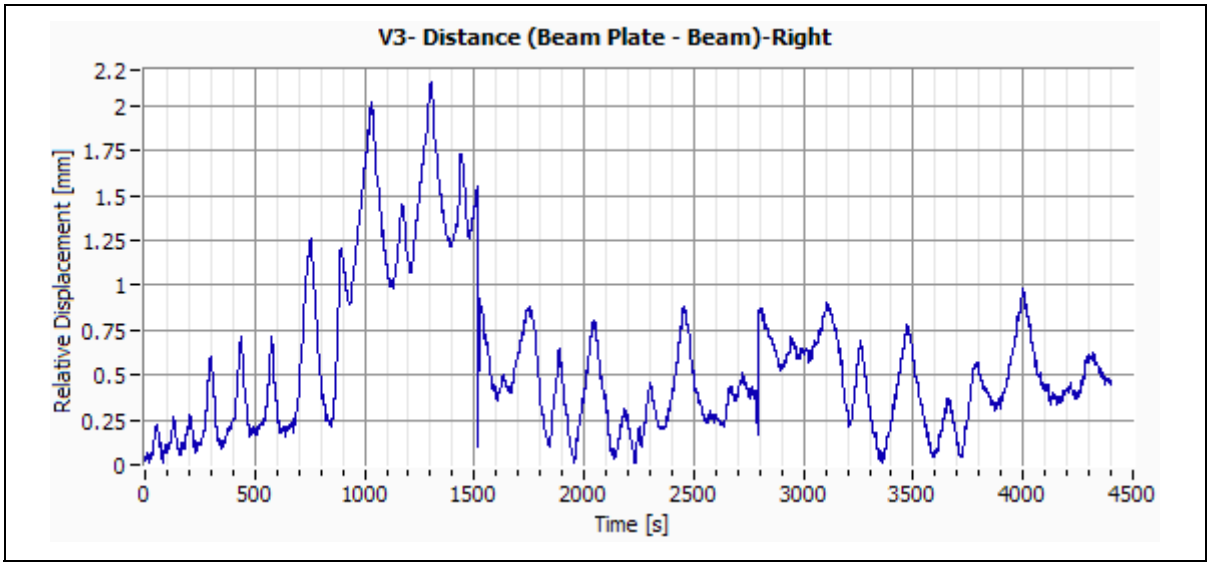

Figure G-28:– Specimen V3 – Distance (Beam Plate – Beam) – Right.

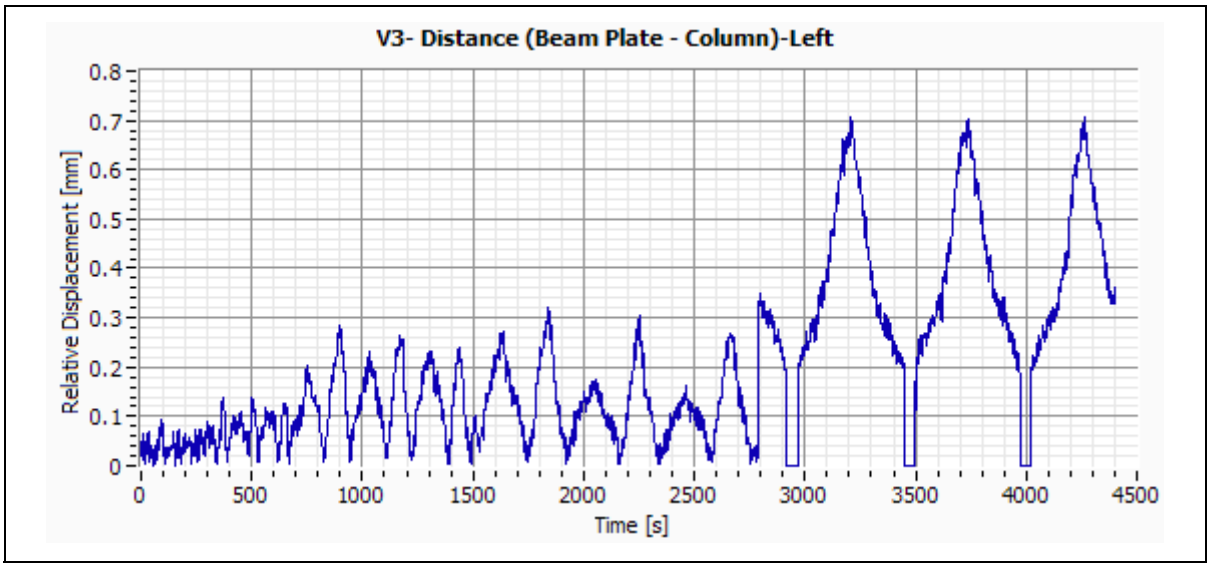

Figure G-29:– Specimen V3 – Distance (Beam Plate – Column) – Left.

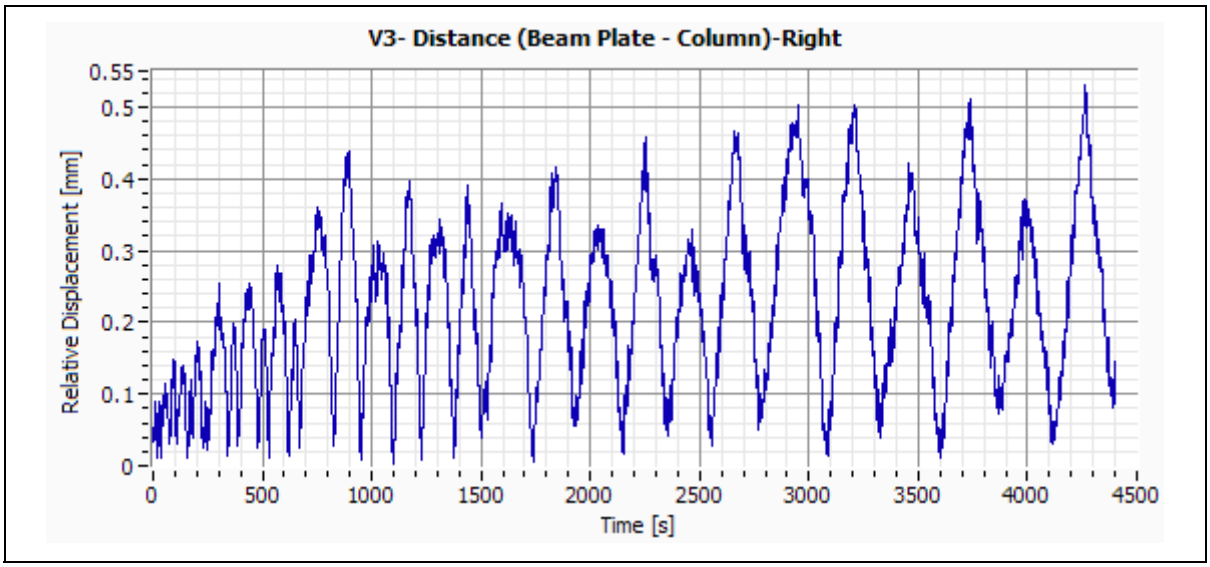

Figure G-30:– Specimen V3 – Distance (Beam Plate – Column) – Right.

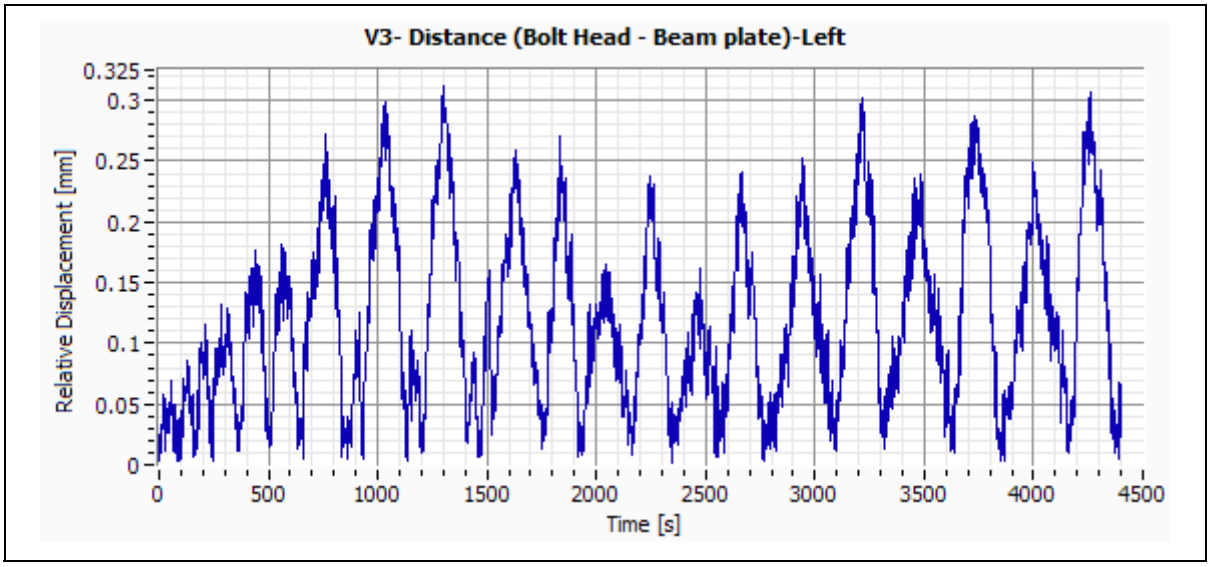

Figure G-31:– Specimen V3 – Distance (Bolt Head – Beam Plate) – Left.

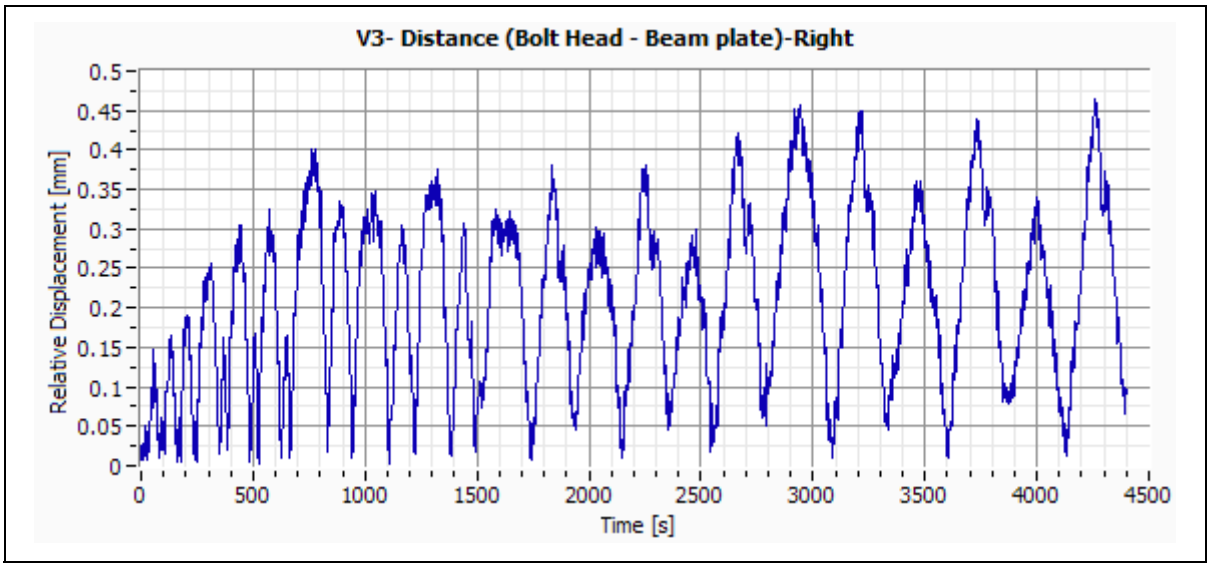

Figure G-32:– Specimen V3 – Distance (Bolt Head – Beam Plate) – Right.

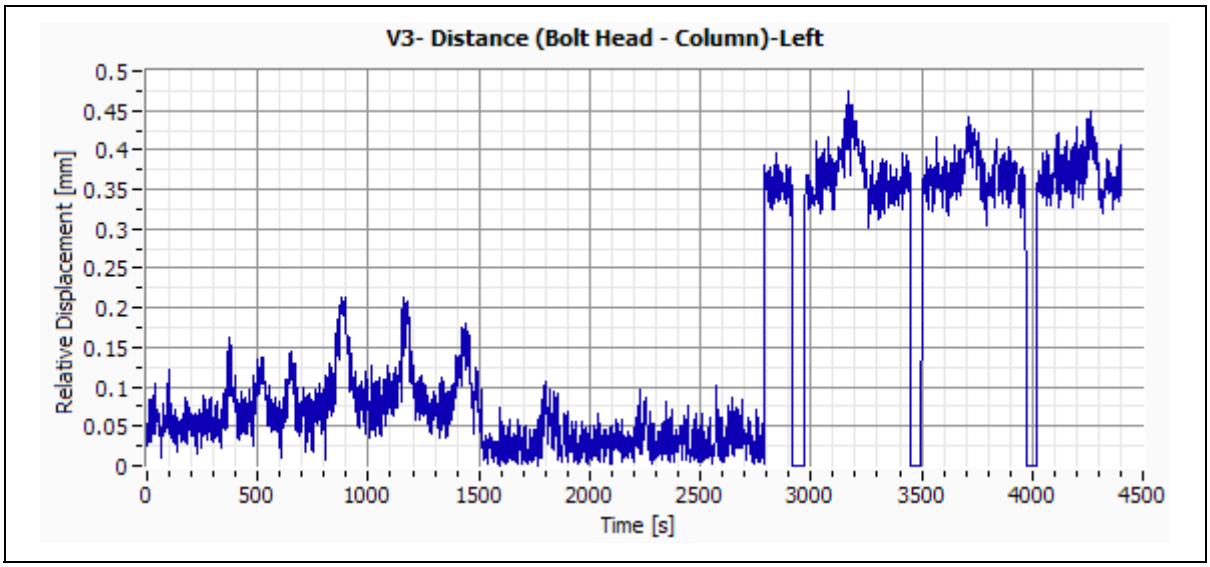

Figure G-33:– Specimen V3 – Distance (Bolt Head – Column) – Left.

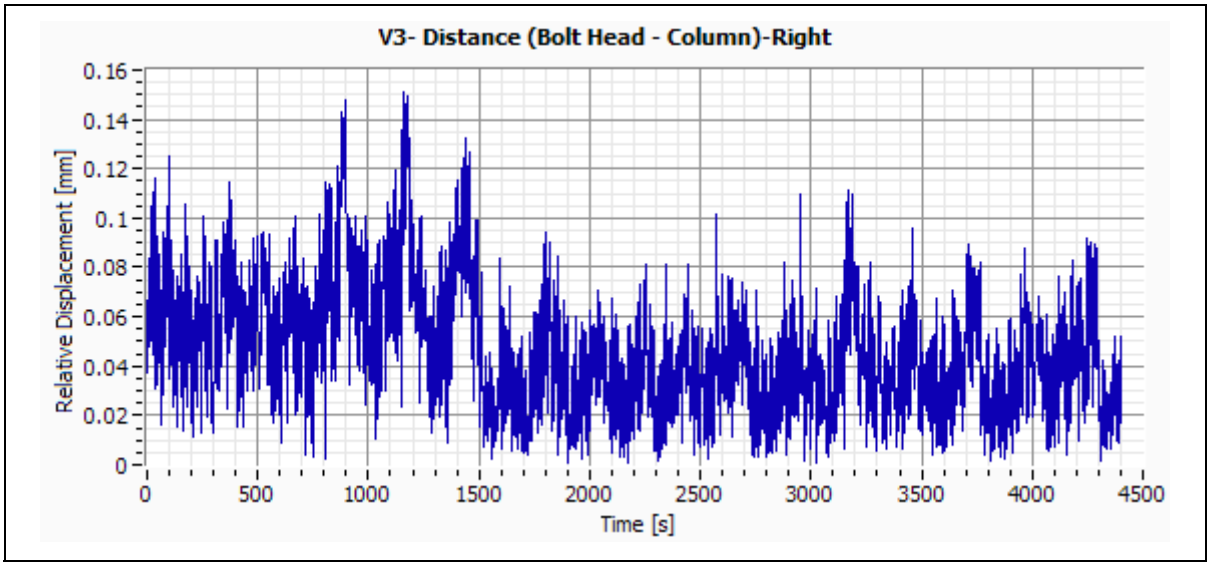

Figure G-34:– Specimen V3 – Distance (Bolt Head – Column) – Right.

G.8 Specimen V4

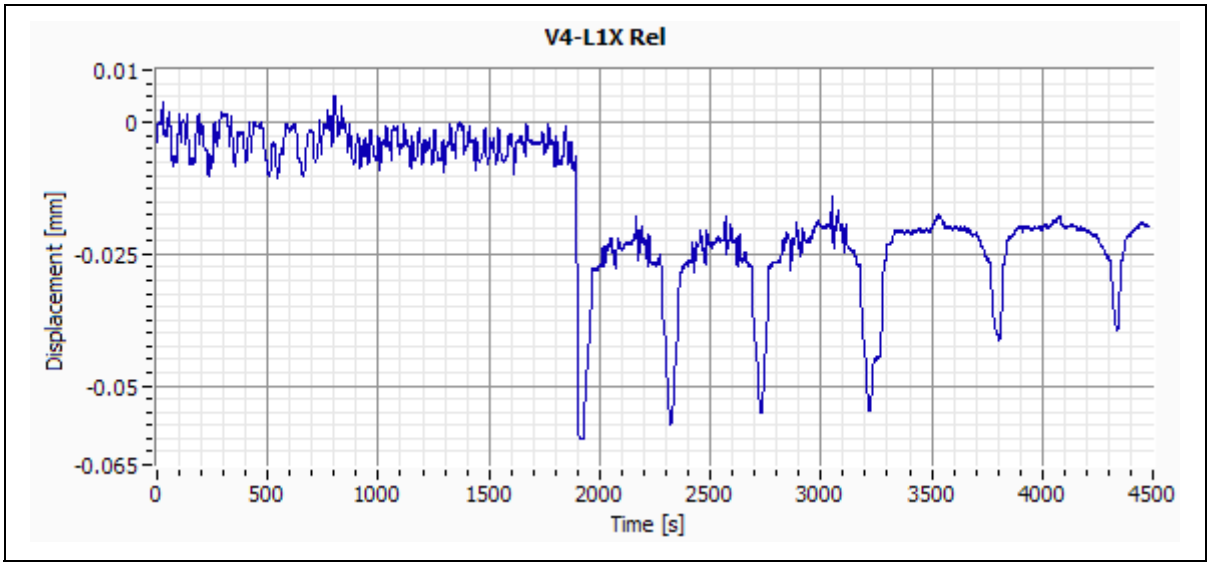

Figure G-35:– Specimen V4 – Column Central Point Relative Displacement – X Direction.

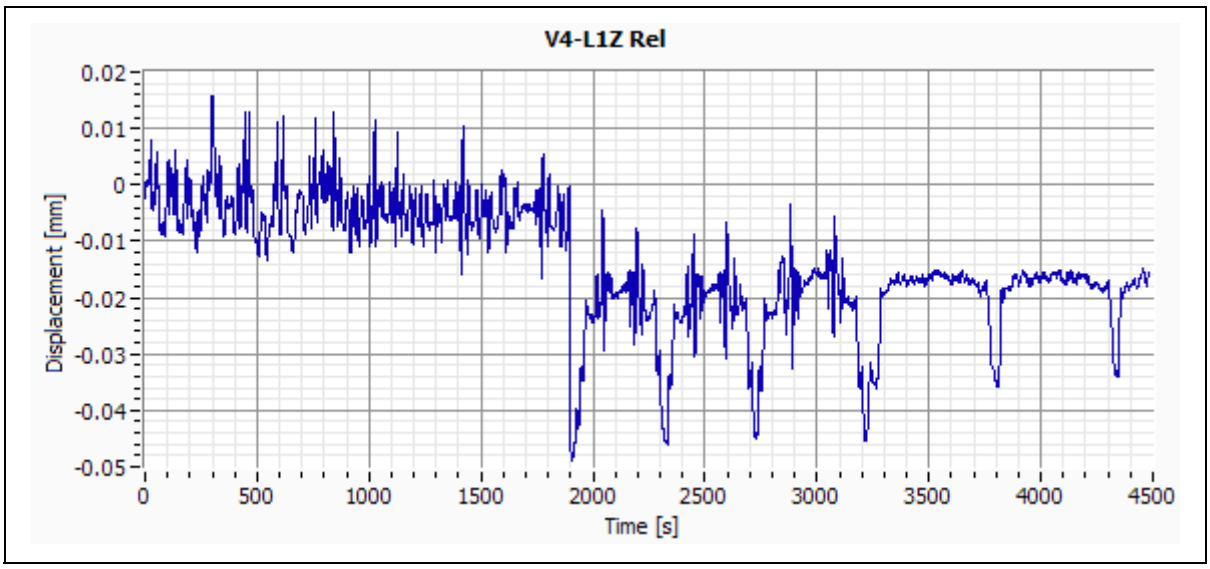

Figure G-36:– Specimen V4 – Column Central Point Relative Displacement – Z Direction.

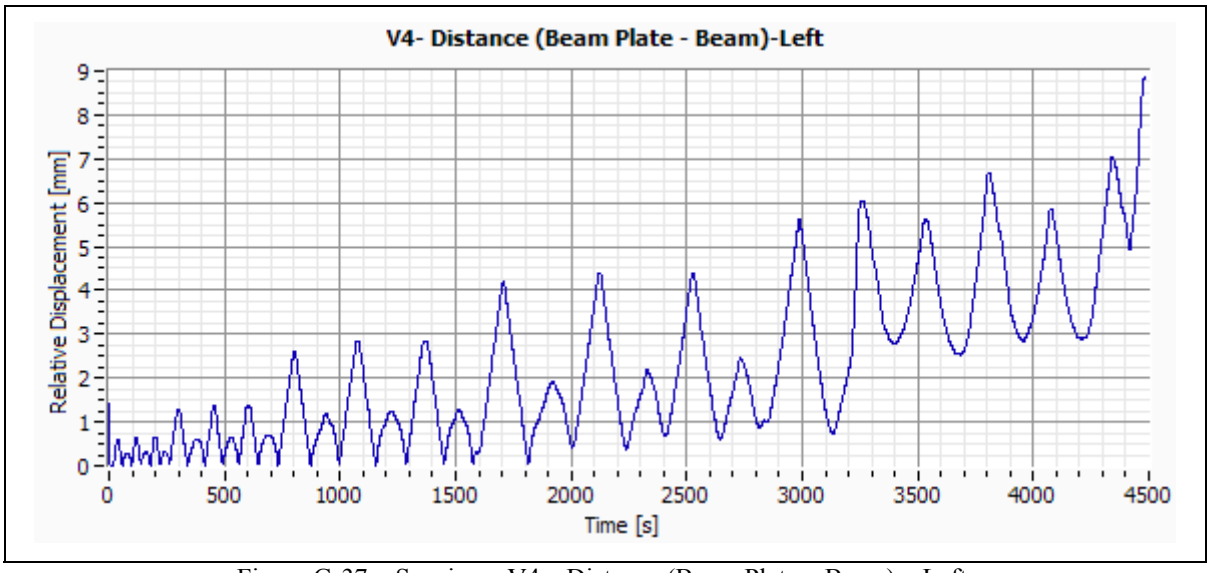

Figure G-37:– Specimen V4 – Distance (Beam Plate – Beam) – Left.

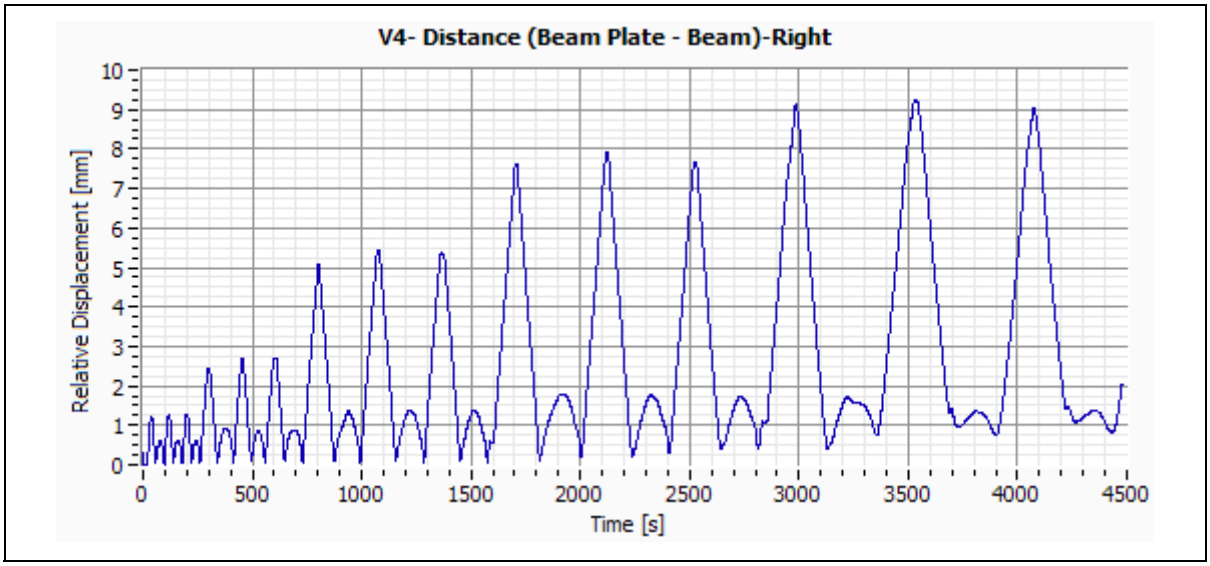

Figure G-38:– Specimen V4 – Distance (Beam Plate – Beam) – Right.

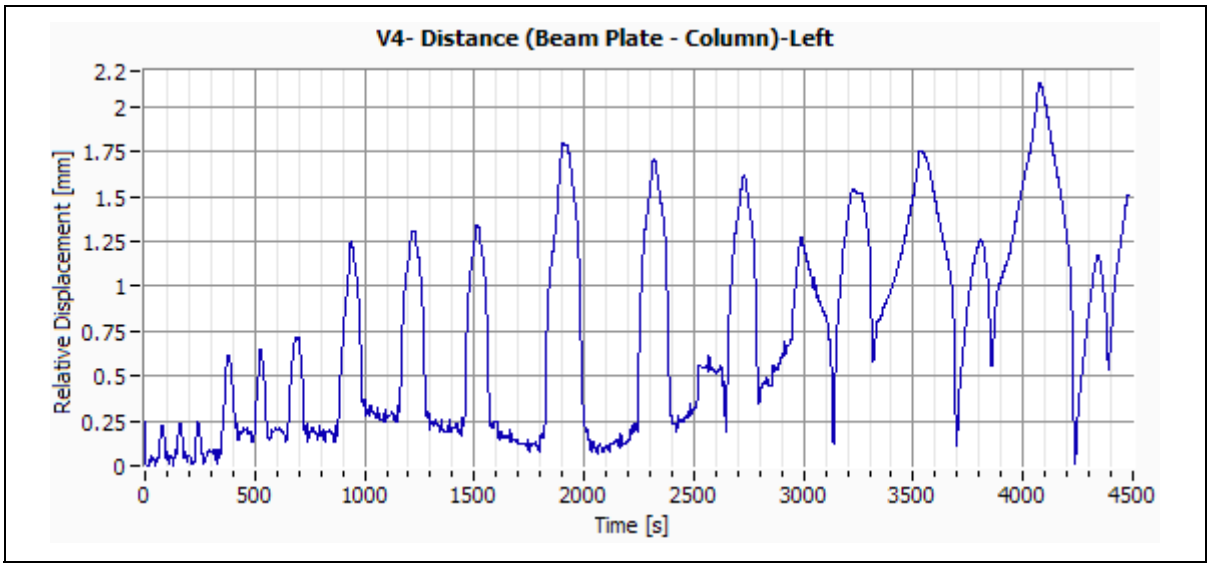

Figure G-39:– Specimen V4 – Distance (Beam Plate – Column) – Left.

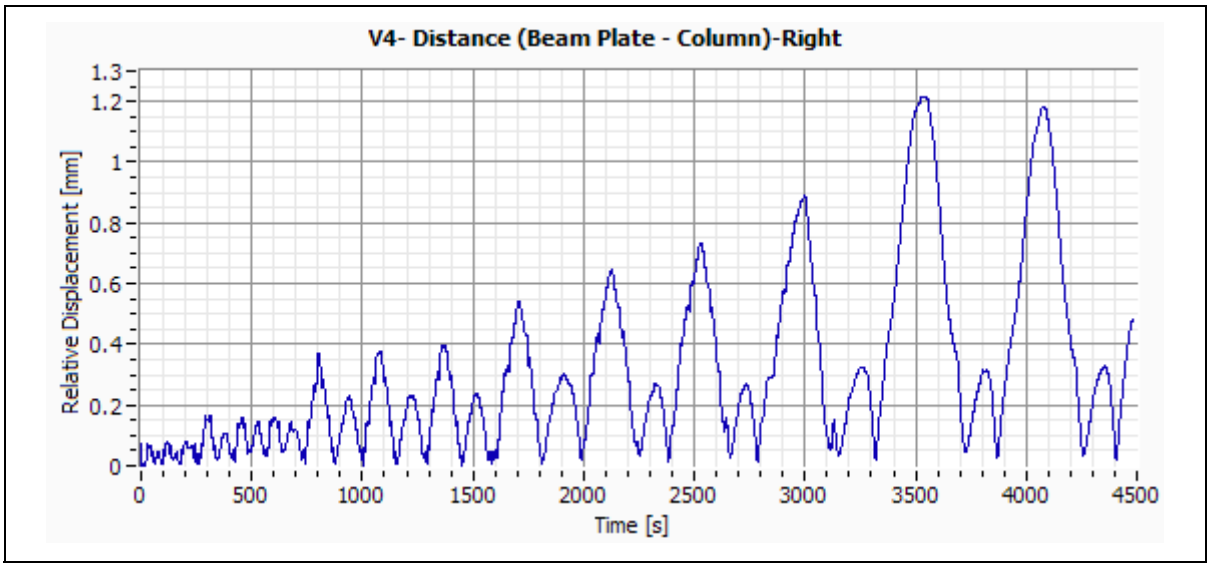

Figure G-40:– Specimen V4 – Distance (Beam Plate – Column) – Right.

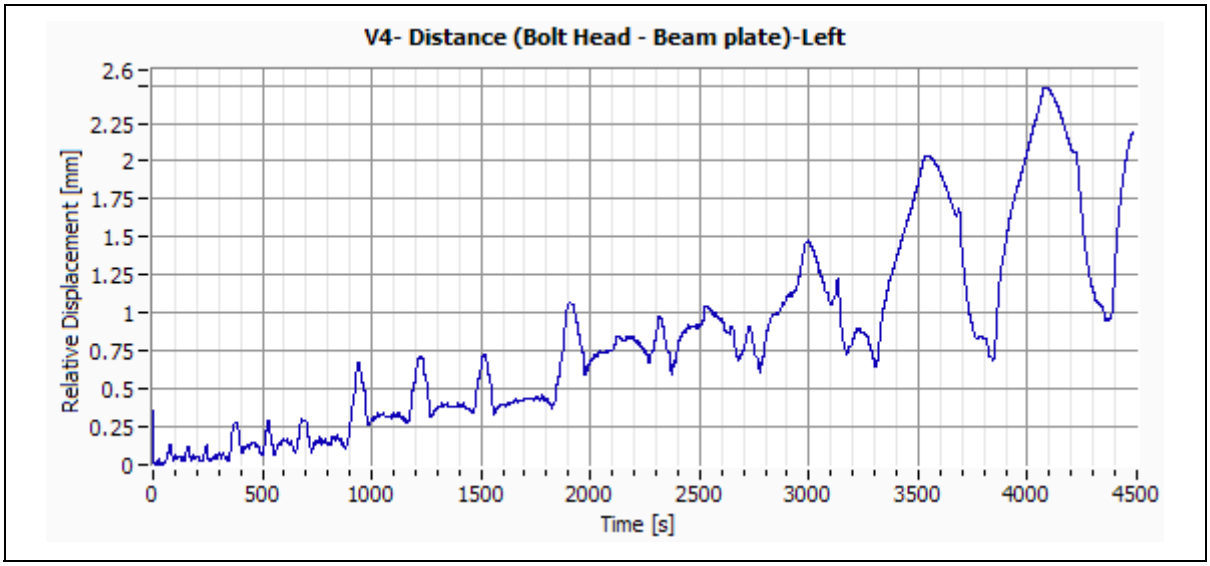

Figure G-41:– Specimen V4 – Distance (Bolt Head – Beam Plate) – Left.

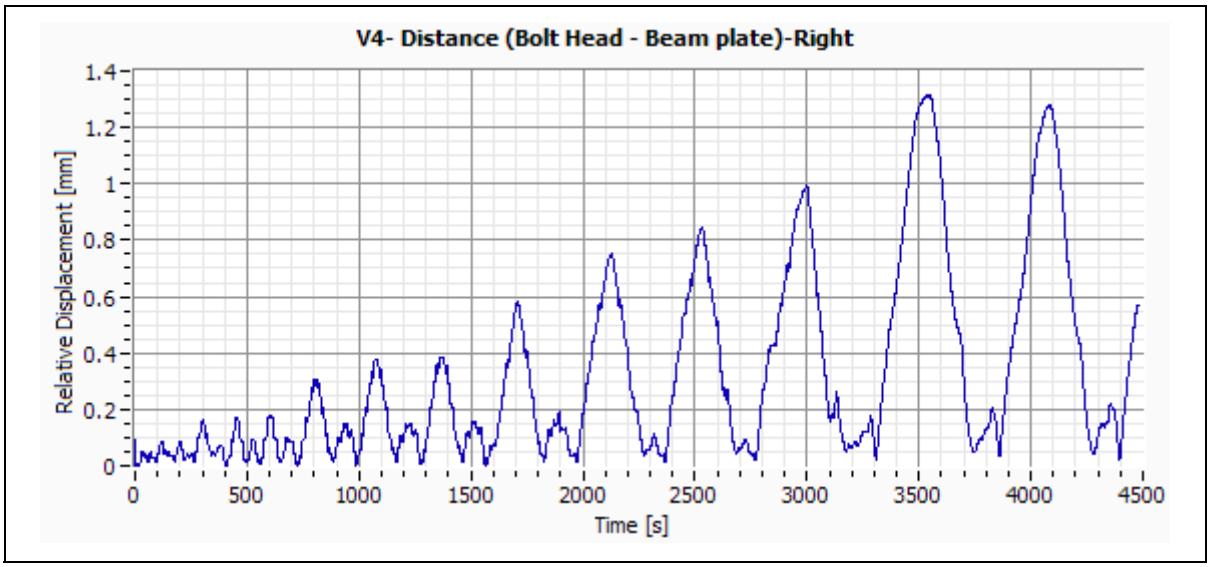

Figure G-42:– Specimen V4 – Distance (Bolt Head – Beam Plate) – Right.

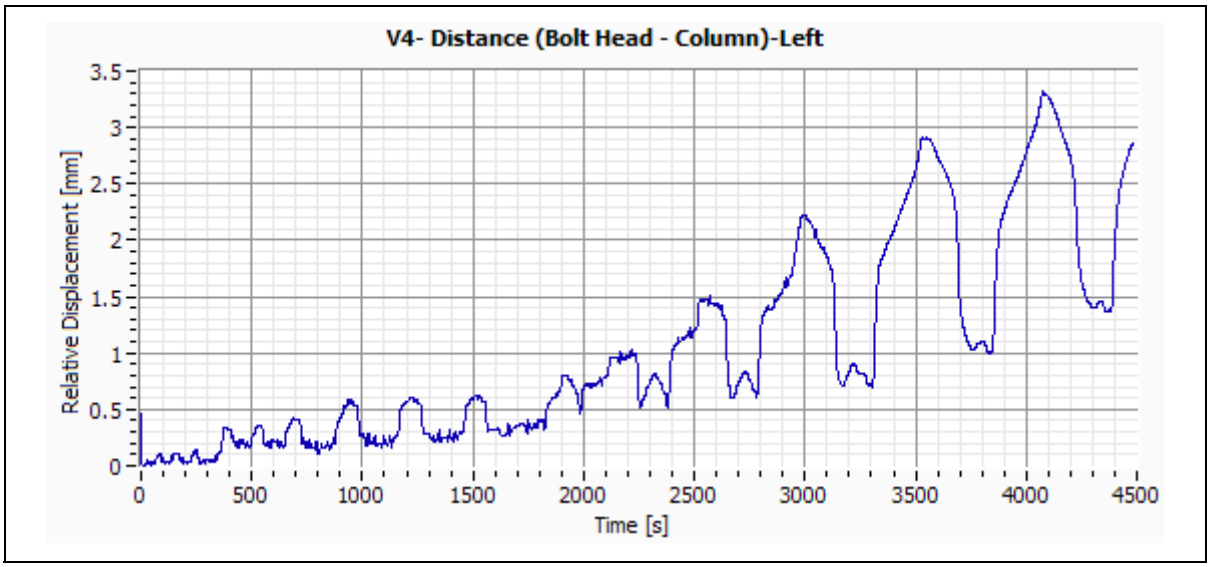

Figure G-43:– Specimen V4 – Distance (Bolt Head – Column) – Left.

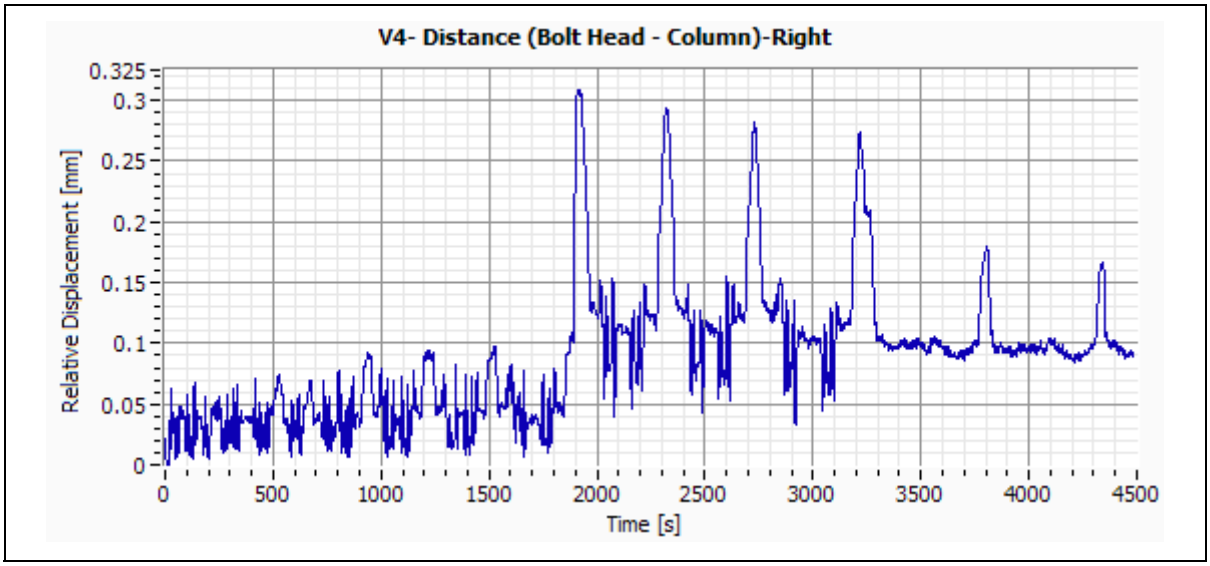

Figure G-44:– Specimen V4 – Distance (Bolt Head – Column) – Right.

G.9 Specimen V5

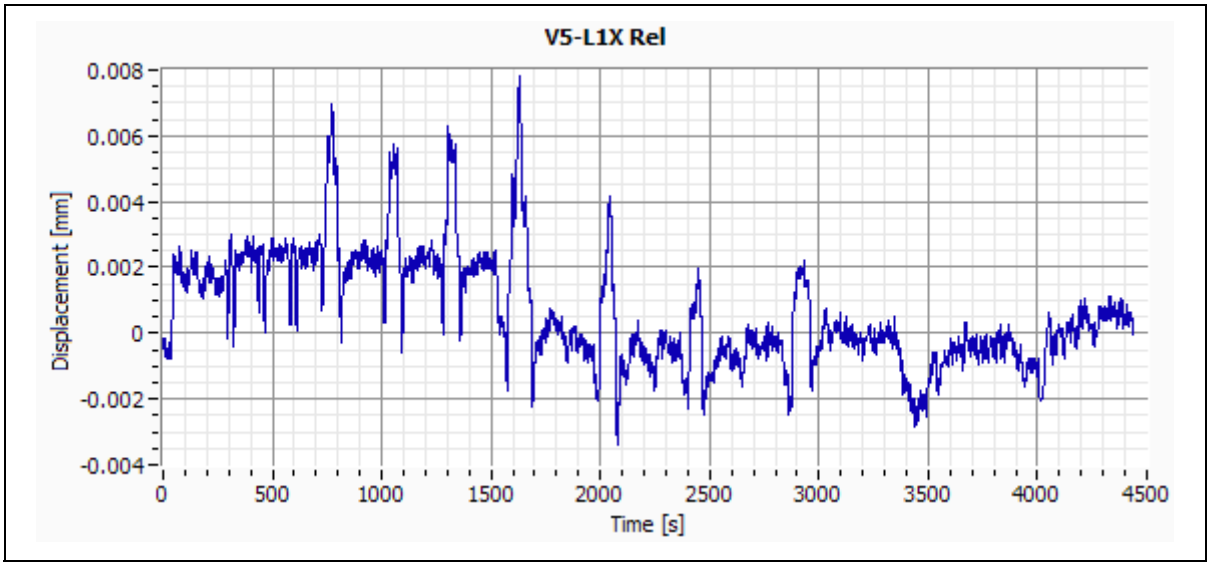

Figure G-45:– Specimen V5 – Column Central Point Relative Displacement – X Direction.

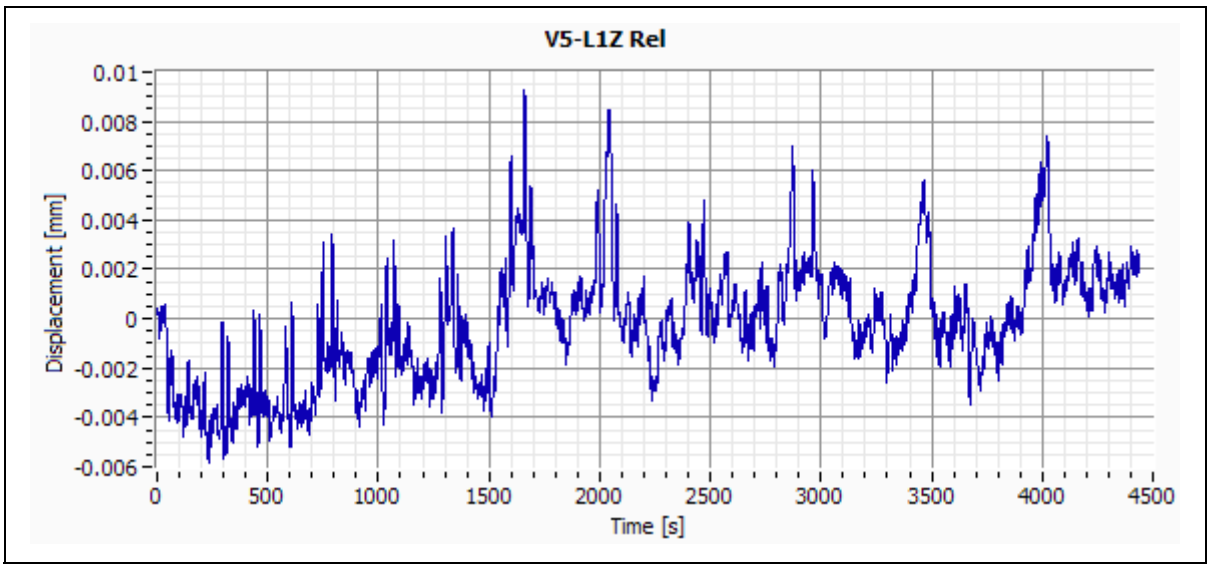

Figure G-46:– Specimen V5 – Column Central Point Relative Displacement – Z Direction.

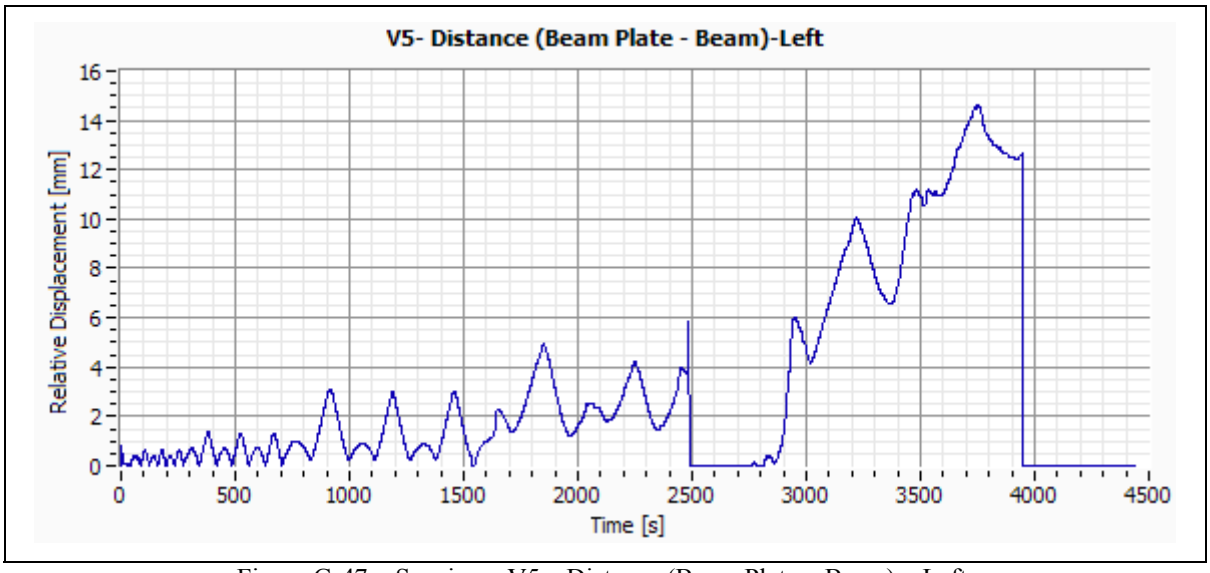

Figure G-47:– Specimen V5 – Distance (Beam Plate – Beam) – Left.

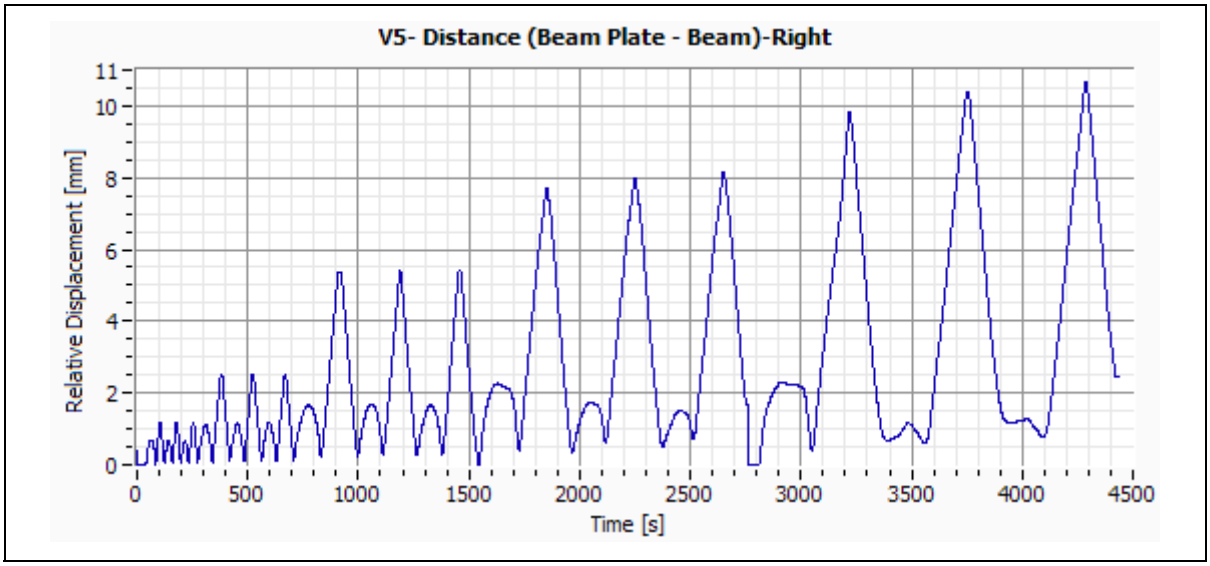

Figure G-48:– Specimen V5 – Distance (Beam Plate – Beam) – Right.

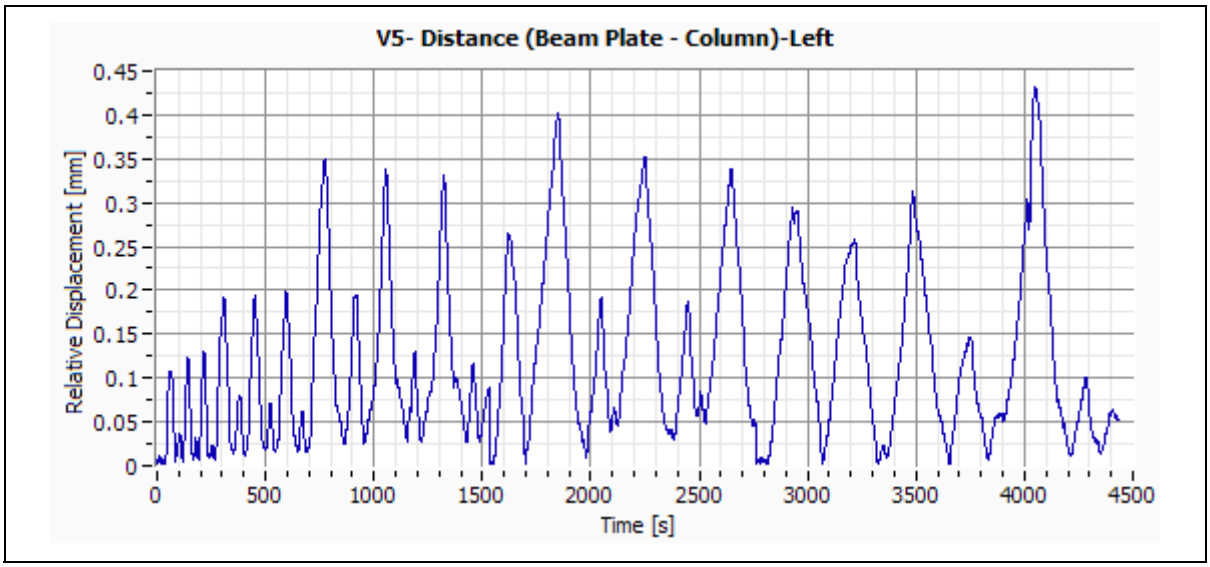

Figure G-49:– Specimen V5 – Distance (Beam Plate – Column) – Left.

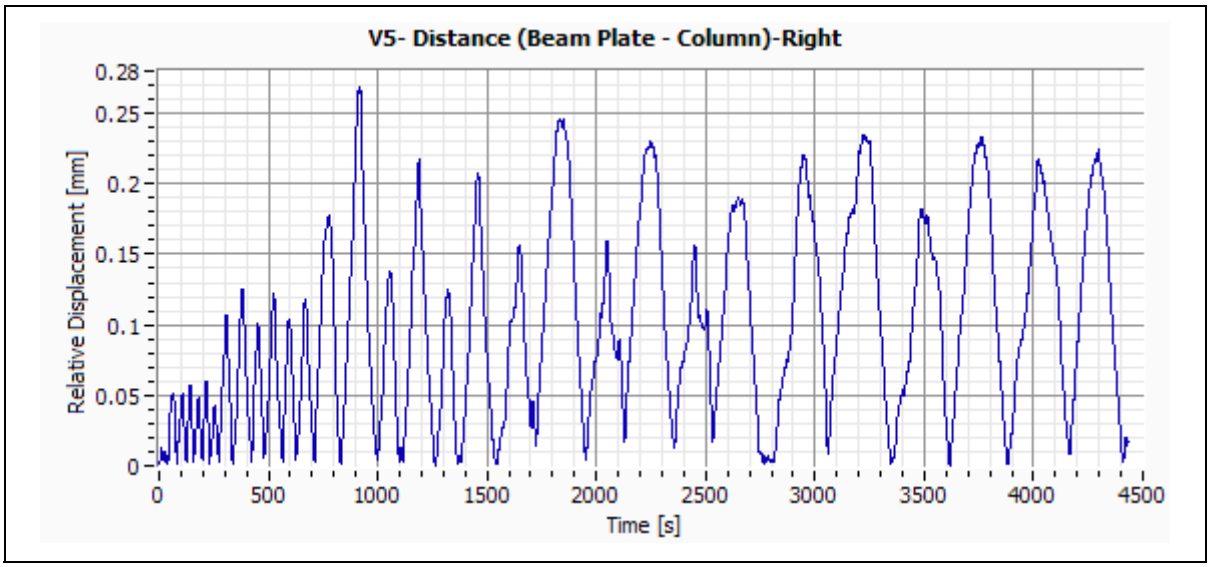

Figure G-50:– Specimen V5 – Distance (Beam Plate – Column) – Right.

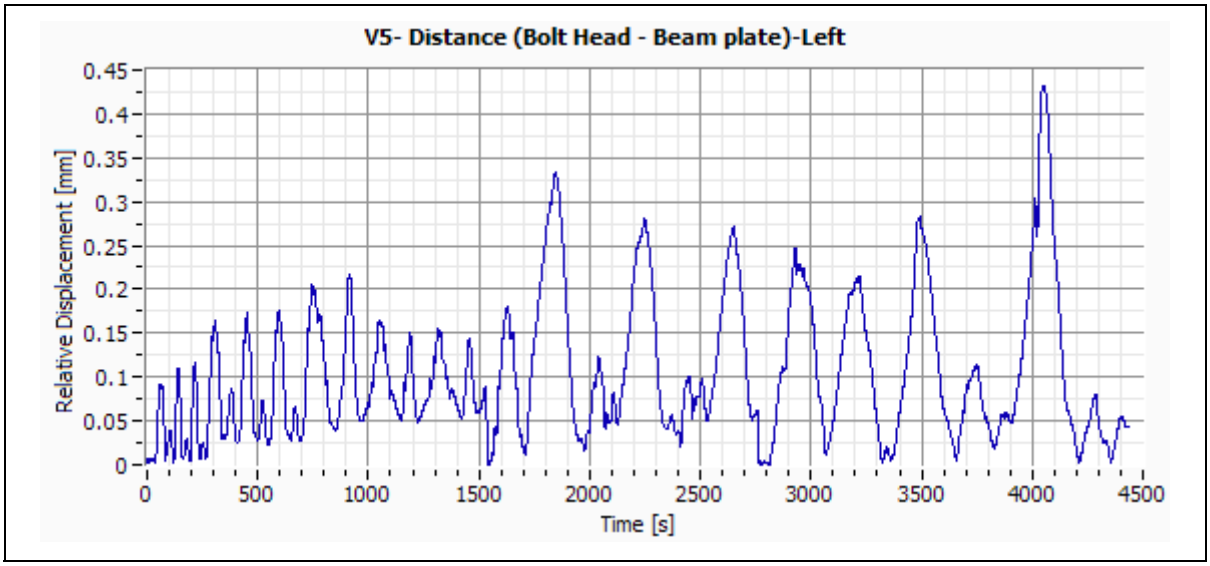

Figure G-51:– Specimen V5 – Distance (Bolt Head – Beam Plate) – Left.

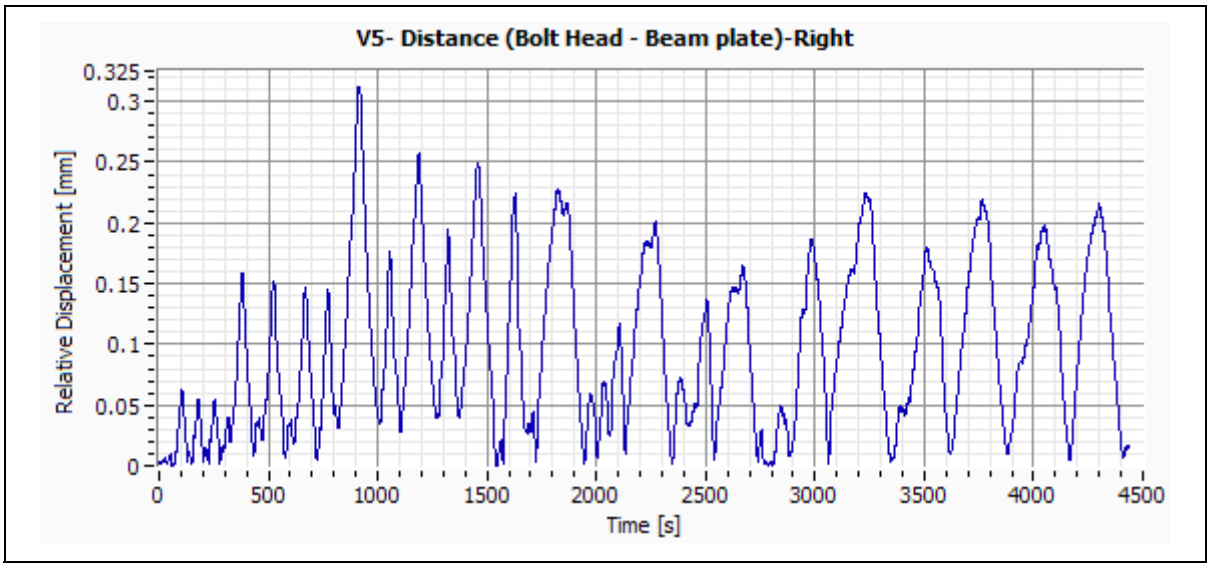

Figure G-52:– Specimen V5 – Distance (Bolt Head – Beam Plate) – Right.

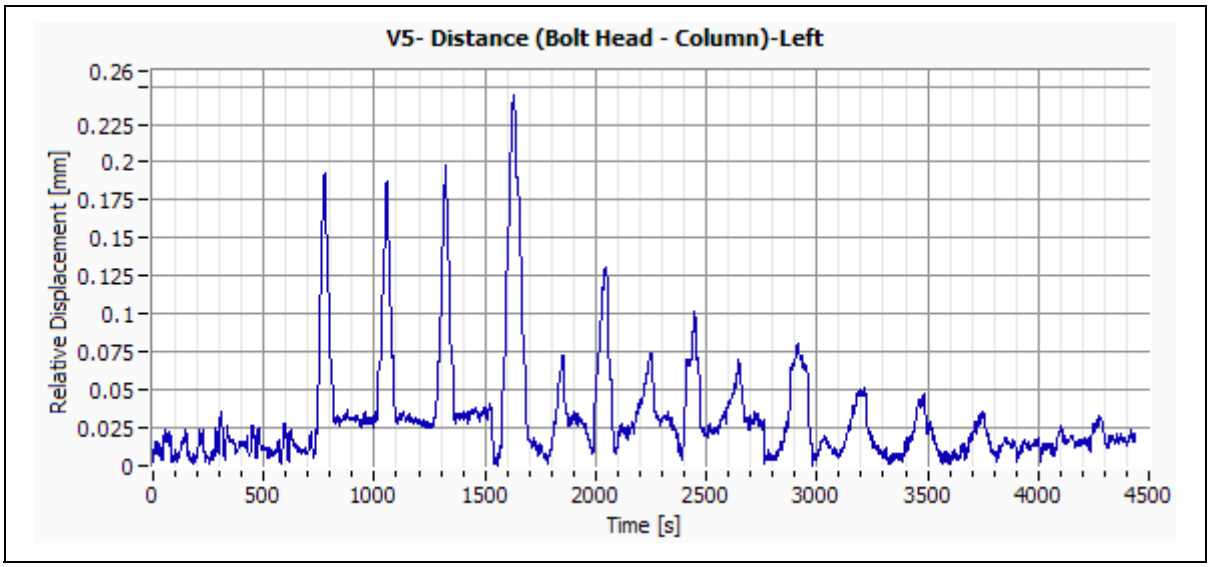

Figure G-53:– Specimen V5 – Distance (Bolt Head – Column) – Left.

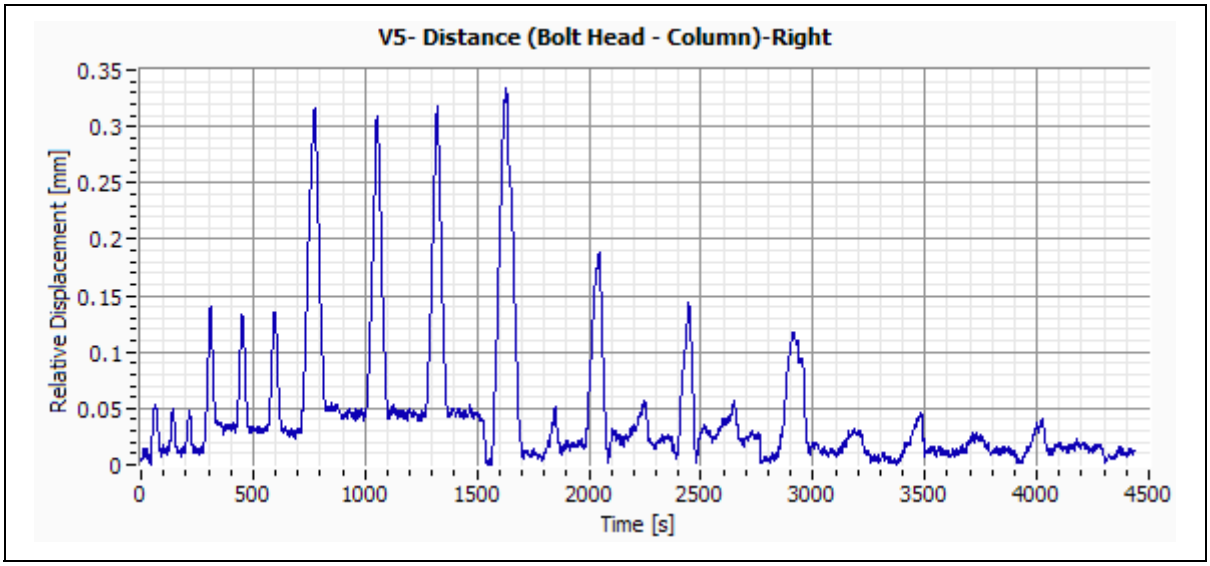

Figure G-54:– Specimen V5 – Distance (Bolt Head – Column) – Right.

G.10 Specimen VL1

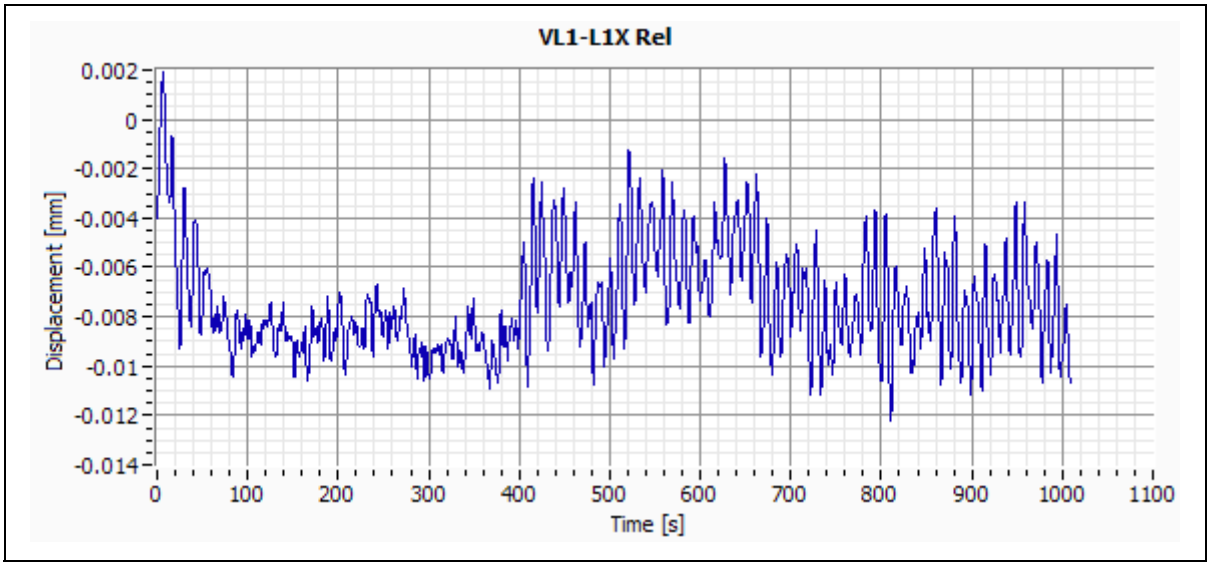

Figure G-55: – Specimen VL1 – Column Central Point Relative Displacement – X Direction.

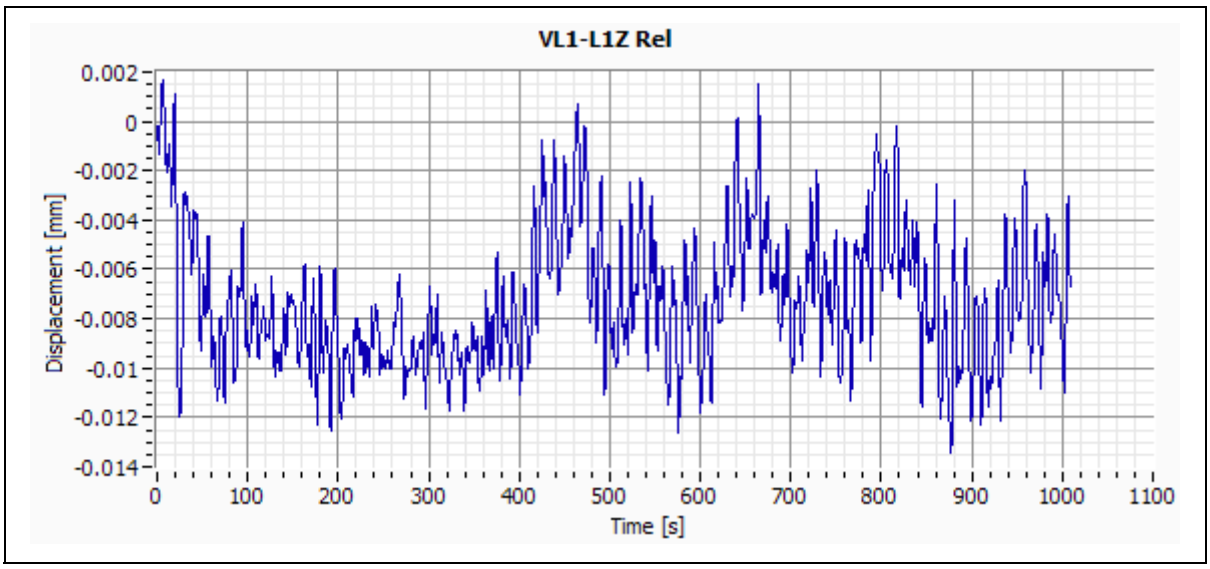

Figure G-56: – Specimen VL1 – Column Central Point Relative Displacement – Z Direction.

G.11 Specimen VL2

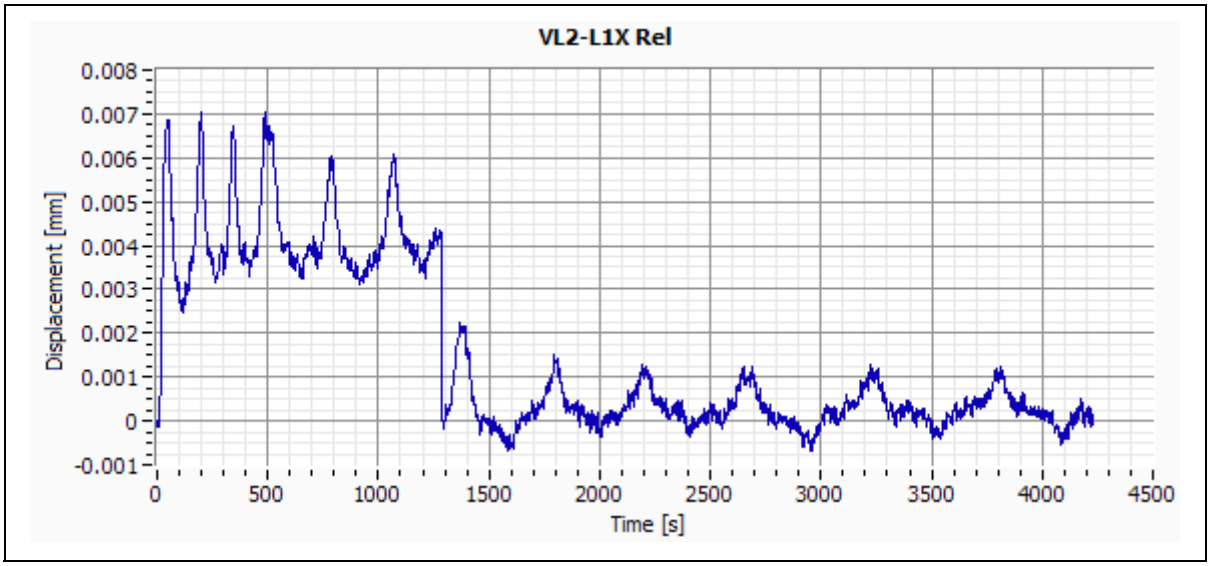

Figure G-57:– Specimen VL2 – Column Central Point Relative Displacement – X Direction.

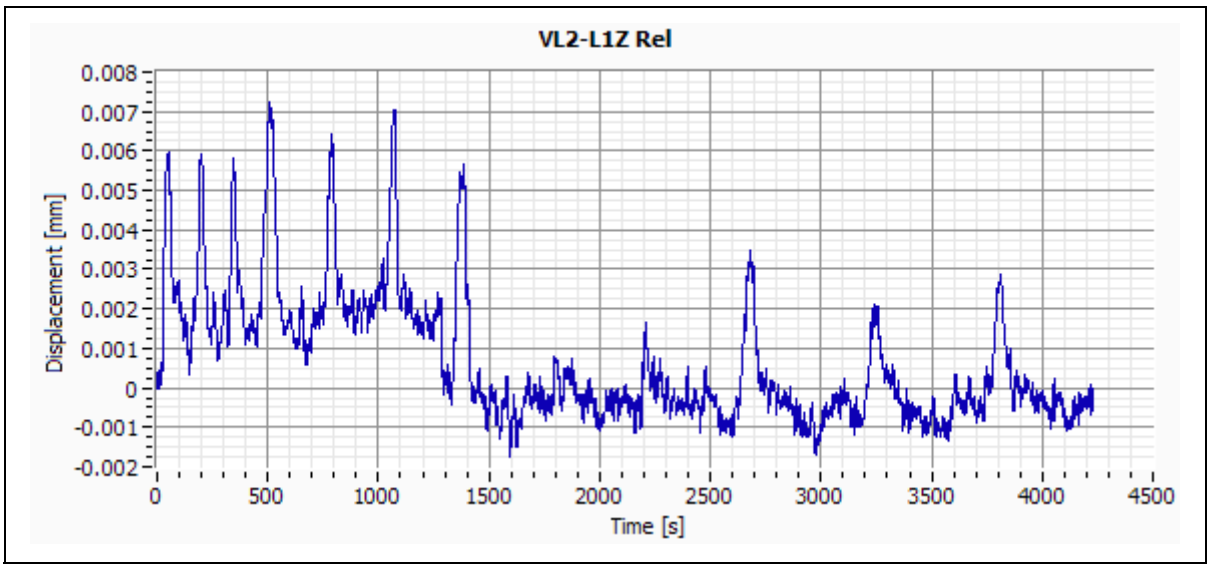

Figure G-58:– Specimen VL2 – Column Central Point Relative Displacement – Z Direction.

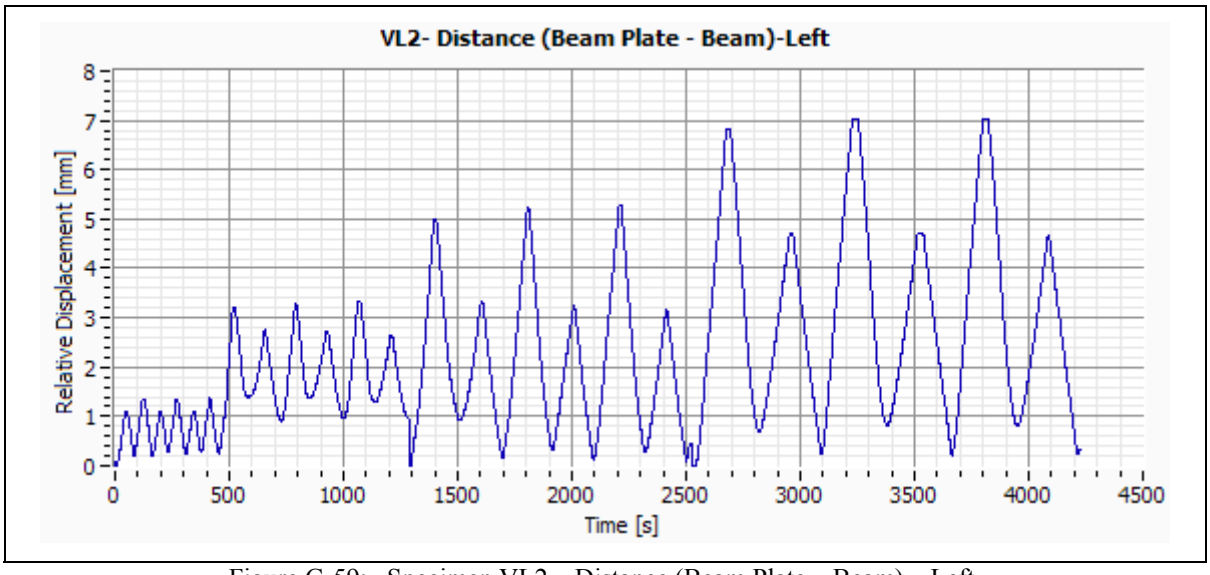

Figure G-59:– Specimen VL2 – Distance (Beam Plate – Beam) – Left.

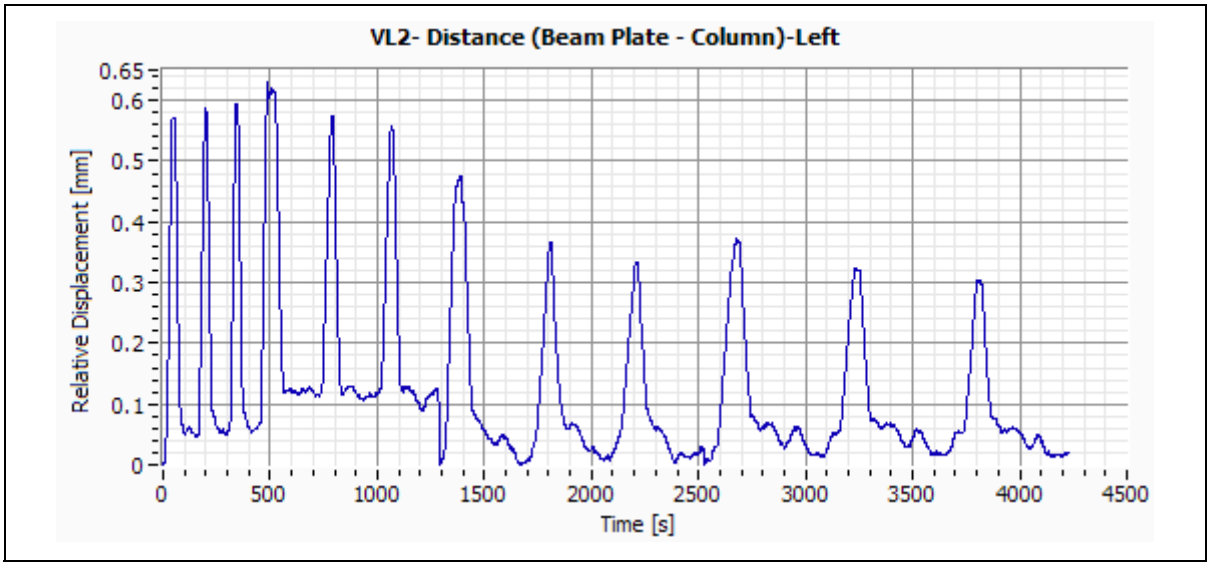

Figure G-60:– Specimen VL2 – Distance (Beam Plate – Column) – Left.

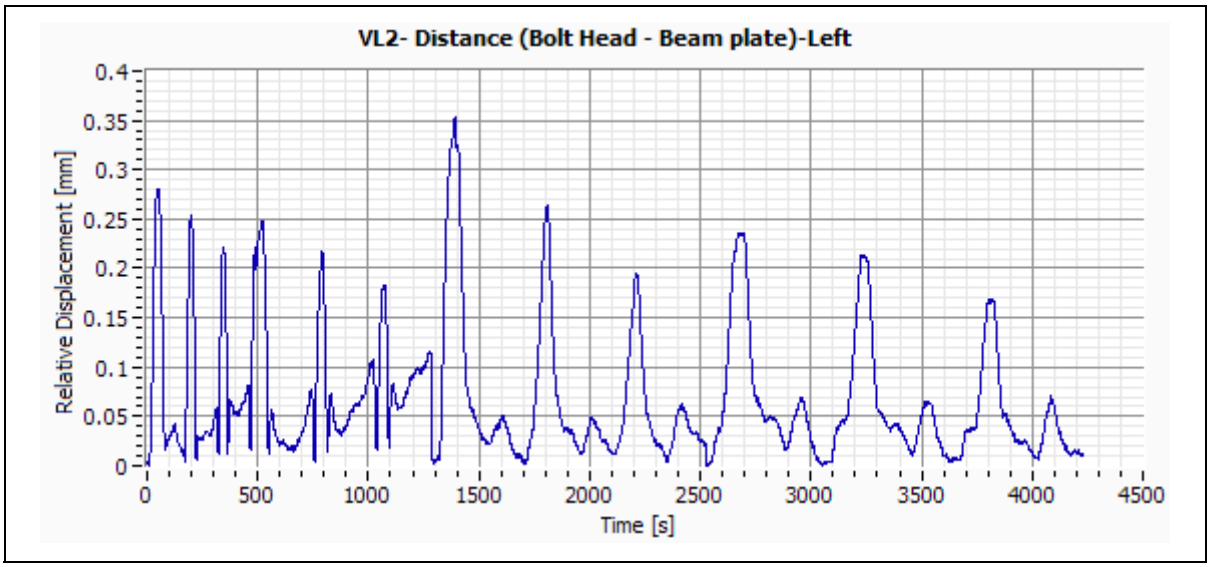

Figure G-61:– Specimen VL2 – Distance (Bolt Head – Beam Plate) – Left..

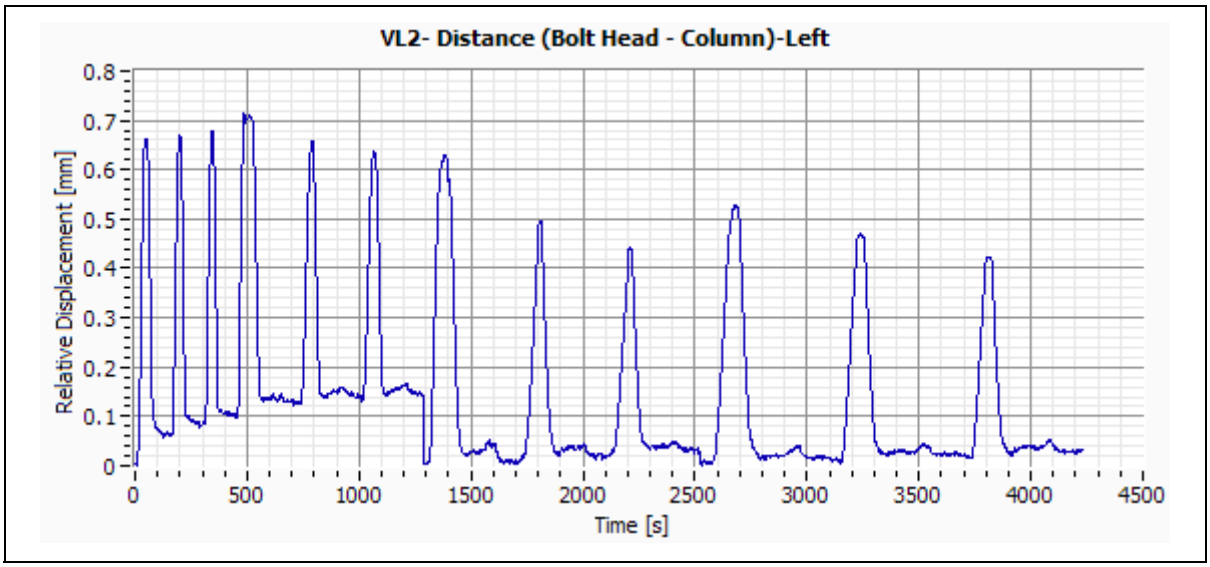

Figure G-62:– Specimen VL2 – Distance (Bolt Head – Column) – Left.

G.12 Specimen VL3

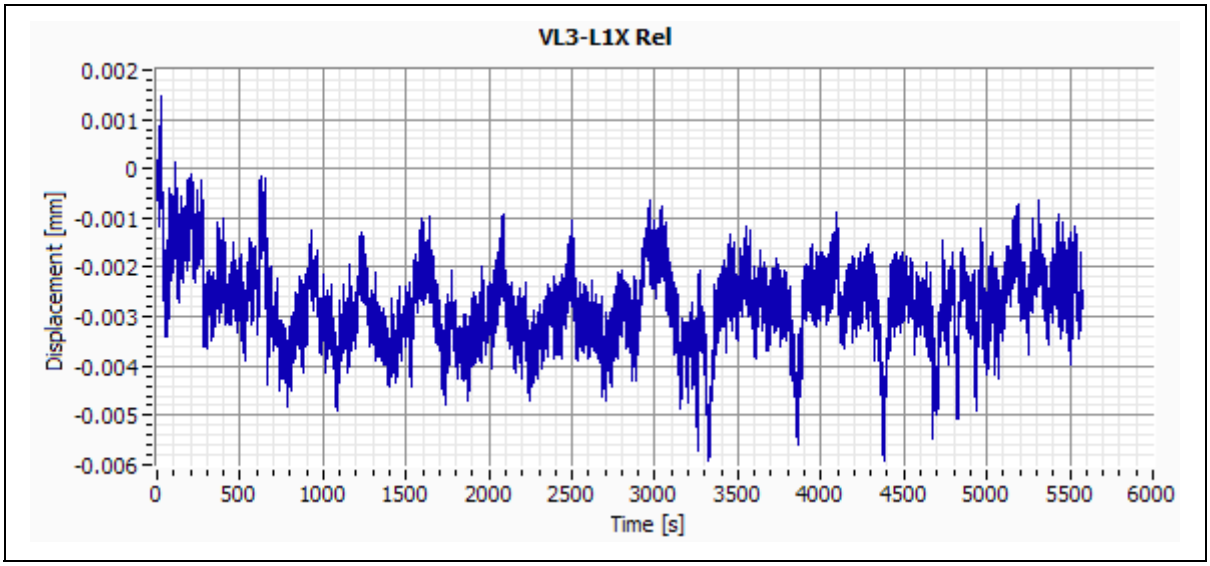

Figure G-63:– Specimen VL3 – Column Central Point Relative Displacement – X Direction.

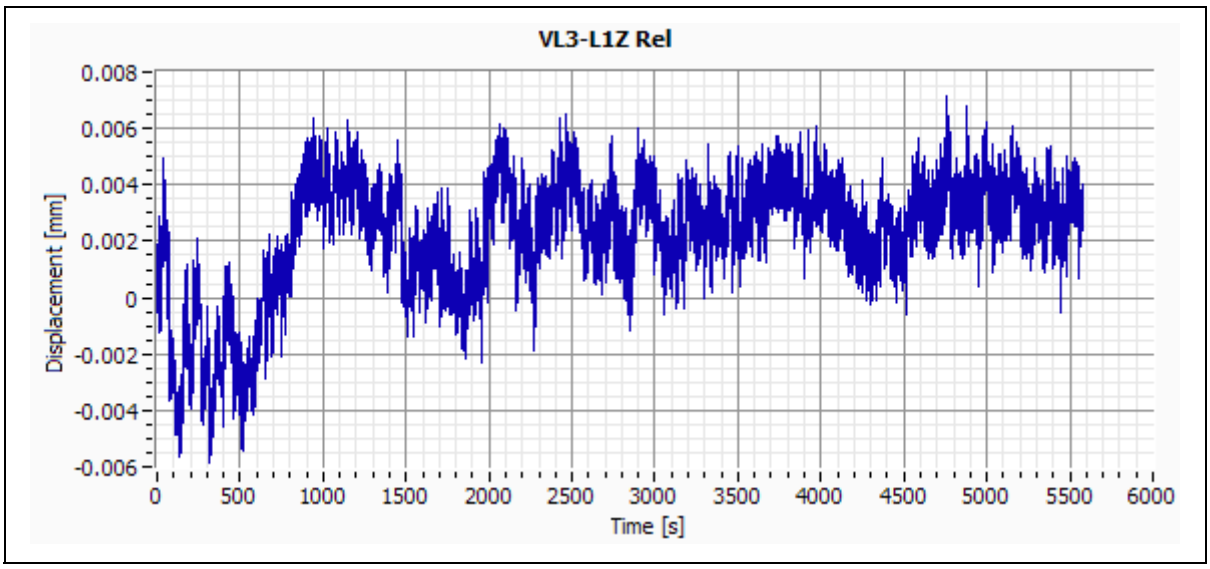

Figure G-64:– Specimen VL3 – Column Central Point Relative Displacement – Z Direction.

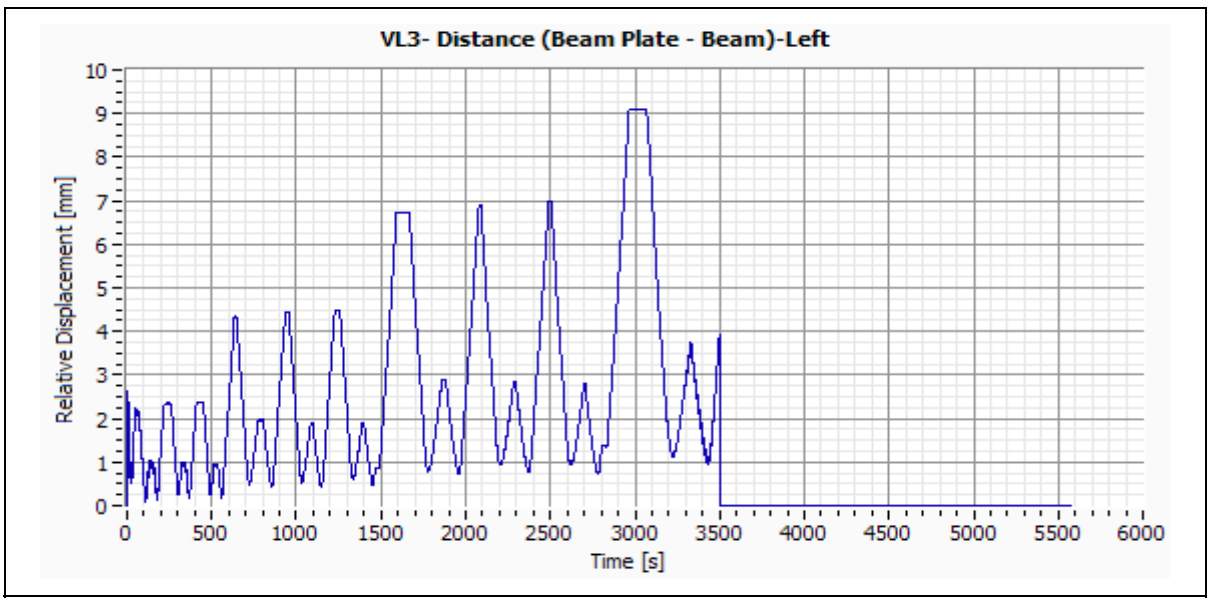

Figure G-65:– Specimen VL3 – Distance (Beam Plate – Beam) – Left.

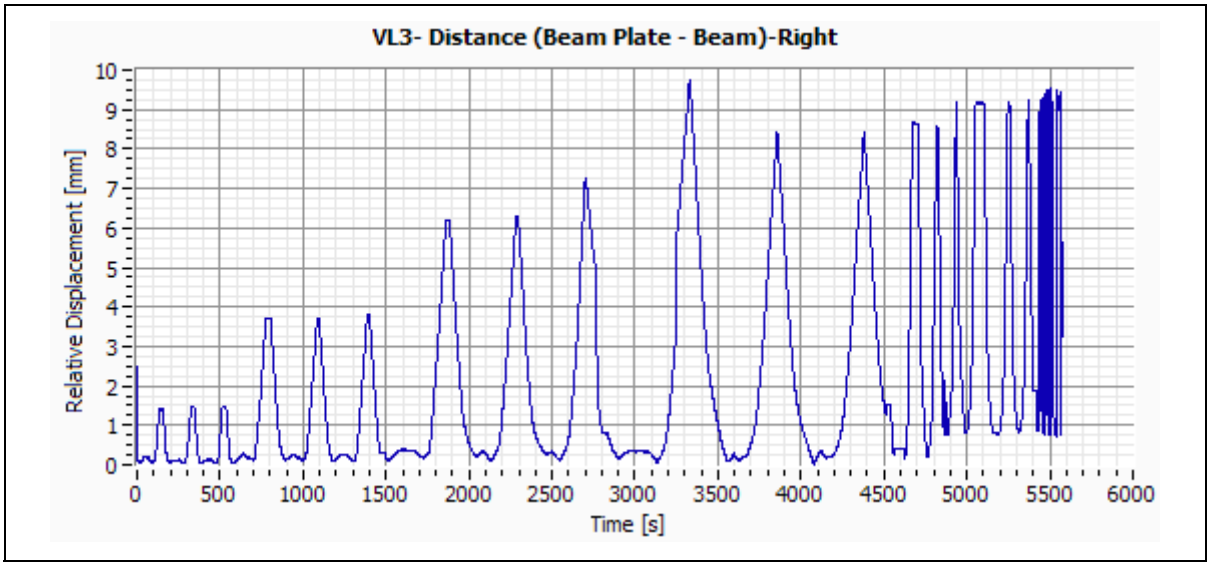

Figure G-66:– Specimen VL3 – Distance (Beam Plate – Beam) – Right.

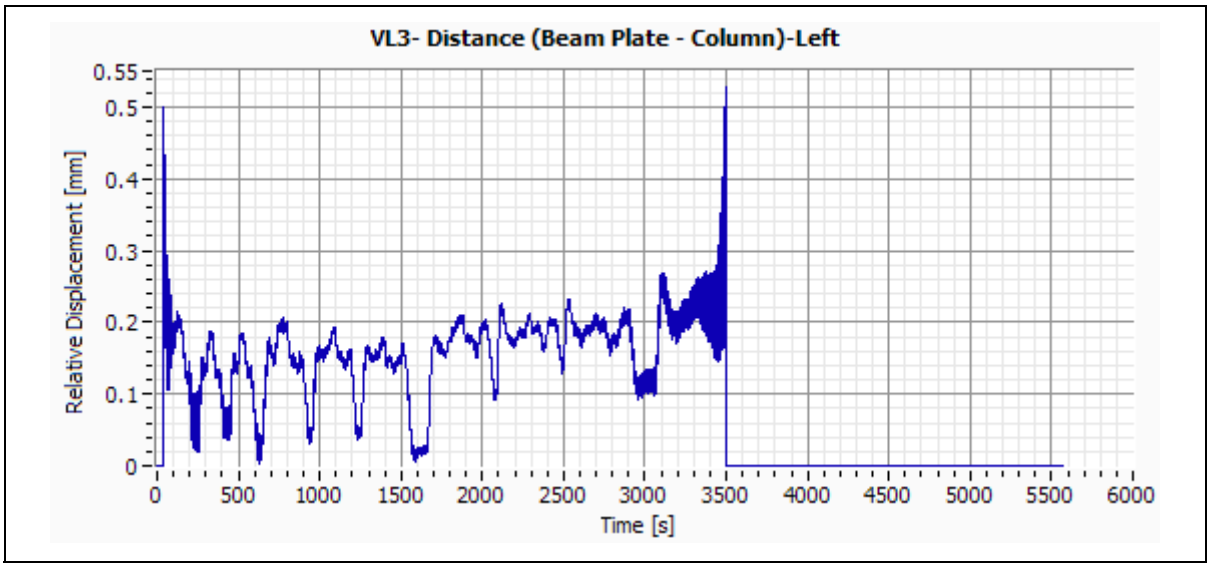

Figure G-67:– Specimen VL3 – Distance (Beam Plate – Column) – Left.

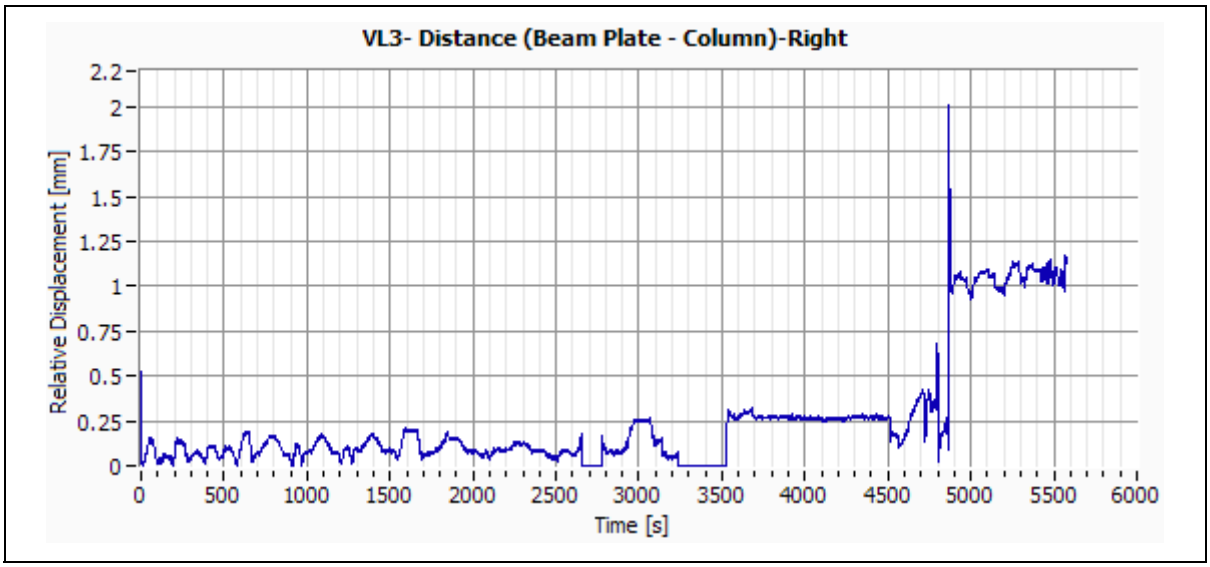

Figure G-68:– Specimen VL3 – Distance (Beam Plate – Column) – Right.

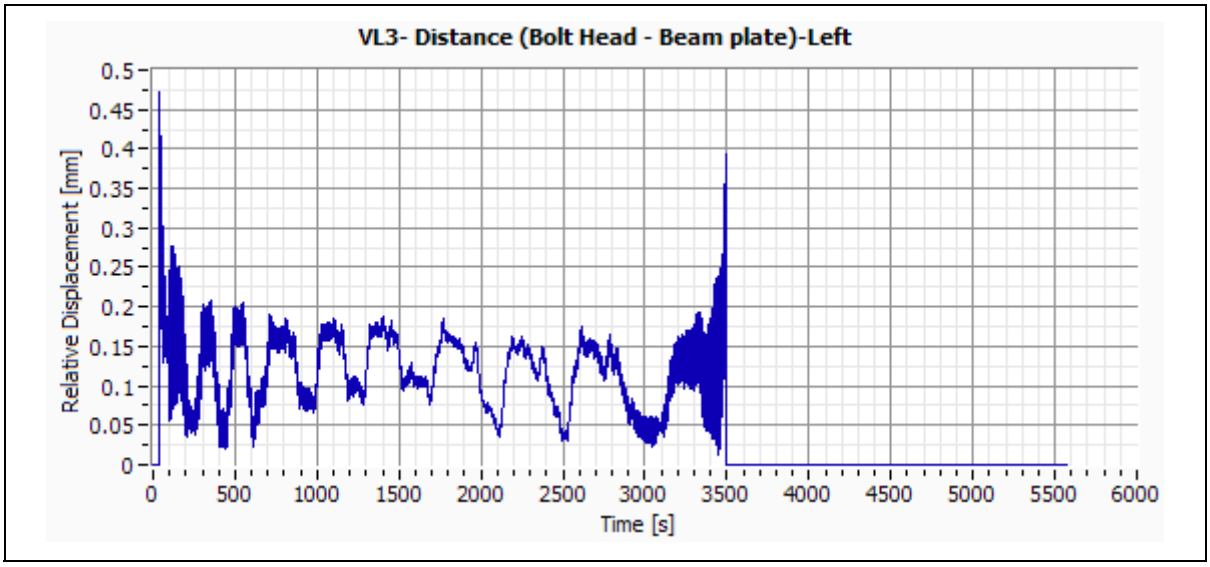

Figure G-69:– Specimen VL3 – Distance (Bolt Head – Beam Plate) – Left..

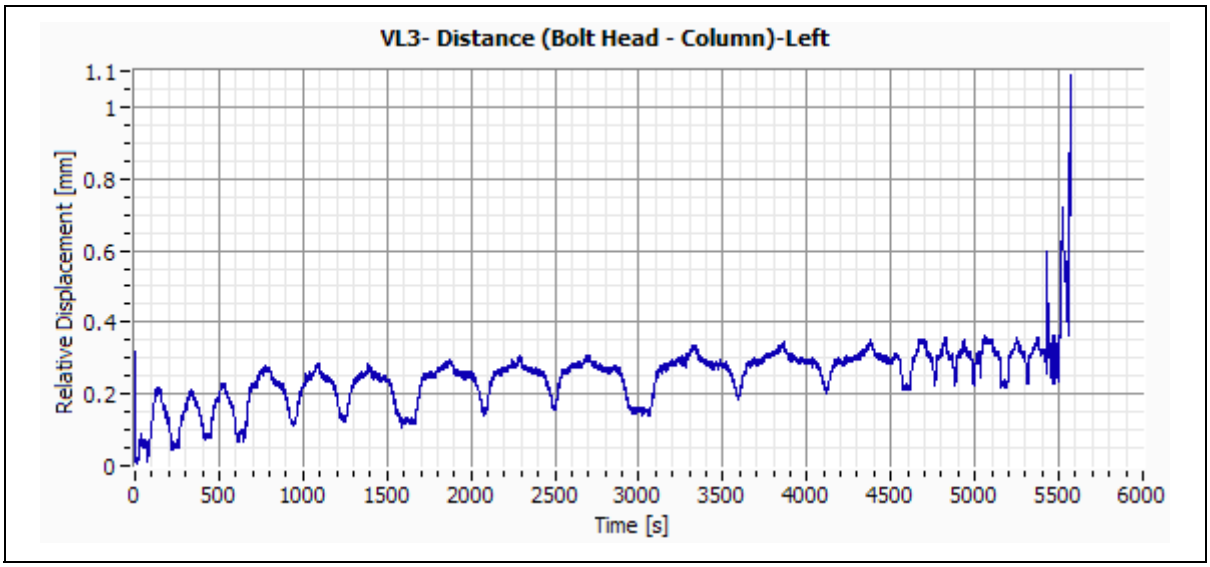

Figure G-70:– Specimen VL3 – Distance (Bolt Head – Column) – Left.

G.13 Specimen VL4

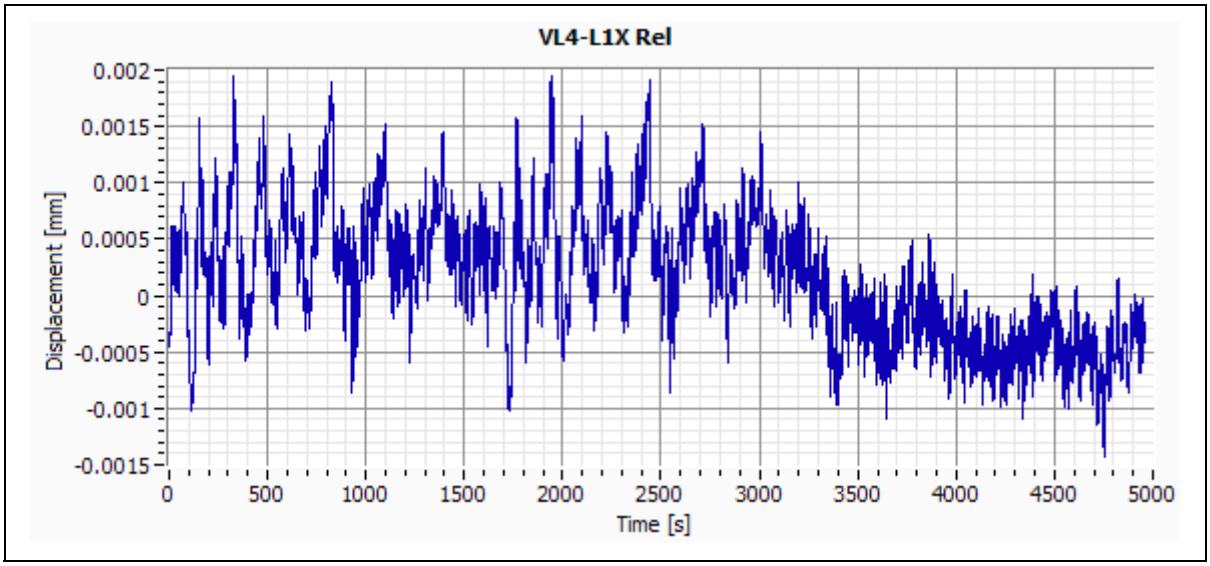

Figure G-71:– Specimen VL4 – Column Central Point Relative Displacement – X Direction.

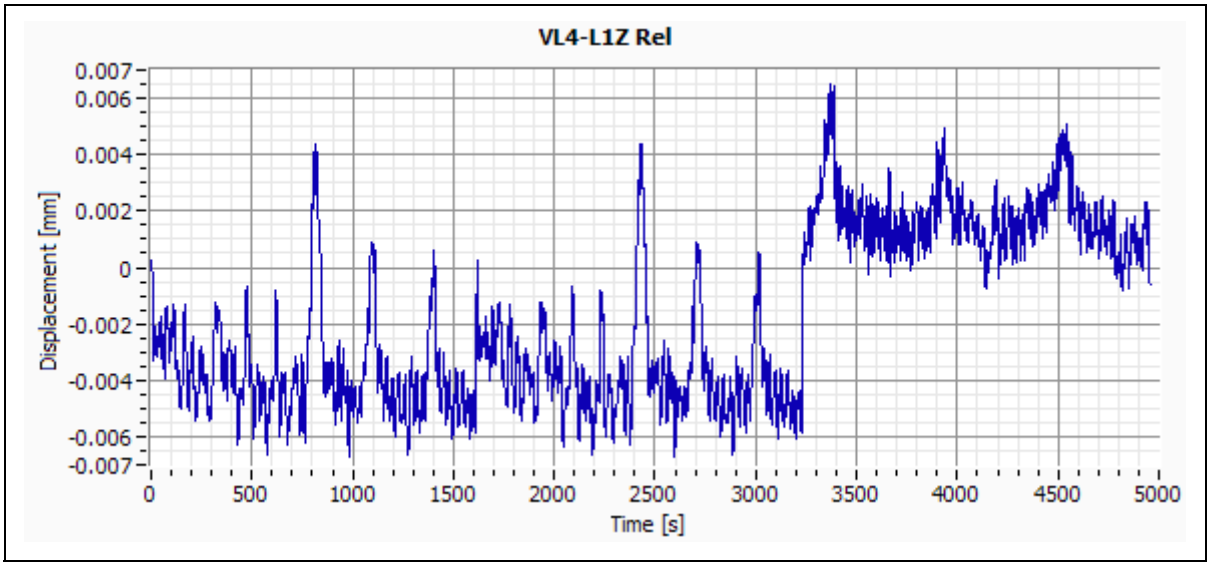

Figure G-72:– Specimen VL4 – Column Central Point Relative Displacement – Z Direction.

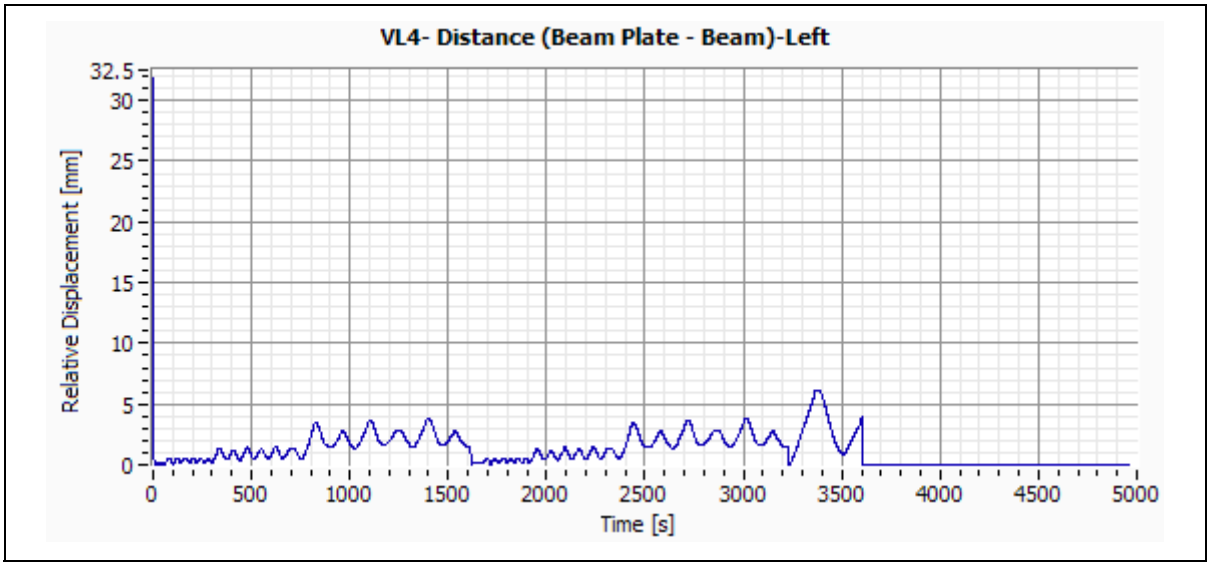

Figure G-73:– Specimen VL4 – Distance (Beam Plate – Beam) – Left.

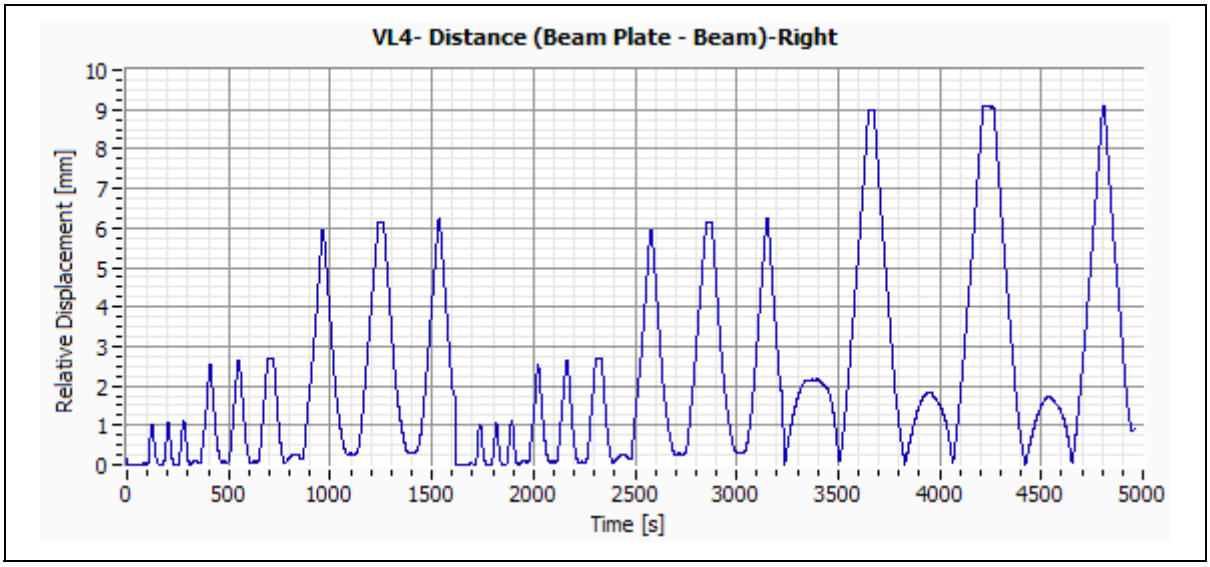

Figure G-74:– Specimen VL4 – Distance (Beam Plate – Beam) – Right.

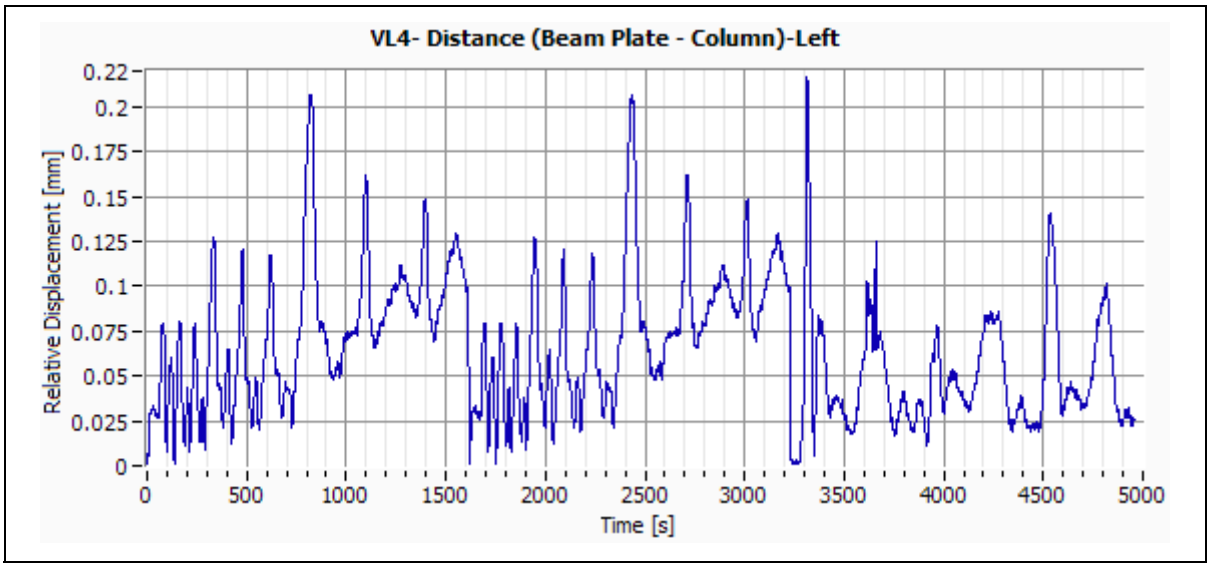

Figure G-75:– Specimen VL4 – Distance (Beam Plate – Column) – Left.

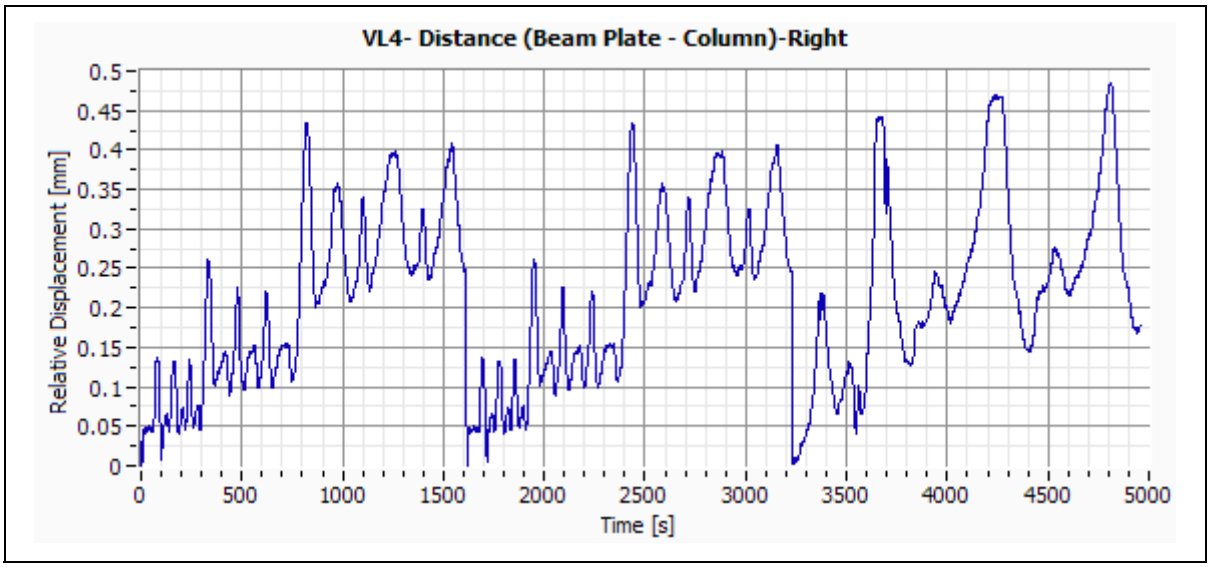

Figure G-76:– Specimen VL4 – Distance (Beam Plate – Column) – Right.

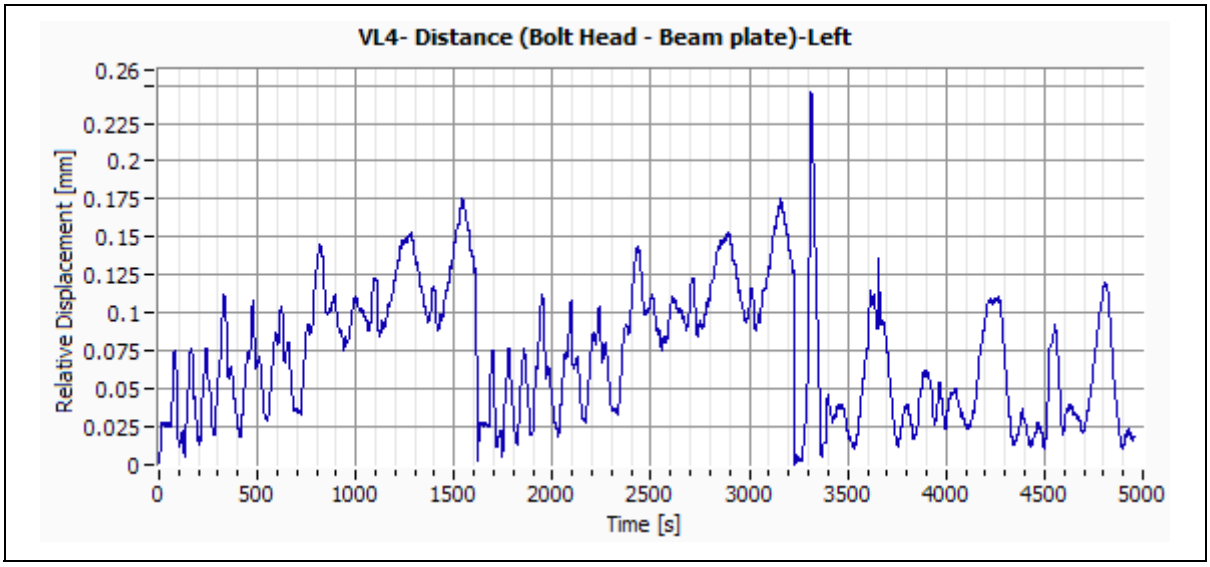

Figure G-77:– Specimen VL4 – Distance (Bolt Head – Beam Plate) – Left..

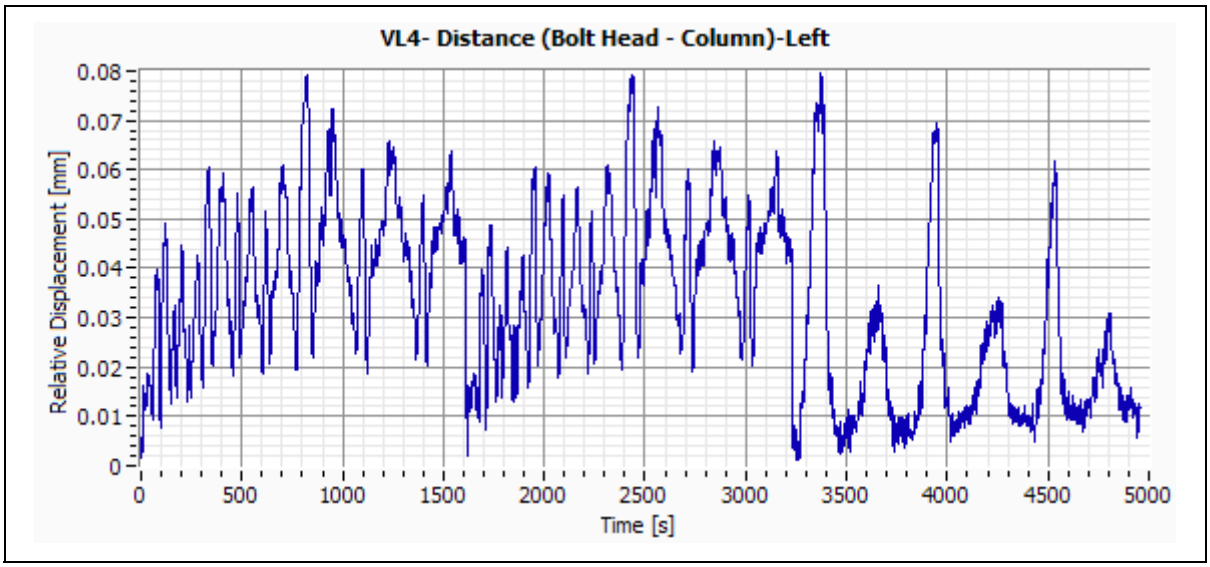

Figure G-78:– Specimen VL4 – Distance (Bolt Head – Column) – Left.

G.14 Specimen VL5

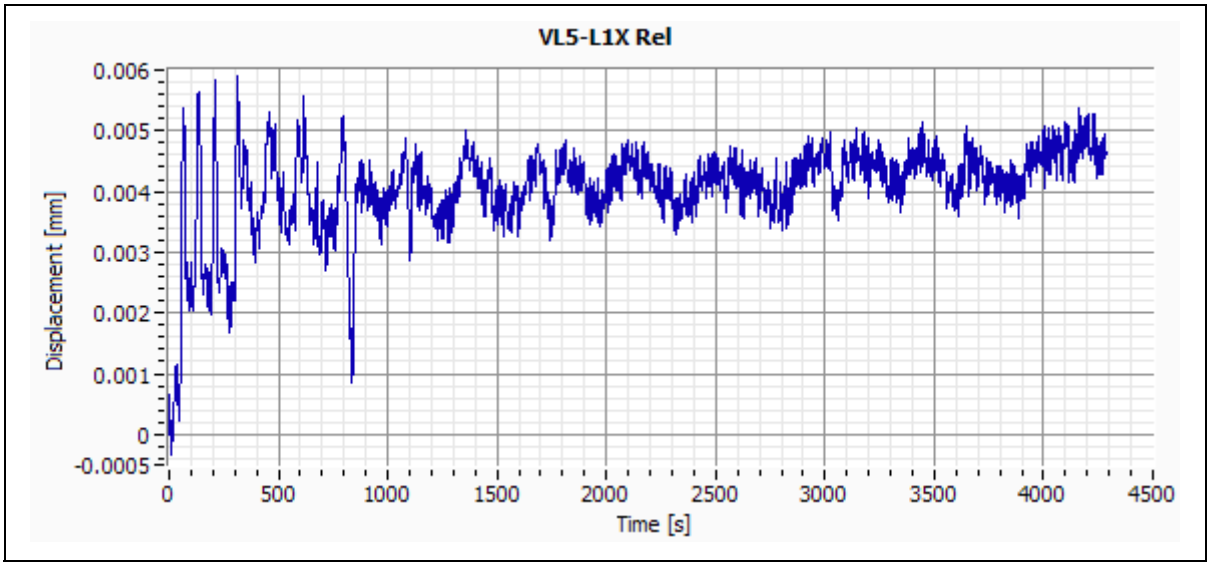

Figure G-79:– Specimen VL5 – Column Central Point Relative Displacement – X Direction.

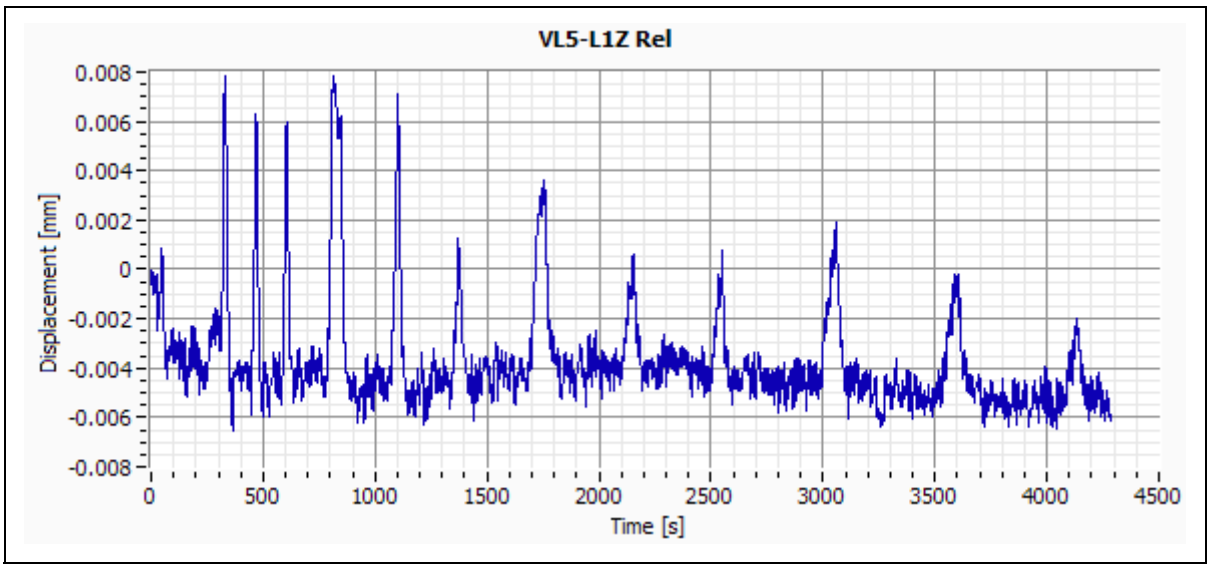

Figure G-80:– Specimen VL5 – Column Central Point Relative Displacement – Z Direction.

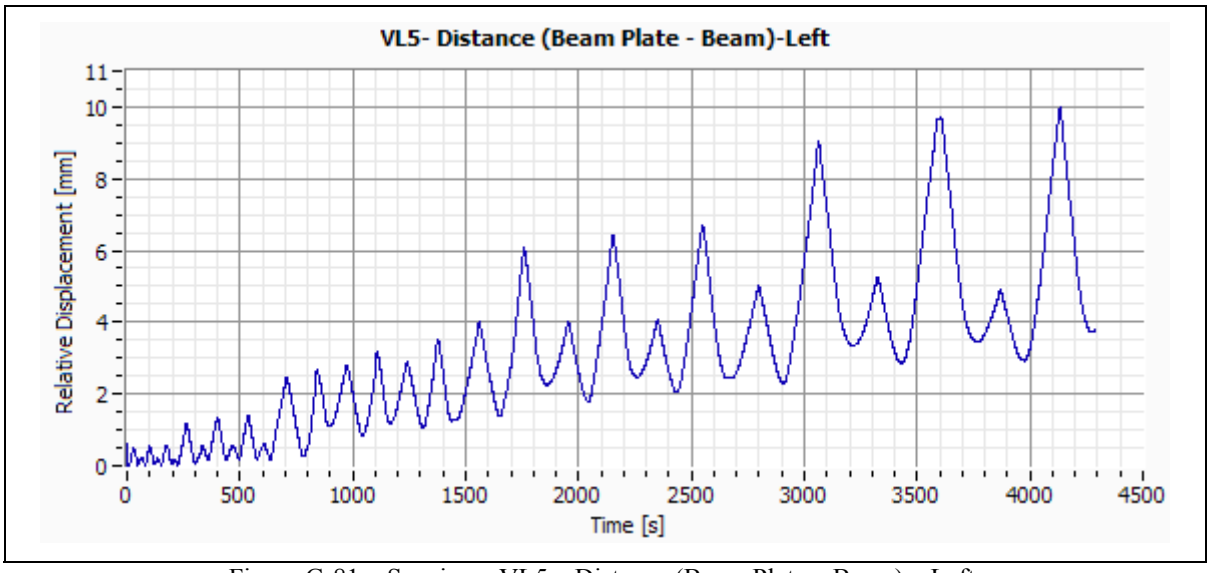

Figure G-81:– Specimen VL5 – Distance (Beam Plate – Beam) – Left.

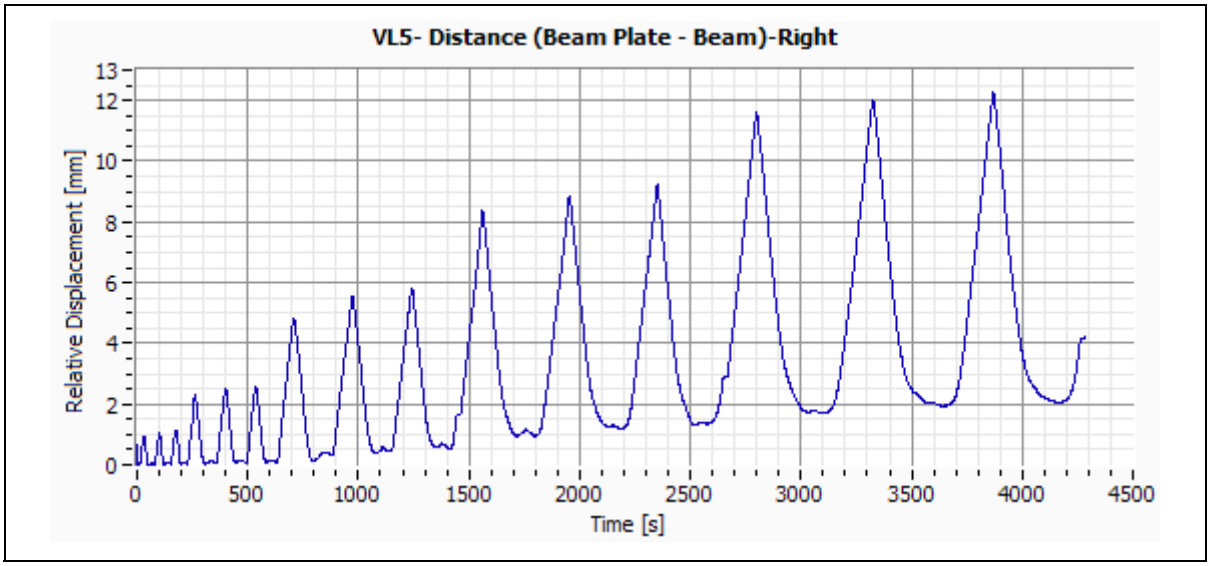

Figure G-82:– Specimen VL5 – Distance (Beam Plate – Beam) – Right.

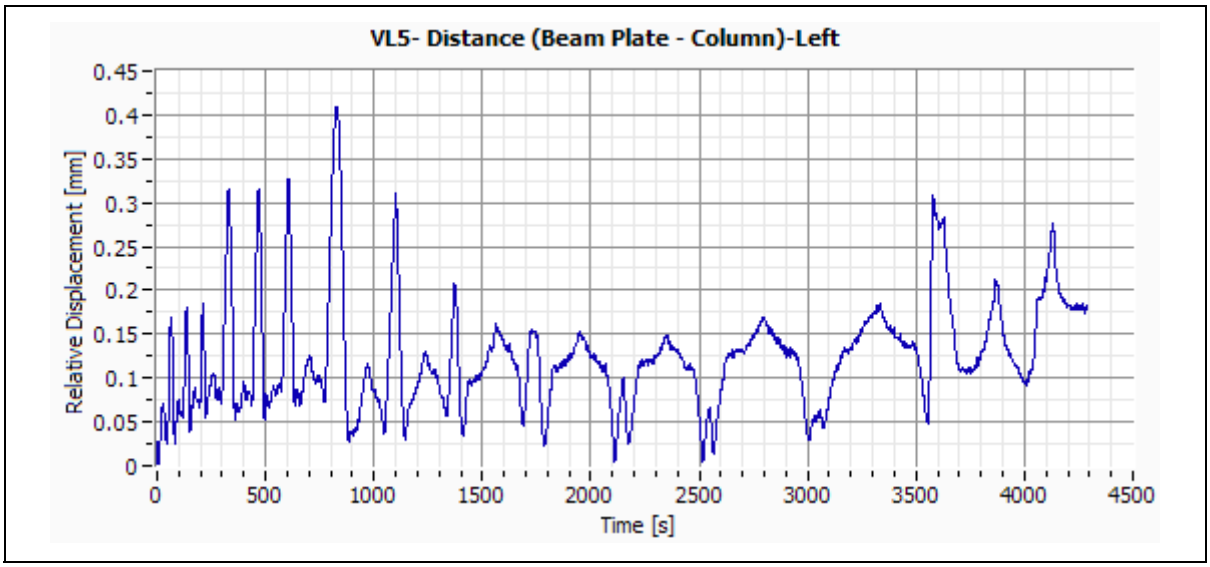

Figure G-83:– Specimen VL5 – Distance (Beam Plate – Column) – Left.

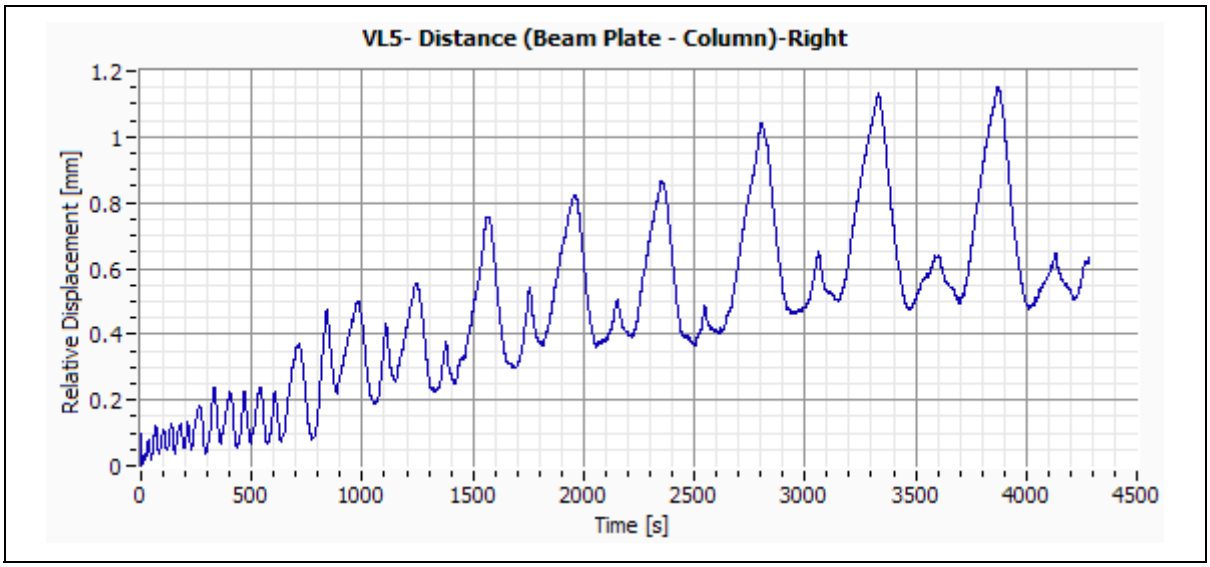

Figure G-84:– Specimen VL5 – Distance (Beam Plate – Column) – Right.

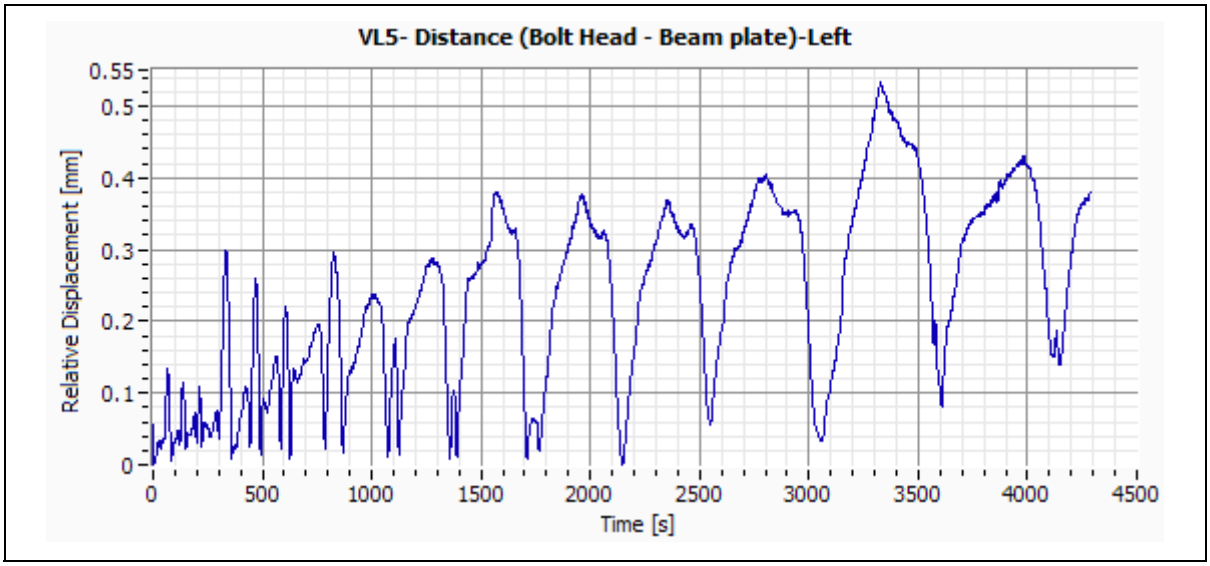

Figure G-85:– Specimen VL5 – Distance (Bolt Head – Beam Plate) – Left..

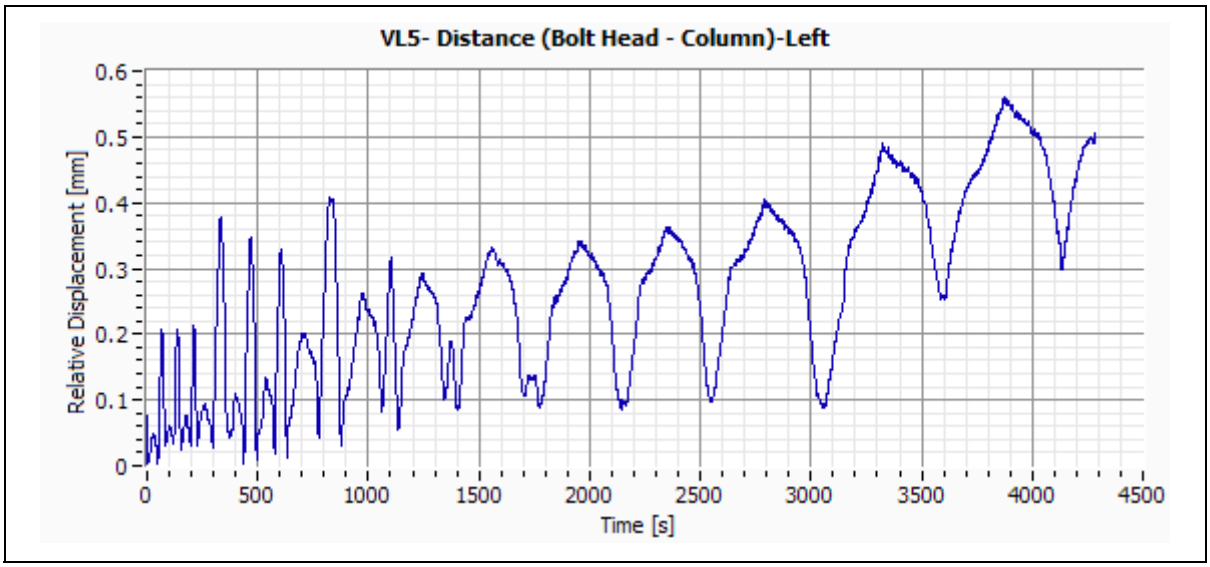

Figure G-86:– Specimen VL5 – Distance (Bolt Head – Column) – Left.

ANNEX H CONNECTIONS MOMENTS AND ROTATIONS

Contents:

List of Figures:

H.1 Specimen P1

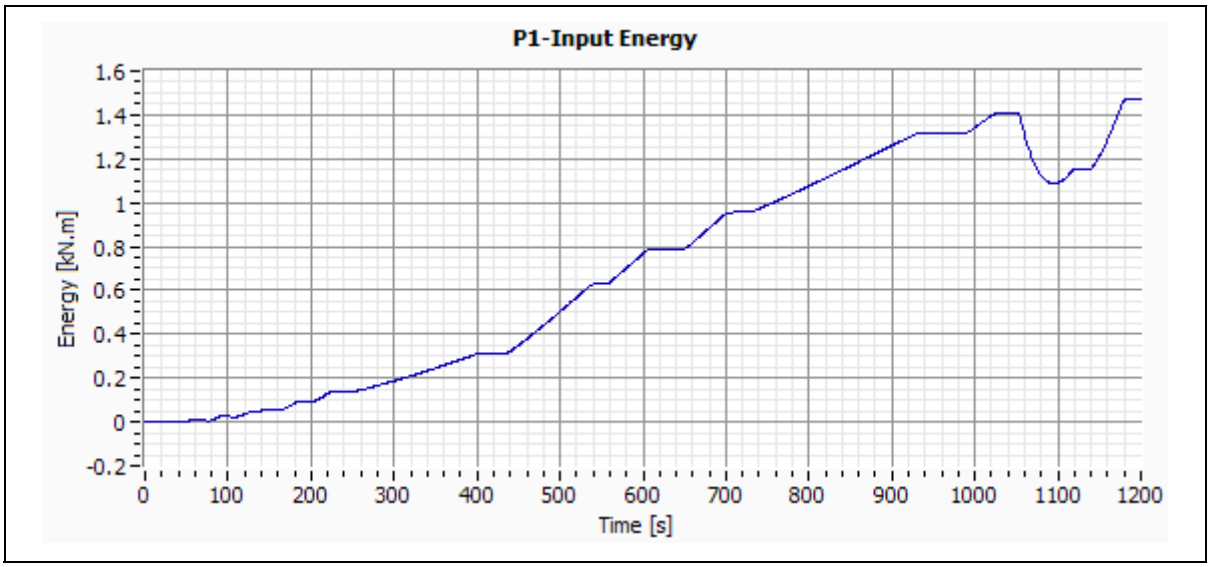

Figure H-1: Specimen P1 – Input Energy.

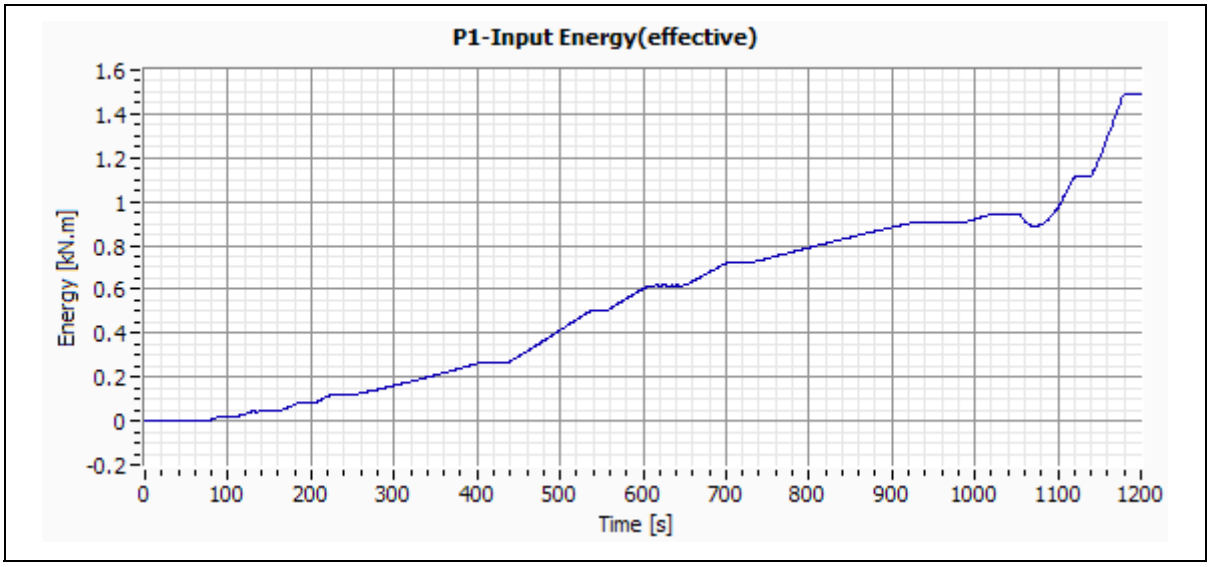

Figure H-2: Specimen P1 – Input Energy (Effective).

H.2 Specimen P2

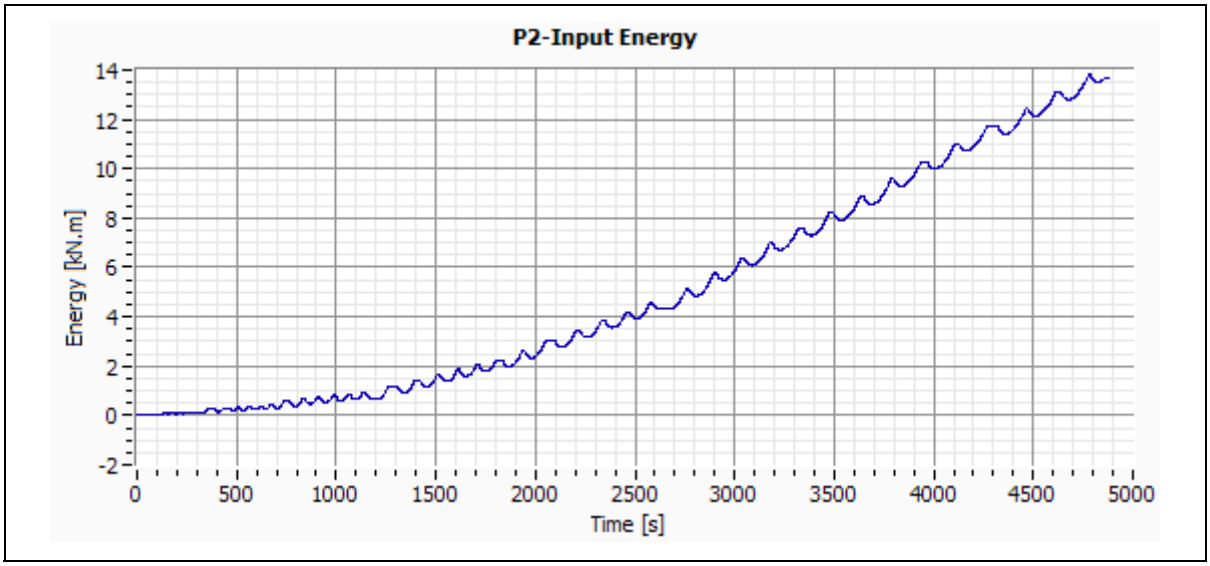

Figure H-3: Specimen P2 – Input Energy.

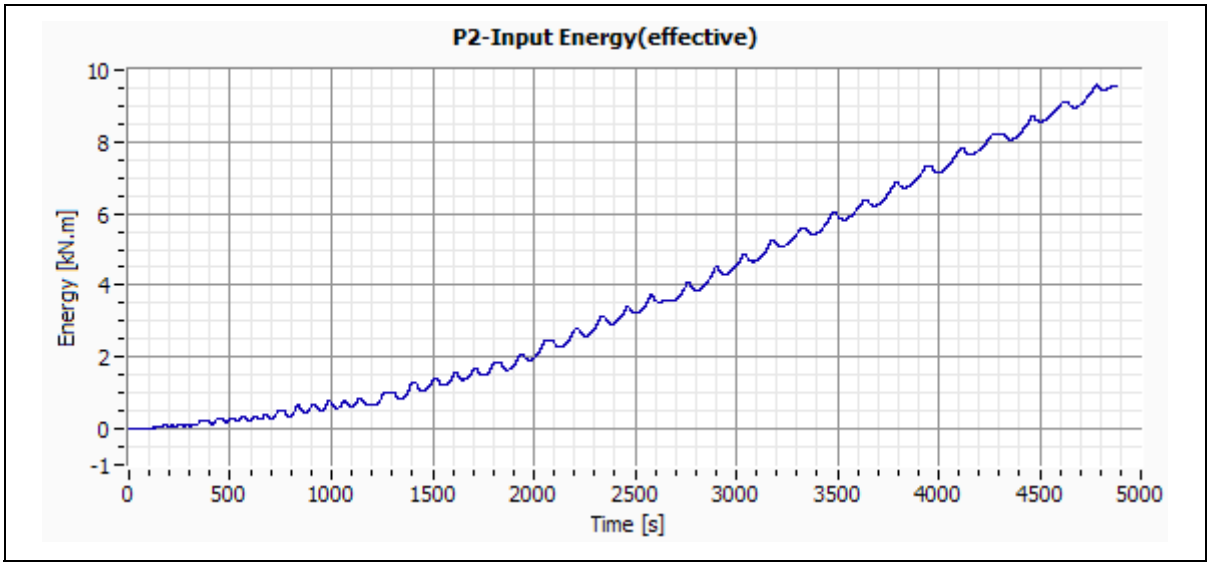

Figure H-4: Specimen P2 – Input Energy (Effective).

H.3 Specimen P3

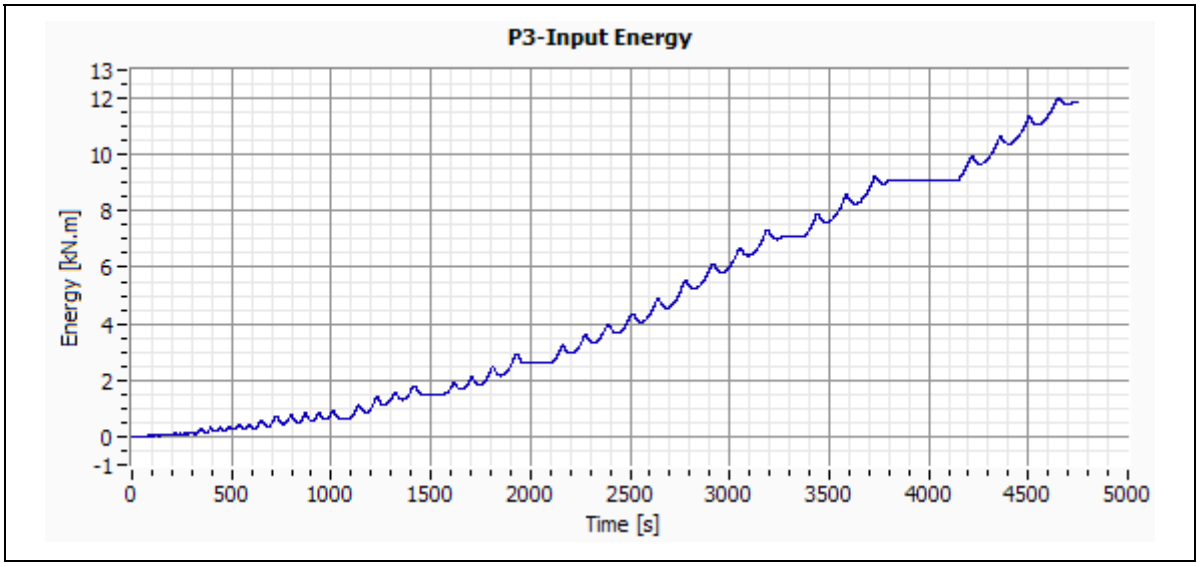

Figure H-5: Specimen P3 – Input Energy.

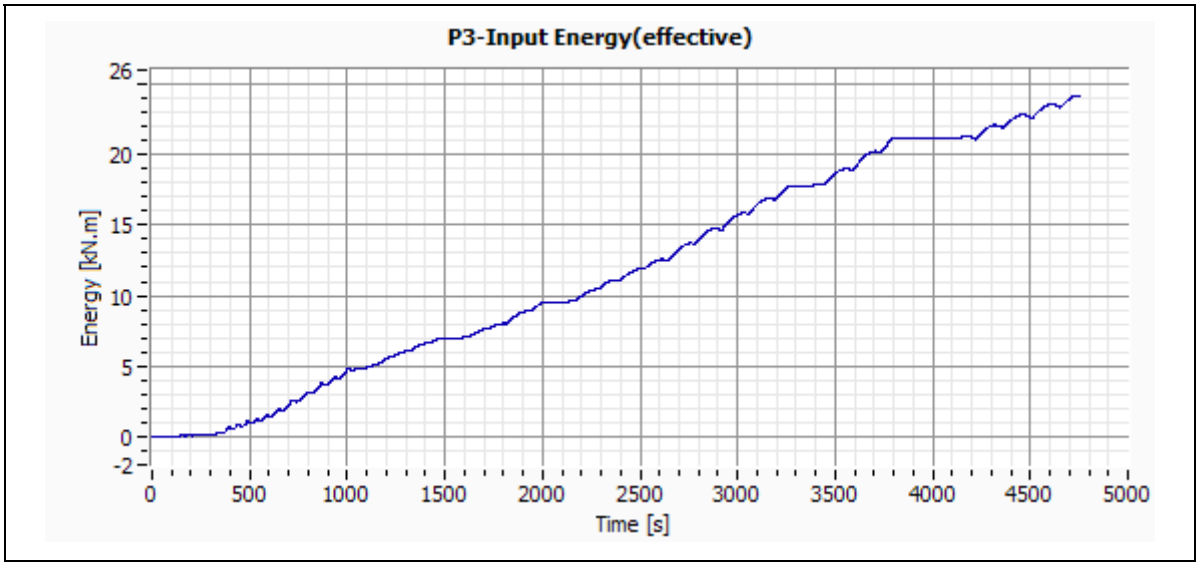

Figure H-6: Specimen P3 – Input Energy (Effective).

H.4 Specimen P4

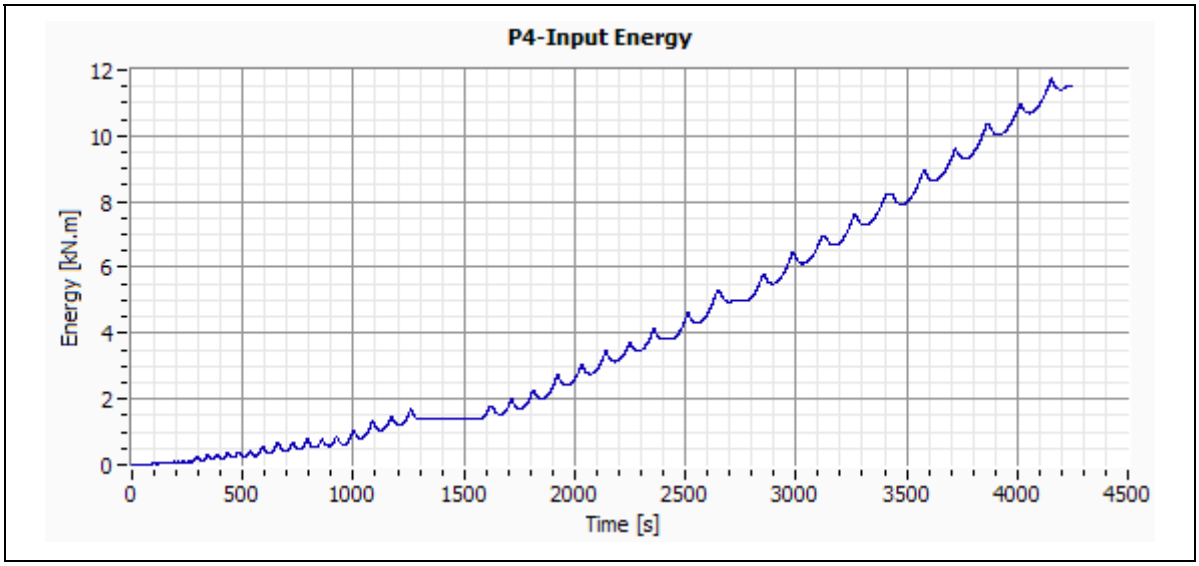

Figure H-7: Specimen P4 – Input Energy.

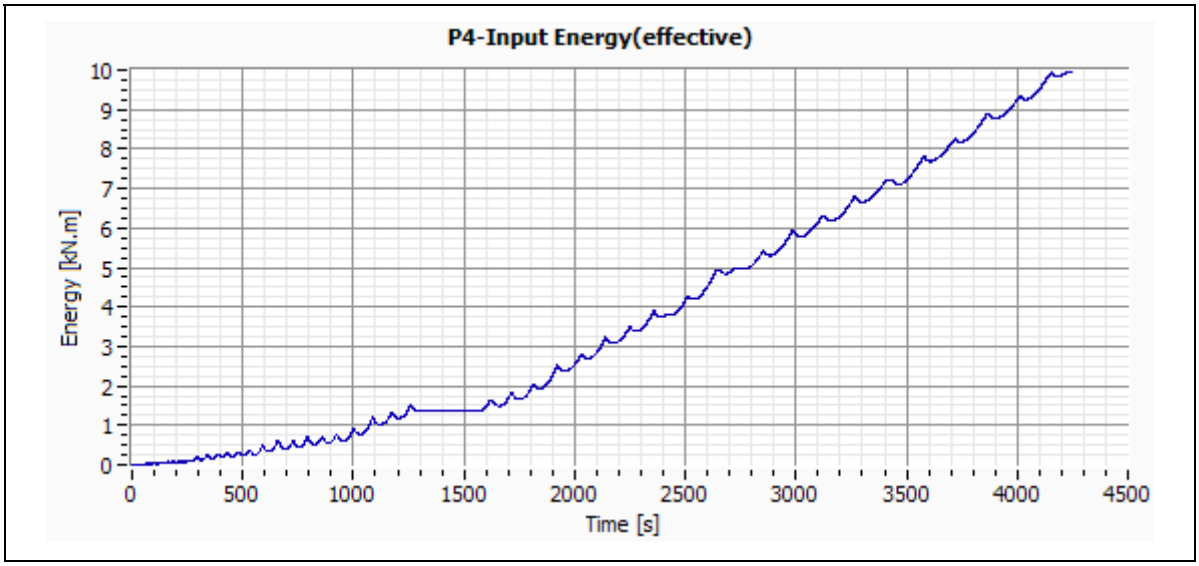

Figure H-8: Specimen P4 – Input Energy (Effective).

H.5 Specimen V1

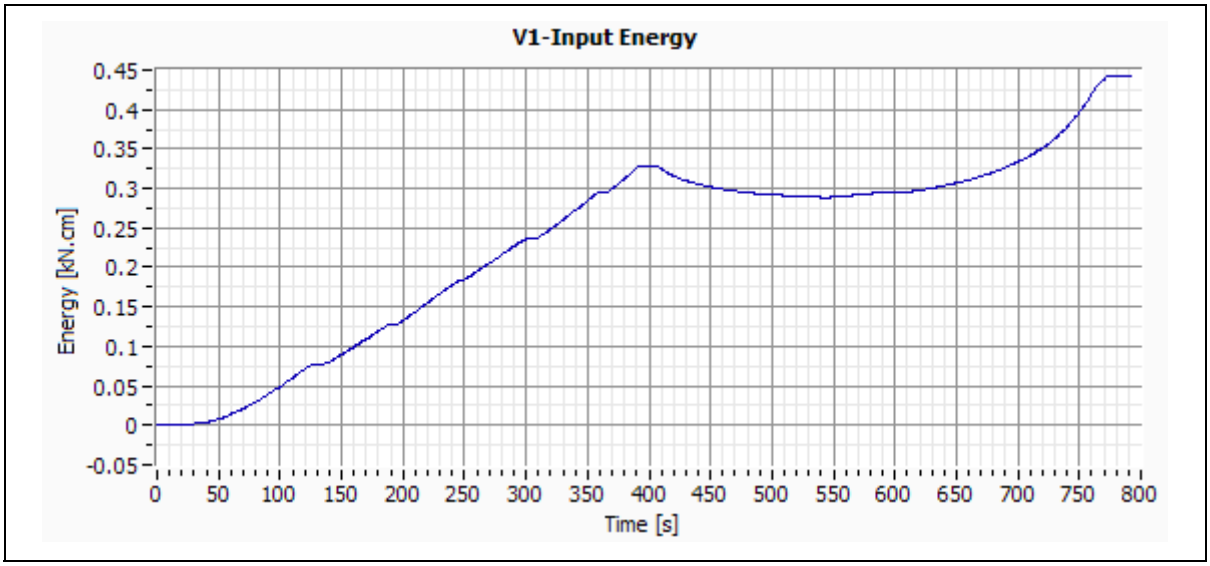

Figure H-9: Specimen V1 – Input Energy.

H.6 Specimen V2

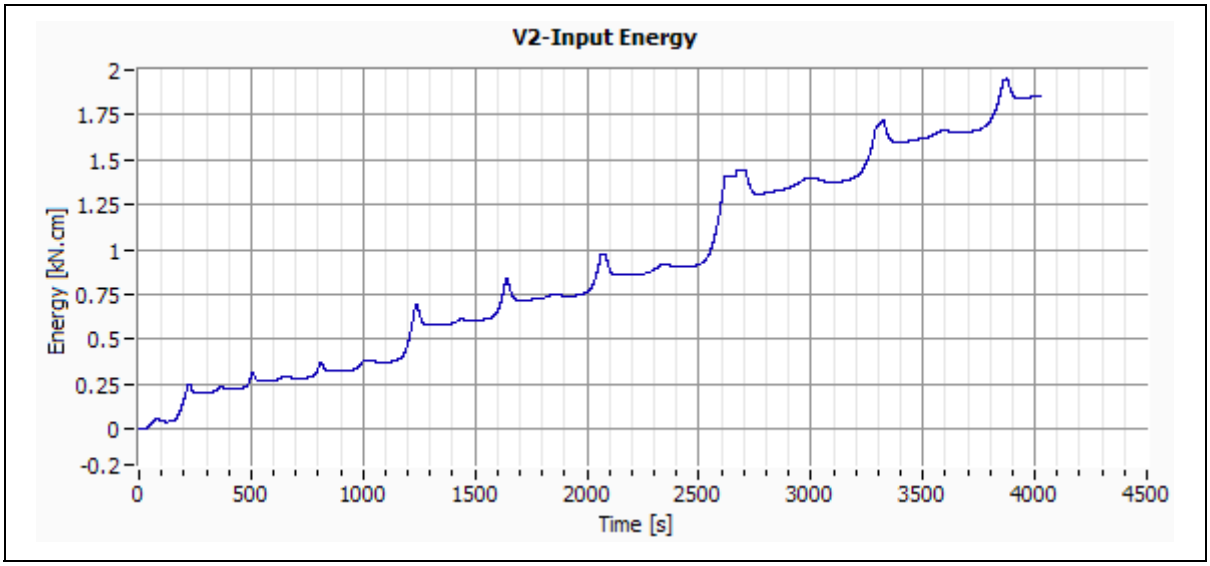

Figure H-10: Specimen V2 – Input Energy.

H.7 Specimen V3

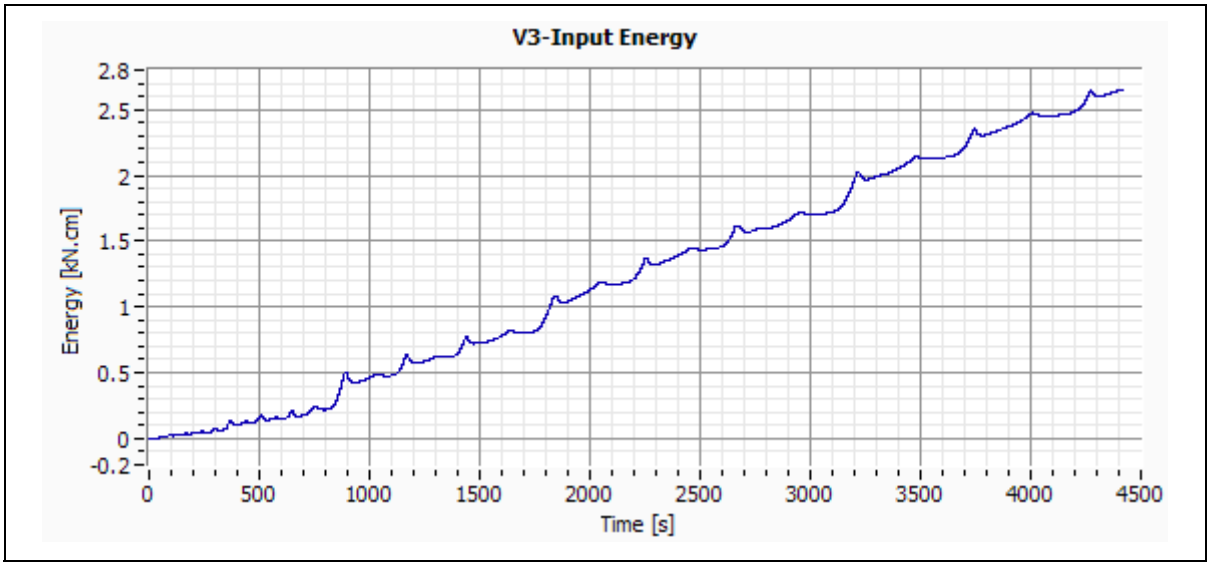

Figure H-11: Specimen V3 – Input Energy.

H.8 Specimen V4

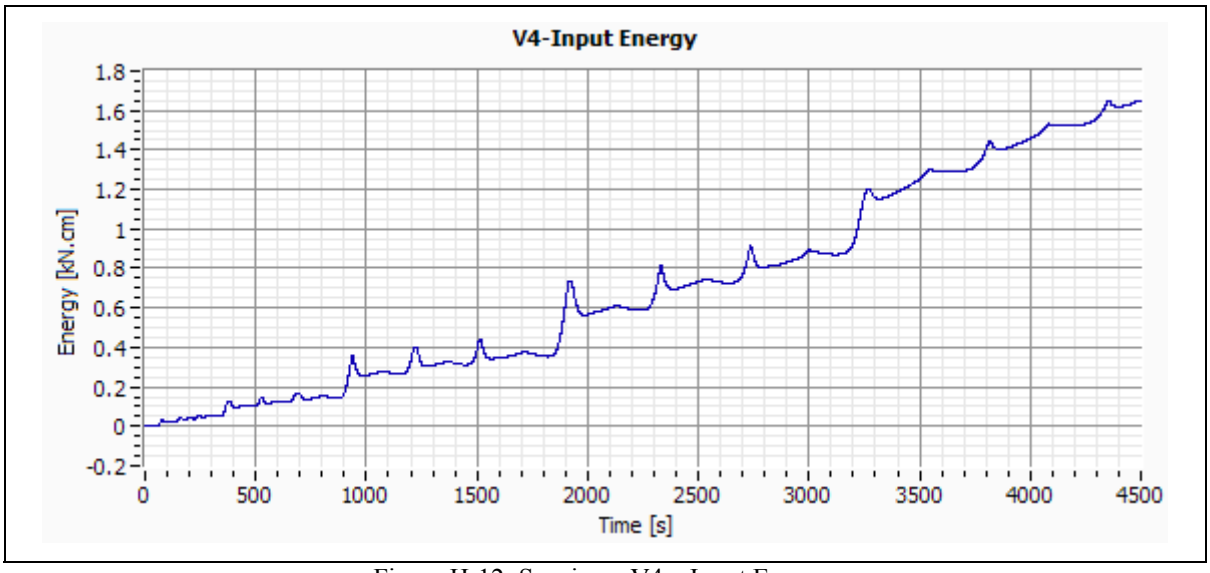

Figure H-12: Specimen V4 – Input Energy.

H.9 Specimen V5

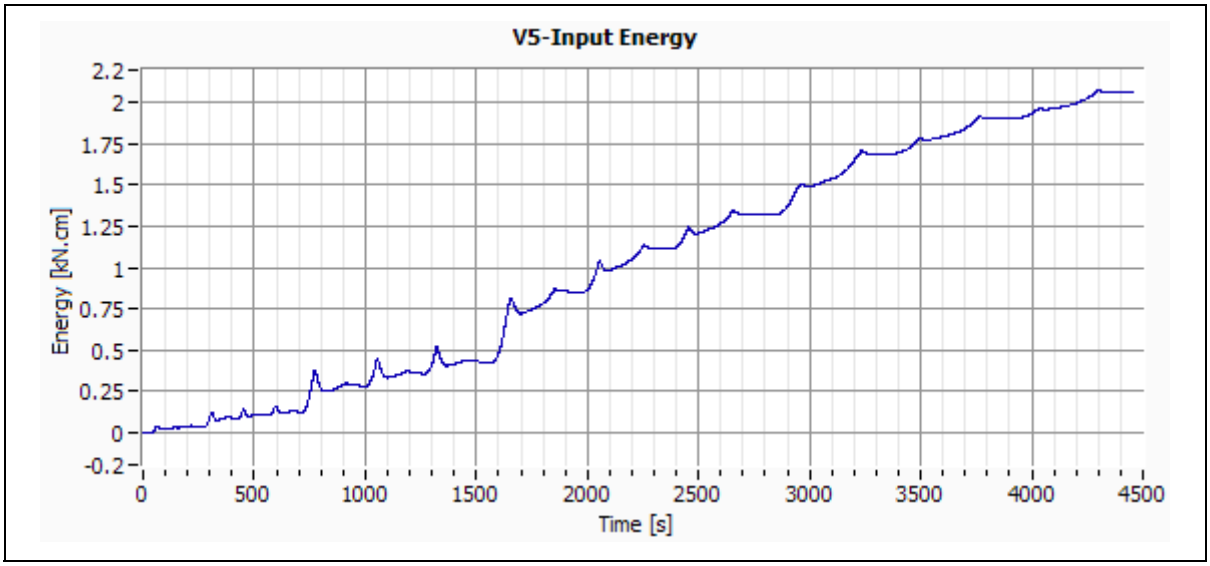

Figure H-13: Specimen V5 – Input Energy.

H.10 Specimen VL1

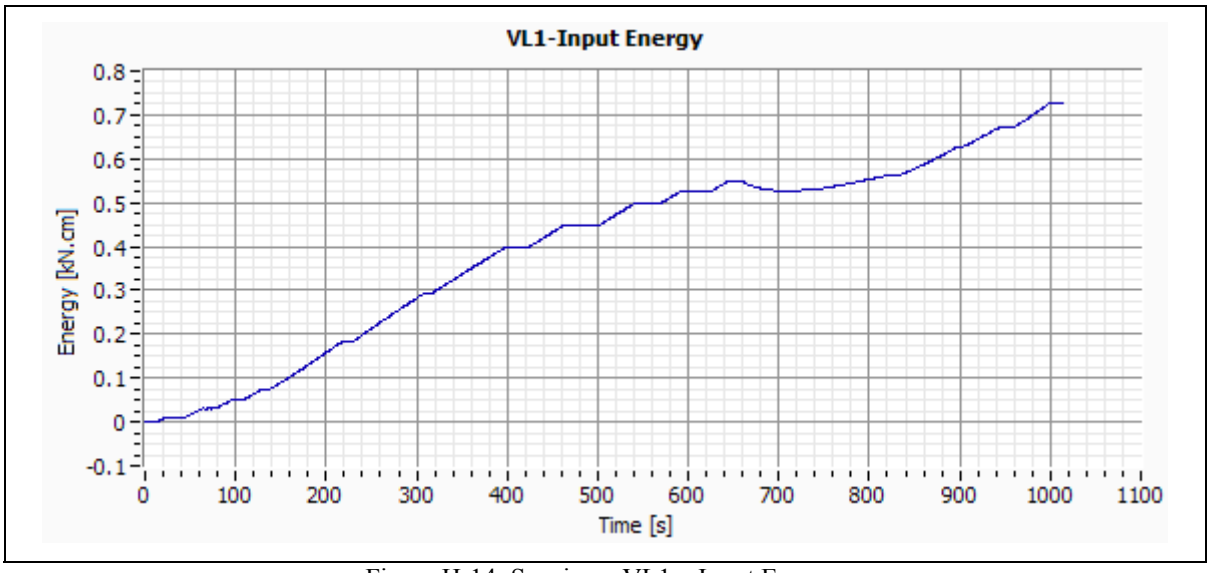

Figure H-14: Specimen VL1 – Input Energy.

H.11 Specimen VL2

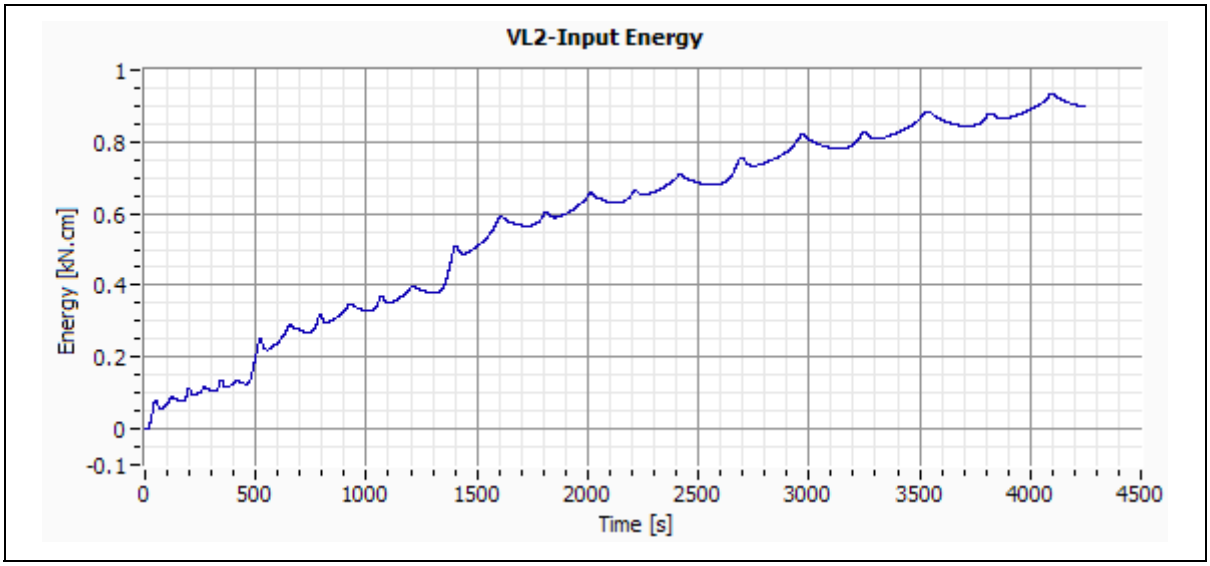

Figure H-15: Specimen VL2 – Input Energy.

H.12 Specimen VL3

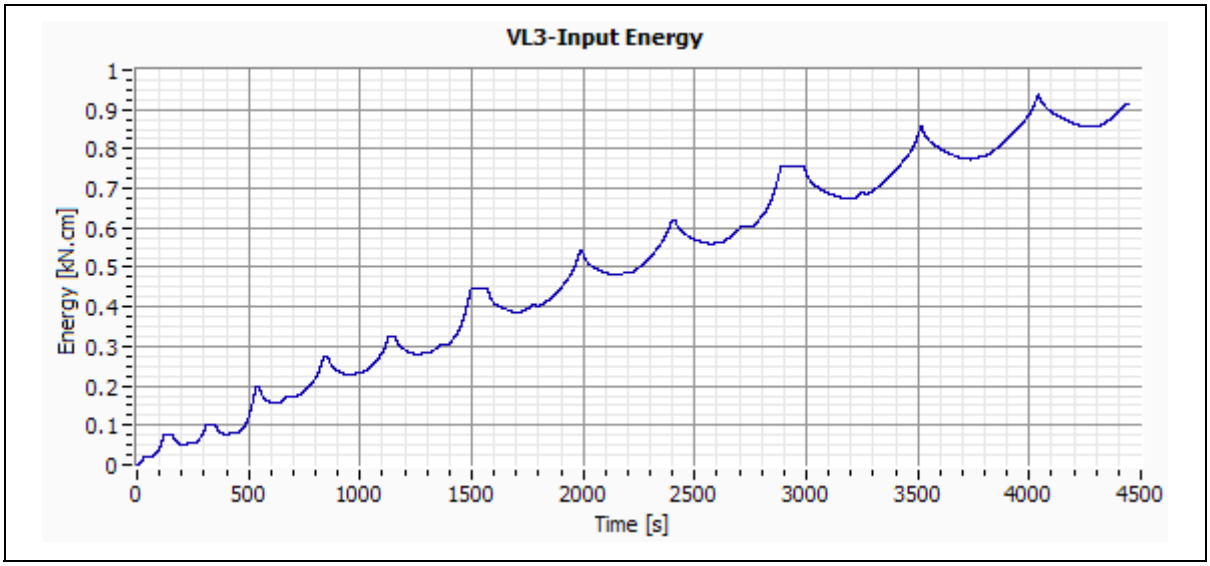

Figure H-16: Specimen VL3 – Input Energy.

H.13 Specimen VL4

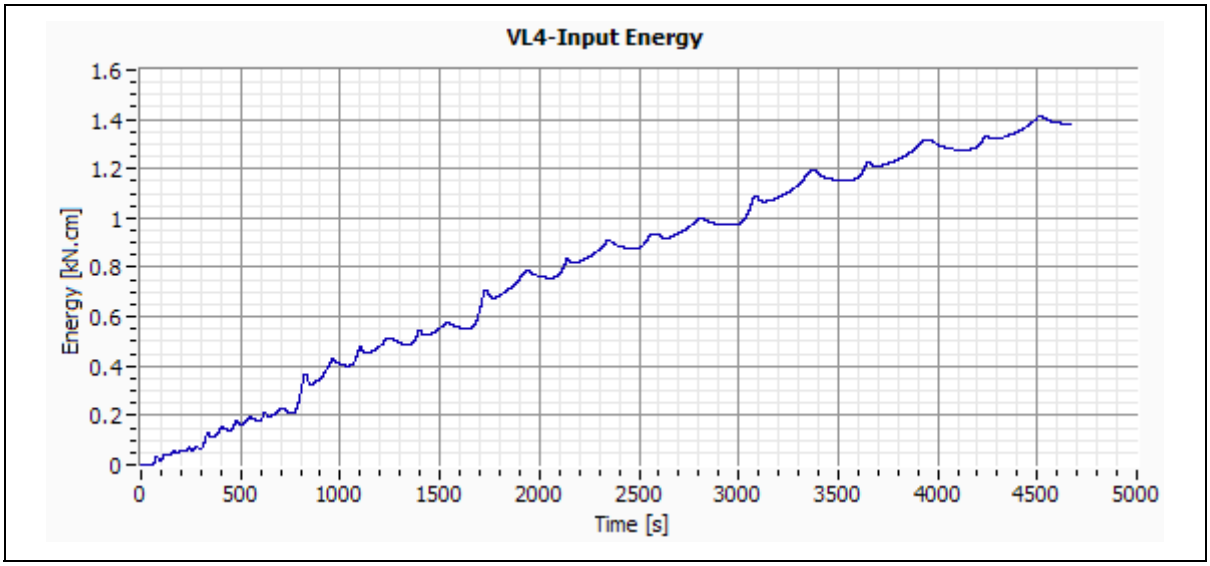

Figure H-17: Specimen VL4 – Input Energy.

H.14 Specimen VL5

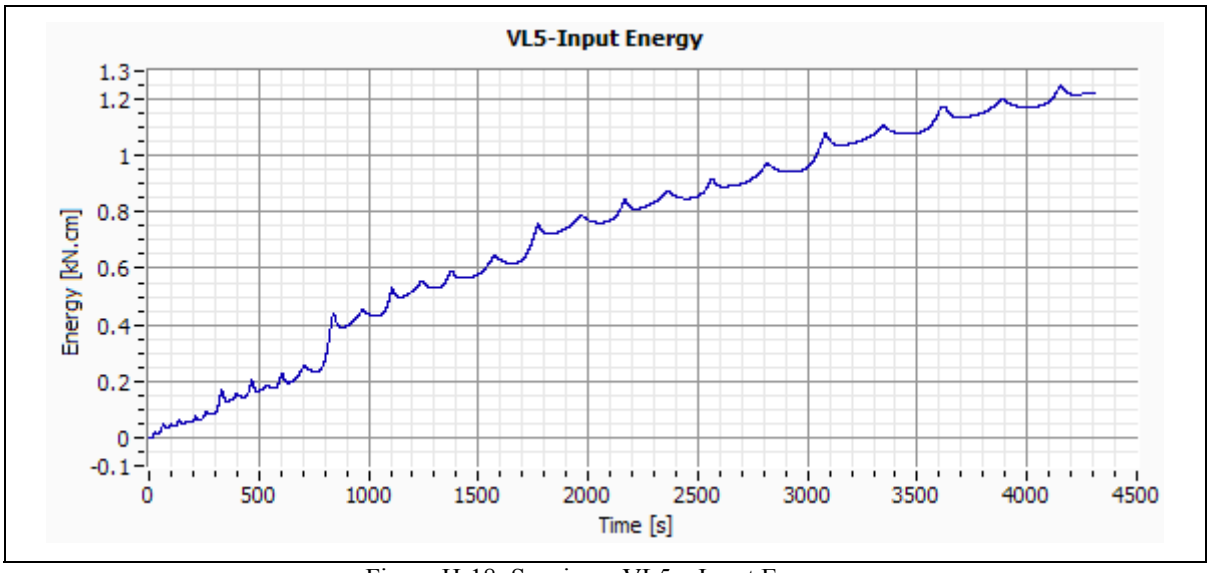

Figure H-18: Specimen VL5 – Input Energy.

Divisão de Edições e Artes Gráficas - LNEC